

**GEOPHYSICAL SITE CHARACTERIZATION OF THE MCQUAT LAKE SYNFORM  
MARY RIVER DISTRICT, BAFFIN ISLAND CANADA**

by

**RYAN FERGUSON**

A thesis submitted in partial fulfilment of the requirements for the degree of

Master of Science

In

Geophysics

Department of Physics

University of Alberta

© Ryan Ferguson, 2018

## ABSTRACT

Arctic drilling programs are expensive and time consuming and deliver very little data regarding the local and regional geological structure. By performing multiple passive and active geophysical surveys, a better understanding of both local and regional geology can be determined. This thesis combines an airborne magnetic survey with a ground based gravity survey and four localized 2D seismic refraction surveys to perform a site analysis and characterization of a subsurface iron ore body to assist in outlining future exploration and mining goals.

Seismic data processing was hindered by poor data quality as a result of a permafrosted surface layer. Strong surface waves propagated quickly through this layer, yielding seismic amplitudes stronger than both the first refraction arrivals and near surface reflections. Ground roll was mitigated using a combination of Ormsby trapezoidal filters, curvelet SVD filters, FK filtering and Radon transforms to improve first arrival amplitudes and selection. Resulting first arrivals were selected and combined with survey geometry to create tomographic and velocity models using Schlumberger VISTA™ Seismic Suite and Optim SEISOPT 2D™.

Refraction tomography and velocity models were compared against magnetic and gravitational inversion models created using Oasis Montaj Geosoft™ and agreements between all datasets were found to be very strong. Potential high-grade zones identified by strong magnetic susceptibility also correlated with high density and high velocity areas. Velocities in both the VISTA and Optim model were higher than expected in deeper regions, an effect likely caused by poor surface static corrections and permafrost alteration of shallower layers. The overall ore body was found to be approximately 250 meters thick and trend east west. The ore body plunges westward at approximately 3 degrees and dips northward at approximately 70 degrees. A final model highlighting overburden thickness was created to determine future mining feasibility and found that the total overburden thickness in the region was a minimum of 80 meters.

## ACKNOWLEDGEMENTS

The completion of this thesis would not have been possible if not for the funding provided by Baffinland Iron Mines Corporation and the research experience and assistance of the University of Alberta's Experimental Geophysics Group. Special thanks go out to Dr. Thomas Iannelli and Mike Zurowski of Baffinland Iron Mines for committing to the support of this Thesis. Extra thanks and recognition go to Project Geologist Meghan Dammeier (MacLeod) for both her assistance in understanding the regional geology of the McQuat Lake Synform, iron ore enrichment processes, and assistance in writing the thesis.

Dr. Douglas Schmitt is thanked for his infallible support and expertise over the entire project, beginning with the grassroots of putting together a survey, being jammed in a small tent for the duration of the survey, and through the processing to the final edits and repeated back and forth emails over all the details both large and small. His infinite patience, jovial attitude, sense of humor, supervision, editing and lab assistance were invaluable, and the project would not have been possible without him. Discussing the finer points of the project with Dr. Schmitt and hammering out all the problems and details over potent potables at the Faculty Club will be fond memories I will cherish.

Additional thanks go out to Dr. Schmitt's Experimental Geophysics Group, a better group of colleagues could not be asked for. Never before has a group of geophysicists been able to consume so many potent potables yet still be able to achieve so much in so little time. Special recognition for this project goes out to Randy Kofman, Oliver Ong, Tariq Mohammed, and Farhanah Mohammed for their invaluable expertise and assistance in the Rock Physics Lab. Further recognition is given to Peter Dao, Ilya Inozemtsev and Mario St-Arnaud for their dedicated assistance in the field during both the survey preparatory work and data collection on Northern Baffin Island.

## TABLE OF CONTENTS

CHAPTER 1	INTRODUCTION .....	1
1.1	STATEMENT OF PURPOSE .....	1
1.2	LOCATION OF MCQUAT LAKE SYNFORM, MARY RIVER CAMP, ACCESS, AND PHYSIOGRAPHY.....	1
1.3	EXPLORATION HISTORY AND PREVIOUS WORK.....	2
CHAPTER 2	BACKGROUND GEOLOGY .....	7
2.1	DOME AND KEEL TECTONICS .....	7
2.2	IRON ORE FORMATIONS .....	8
2.2.1	IRON ORE ENRICHMENT .....	8
2.3	GEOLOGICAL HISTORY OF THE MARY RIVER GROUP AND NORTHERN BAFFIN ISLAND.....	10
2.3.1	REGIONAL GEOLOGY .....	10
2.3.2	COMMITTEE BAY BELT .....	11
2.3.3	MARY RIVER GROUP .....	11
2.3.4	MCQUAT LAKE SYNFORM .....	13
2.4	Summary .....	15
CHAPTER 3	GEOPHYSICAL BACKGROUND, SURVEY DESIGN AND IMPLEMENTATION .....	18
3.1	GEOPHYSICAL BACKGROUND .....	18
3.1.1	SEISMIC REFRACTION.....	18
3.1.2	GRAVITY .....	23
3.1.3	MAGNETISM.....	24
3.2	SURVEY DESIGN.....	27
3.3	SURVEY IMPLEMENTATION .....	29
3.4	CHAPTER SUMMARY .....	32
CHAPTER 4	ROCK PHYSICS .....	34
4.1	INTRODUCTION .....	34
4.1.1	ULTRASONIC MEASUREMENT METHOD .....	34
4.1.2	ULTRASONIC MEASUREMENT RESULTS P WAVE .....	40
4.1.3	ULTRASONIC MEASUREMENT RESULTS S WAVE .....	43
4.2	GRAIN DENSITY MEASUREMENTS.....	43
4.3	MAGNETIC SUSCEPTIBILITY.....	50
4.4	Whole Rock Analysis .....	50
4.4.1	X-RAY FLUORESCENCE.....	50
4.4.2	X-RAY POWDER DIFFRACTION .....	52

4.5 SUMMARY .....	52
CHAPTER 5 MAGNETIC AND GRAVITY INVERSIONS.....	57
5.1 MAGNETIC GRIDDING .....	57
5.1.1 SENSOR AND SURVEY.....	57
5.1.2 RESULTING MAGNETIC FIELD.....	58
5.2 MAGNETIC INVERSION MODEL.....	59
5.2.1 MAGNETIC INVERSION RESULTS.....	60
5.3 GRAVITY GRIDDING.....	63
5.3.1 SENSOR AND SURVEY.....	63
5.3.2 RESULTING BOUGUER ANOMALY .....	65
5.4 GRAVITY INVERSION MODEL .....	66
5.4.1 GRAVITY INVERSION RESULTS.....	67
5.5 SUMMARY .....	67
CHAPTER 6 SEISMIC REFRACTION ACQUISITION AND ANALYSIS.....	71
6.1.1 RAW SEISMIC DATA.....	71
6.1.2 FIRST BREAK PICKS .....	74
6.2.1 ORMSBY TRAPEZOIDAL FILTER.....	75
6.2 FK DOMAIN, RADON TRANSFORMS AND FILTERING .....	75
6.2.1 REFRACTION STATICS.....	75
6.2.2 FREQUENCY WAVENUMBER FILTER.....	79
6.2.4 TAU P FILTER .....	80
6.3 REFRACTION TOMOGRAPHY MODELS.....	82
6.3.1 SEISOPT 2D MODELS .....	82
6.3.2 VISTA SEISMIC SUITE REFRACTION STATIC MODELS .....	84
6.4 SUMMARY .....	94
CHAPTER 7 PROPOSED SITE CHARACTERIZATION MODEL.....	95
7.1 INTRODUCTION.....	95
7.2 REFRACTION MODEL COMPARISON .....	95
7.3 MAGNETIC MODEL COMPARISON .....	102
7.4 BOUGUER ANOMALY MODEL COMPARISON.....	103
7.5 FINAL PROPOSED ORE BODY TOMOGRAPHY.....	110
7.5.1 ROCK PHYSICS INCORPORATION AND HIGH-GRADE ZONES.....	110
7.6 SUMMARY .....	114

CHAPTER 8	CONCLUSIONS AND FINAL OVERBURDEN MODEL.....	115
8.1	INTRODUCTION.....	115
8.2	SITE CHARACTERIZATION MODEL.....	115
8.3	APPLICATIONS.....	117
8.4	FUTURE WORK AND RECOMMENDATIONS.....	117
REFERENCES.....		120
APPENDIX.....		128

## LIST OF FIGURES

FIGURE 1.1: LOCATION OF BAFFIN ISLAND CANADA, MARY RIVER MINING CAMP AND THE MCQUAT LAKE SURVEY SITE. RAW IMAGE SOURCE: WIKIPEDIA COMMONS. ....	3
FIGURE 1.2: MARY RIVER EXPLORATION CAMP.....	4
FIGURE 1.3: BAFFINLAND IRON MINES PRIMARY DEPOSIT LOCATIONS ON REGIONAL GEOLOGY MAP.....	5
FIGURE 2.1: CARTOON SCHEMATIC OF THE EVOLUTION OF DOME AND KEEL TECTONICS.....	7
FIGURE 2.2: SUPERGENE-MODIFIED HYPOGENE ENRICHMENT MODEL BASED ON THE NORTH DEPOSIT OF MOUNT TOM PRICE, AUSTRALIA. ASCENDING BRINES OF DIFFERENT TEMPERATURE ALTER BIF'S AND REMOVE SILICA TO ALTER BIF'S TO ANKERITE AND APATITE. DESCENDING SURFACE WATERS ENRICH IRON TO MARTITE AND HEMATITE AND REMOVE ANKERITE, APATITE AND LEAVES MICROPLATEY HEMATITE. USED WITH PERMISSION FROM CLOUT AND SIMONSON, 2005. ....	9
FIGURE 2.3: REGIONAL GEOLOGY OF THE CHURCHILL PROVINCE. ....	12
FIGURE 2.4: ARCHEAN AND PALEOPROTEROZOIC TERRANES COMPRISING BAFFIN ISLAND, CANADA. ....	14
FIGURE 2.5: STRATIGRAPHIC CORRELATIONS BETWEEN THE MARY RIVER GROUP AT THE 37 G, E, AND H MAP PARCELS, PRINCE ALBERT GROUP, AND WOODBURN LAKE GROUP OF THE COMMITTEE BAY BELT.....	15
FIGURE 2.6 GEOLOGY OF THE MCQUAT LAKE SYNFORM.....	17
FIGURE 3.1: TOP: TOTAL MAGNETIC ANOMALY FIELD .....	29
FIGURE 3.4: TOP: SEISMIC SHOT LOCATIONS REPRESENTED BY CIRCLES OVER MAGNETIC ANOMALY.....	33
FIGURE 4.1: PREPPED CORE PLUGS FROM 18.5 AND 94 METERS DEPTH. ....	35
FIGURE 4.2: 6061 T6 MACHINED ALUMINUM ENDCAP WITH COMPRESSIONAL WAVE PIEZOELECTRIC TRANSDUCER .....	36
FIGURE 4.3: TOP: EXPANDED VIEW OF CORE SAMPLE AND END CAP SET UP RIGHT BEFORE .....	37
FIGURE 4.4: CORE PLUG FROM 126 METERS DEPTH HIGHLIGHTING ORIENTATION ALL CORE PLUGS WERE ALIGNED TO.....	39
FIGURE 6.8: TOP: LINE 2 SHOT 98 SHOT GATHER AFTER TAU-P FILTER APPLIED TO REMOVE LINEAR (CONSTANT .....	39
FIGURE 4.5: ULTRASONIC COMPRESSIONAL WAVEFORMS FOR CORE PLUG FROM 18.3 METERS. ....	41
FIGURE 4.5: CALIBRATED ULTRASONIC P WAVE VELOCITIES VS. CONFINING PRESSURE FROM CORE PLUGS.....	44
FIGURE 4.7: ULTRASONIC SA WAVE VELOCITY VS. HYDROSTATIC CONFINING PRESSURE FOR ALL CORE PLUG SAMPLES.....	45
FIGURE 4.8: ULTRASONIC Sb WAVE VELOCITY VS. HYDROSTATIC CONFINING PRESSURE FOR ALL CORE PLUG SAMPLES .....	46
FIGURE 4.9: XRD SPECTRUM FOR CORE SAMPLE 37.2 M. ....	55
FIGURE 4.9: XRD SPECTRUM FOR CORE SAMPLE 37.2 M. ....	55
FIGURE 4.10: XRD SPECTRUM FOR CORE SAMPLE 94.2 M. ....	56
FIGURE 5.1: TOTAL MAGNETIC INDUCTION (TMI) FIELD FOR REGION WEST OF DEPOSIT 4 AND THE CENTRAL BORDEN FAULT.....	58
FIGURE 5.2: MAGNETIC SUSCEPTIBILITY MODEL SHOWING MAGNETIC SUSCEPTIBILITY VALUES OF 0.3 SI AND GREATER ....	61

FIGURE 5.3: MAGNETIC SUSCEPTIBILITY MODEL HIGHLIGHTING THE TWO POSSIBLE HIGH-GRADE ZONES. ....	62
FIGURE 5.4: HIGH RESOLUTION SUSCEPTIBILITY CLOSE UP OF POTENTIAL HIGH-GRADE ZONE. ....	64
FIGURE 5.6: BOUGER ANOMALY OVERLAYING THE MAGNETIC ANOMALY.....	66
FIGURE 5.7: DENSITY MODEL OF THE SUBSURFACE ORE BODY. ....	69
FIGURE 5.8: DENSITY MODEL OF THE SUSPECTED HIGH-GRADE ZONE WITH HIGHER DENSITIES. ....	70
FIGURE 6.1: RAW SEISMIC SHOT GATHER FROM LINE 2. 250 MS AGC. IT IS IMPORTANT TO NOTICE THAT EXCEPTIONALLY STRONG SURFACE WAVES CLOSELY FOLLOW FIRST ARRIVALS. ....	72
FIGURE 6.2: TOP: NEAR OFFSET FIRST BREAK SELECTION FOR LINE 2 RUNNING EAST-WEST. NEAR OFFSETS EXHIBIT 2 DISTINCT VELOCITY SLOPES OF APPROXIMATELY 2800 M/S AND 4500 M/S. SHINGLING EFFECT IS NOTICED ON THE WESTERN SIDE OF THE LINE CAUSED BY A LARGE ROCKY CLIFF. ....	76
FIGURE 6.5: REFRACTION STATICS AND TOMOGRAPHY ANALYSIS.....	78
FIGURE 6.4: WATERFALL DIAGRAM OF ALL TRACES IN LINE 2 SHOT 98.....	78
FIGURE 6.6: LEFT: FK DOMAIN FOR LINE 2 SHOT 98. ....	79
FIGURE 6.7: TOP: SHOT GATHER FROM LINE 2 SHOT 98 AFTER FK FILTER, 15/25/70/85 HZ ORMSBY FILTER, AND 250 MS AGC APPLIED.....	81
FIGURE 6.8: TOP: LINE 2 SHOT 98 SHOT GATHER AFTER TAU-P FILTER APPLIED TO REMOVE LINEAR (CONSTANT .....)	83
FIGURE 6.9: LINE 2 VELOCITY MODEL FROM SEISOPT 2D TOMOGRAPHY SOFTWARE. ....	86
FIGURE 6.10: LINE 3 VELOCITY MODEL FROM SEISOPT 2D TOMOGRAPHY SOFTWARE. ....	87
FIGURE 6.11: LINE 4 VELOCITY MODEL FROM SEISOPT 2D TOMOGRAPHY SOFTWARE .....)	88
FIGURE 6.12: LINE 5 VELOCITY MODEL FROM SEISOPT 2D TOMOGRAPHY SOFTWARE. ....	89
FIGURE 6.13: LINE 2 TOMOGRAPHY MODEL FROM VISTA SEISMIC SUITE. MODEL RUNS EAST (FIELD STATION 1) TO WEST (FIELD STATION 240).....	90
FIGURE 6.14: LINE 3 TOMOGRAPHY MODEL FROM VISTA SEISMIC SUITE. ....	91
FIGURE 6.15: LINE 4 TOMOGRAPHY MODEL FROM VISTA SEISMIC SUITE. ....	92
FIGURE 6.16: LINE 5 TOMOGRAPHY MODEL FROM VISTA SEISMIC SUITE. ....	93
FIGURE 3.4 REVIEW: QUICK REFERENCE OF SURVEY LINES (GREEN) OVERLAYING ALL SHOT LOCATIONS (CIRCLES). ....	96
FIGURE 7.1: LINE 2 VELOCITY AND TOMOGRAPHY MODEL .....)	98
FIGURE 7.2: LINE 3 VELOCITY AND TOMOGRAPHY MODEL .....)	99
FIGURE 7.3: LINE 4 VELOCITY AND TOMOGRAPHY MODEL .....)	100
FIGURE 7.4: LINE 5 VELOCITY AND TOMOGRAPHY MODEL .....)	101
FIGURE 7.5: SEISOPT 2D SEISMIC SECTIONS LINED UP OVER MAGNETIC ANOMALY. ....	104
FIGURE 7.6: SEISOPT 2D SEISMIC LINE 4 INTERSECTING IRON ORE BODY.....	105
FIGURE 7.7: SEISOPT 2D SEISMIC LINE 5 INTERSECTING IRON ORE BODY.....	106

FIGURE 7.8: SEISOPT 2D SEISMIC LINE 3 INTERSECTING IRON ORE BODY.....	107
FIGURE 7.9: ORE SURFACE AS ESTIMATED USING VISTA SEISMIC TOMOGRAPHY.....	108
FIGURE 7.10: TOP: ORE BODY SURFACE OVERLAYING MAGNETIC SUSCEPTIBILITY MODEL.....	109
FIGURE 7.11: TOP: ORE BODY SURFACE OVERLAYING GRAVITY DENSITY MODEL. RELATIVE.....	112
FIGURE 7.12: VISTA SEISMIC SUITE MODELLED SUBTERRANEAN SURFACES FOR THE FRACTURED FROZEN LIMESTONE LAYER (TOP) AND THE SOLID LIMESTONE LAYER (BOTTOM).....	113
FIGURE 8.1: FINAL OVERBURDEN THICKNESS MODEL. ....	116

**LIST OF TABLES**

TABLE 3.1: LIST OF LOCAL MINERALS AND THEIR MAGNETIC SUSCEPTIBILITIES .....	25
TABLE 4.1: PHYSICAL PROPERTIES OF CORE SAMPLES.....	48
TABLE 4.2: ULTRASONIC VELOCITIES OF CORE SAMPLES .....	49
TABLE 4.3: MAGNETIC SUSCEPTIBILITIES OF CORE SAMPLES THROUGH ENTIRE BOREHOLE .....	51
TABLE 4.4: XRF RESULTS OF CORE SAMPLES FROM ALS MINERALS.....	53
TABLE 4.5: XRD ASSEMBLAGES OF CORE SAMPLES .....	54

## LIST OF EQUATIONS

EQUATION 3.1: SNELL'S LAW .....	18
EQUATION 3.2: CRITICAL REFRACTION ANGLE .....	18
EQUATION 3.3: REFRACTION TRAVEL TIME FOR FLAT LAYER CASE .....	19
EQUATION 3.4: FORWARD MODELLED TRAVEL TIME FOR RAY TRAVELLING THROUGH CELL STRUCTURE OF DISCONTINUOUS VELOCITIES .....	20
EQUATION 3.5: FORWARD MODELLED TRAVEL TIME FOR RAY TRAVELLING THROUGH CELL STRUCTURE OF DISCONTINUOUS SLOWNESS'S .....	20
EQUATION 3.6: LINEARIZED SYSTEM OF EQUATIONS FOR FORWARD MODELLED TRAVEL TIMES .....	20
EQUATION 3.7: STANDARD FORMAT OF LINEARIZED INVERSIONS .....	21
EQUATION 3.8: LINEAR INVERSION MODEL FOR VELOCITY ARRAY .....	21
EQUATION 3.9: SINGULAR VALUE DECOMPOSITION OF PATH LENGTH MATRIX FROM EQUATION 3.8 .....	21
EQUATION 3.10: VELOCITY INVERSION WITH DAMPING PARAMETER .....	21
EQUATION 3.11: SIMPLIFIED DAMPED SINGULAR VALUE DECOMPOSITION INVERSION .....	21
EQUATION 3.12: DAMPED ITERATIVE STATIONARY RECONSTRUCTION TECHNIQUE .....	21
EQUATION 3.13: DAMPED ITERATIVE STATIONARY RECONSTRUCTION TECHNIQUE VARIABLES .....	22
EQUATION 3.14: DAMPED LEAST SQUARES SOLUTION FOR VELOCITY INVERSION FROM DAMPED ITERATIVE STATIONARY RECONSTRUCTION TECHNIQUE .....	22
EQUATION 3.15: SUCESSIVE QUADRATIC MINIMIZATION OF VELOCITY MODEL DISCREPANCY .....	22
EQUATION 3.16: MINIMIZATION OF FORWARD MODELLED DATA WITH MEASURED DATA .....	22
EQUATION 3.17: REGULARIZATION PARAMETER FOR EQUATION 3.15 .....	22
EQUATION 3.18: INVERSION EQUATION USED BY VISTA SEISMIC SUITE .....	22
EQUATION 3.19: VERTICAL COMPONENT OF GRAVITATION FIELD AT POINT I .....	23
EQUATION 3.20: LINEARIZATION OF GRAVITY FIELD CONTRIBUTIONS FROM EQUATION 3.19 .....	24
EQUATION 3.21: QUANTIFICATION OF DENSITY CELL TO TOTAL BOUGUER FIELD .....	24
EQUATION 3.22: MISFIT EQUATION FOR BOUGUER FORWARD MODELLING WITH MEASURED DATA .....	24
EQUATION 3.23: FORWARD MAGNETIC FIELD EQUATION .....	26
EQUATION 3.24: TOTAL MAGNETIC FIELD AT POINT I CAUSED BY CELL STRUCTURE OF MAGNETIC SUSCEPTIBILITIES. 26	26
EQUATION 3.25: LINEARIZED SYSTEM OF EQUATIONS FOR TOTAL MAGNETIC FIELD .....	26
EQUATION 3.26: TIKOHONOV MINIMUM GRADIENT REGULARIZATION OF EQUATION 3.25 .....	26

EQUATION 3.27: OBJECTIVE FUNCTION OF EQUATION 3.26 .....	26
EQUATION 3.28: MODEL OBJECTIVE FUNCTION FOR MAGNETIC FIELD USED TO MINIMIZE FORWARD MODELLED AND MEASURED DISCREPANCIES.....	26
EQUATION 4.1: CORE SAMPLE TRAVEL TIME EQUATION .....	40
EQUATION 4.2: VOLUME OF A CYLINDER.....	43
EQUATION 4.3: GARDNER'S EQUATION .....	47
EQUATION 4.4: MAGNETIC SUSCEPTIBILITY OF A CORE SAMPLE .....	50
EQUATION 6.1: GENERALIZED RADON TRANSFORM.....	80
EQUATION 6.2: LINEAR INTERGRATION CURVE FOR RADON TRANSFORM .....	80
EQUATION 6.3: PARABOLIC INTERGRATION CURVE FOR RADON TRANSFORM .....	80
EQUATION 6.4: HYPERBOLIC INTERGRATION CURVE FOR RADON TRANSFORM .....	80
EQUATION 6.5: REFERENCE DEPTH OF REFLECTION EVENT FOR RADON TRANSFORM .....	80
EQUATION 7.1: P WAVE VELOCITY IN TERMS OF ELASTIC MODULI AND DENSITY.....	110
EQUATION 7.2: S WAVE VELOCITY IN TERMS OF ELASTIC MODULI AND DENSITY .....	110

## **CHAPTER 1 INTRODUCTION**

### **1.1 STATEMENT OF PURPOSE**

This thesis presents the results from a collaboration between the University of Alberta Experimental Geophysics Group and Baffinland Iron Mines Corporation. It is the final product of 3 subsequent field seasons focusing on the design and implementation of a high resolution seismic survey at the McQuat Lake Synform on Northern Baffin Island, Canada. The purpose of this study is to determine the feasibility of using high resolution seismic in conjunction with ground magnetic, airborne magnetic, and ground based gravity surveys as a cost-effective replacement to drilling to create accurate shallow subsurface models of iron ore deposits. The difficulty in the project above is a result of the permafrost layer creating stronger surface waves that can overpower reflections in the near surface. Proper processing techniques in addition to using refraction tomographic models are employed.

This thesis is divided into 8 chapters. Chapters 1 and 2 introduce this thesis and will describe the location and geological history of the Mary River Group Iron Formation. Chapter 3 provides background on the geophysical principles used to perform the processing and inversion of the acquired data to create the geophysical models, and discuss survey design and implementation of the seismic survey. Chapter 4 presents a series of laboratory physical property measurements on acquired core that give representative ranges of values against which the geophysical observations might be interpreted. Chapter 5 focuses complementary gravity and magnetic surveys at the site leading to a final interpreted model of the ore body. Chapter 6 examines the 2D seismic reflection and refraction data collected, the processing and filtering algorithms performed, and the resulting velocity and tomography models. Chapter 7 provides a final integrated interpretation giving models for the ore body and its overburden. This will then be reaffirmed in the conclusion in chapter 8 which points to directions for additional future work to better delineate the resource.

### **1.2 LOCATION OF MCQUAT LAKE SYNFORM, MARY RIVER CAMP, ACCESS, AND PHYSIOGRAPHY**

Baffinland Iron Mines is headquartered in Toronto, Ontario Canada. Primary mining operations are facilitated out of Mary River, located in the central northern region of Baffin Island Canada approximately 950 km NNW of the territorial capitol of Iqaluit. An ice-free port and ship loading facility is located 100km NW of Mary River in Milne Inlet and is open approximately 10 months a year. Mary River is a year-round fully operational iron ore mine focusing on mining and processing high grade hematite and magnetite into iron ore pellets and fines. The current mine located at the Mary River camp has an expected lifetime of

30 or more years with over 1 billion tons of hematite and magnetite mapped in 3 main deposits. The surrounding metamorphic zones host more potential high-grade deposits and exploration is ongoing. The current exploration program out of Mary River is primarily focused on discovering and mapping new iron ore deposits in conjunction with sampling and mapping potential gold and other rare metal deposits.

The McQuat Lake study area is located approximately 25 km NW of the Mary River mine site. The Mary River mine is operated primarily by Inuit personnel on shifts out of the nearby hamlet of Pond Inlet. Pond Inlet supports a primarily Inuit population of roughly 1600 people. The main employers of the town are The Government of Canada and Baffinland Iron Mines Corporation. The Mary River campsite and Aerodrome are owned and maintained by the Baffinland Iron Mines Corporation. Access to the Mary River Aerodrome is restricted to Charter Aircraft and Canadian Helicopters aircraft (See Figure 1.2 for aerial view of Mary River exploration camp).

The McQuat Lake survey zone is located in UTM zone 17N and is centered at 536500 meters easting and 7928750 meters northing, approximately 30 km WNW of Mary River located at 558052 meters easting and 7914605 meters northing (71.314219 N, -79.27252 W). See Figure 1.1 for map view of Baffin Island, Mary River camp, and survey site. The study area lays ovetop of the Central Borden Fault, separating Banded Iron Formation Outcrop in the north from the Turner Cliffs Limestone formation to the south of the fault. High grade iron ore formations and Banded Iron Formations form steep ridgelines and are typical along the north edge of the Central Borden fault. These outcrops increase in grade Eastward from McQuat Lake towards the Mary River mine site and Deposits 1, 2, and 3. The area surrounding the Central Borden fault, including the study site are blanketed by a layer of glacial till of variable thickness.

### **1.3 EXPLORATION HISTORY AND PREVIOUS WORK**

The first expedition to chart Baffin Island was led by Martin Frobisher in 1576 during his search for the North-West Passage. Frobisher landed near present day Iqaluit and discovered large samples of iron pyrite. Iron ore was first discovered on Baffin Island near Frobisher Bay, south of Iqaluit during the second polar expedition of Charles Francis Hall spanning from 1864 to 1869 (Nourse, 1879). In 1921, the Fifth Thule Expedition discovered Nuluujaaq Mountain and used this as a marker for creating a cartographic map of the Cockburn Region spanning the western coasts of Baffin Island, 150 km south of the present-day Mary River (Mathiassen, 1933).



Figure 1.1: Location of Baffin Island Canada, Mary River mining camp and the McQuat Lake Survey Site. Raw Image source: Wikipedia Commons.

Baffinland Iron Mines current mining complex rests at the base of what is referred to as 'Deposit 1', which consists of a large iron ore escarpment standing roughly 700 meters above sea level. This large black mountain was discovered from the air by Murray Watts, president of British Ungara Exploration and his pilot Ron Sheardon in 1962. In 1963 Baffinland Iron Mines Incorporated was formed. Financed by Southern African and London Anglo-American Mining corporations, early exploration on Deposit 1 and



*Figure 1.2: Mary River exploration camp.*

the surrounding region began. Exploration was abandoned in 1966 because of falling prices for iron ore on the world market due to larger and more easily accessible discoveries in Brazil and Australia.

In 2004, due to an increase in the price of iron ore, Baffinland Iron Mines Corporation was created and resumed exploration. In the following 5 years, working on a seasonal basis, Deposits 1 through 5 were thoroughly explored (Figure 1.3). Definition drilling on deposits 1 through 5 was performed and in 2010 a large bulk sample program was performed on the top of deposit 1. Regional exploration also resumed, resulting in potential deposits 6 through 8 being discovered, and the Ege Bay property also being explored regionally. Deposit 1 contains high grade iron ore, and over its lifetime is expected to produce 750 million tonnes, with nearby deposits 2 and 3 being able to contribute shortly thereafter, giving the local mine a life span of roughly 100 years. In 2011 a joint takeover of Baffinland Iron Mines Corporation was finalized with 70 percent of the company being bought by ArcelorMittal S.A. based out of Luxembourg and 30 percent being bought by Nunuvut Iron Ore Acquisitions Inc., a U.S. based equity fund. Mining began on

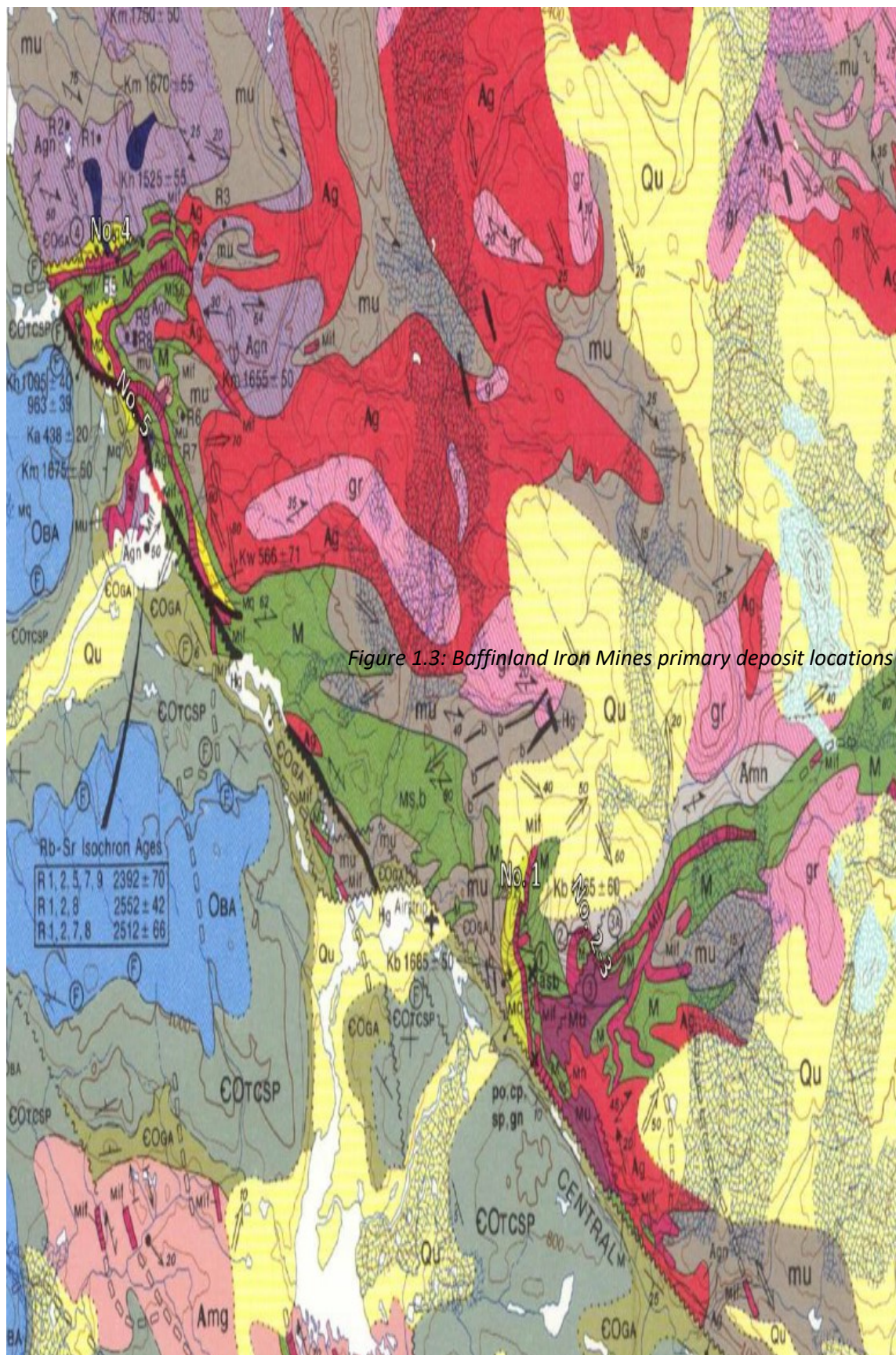


Figure 1.3: Baffinland Iron Mines primary deposit locations on regional geology map, 1978.

deposit 1 in 2014 after a large upgrade of the shipping port in Milne Inlet and the haul road spanning 100 km between Mary River Camp and Milne Inlet port facility (BIM, 2017).

In 1965 the Geological Survey of Canada (GSC) sponsored the mapping program led by G.D. Jackson and G.A. Gross (Jackson, 1965, 1966; Gross, 1966). G.D. Jackson focused on a 750-square mile area of Iron Ores, including the Mary River group, and is responsible for outcrop mapping of the 37G/5 and 37G/6 map sheets at a 1:50000 scale. In 1969 G.D. Jackson returned to Baffin Island with Operation Bylot (Jackson, 1969) where he conducted extensive helicopter mapping of Northern Baffin Island and produced larger scale maps of the region (1: 250,000). Researchers with the GSC have continued to study the Mary River Group, with most of the work being done in the early 21<sup>st</sup> century: Jackson and Berman, 2000, Bethune and Semmel, 2003, Scott et. Al., 2003, Young et. Al., 2004 and Johns and Young, 2006. Baffinland Iron Mines has also sponsored numerous B.Sc. and M.Sc. thesis (including this one) which focus on the mineralogy and enrichment of Deposit 1 (Macleod, 2009, Nicpon, 2011, Fulcher, 2011), and surrounding geological setting of Deposits 1 through 5 (Macleod, 2012).

In 2014 Baffinland Iron Mines sponsored the geophysical M.Sc. project of I. Inozemtsev (2015) in which a land based vector magnetic survey was performed to provide better magnetic measurements in order to better remove the remnant magnetic field from the region.

## CHAPTER 2 BACKGROUND GEOLOGY

This chapter will provide a brief overview of the complex geology and tectonic processes leading to the formation of the Mary River group and enrichment of the iron ore bodies. The Mary River Group is expected to have undergone deformation via a method called dome and keel tectonics which will be outlined. Typical formation of iron ore in greenstone belts will be laid out, followed by the primary enrichment process. Geological history starting at a national scale with the Committee Bay Belt and zooming in to a local scale with the Mary River Group and McQuat Lake Synform will then be discussed.

### 2.1 DOME AND KEEL TECTONICS

Marshek et al. (1998) has proposed a four-stage model for dome and keel creation. During stage 1, a Paleoproterozoic contractional orogen will thicken the supercrustal sequence. This thickening in iron rich zones creates a large density increase, isostatically forcing the basement rock deeper and to higher temperatures. Stage 2 occurs during the following orogenic collapse, which pulls the now hot basement upwards into the cool supercrustal rocks along fault systems and shear zones. This results in a large

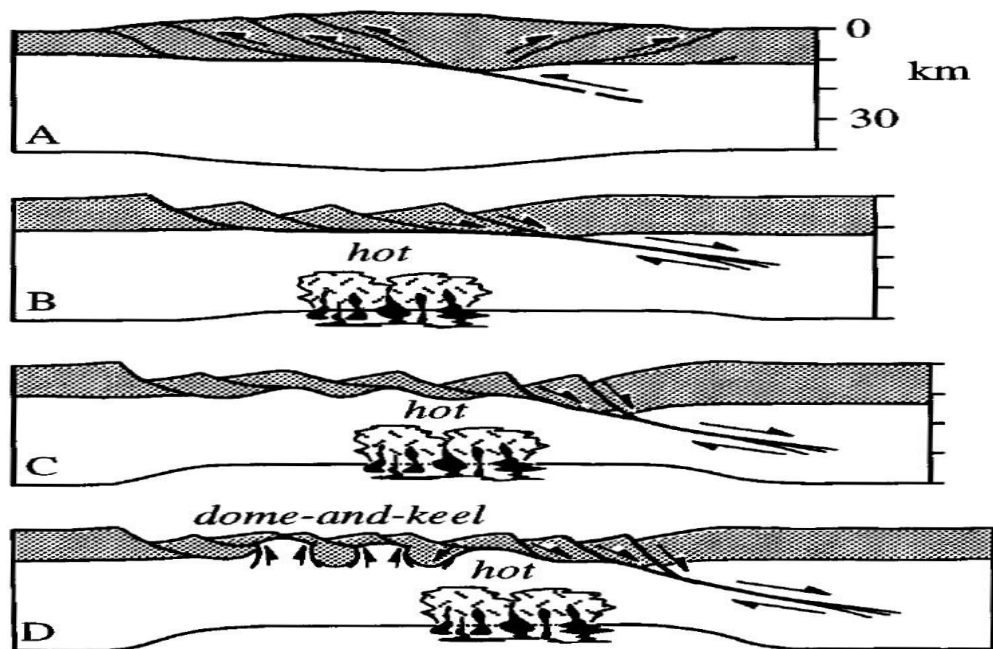


Figure 2.1: Cartoon schematic of the evolution of dome and keel tectonics. A dense faulted layer will rest upon a denser layer. The introduction of heat will cause lower layer to become less dense resulting in a vertical instability. The upper layer will fracture and begin sinking into the lower layer, resulting in steeply dipping lenses of the upper layer spaced between regions of the lower layer. (Marshak et al., 1998)

density inversion between the dense, cold supercrustal rocks on top of the warm, viscous less dense basement rocks. During step 3, hot basement rocks begin to rise into shear zones. Regional extension will assist this process by creating additional high angle basement penetrating shear areas. Finally step 4 will result in highly compressed steep sided keel zones. Dome borders adjacent to keels will be locally inverted. Supercrustal rocks in keels are heated during the entire process and metamorphosed to high grade. Dome and keel formation has been shown to occur during the Paleoproterozoic Orogeny roughly 500 Ma after the supercrustals were laid down (Marshak et al., 1998).

## **2.2 IRON ORE FORMATIONS**

Canadian greenstone belt formations vary in age between 3 and 2.5 Ga. High grade iron ore is enriched from a banded iron formation (BIF) or a granular iron formation (GIF) proto-ore. BIFs exhibit distinct chert bands and are thought to form in basins deep beneath the influence of surface waves (Cloud, 1983, Klein, 2005). GIFs show crude banding that is very difficult to see. These sedimentary formations were deposited in shallow oceans where surface wave energy influenced them (Cloud and Simonson, 2005). BIF's and GIF's may be subdivided into 4 distinct facies according to the mineralogy and include: oxides, silicates, carbonates, and sulfides (James, 1954). Iron oxides (such as hematite  $\text{Fe}_2\text{O}_3$ , and magnetite  $\text{Fe}_3\text{O}_4$ ) are widespread throughout the planet, whereas iron carbonates (siderite,  $\text{FeCO}_3$ ) are rarer. Iron silicates show finely laminated layers of magnetite and hematite iron ore with chert. Iron sulfides are commonly banded with chert and, due to the presence of sulfur, are rarely economic.

Most iron ore deposits in Canada are hosted in greenstone belts, and vary in location across Canada from British Columbia to Nunavut and Newfoundland. The Mary River Group iron formation is an Algoma type iron formation, formed between 3.5 and 2.6 Ga (Gross, 1965, 1980). It exhibits typical thin (less than 100m) lenses of BIF to high grade iron ore spanning over a limited areal extent (less than 100 km square) (Gole and Klein, 1981; Clout and Simpson, 2005).

### **2.2.1 IRON ORE ENRICHMENT**

Typical BIFs host approximately 15 to 40 wt. % iron. High grade iron ores are defined as having greater than 60 wt % Fe. They are divided into 2 main types: martite-goethite ores, hosting 56 to 63 wt. % Fe, and high-grade hematite ores, hosting 60 to 68 wt. % Fe (Morris, 1985, Beukes et al., 2002). Martite ores are formed primarily in chert and carbonate iron deposits when during the enrichment process chert and carbonates are replaced with goethite. High grade hematite ores undergo microplatey hematite replacement where silicate and carbonate bands are replaced with thin, 20 to 200 um plates of hematite

(Morris, 1985). The primary banding is preserved during the enrichment process, resulting in an anisotropic medium.

High grade iron ores that contain magnetite and hematite typically have an increased density and are expected to have a high seismic velocity relative to that of BIF and GIF, dependent upon porosity. Consequently, we expect that high-grade lenses of iron ore exclusively hosting BIF's and GIF's will have higher seismic velocity than the surrounding less economic zones, although some of the laboratory measurements in Chapter 4 may provide some exceptions to this expectation due to the existence of higher porosity values in the high-grade ore.

Enrichment of BIF and GIF to high grade is caused by hydrothermal fluid selectively removing  $\text{SiO}_2$ ,  $\text{MgO}$ ,  $\text{CaO}$ , and  $\text{CO}_2$ . The process which causes this is still actively debated, and can be different depending on region. Different processes have resulted in iron formations grading both upwards and downwards, having a big impact on seismic velocity measurements. The past two decades have seen 6 primary models

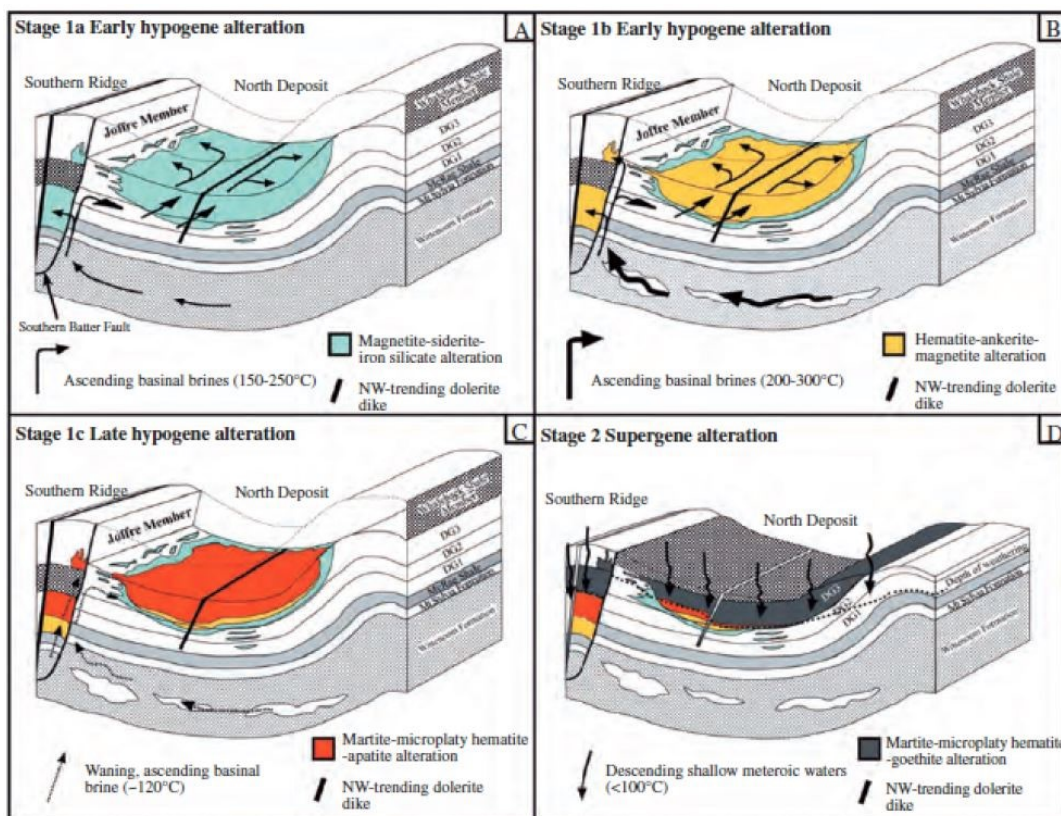


Figure 2.2: Supergene-modified hypogene enrichment model based on the North Deposit of Mount Tom Price, Australia. *Ascending brines of different temperature alter BIF's and remove silica to alter BIF's to ankerite and apatite. Descending surface waters enrich iron to martite and hematite and remove ankerite, apatite and leaves microplaty hematite. Used with permission from Clout and Simonson, 2005.*

proposed: Syngenetic (King, 1989; Lascelles, 2002, 2008), diagenetic (Findlay, 1994; Lascelles, 2007), supergene (MacLeod, 1966; Morris, 1985; Beukes et al., 2003), synorogenic (Li et al., 1993; Powell et al., 1999), hypogene (Lobato et al., 2008), and supergene-modified hypogene (Barley et al., 1999; Taylor et al., 2001). The supergene-modified hypogene has become the preferred model and will be discussed below. An annotation of the states of supergene-modified hypogene alteration is given in Figure 2.2. In the supergene-modified hypogene model of BIF formation, iron ores grade upwards from hydrothermally altered high grade zones into non-enriched BIF (Beukes et al., 2002). The model has a variety of alterations based on timing, deformation, carbonate proto-ore and type of hydrothermal fluid involved, but all follow the same principle steps (Barley et al., 1999; Hagemann et al., 1999; Thorne et al., 2004). In the first step of the process, hydrothermal brines flow up into the base of the BIF unit through faults and fractures. The hydrothermal fluid flows are divided into 3 different flows. Initially, a warm (150°C to 250°C) fluid will ascend into the rock mass removing silica from the chert banding and increase the Fe wt %. This will be followed by a much hotter fluid pulse, (200°C to 300°C) which alters the BIF to hematite, ankerite and magnetite. Finally, colder fluid (120°C) will form martite, microplatey hematite and apatite and dissolve ankerite to create porosity in the iron formation.

During step 2, descending surface water flowing downwards through faults, cracks, fissures, and porous rocks will alter the enriching iron to martite, microplatey hematite, and goethite. Any leftover apatite and ankerite is removed. During step 3, carbonates and any remaining silicates are leached out. In step 4, supergene processes leach out final bits of apatite. The result is a microplatey hematite ore that grades upward towards the surface. Rosiere and Rios (2004) outline a slight alteration to the model to explain more magnetite rich high-grade ores in which enrichment depends on a proximity to brine and hydrothermal fluid. Dome and keel tectonics is vital to providing a heat source for dehydrating rocks and providing pathways for hydrothermal fluid to flow.

## **2.3 GEOLOGICAL HISTORY OF THE MARY RIVER GROUP AND NORTHERN BAFFIN ISLAND**

### **2.3.1 REGIONAL GEOLOGY**

Northern Baffin Island and the Mary River group are members of the Committee Bay Belt in the NW Churchill Province. The Churchill Province extends between the Northern regions of Saskatchewan in its SW corner to Greenland in its NE corner. The Churchill Province is split into 2 zones, the Mesoarchean Rae in the north and the NeoArchean Hearne in the South (Stockwell, 1982; Hoffman, 1988). The Mary River Group is contained within the northern Rae Craton, which is bounded to the north by the Paleoproterozoic Thelon Tectonic Zone and the Archean Queen Maud Block. To the south the Rae craton

is bordered by the Paleoproterozoic Baffin Orogen, which is the NE section of the TransHudson Orogeny, a large-scale collision event occurring between 2.0 and 1.8 Ga which banded the Churchill Province to the Superior Province (Henderson et al., 1980; Hoffman, 1990a, b; Jackson et al., 1990a, b; St-Onge et al., 1999). The Rae Craton is composed of Archean greenstone belts separated by Neoproterozoic volcanic and intrusive complexes. The plutonic crust is the structural basement to all overlying units.

### **2.3.2 COMMITTEE BAY BELT**

The McQuat Lake Synform is contained within the Committee Bay Belt (CBB). The CBB is composed of discontinuous greenschist to upper amphibolite facies intruded by large felsic plutons (Jackson and Taylor, 1972; Jackson and Berman, 2000). The Mary River Group (MRG), the Woodburn Lake Group (WLG) and the Prince Albert Group (PAG) all make up the CBB (Heywood, 1967; Jackson, 1966; Jackson and Taylor, 1972; Berman et al., 2005; Johns and Young, 2006). The WLG makes up the southern end of the CBB. It is composed of a Mesoarchean basement gneiss dated by MacLeod and Duke (2011) at 2.87 Ga. This is superimposed by a Neoproterozoic volcanic sedimentary assembly dating 2.74 to 2.63 Ga (Zaleski et al., 1999; Zaleski et al., 2001). The sedimentary assemblage is primarily composed of komatiitic felsic volcanic sequences containing greywacke assemblages, abundant quartzite and lesser iron formations. On top of the sedimentary layer is a Paleoproterozoic quartzite.

The PAG spans the central domain of the CBB. It contains the same Mesoarchean basement gneiss that we see in the WLG. Superimposed on this layer is a similar Neoproterozoic volcanic sedimentary assemblage dating 2.73 to 2.69 Ga (Skulski et al., 2003). The lower volcanic sedimentary package is dominated by basalt, rhyolite lapilli tuff, and komatiite. The middle of the volcanic sedimentary package hosts wacke, pelite, iron formation and quartzite intermixed with felsic tuffs and ultramafic sills. The upper sequence is composed of wackes and semipelite.

### **2.3.3 MARY RIVER GROUP**

The Mary River Group (MRG) spans the CBB between the Grant-Suttie Bay Inlet and Eclipse Sound and Bylot Island. Geological units have been determined by numerous studies throughout the past half century including: Blais (1964), Jackson (1965, 1969), Crawford (1973), Young et al. (2004), Johns and Young (2006), MacLeod and Duke (2009a, b), and MacLeod (2010). It is discontinuously exposed in lenticular outcrops spanning up to 65 km in length. The MRG is composed of a dome and keel tectonic setting, with supercrustal assemblages of Archean MRG appearing in the keels bordering the domal bodies of Archean plutonic gneiss and migmatites. The basement of the MRG is a mixed felsic-mafic gneiss and nebulitic

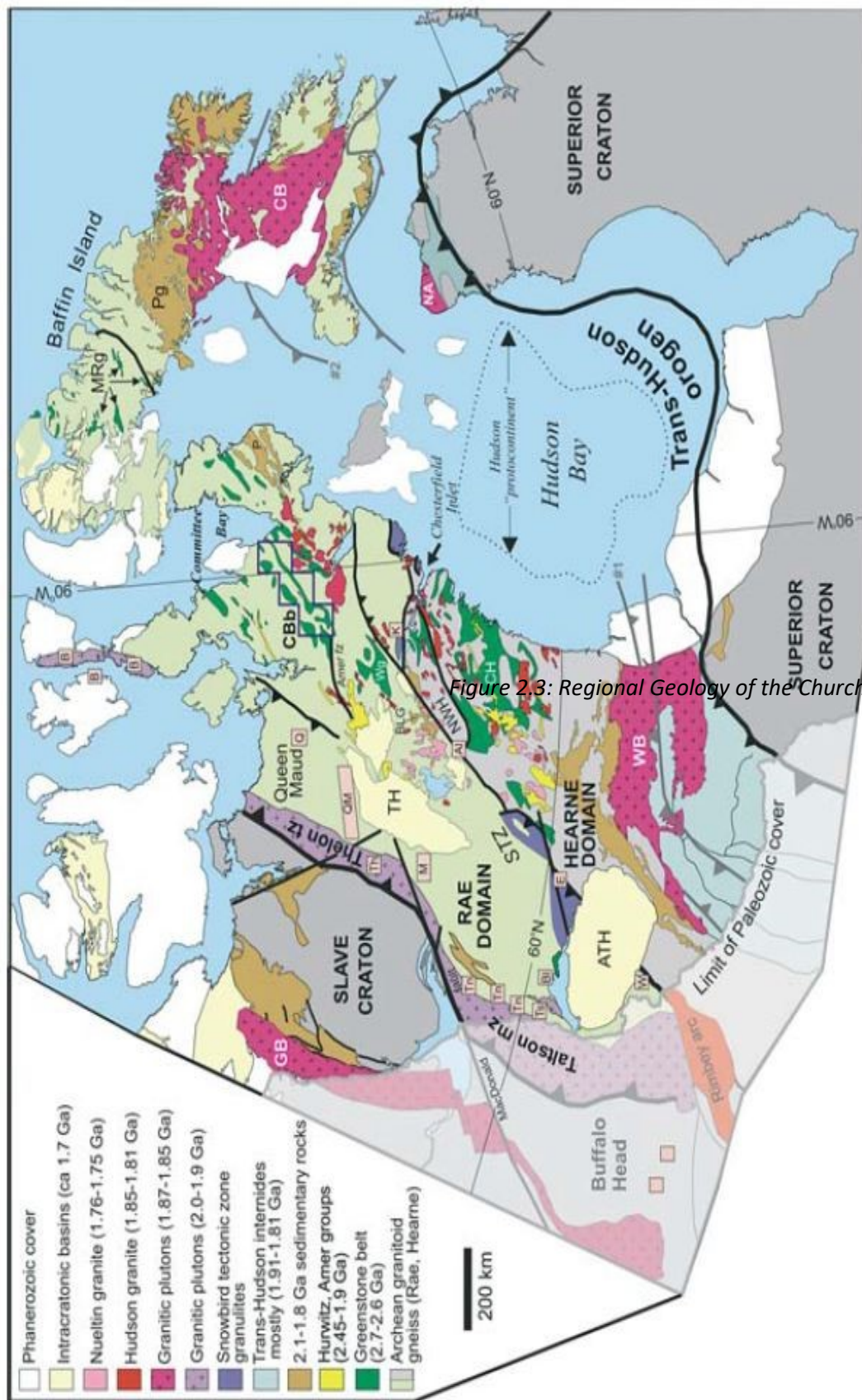


Figure 2.3: Regional Geology of the Churchill Province. Used with permission

granitic migmatites from the Hudsonian. MacLeod and Duke (2011) have further subdivided these gneisses based on their fabric into dome core, dome margin and massive gneiss sheets. Moving shallower through the basement, sheets of K-feldspar and augen gneiss are observed.

The supercrustal keel structure of the MRG are composed of psammitic to silicate wacke superimposed by quartzite and komatiite. Iron bands occur at the wacke-komatiite boundary. Iron high grade zones are found throughout the MRG, hosted in the Algoma type iron formations. Chlorite schist and aluminous gneiss are found in association with the banded iron formation and high-grade iron formations, but these are not classified as part of the MRG. They are formed by hydration occurring along the dome keel boundary. Iron ores present in the MRG are found in 3 assemblages: Oxide, silicates, and carbonates. Iron oxides show mm scale banding of magnetite and chert, whereas silicate irons are largely seen as BIF's with finely laminated quartz, cummingtonite/grunerite and magnetite layers. These iron formations create discontinuous outcrops of vary grade and thickness, stretching for tens of kilometers. Economic high-grade zones have been found to be up to two hundred meters thick.

#### **2.3.4 MCQUAT LAKE SYNFORM**

The McQuat Lake Synform hosts economic deposits 4 and 5 within Baffinland Iron Mines surface claims. A detailed surface scale map can be seen in Figure 2.6. Deposits 4 and 5 run parallel to the Central Borden Fault and are labeled in Figure 2.6 as Dep. 4 and Dep. 5 respectively, they are made up of the oxide BIF zones in the figure. Deposit 4 extends east to west approximately 5km before becoming thin and uneconomic on the eastern boundary at the edge of the mining lease and terminating at the Central Borden Fault on the west. The Central Borden Fault runs NW to SE through figure 2.6 separating the Paleozoic carbonates from the complex fold structures of the MRG to the NE. Deposit 4 is a first order fold closure plunging to the East. The northern limb of deposit 4 is an isoclinal fold that terminates to the east. Quartzite appears throughout the entire length of deposit along the external and internal keel margins. The BIF zones are superimposed on psammite wackes which exhibit as well layered, dark, quartzofelspathic to biotitic metasedimentary rocks. Drilling in the region has revealed that iron layers are primarily composed of magnetite up to 77m thick. The magnetite is heavily sulphurated with pyrite (MacLeod, 2012). The survey area for this study is adjacent to Deposit 4 on the south side of the Central Borden fault, highlighted in figure 2.6 by the red square. It is expected to have very similar mineralogical

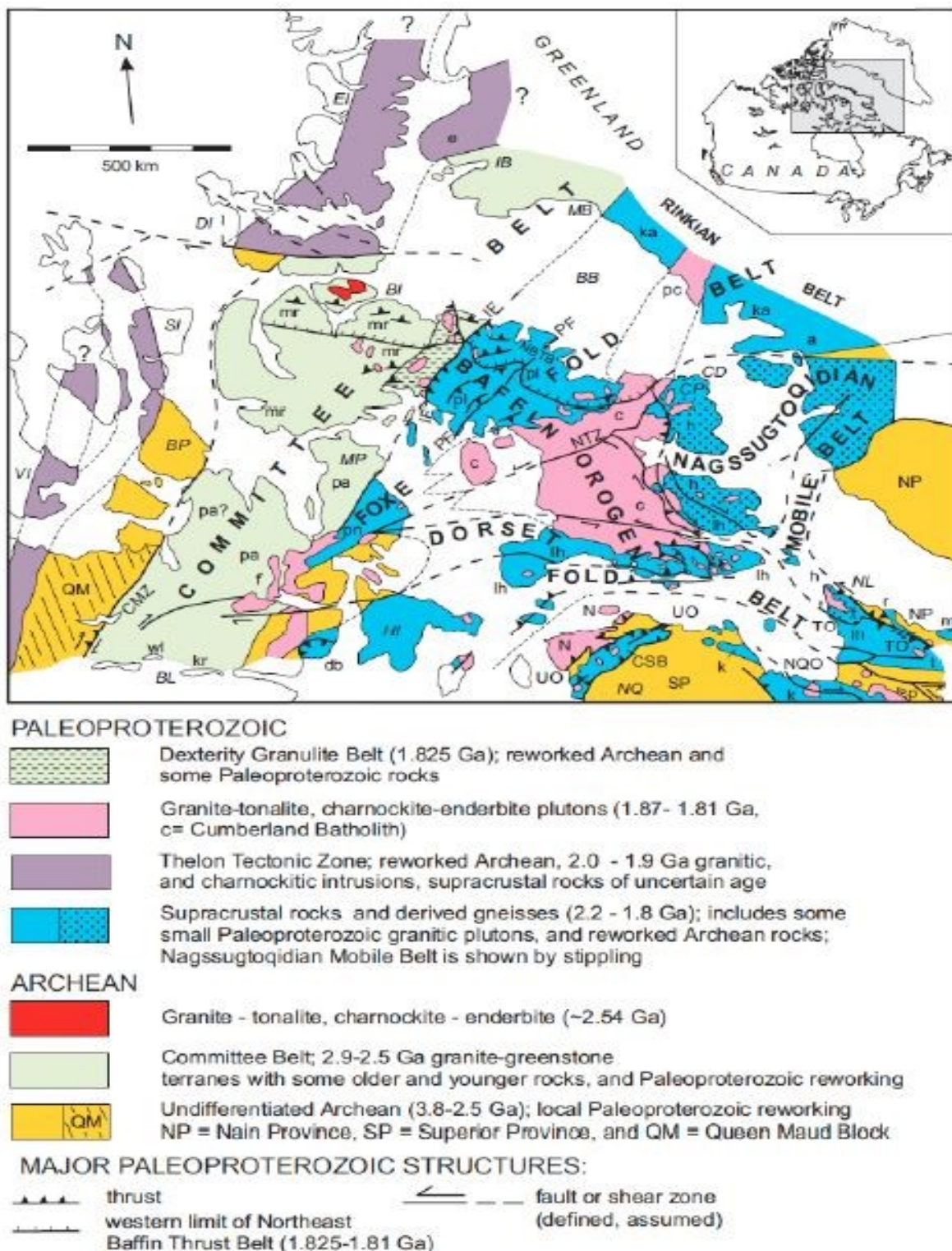


Figure 2.4: Archean and Paleoproterozoic terranes comprising Baffin Island, Canada. Used with permission from Jackson and Berman, 2000.

composition to Deposit 4. The ore zone is overlain by a thick carbonate sequence belonging to the Ship Point Formation, composed mostly of Paleozoic carbonates and limestone. A thin layer of Gallery Formation sandstone lays between the Iron ore zone and the Ship Point Formation. The upper layer of the Paleozoic carbonates is suspected to be highly fractured. Glacial till covers roughly 60 percent of the surface region, with outcrops of Ship Point limestone and Gallery sandstone visible at lower elevations.

## 2.4 Summary

This thesis will focus on the investigation of the continuation of Deposit 4's western limb extending beyond the Central Borden Fault. A seismic survey will be performed to build a velocity and subsurface tomography model mapping the boundaries of the Ship Point Formation and possibly the Gallery sandstones if vertical resolution is high enough. Core analysis information taken from boreholes on Deposit 4 (across the Central Borden Fault from the survey site) will be used to correlate seismic velocity,

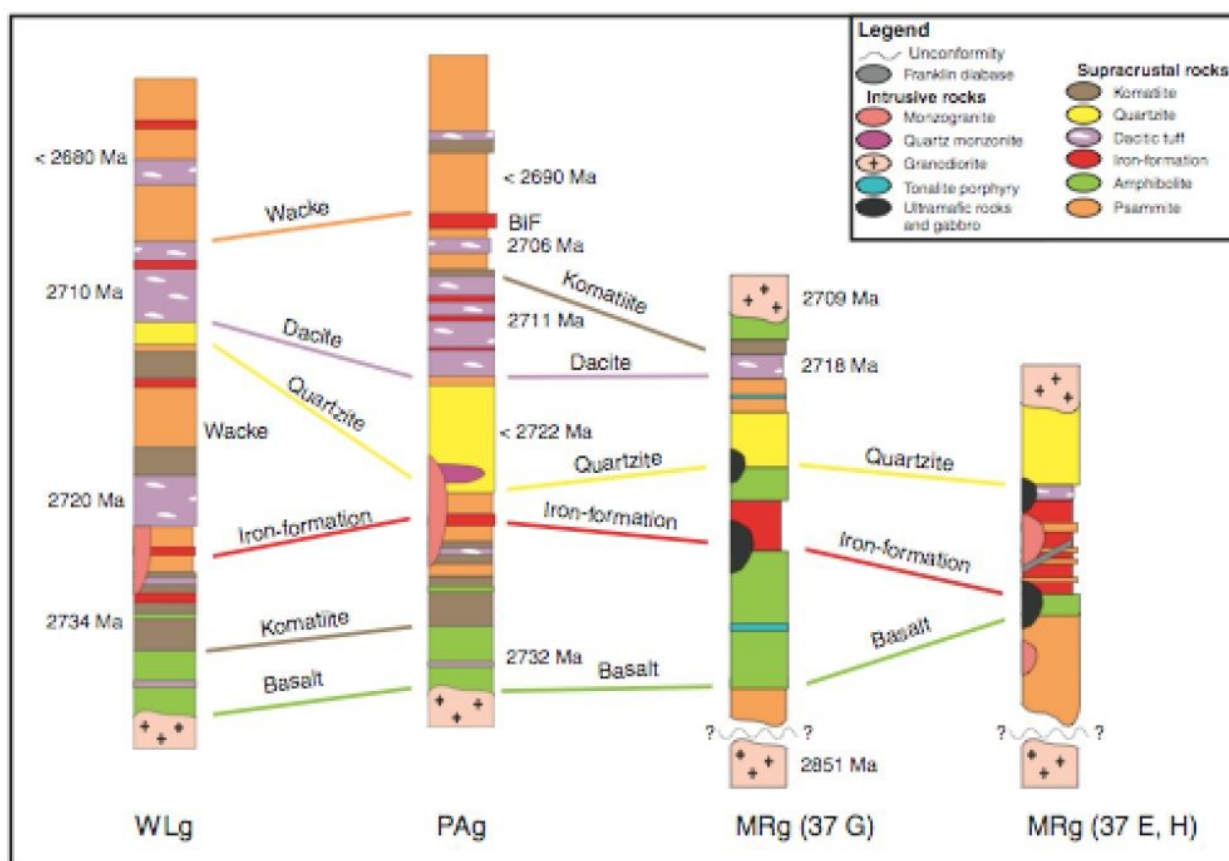
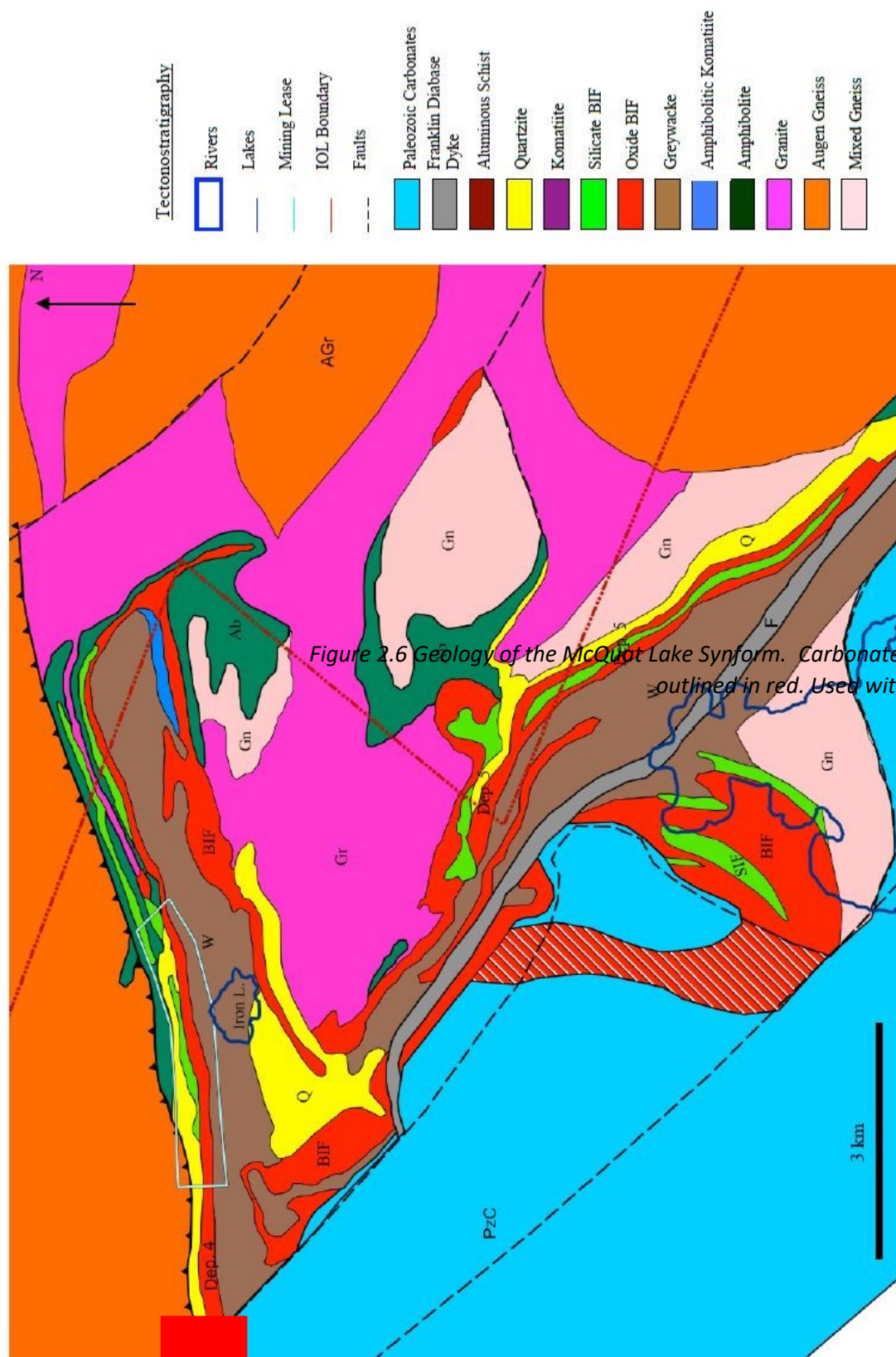


Figure 2.5: Stratigraphic correlations between the Mary River Group at the 37 G, E, and H map parcels, Prince Albert Group, and Woodburn Lake Group of the Committee Bay Belt. Used with permission from Johns and Young, 2006.

magnetic and gravitational data in an effort to determine the overburden thickness of the Paleozoic carbonates and determine potential high-grade zones within the western extension of Deposit 4.



## CHAPTER 3 GEOPHYSICAL BACKGROUND, SURVEY DESIGN AND IMPLEMENTATION

Chapter 3 will focus on explaining the geophysical principles used to process the acquired magnetic, gravitational and seismic datasets from raw data to completed inversions. Basic geophysical principles will be discussed followed by more complex inversion methods. The design for the seismic survey will be reviewed followed by the in-field practices used to acquire the raw data.

### 3.1 GEOPHYSICAL BACKGROUND

#### 3.1.1 SEISMIC REFRACTION

The principles of seismic refraction allow us to construct geologically representative models of the subsurface from observing a series of seismic traveltimes from a source to receivers. The principles of seismic refraction are outlined in many textbooks (e.g., Reynolds, 2011; Lillie, 1999) and only a short introduction need be given here.

Seismic refraction is based on the principle of Snell's Law, which states that as a ray path crosses an interface where there is a velocity contrast, the angle of incidence will differ from the angle of refraction based on the strength of the velocity contrast. Snell's law is as follows:

$$\frac{\sin \phi_1}{V_1} = \frac{\sin \phi_2}{V_2} \quad (3.1)$$

Where  $V_1$  and  $V_2$  are the seismic velocities of the layers containing the incident and refracted waves, respectively, and  $\phi_1$  and  $\phi_2$  are the incident and refracted angles, respectively, of the raypath as measured from the line perpendicular to the boundary between the two layers. The ray is critically refracted at the critical incidence angle  $\phi_c$ :

$$\phi_c = \sin^{-1} \left( \frac{V_1}{V_2} \right) \quad (3.2)$$

which essentially means that angle of refraction  $\phi_2 = 90^\circ$ . At this point a 'head' wave refraction is created that propagates away from the source point with an apparent speed of  $V_2$  as measured at the surface from the times of the 'first breaking' arrivals. If an array of geophones is laid out linearly from the seismic source, then one is able to determine  $V_2$  from the linear slope of a plot of these times versus their offset  $x$  from the source.

Ray refraction caused by first break arrivals recorded by the geophone array will crudely mimic the velocity of each layer via the reciprocal of the slope of the first arrival time band. By tracing specific rays through different horizontally continuous layer cases, the following formula describes, for example, the travel times for a flat-lying multi-layer case:

$$T(x) = x/V_n + \sum_{i=1}^{n-1} \frac{2z_i \cdot \cos \phi_{ci}}{V_i} \quad (3.3)$$

where  $x$  is the horizontal distance along the survey line,  $V_n$  is the velocity of the bottommost  $n$ th layer,  $z_i$  is the thickness of the  $i^{\text{th}}$  layer,  $V_i$  is the velocity of the  $i^{\text{th}}$  layer, and  $\phi_{ci}$  is the critical angle between the layers  $i$  and  $i+1$ . Using the above formula and velocities determined from the raw seismic data (via the slope and intercept method), we can determine layer thicknesses by simply observing traveltimes. This simple method works for flat horizontally continuous layers as long as the velocities continue to increase into the earth. Geometric considerations allow it to be used to study dipping layers if there are forward and reverse shots using Hagedoorn's plus minus method (Hagedoorn, 1959). In short, the refraction method is a useful way to study horizontally layered geology.

However, as the cases become more complicated, more vigorous analysis methods are required. For example, a horizontal step discontinuity results in a shingling effect (Cassinis and Borgonovi, 1996) in the first break times. A steady increase in velocity with depth (due to compaction or grading downwards) will result in curved first breaks rather than distinct slopes and critical points. Velocity inversions (i.e. a decrease in velocity with depth) will result in the inbound ray refracting away from normal and will not yield a critical refraction. This will result in the layer being invisible when attempting to interpret the data with the velocity of any underlying layer being more of an average. Additionally, thin layers with thicknesses less than the principle wavelength of the seismic energy travelling downwards will not yield a detectable critical refraction, and as such are missed.

Seismic refraction inversion methods and software have been developed over the past century to combat the above issues and produce trustworthy results. Generally, there have been two main approaches to refraction first break interpretation: The delay time using the generalized reciprocal method (GRM) (Palmer, 1981), and wavefront construction using Hagedoorn's  $\pm$  method (Dufour and Foltinek, 1996). These methods require forward and reverse shots, and have been proven to be effective in simpler cases. Hagedoorn's  $\pm$  method uses intercept times and delay times to calculate the depth to a refractor below any geophone location. Velocities are calculated using a linear regression analysis. The GRM uses refraction migration to determine details about the refractor at depth and map out horizontal

discontinuities. The Vista™ software used in this thesis provides estimates of the near surface velocity structure using variations of Hagedoorn's ± method.

The techniques described above do not require substantial computational resources. More recently, 'seismic tomography' methods in which the observed transit times are inverted for more complex geological structure have been implemented (Sirles et al., 2013). Software packages able to perform this refraction tomographic inversion have become more readily available in the past two decades. In this thesis, we provide seismic tomographic results calculated using Schlumberger's VISTA™ Seismic Suite and the commercial software SEISOPT2D™ (Optim 2005). The mathematical methods will be discussed below.

### 3.1.1.1 REFRACTION TOMOGRAPHY

Successful tomographic inversions either create a model that results in either a plausible velocity distribution to explain the measured travel times or highlight layer boundaries at which velocities are discontinuous. However, the relationship between velocity and traveltime is a non-linear relationship. White (1989) outlines the basis of the method for an iterative tomographic inversion. The practical details for the following method are outlined by Trampert and Leveque (1990) and Lanz et al., (1998). The study area is divided into small cells, and each one assigned a velocity. By tracing rays through the cell structure of a 2D model, the forward travel time problem can be determined:

$$t = \sum_{i=1}^N \frac{dL_i}{v_i} \quad (3.4)$$

Where  $t$  is the total traveltime,  $L_i$  is the path length of the raypath in the  $i^{\text{th}}$  cell and  $v_i$  is the velocity in that cell. However, in undefined areas where the velocity approaches zero, this summation becomes undefined and creates large artifacts in our dataset (common among the poorly sampled edges of most models). To counter this, we use the slowness vector, equal to the reciprocal of the velocity vector:

$$t = \sum_{i=1}^N dL_i * u_i \quad (3.5)$$

Where  $u_i$  is the velocity through cell  $i$ , and  $L_i$  is the path length through cell  $i$ . For multiple rays, the above equation becomes a system of equations:

$$\mathbf{t} = \mathbf{A} \cdot \mathbf{u} \quad (3.6)$$

Where  $\mathbf{A}$  is now a matrix of partial path lengths,  $\mathbf{u}$  is a vector of slowness's covering the entire 2D model, and  $\mathbf{t}$  is a vector of first arrival times. The above equation is of the form:

$$\mathbf{A} \mathbf{x} = \mathbf{b} \quad (3.7)$$

Which is now a linear equation where we wish to solve for  $\mathbf{x}$ , yielding a matrix of slowness values and as such velocity values for the model. Ray tracing is performed through the resulting model to determine the misfit between data and model (Yao et al., 2013). Performing singular value decomposition to minimize any resulting error from the model we get:

$$\mathbf{x} = \mathbf{A}^{-1} \mathbf{b} \quad (3.8)$$

$$\mathbf{A}^{-1} = \mathbf{V} \mathbf{\Lambda}^{-1} \mathbf{U}^T \quad (3.9)$$

Where  $\mathbf{V}$  and  $\mathbf{U}$  are  $m \times m$  and  $n \times n$  orthogonal matrices respectively and  $\mathbf{\Lambda}$  is a diagonal vector of eigenvalues. Errors introduced to the system from the measured travel times will be amplified by the reciprocals of the eigenvalues and as such a damping term must be added:

$$\mathbf{x} = \mathbf{V} \mathbf{\Lambda} (\mathbf{\Lambda}^2 + \mathbf{u}^2 \mathbf{I})^{-1} \mathbf{U}^T \mathbf{b} \quad (3.10)$$

Where  $\mathbf{u}$  is our damping parameter. Simplifying the above equation yields our final model inversion:

$$(\mathbf{A}^T \mathbf{A} + \mathbf{u}^2 \mathbf{I}) \mathbf{x} = \mathbf{A}^T \mathbf{b} \quad (3.11)$$

VISTA™ Seismic Suite (Trampert and Leveque, 1990; Lanz et al., 1998) couples other iterative solution techniques to the damped singular value decomposition above to increase accuracy and reduce processing time. Performing row action methods on the above system, the Stationary Iterative Reconstruction Techniques (SIRT) and Algebraic Reconstruction Technique (ART) are performed to solve the model iteratively. The mathematical SIRT is outlined by Ivanson (1983), and Van Der Sluis and Van Der Vorst (1987). SIRT converges on a least squares solution after rescaling original equations used, providing more accurate models for successive iterations. However, the model solution depends on the input parameterization (geophone spacing and shot locations) and therefore suffers non-uniqueness issues. Trampert and Leveque (1990) provide a damping parameter to reduce noise amplification which yields the Damped Stationary Iterative Reconstruction Technique (DSIRT):

$$\mathbf{x}^{q+1} = [(1 - \theta^2) \mathbf{I} - \mathbf{G}^{-1} \mathbf{A}^T \mathbf{C}^{-1} \mathbf{A}] \mathbf{x}^q + \mathbf{G}^{-1} \mathbf{A}^T \mathbf{C}^{-1} \mathbf{b} \quad (3.12)$$

Where  $\theta$  is the new damping parameter and:

$$\mathbf{G} = \text{diag} (\mu_1 + \sum_i |\mathbf{G}_{ij}|^\alpha) \quad \mathbf{C} = \text{diag} (\mu_2 + \sum_i |\mathbf{G}_{ij}|^{2-\alpha}) \quad (3.13)$$

$$0 \leq \alpha \leq 2$$

The equation above reduces to a classical damped least squares solution similar to that obtained from singular value decomposition, and gives us a final least squares inversion solution of:

$$\mathbf{x}^* = \mathbf{x}^\infty = (\mathbf{A}^T \mathbf{C}^{-1} \mathbf{A} + \theta^2 \mathbf{G})^{-1} \mathbf{A}^T \mathbf{C}^{-1} \mathbf{b} \quad (3.14)$$

The above DSIRT inversion converges quickly and depends only on  $\mathbf{G}$  and  $\mathbf{C}$ , which depend on the parameterization created by the shot and geophone spacing.

VISTA™ seismic suite pairs DSIRT with ART, DSVD, and applies a quadratic minimization to minimize the discrepancy between measured traveltimes and model response traveltimes. The method creates a model  $\mathbf{x}^0$  and creates new models successively based on discrepancy of data and the model response.

$$\mathbf{S}_{k+1} = \mathbf{S}^k + \Delta \mathbf{S}^k = \mathbf{S}^k + \mathbf{L}^T (\mathbf{S}^k) (\mathbf{t} - \mathbf{L}(\mathbf{S}^k) \mathbf{S}^k) \quad (3.15)$$

Here  $\mathbf{L}$  is the path matrix for the cell structure and  $\mathbf{S}$  is a vector of slowness values.  $\mathbf{L}^T$  is our inverse operator. Minimizing the model response and measured data yields the equation:

$$\phi_d = \|\mathbf{t} - \mathbf{L} \mathbf{S}\|_2^2 \quad (3.16)$$

Which we can add in to the model equation as a regularization parameter:

$$\phi = \|\mathbf{C} \mathbf{S}\|_2^2 \quad (3.17)$$

Yielding our inversion equation:

$$\Delta \mathbf{S}^k = (\mathbf{C}^T \mathbf{L} + \lambda \mathbf{C}^T \mathbf{C})^{-1} (\mathbf{L}^T (\mathbf{t} - \mathbf{L} \mathbf{S}^k) - \lambda \mathbf{C}^T \mathbf{C} \mathbf{S}) \quad (3.18)$$

Model parameterizations are set by the shot and geophone geometry, common midpoint locations (CMP), and desired max depth (determined by shot offsets). The model begins with a simple gradual layered model and creates a more complex model with each iteration.

### 3.1.1.2 SEISOPT2D REFRACTION TOMOGRAPHY

The SEISOPT™ @2D (Optim, 2005) methodology differs from the more standard inversions in that it inverts the data using a simulated annealing procedure which requires large numbers of iterative calculations and hence substantial computational resources (Pullammanappallil and Louie, 1994; Optim, 2005). As such, it provides a good comparison against the more standard refraction analyses of the

VISTA™ software. As per other inversion techniques, the SEISOPT™ @2D software uses first arrival times and shot/geophone geometry to create a subsurface velocity model based on a two-dimensional cell structure. An adaptive simulated annealing (ASA) (Pullammanappallil and Louie, 1994) method is used to determine the most optimized velocity models from the first arrival ASA algorithm is a method which randomly samples the parameter space before automatically adjusting parameters according to the progression of the ASA algorithm. As the solution space is explored, the probability of large discrepancies between the model response and measured response is decreased. Resulting velocity models created by the ASA algorithm are then tested using Optim's algorithms to select the most optimized model with the minimum travel time error between the model travel times and the observed travel times.

### 3.1.2 GRAVITY

Gravitational anomalies are caused by lateral and vertical density variations in rocks which give rise to local increases or decreases of the gravitational field strength with respect to the predicted gravitation field strength of the region. In a standard gravity survey, the relative values of gravitational acceleration are measured on a series of grid points covering the area of interest. To be useful, these values must be further corrected to account for the effects elevation, latitude, and local terrain with the final result referred to as the Bouguer anomaly (Li and Gotze, 2001). This corrected data should reflect best the variations of density in the subsurface, and it can be inverted to determine the density structures of the bodies responsible for the gravity response.

#### 3.1.2.1 GEOSOFT GRAVITY INVERSION

Oasis Montaj™ potential field software, developed by Geosoft Inc., allows the Bouguer anomaly to be inverted to provide an estimate of the underground density structure. The algorithm is similar to the 3-dimensional gravity inversion methods laid out by Li and Oldenburg (1996, 1998). In the inversion, the earth is divided into a 3-dimensional array of set volume each with a constant but unknown density (Williams et al., 2009; Williams and Oldenburg, 2009). The forward problem for modelling a gravity anomaly is used to determine the inversion. The vertical component of a gravity anomaly at point  $i$  is given by:

$$F_z(\mathbf{r}_i) = \gamma \int_V \rho(\mathbf{r}) \frac{z - z_i}{|\mathbf{r} - \mathbf{r}_i|^3} dv \quad (3.19)$$

Where  $F$  is the Bouguer gravity field (i.e. vertical component of the gravitational acceleration),  $\gamma$  is Newton's gravitational constant ( $6.674 \times 10^{-11} \text{ N}\cdot\text{m}^2/\text{kg}^2$ ), and  $\rho(\mathbf{r})$  is the anomalous mass distribution. Linearizing this problem for all points yields the system of equations:

$$\mathbf{d} = \mathbf{G} \cdot \boldsymbol{\rho} \quad (3.20)$$

Here  $\mathbf{d}$  is the Bouguer anomaly field strength,  $\boldsymbol{\rho}$  is a vector of cell densities, and  $\mathbf{G}$  is a matrix which quantifies the contribution of the  $i$ th datum of a density unit in the  $j$ th cell:

$$G_{ij} = \gamma \int_{\Delta V_j} \frac{z - z_i}{|\mathbf{r} - \mathbf{r}_i|^3} dv \quad (3.21)$$

Resulting models are tested with forward modelling and a minimization equation used to test data misfits:

$$\phi_d = \|\mathbf{W}_d(\mathbf{d} - \mathbf{d}^{obs})\|_2^2 \quad (3.22)$$

Here  $\mathbf{d}^{obs}$  is the data vector,  $\mathbf{d}$  is the predicted data,  $\mathbf{W}_d$  is the diagonal matrix of  $1/\sigma_i$  and  $\sigma_i$  is the standard deviation error associated with the  $i$ th datum. Li and Oldenburg (1996) employ a generalized subspace technique to iteratively find the final model. An objective function is used to minimize uninterpretable models, compare remaining models to an ideal reference model, and require that the resulting model be smooth in all spatial directions. Perturbations are slowly added to the resulting models to minimize the misfit equation and a new misfit target set. Depth weighting parameters are added to overcome the concentration of structures near the surface brought on by the rapid decay of kernels with depth. Readers are encouraged to refer to inversion methods discussed by Li and Oldenburg, (1996) for further detail on gravitation inversion techniques.

### 3.1.3 MAGNETISM

The total magnetic field of a rock body is a combination of the induced magnetic field and the remnant magnetic field. The induced magnetic field is a result of the earth's magnetic field inducing a magnetic field in the rock body with a total induced magnetic field strength relative to the magnetic susceptibility of the material. The remnant magnetization is the magnetic field remaining surrounding the rock when all external fields have been removed. It is typically imprinted on the rock or mineral during formation and remains throughout time.

Magnetic methods rely upon the physical rock properties of the minerals to create a magnetic field that can be detected from the surface. The magnetic field strength in the vicinity of rocks and minerals is

Mineral/Rock Type	Magnetic Susceptibility by volume $\chi$ (SI x 10 <sup>-3</sup> )
Dolomite	0 to 1
Limestone	0 to 3
Granite	0 to 50
Hematite	0.5 to 35
Magnetite	1200 to 19200

*Table 3.1: Magnetic susceptibility values for common rocks and minerals* Figure 4.4: Core plug from 126 meters depth highlighting orientation all core plugs were aligned *toward minerals found in McQuat Lake/Deposit 4 area.*

affected by their magnetic susceptibility causing an induced magnetic field. The Magnetic susceptibility  $k$  is a unitless material property that relates the magnetization  $\mathbf{M}$  of the object induced by an applied magnetic field of strength  $\mathbf{H}$  via  $\mathbf{M} = k\mathbf{H}$ . Iron ores such as BIF contain many minerals with high values of  $k$  such as magnetite and hematite. Consequently, rocks containing these minerals are also highly ferromagnetic and will have a high  $k$  relative to many of the formations surrounding them. The induced magnetism of these rocks when placed in the Earth's magnetic field generally produces an anomaly in the magnetic field strength in their vicinity, which can be detected. The magnetic susceptibilities for a variety of rock types have been compiled (Parasnis (1986), Sharma (1986), and Telford et al. (1990)) and some representative ranges are given in Table 3.1. As seen in Table 3.1, hematite's lower magnetic susceptibility relative to magnetite can cause it to have a weaker magnetic field, making it difficult to detect with magnetic survey methods even though it is rich in Fe.

### 3.1.3.1 OASIS MONTAJ GEOSOFT MAGNETIC VECTOR INVERSION

Most of magnetic inversions to date have assumed that the measured magnetic field of a mineral body is formed in response solely to the magnetic induction of the mineral body. However, recent studies (Morris et. Al., 2007, Fournier 2015) have determined that the remnant magnetization from the mineral's history is more prevalent than previously anticipated. Therefore, not only does the strength of the total magnetic field affect the inversion model results, but also the directions and magnitudes of the remnant magnetic field.

The Oasis Montaj Geosoft™ program performs a voxel Magnetic Vector Inversion (MVI), which considers both the induced magnetization and remnant magnetization (Ellis et al., 2012; MacLeod and Ellis, 2013). This inversion is performed using only the measured total magnetic field strength and if available, the magnetic susceptibility of the mineral body. Due to the unusually large strength of the induced magnetic

field caused by the iron ore body, and results found by Inozemtsev (2014), the remnant magnetic field is considered to be negligible during this inversion. The conventional inversion of scalar magnetic induction is replaced with a vector inversion which solves for both magnetic amplitude and direction (Williams et al., 2009; Williams and Oldenburg, 2009). Mathematical modelling uses the common definition of Tikhonov minimum gradient regularization (Zdhanov, 2002; Li and Oldenburg, 1998) and the resulting forward model solved analytically. This however increases the variables and models created. Investigating the forward magnetic field problem, we start with the integral:

$$\mathbf{B}(\mathbf{x}_j) = \nabla \int_V \mathbf{M}(\mathbf{x}) \cdot \nabla \frac{1}{|\mathbf{x} - \mathbf{x}_j|} \delta x^3 \quad (3.23)$$

where  $\mathbf{B}$  is our total magnetic field a distance  $\mathbf{x}$  from our volume and  $\mathbf{M}$  is our magnetization vector. As above with gravity, we will break our source volume  $V$  down into a three-dimensional array of cells, each containing a constant magnetization  $m_k$ :

$$\mathbf{B}_\beta(\mathbf{x}_j) = \sum_{k,\alpha}^{N,3} m_{k,\alpha} \int_{V_k} \delta_\alpha \delta_\beta \frac{1}{|\mathbf{x} - \mathbf{x}_j|} \delta x^3 \quad (3.24)$$

which measures our magnetic field strength at some point  $j$  caused by a collection of magnetic cells. To linearize our equation, the above forward problem can be represented by the system of equations:

$$\mathbf{B} = \mathbf{G} \cdot \mathbf{m} \quad (3.25)$$

The above linear system is regularized using a Tikhonov Minimum Gradient Regularizer, yielding the MVI formula:

$$\text{Min } \phi(\mathbf{m}) = \phi_D(\mathbf{m}) + \lambda \phi_M(\mathbf{m}) \quad (3.26)$$

where  $\phi$  is our total objective function. It is composed of the data term:

$$\phi_D(\mathbf{m}) = \sum_j^M \left| \frac{\mathbf{G}_j \mathbf{m} - \mathbf{B}_j}{e_j} \right|^2 \quad (3.27)$$

which describes our data objective function in terms of the data equation and error. The model term:

$$\phi_M = \sum_\gamma^3 |w_\gamma \delta_\gamma \mathbf{m}|^2 + |w_0 \mathbf{m}|^2 \quad (3.28)$$

describes the model objective function in terms of the gradient ( $\delta_\gamma$ ) and the amplitude of the model.  $w_\lambda$  and  $w_o$  are weighing terms to dampen errors. Our regularization parameter  $\lambda$  is chosen to create a satisfactory fit with the dataset.

### 3.2 SURVEY DESIGN

The aeromagnetic survey was designed to cover the entire region of Deposits 4, 5, and the McQuat Lake area. Aeromagnetic data were collected by New Sense Geophysics in 2008 with a helicopter based acquisition system. Approximate height above topography was between 30 and 70 meters measured by a radar altimeter. Lines were flown with 100-meter line spacing in a North-South orientation over the McQuat Lake area as that was perpendicular to strike. Tie lines were flown in an East-West Orientation parallel to strike. Deposits 4 and 5 trend NW to SE and as such mag lines were flown perpendicular in a NE to SW orientation with tie lines being flown NW to SE along strike. Aeromagnetic data were processed, and quality checked using Oasis Montaj Geosoft™ coupled with Natural Resources Canada topography maps of grids 37g\_5 and 47h\_8. A higher resolution ground based magnetic survey was performed immediately East of the McQuat lake survey site in 2011 and 2012 spanning the outcropping surface deposits of deposits 4 and 5. The resulting magnetic map was then used to plan the gravity program executed in August 2013 and the seismic field program executed in April and May 2015.

The ground based gravity survey was planned around hematite zones showing little to no magnetic signature for the McQuat lake area, and a tight spacing coverage for the Deposits 4 and 5 areas. Gravity readings were spaced out approximately 200 to 300 meters with 200 meters between gravity lines. Survey lines were offset vertically by 100 to 150 meters to create a triangular effect between all gravity stations to improve the minimum curvature modelling of the surface anomaly.

The seismic survey was designed around the magnetic data, gravity data, and regional geology data. Seismic energy was expected to pass through 5 distinct layers as it travelled downward: glacial till, fractured and permafrost limestone, solid limestone, steeply dipping banded iron formation, and high-grade lenses within the banded iron formation. No legacy seismic data were available for the region for the 1km depth required. Shallower construction oriented refraction surveys had been performed at the nearby port of Milne Inlet but were of little use in planning this survey.

To determine the best seismic source for the seismic survey, models of the overburden and iron formation were created in MATLAB™ using geological data and a range of geophysical properties of limestone and BIF to determine what would result in the best signal to noise ratio. White noise of different strengths

was added to the resulting reflection spectrum before being convolved with a minimum phase wavelet. It was determined that due to the absence of serious velocity changes at layer boundaries in the limestone and velocity alterations caused by the permafrost, that a half pound of gelatin nitroglycerine based dynamite be used in conjunction with an electric detonator.

Five one-kilometre lines were laid out in a simple grid pattern to best determine overburden thickness. Only 1km worth of seismic line was available at any time, therefore the line had to be moved every night and set up for the next day. It is expected that the ore body plunges to the west, making the more economic ore zone closer to the eastern edge of the McQuat Lake Synform near the Central Borden Fault, and as such this is the region focused on. The magnetic high trends east to west and exhibits a longer wavelength than that of the surface iron ore bodies directly east of the Central Borden Fault. Lines 2 and 3 were laid out from east to west starting at the cliff edge of the Central Borden Fault and stretching into the western weakly magnetic zone thought to be hematite. The lines were laid through the direct center of the magnetic high along strike and were laid out with a 100m overlap in the middle to assist connecting them later into one longer line. Lines 1, 4, and 5 were laid out north to south perpendicular to the strike of the magnetic high, with the lines centered over the magnetic high and the south ends of the lines pushed up against McQuat Lake. The north to south lines were spaced out with 800 meters between them along the eastern edge of the McQuat Lake Synform.

A shot plan was devised to maximize the fold directly over the center of each line at the peak of the magnetic high. Off end shots were added to the north ends of lines 1, 4 and 5 at 50 and 100 meters off the lines. No southern off end shots were added due to the presence of the lake. Line 2 had one off end shot set at 40 meters located directly below the cliffs of the Central Borden Fault, and shots at 40 and 80 meters off the western side of the line. Line 3 had off end shots at 100 meters off its eastern side and 20 meters off of its western side. A further western off end could not be achieved due to the presence of a half frozen/half melted river that was deemed too dangerous to cross.

Logistical concerns and dangerous goods transportation regulations hampered efforts to obtain desired source explosives. As such, 1Kg Trojan Spartan Boosters from Dyno Nobel that were already available at the mine site were used in conjunction with non-electric spark detonators and primer cord. Due to budgetary constraints, deeper borehole blast sources could not be drilled. To limit fly rock for safety concerns, small holes were drilled by hand to a depth of 0.5m to 0.75m to pack explosives into.

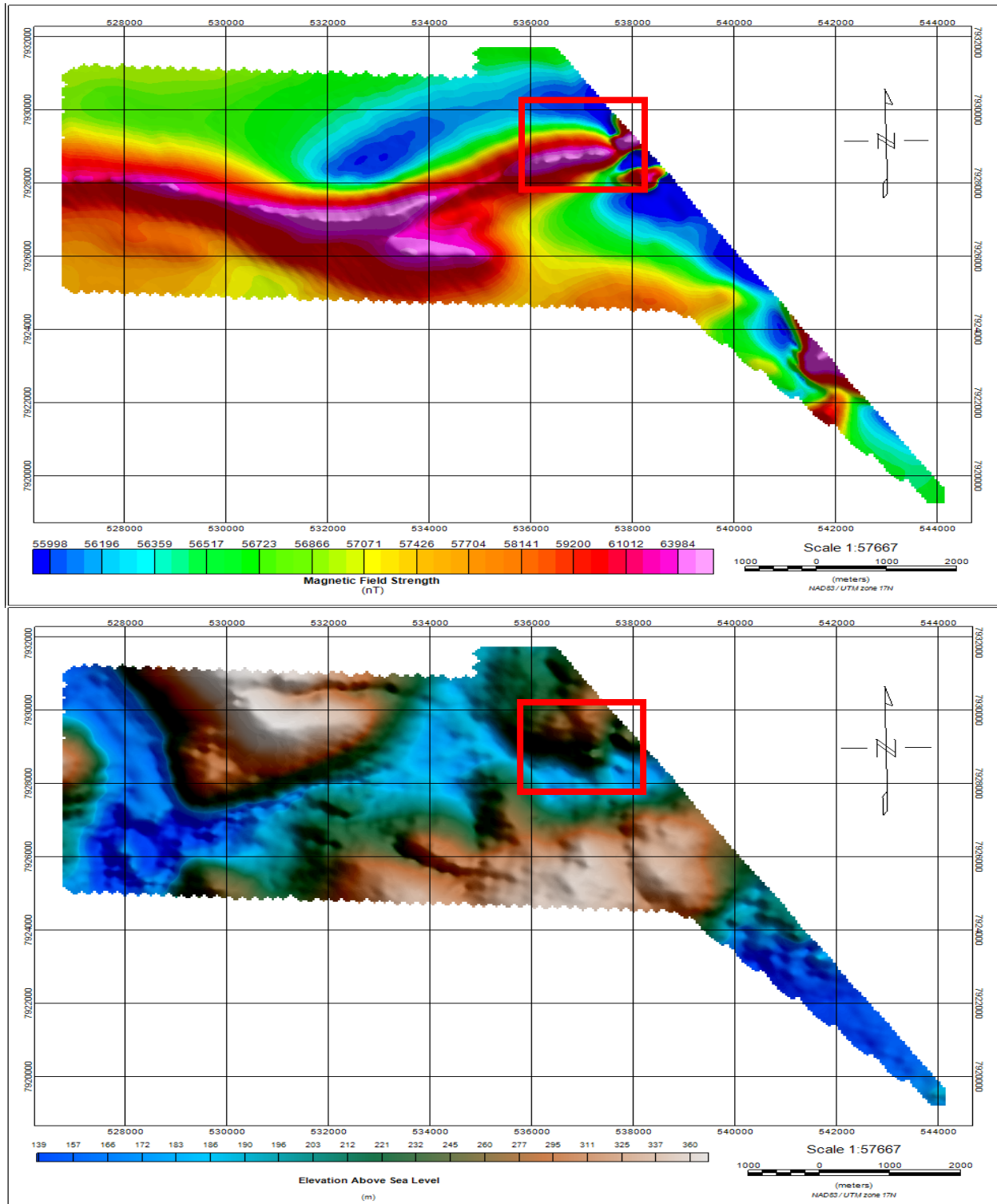


*Figure 3.1: Top: Total magnetic anomaly field for region SW of the Central Borden Fault and outcropping regions of Deposits 4 and 5. Survey zone is highlighted in red.*

*Bottom: High resolution digital terrain model created using airborne aeromagnetic altimeter and GPS elevation. Survey zone is highlighted in red.*

### 3.3 SURVEY IMPLEMENTATION

The seismic field program was enacted in May of 2015. In early May, preparatory work began on the McQuat Lake site. A combination of large F350 Superduty trucks and 600cc Skandi Utility snowmobiles were used to access the remote site. Inuit built komatiks were used to haul equipment to the survey site. At site, a gas-powered Atlas-Copco Combi Cobra Hammer Drill was used with an 18-inch length drill rod and 2.5 inch diameter carbide drill bits to create the 0.5 to 0.75 meter deep blast holes. The majority of the survey site was still covered in snow, and deep snow drifts were dug into until frozen glacial till was hit, and a blast hole could be drilled. A Mastercraft 4hp Shopvac attached to a Yamaha 5000 generator was used to remove dust from the holes to prevent the hammer drill from jamming. Upon completion of the drilling, a pool noodle was cut into 4-inch segments and used to plug the holes to prevent snow from filling them in and cave ins.

A GPS base station was installed at the highest point in the center of the survey site. Due to the gently sloping topography and no tree cover, the GPS signal was extremely strong throughout the entire survey zone. A rebar rod was hammered into the ground and secured in place using limestone rocks to provide a repeatable reference location. It is assumed to be exact during the entire duration of the survey site as the temperature never warmed up enough to cause the surface glacial till to melt and shift. A Trimble™ R8 Kinematic GPS was set up over top of rebar and allowed to collect for 12 hours. This data were then sent into the Canadian Spatial Reference System to create a base station accurate to half a centimeter. Following this, a Trimble™ R6 base station and rover setup was used with a radio link to measure all shot points to half a centimeter accuracy horizontally and one-centimeter accuracy vertically.

During the first week of April 2015, seismic refraction and reflection data were collected using the University of Alberta's seismic collection equipment. Ten 96-meter seismic geophone lines with 4 m geophone spacing were moved to site using the snowmobiles and komatiks. In addition, 240 geophones and 10 24-channel Geode™ (Geometrics, San Jose) boxes were brought out along with all the supporting cables. Due to the limited access, a small tent was set up to act as a seismic recording 'doghouse'. Geophones were placed primarily in glacial till and had excellent coupling. Small sets of each line were placed in deep snow drifts and buried or along rocky scree slopes in which case coupling could be very poor. The GPS location of each Geophone was recorded using the above-mentioned Trimble™ Kinematic GPS system.

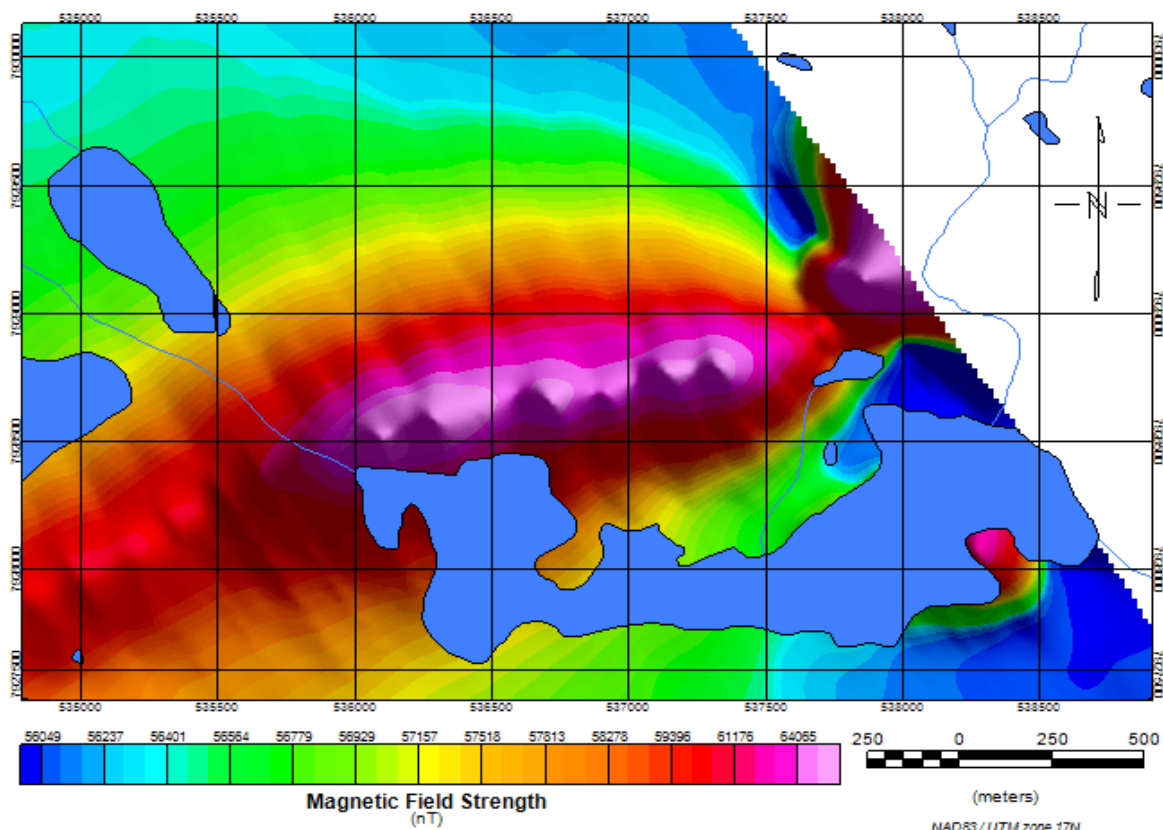


*Figure 3.2: Magnetic anomaly map with local lakes and rivers. Survey was performed north of main lake covering south central portion of map.*

Each line was shot slowly along the length of the line, with boosters being primed and placed down the hole one at a time as they were shot. A 100-meter radius safe zone was established, which was later increased to 250 meters due to the strength of the boosters and the fly rock created. Initially, a trigger geophone was set up 1m away from the blast hole and used to trigger the system and set a 0 time. However, the system was both difficult to move and unreliable. As such, the recording system was triggered manually from the doghouse with an 8 second recording time and a radio fire command issued. Shortly thereafter (2 to 3 seconds) the shot would be detonated. Zero time was then later corrected within the VISTAset using VISTA™ Seismic Suite. At the end of each day, the seismic line would be picked up and moved over onto the next planned out line.

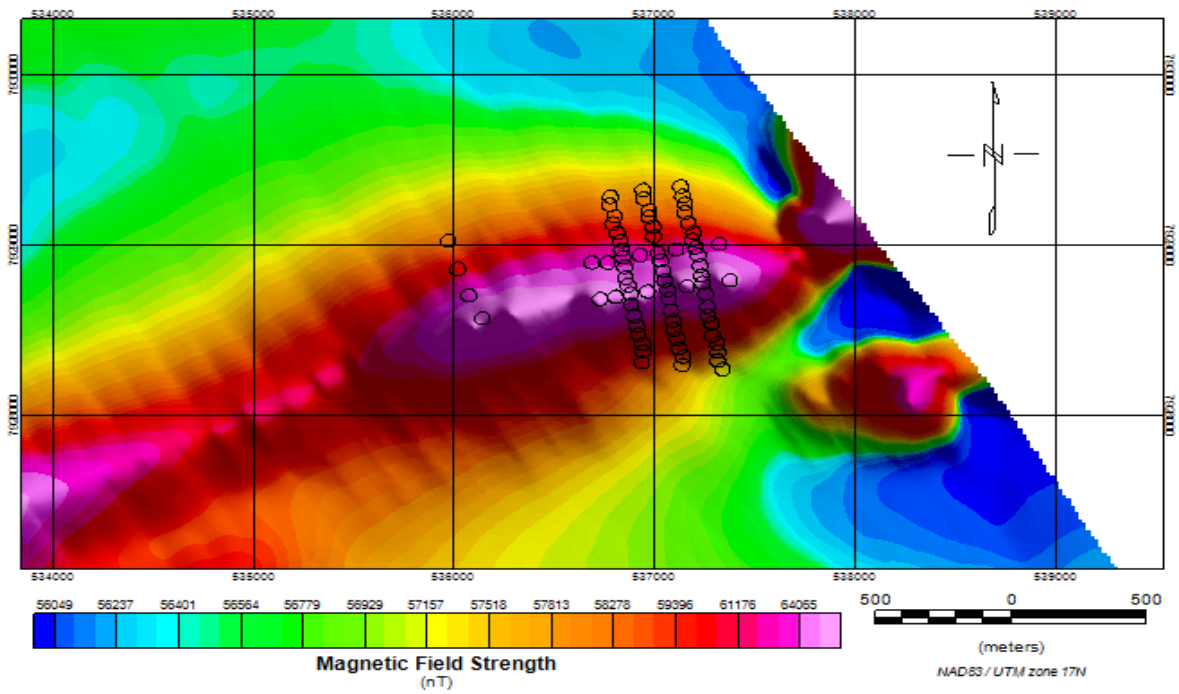


Figure 3.3: Gravity survey locations.

### 3.4 CHAPTER SUMMARY

The above methods were used to collect raw data while in the field, and process datasets through inversion to final subsurface models. Data collected followed standard field practices adapted for the harsh northern environment and limited field time available. Inversion methods were based on modelling data to a reasonable fit within geological datasets while minimizing misfit between forward model results and acquired data.

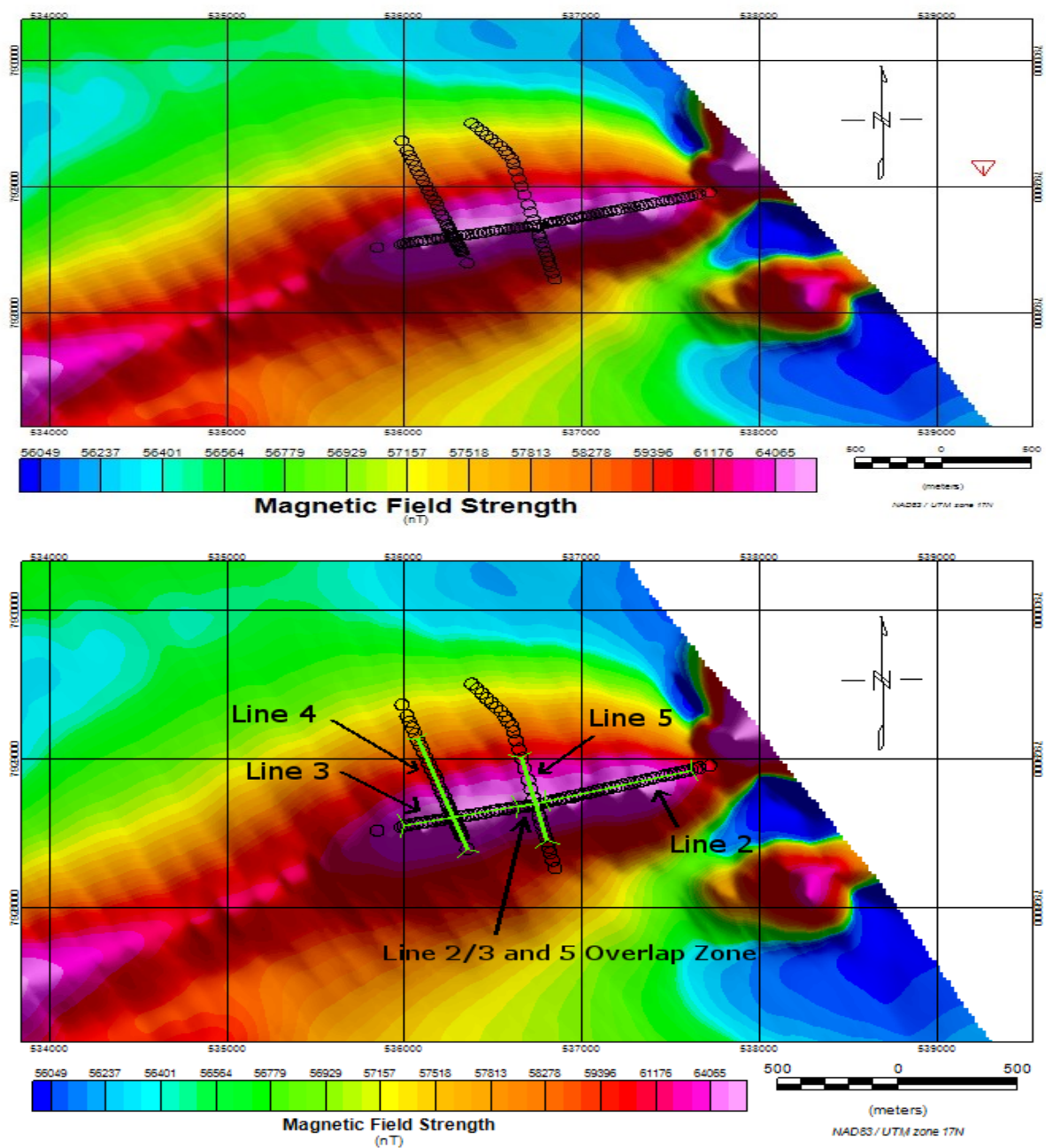


Figure 3.4: Top: Seismic Shot locations represented by circles over magnetic anomaly. Core plug borehole MR4-10-196 highlighted by red triangle.

Bottom: Survey geophone lines (green) and source (circles) locations overlaying magnetic anomaly.

## **CHAPTER 4     ROCK PHYSICS**

### **4.1 INTRODUCTION**

It is common practice to acquire measurements from a borehole of compressional and shear wave velocities, mass and density as functions of depth in the area of interest in order to provide some physical property and geological structure constraints against which the remotely acquired surface geophysical data may be compared. We did not have here, however, this luxury as no geophysical logging was carried out. There are currently no boreholes yet drilled into the survey site. To partially overcome this deficiency, we attempt to obtain some physical property values on core samples taken from a nearby borehole (approximately 2.7 km away from center of study area, across the Central Borden Fault). We expect that the geology at the site is similar to that of the borehole and as such the values measured will give us some indication of what might be expected.

The geology may complicate the assumption. Borehole MR4-10-196 from Baffinland Iron Mines was selected as the sample borehole as it was the closest hard rock exploration borehole to the survey site at approximately 2.7 km away. However, the Central Borden Fault with an 80m throw changed the topography between the McQuat Lake Survey Site and the selected borehole. As such, it was assumed that the core sampled from borehole MR4-10-196 would only be representative of approximately 80m depth and deeper due to uplift and weathering to the east of the Central Borden Fault escarpment.

Here we describe a set of preliminary laboratory wave speed and density measurements on the core samples. The results are presented and the implications for field observations discussed. Directions for future work on these samples, particularly with regards to the determination of seismic anisotropy, is mentioned.

#### **4.1.1 ULTRASONIC MEASUREMENT METHOD**

##### **4.1.1.1 SAMPLE PREPARATION**

Borehole MR4-10-196 recovered NQ core (~47.6 mm diameter) from 9m depth to approximately 180m depth. Visual inspection of the core revealed limestone spanning 9m to 14m transitioning into a low-grade BIF below this. At 85m depth a low-grade magnetite was encountered. At 120m depth the lithology changed into the basement chlorite rich greenstone schists.

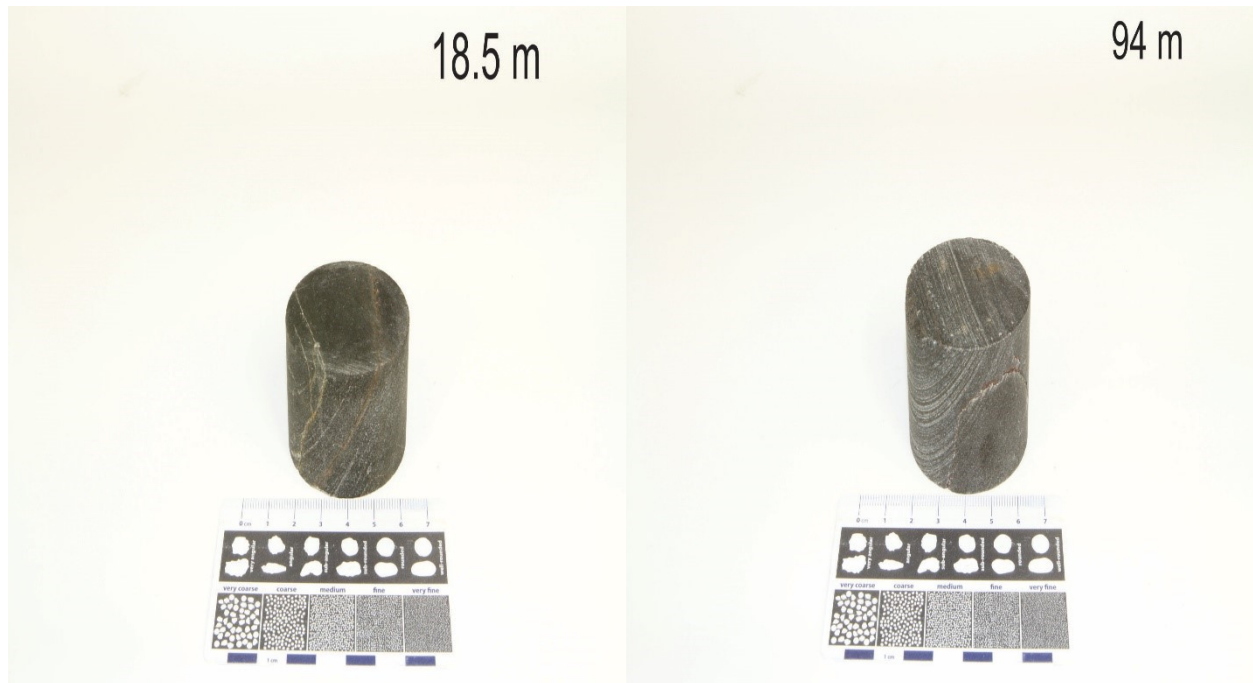


*Figure 4.1: Prepped core plugs from 18.5 and 94 meters depth. It is important to mention the crack propagating through the 94-meter sample from the bottom center to the right middle. It is expected this crack had a significant impact on ultrasonic velocity.*

The sampling strategy consisted of cutting 20cm long segments whose centres were spaced each 3m along the 171m length of the available core, providing 53 samples. These core segments were then shipped from the Baffinland Iron Mine core repository at Mary River to the University of Alberta for processing and analysis.

Given the limited resources available, a subset of 13 representative segments, at a spacing of roughly 10m along the depth of the borehole, were selected for final detailed analysis. These were cut into five to eight cm lengths using a high-speed rock saw. Their end surfaces were then surface ground to ensure they were parallel using a round surface grinder with a magnetic stabilizing base for the sample tray. Figure 4.1 exhibits finished sample photos of samples 18.3 meters and 94 meters, photographs of the other samples are provided in the appendix. All finished surfaces were double checked using a simple carpenter set square. Finalized sample lengths were then measured using calipers accurate to 0.005 mm.

#### **4.1.1.2 LABORATORY MEASUREMENTS**

The laboratory procedure followed those for the transit time method described previously from the laboratory (Molyneux and Schmitt (2000), Cholach et. al. (2005)). Core sampled was NQ dimension core with a nominal diameter of 47.6 mm. Two endcaps were machined out of 6061 T6 aluminum to be

approximately 40 mm long and 47.6 mm in diameter to match the width of the core. Two grooves were lathed into the endcap 10 mm and 20 mm from the bottom to house rubber O rings. A 3-mm diameter hole was drilled 10 mm into the top surface near the edge of the end cap and tapped with screw threads to be used as a grounding point. Figure 4.2 exhibits a finished endcap. Piezoelectric ceramic transducers (Material # 840, BaTiO<sub>3</sub>, 1 MHz resonance frequency) were silver epoxied to the top of each endcap in a mirror pattern so that paired transducers would be lined up when end caps were installed. The compressional wave transducer measured 20mm in diameter and 2.1 mm thick and the shear wave transducers measured 15mm square and 1.16 mm thick. One compressional wave transducer and two shear wave transducers were installed, with the shear wave transducers being oriented perpendicular to each other to create shear waves in both the X and Y directions. This arrangement provides some measure of the anisotropy of these layered samples. More advanced techniques are necessary to fully understand the anisotropy (e.g. Ong et al, 2016).

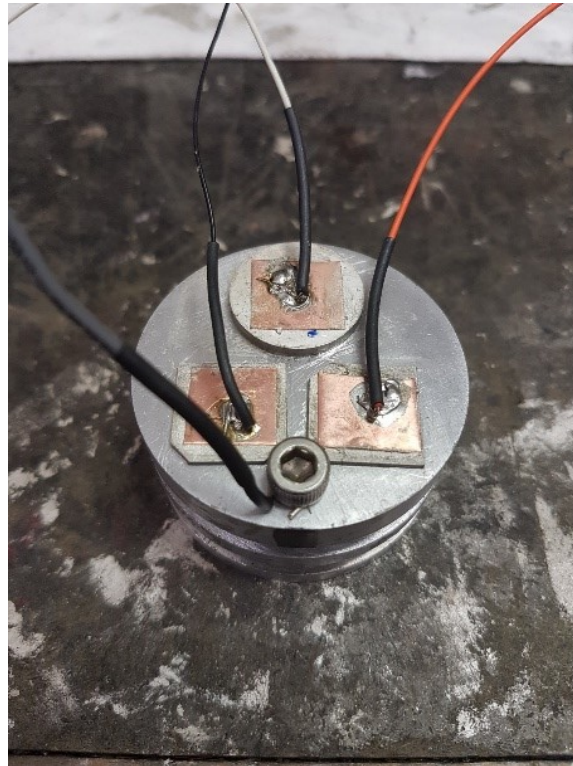


*Figure 4.2: 6061 T6 machined aluminum endcap with compressional wave piezoelectric transducer at the top (circular transducer), two shear wave transducers perpendicular to each other in the middle (square with tapered corner), and a ground screw at the bottom. All electronics and soldered connections were then covered in flexane to seal.*

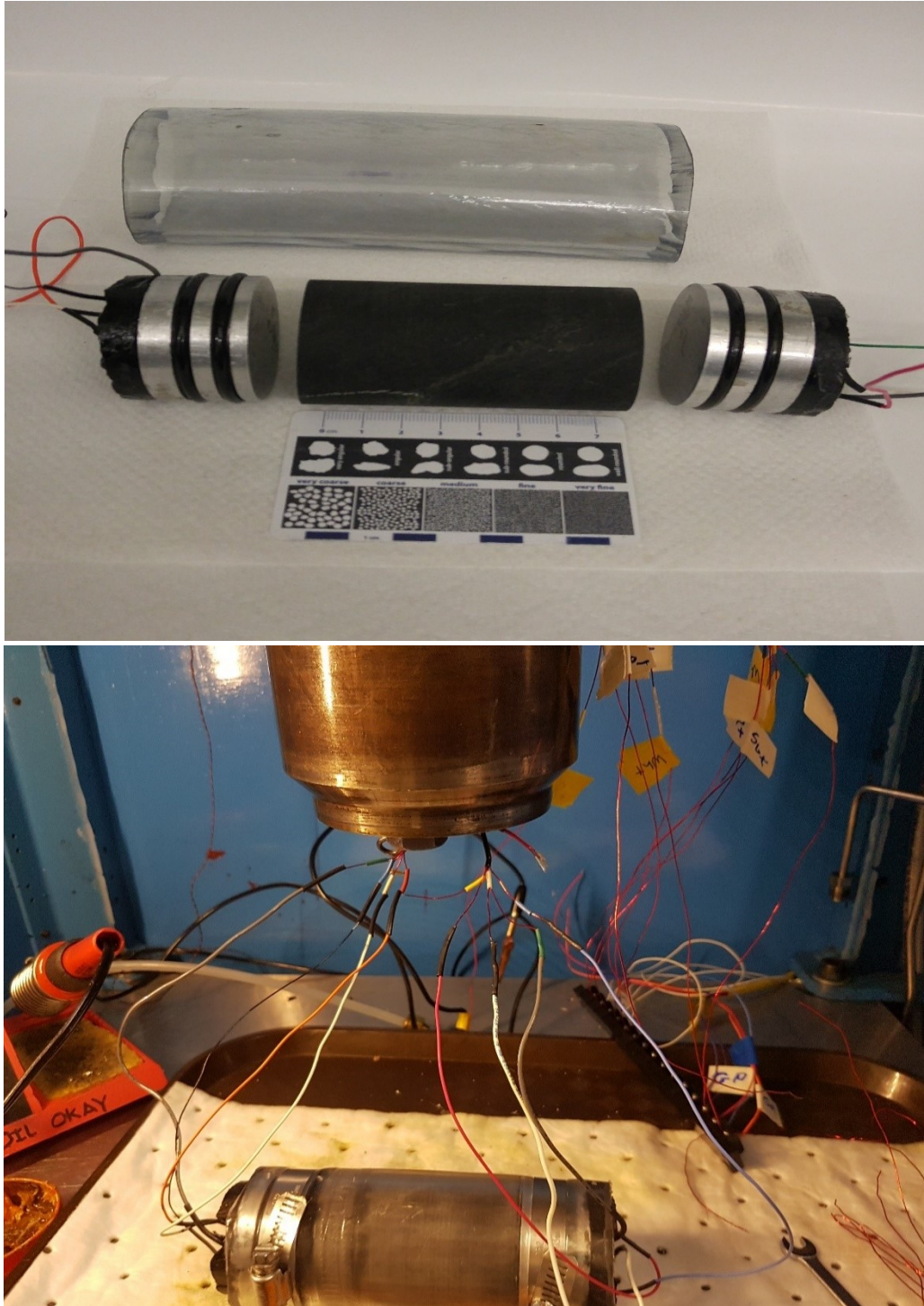


*Figure 4.3: Top: Expanded view of core sample and end cap set up right before insertion into the pressure vessel.*

*Bottom: Core plug sample encased in PVC tubing with endcaps sandwiched on ends. Transducer wires have all been connected through pressure vessel seal and to LabView software.*

The surface of the endcap was large enough so that each transducer could be epoxied directly to the top surface of the end cap. A thin 0.2mm thick copper sheet was then cut and silver epoxied to the surface of each transducer so that a wire may be soldered to each transducer individually. Small 20-gauge wire was then soldered to the surface of each copper sheet, taking care not to let any solder drip over and create a short. A screw was used to connect a thicker 14-gauge wire to the previously tapped hole to be used as a ground and support weight when in the pressure vessel. Finally, a wax paper mold was wrapped around the circumference of the end cap and Flexane 80 Liquid poured in 15 mm deep to completely seal all transducers and wire connection points.

O-rings were inserted onto the finished end caps and the end caps pressed against the polished surfaces of the core sample. The sandwiched core sample and endcaps were then pressed into 47.6 mm (1.85 inch) diameter Kuri Tec Klearon 73 clear PVC tubing cut to a length able completely enclose both end caps and core sample. This process created air pockets in the contact zone between the endcap and the core sample. Toothpicks were gently inserted in the space between the endcap and the PVC tubing to create an air pathway, and a press used to squeeze the air out, then the toothpicks removed. Pipe clamps were then fastened over each O ring to ensure the rock sample was sealed.

Core plug orientations were always aligned with the orientation directions shown in Figure 4.4. The updip edge of the core plug was always aligned to be the top right of the core plug (origin of the coordinate system in Figure 4.4). End caps were oriented onto the core plugs so that the S wave transducers were on the right (updip) half of the core plug, and P wave transducer in the middle on the left (downdip) half of the core plug. Shear waves were then aligned so that the S wave transducer creating the shearwave designated Sa would propagate through the sample with displacement in the X direction, and the S wave transducer creating the shearwave designated Sb would propagate through the sample with displacement in the Y direction. Due to the thinly bedded layers, the core plug is expected to be highly anisotropic, and a large difference is expected to be observed in the Sa and Sb waves. However, the near 45 degree angle in bedding in many of the core samples caused by the non-perpendicular strike of the drill with the ore body will result in very similar wave speeds and little anisotropic difference.

To simulate pressure and temperature at depth, a model R4-20-30 O-Ring Closure Reactor High Pressure Chamber from High Pressure Equipment Co. was used. Endcap wires were soldered to 45-gauge plated wires running through small access points in the lid of the high-pressure vessel. The 45-gauge plated wires then ran to the computer pulsing system. The sample was suspended from the lid of the pressure vessel using loops of 45-gauge wire connected to the lid of the pressure vessel and the screw points on the pipe

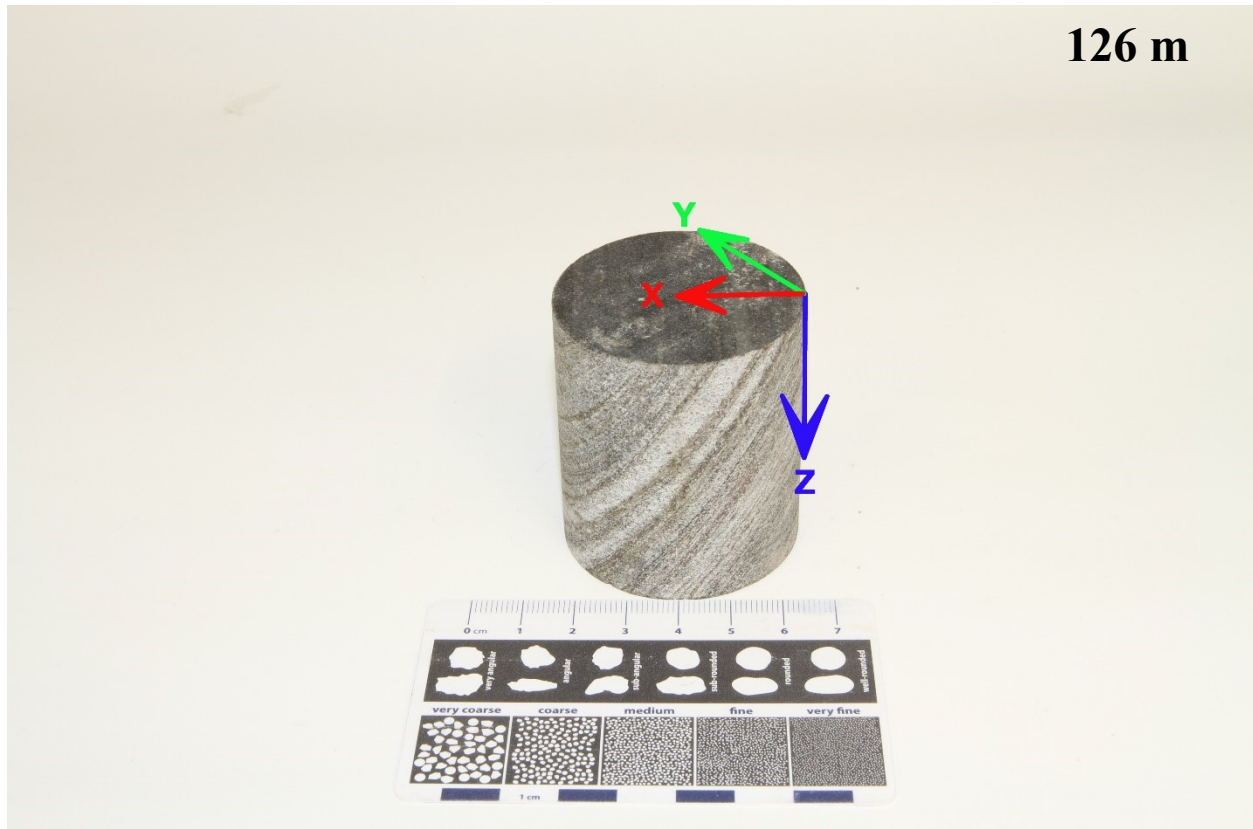


*Figure 4.4: Core plug from 126 meters depth highlighting orientation all core plugs were aligned to prior to attachment of end caps with transducers. The top right half of the core plug (where the origin of the coordinate system is located) is referred to as the up-dip side, while the left half is referred to as the down-dip side.*

clamps of the core sample. Wires were taped and tied tightly to not get snagged on the seal of the pressure vessel as the core sample was lowered inside. Oil was pumped into the pressure vessel using a Quizix™ Q5000 Series High Pressure pump to increase pressure.

Ultrasonic travel time measurements were taken at intervals becoming gradually larger with increasing pressure from 2 MPa to 200 MPa on both increasing pressure and decreasing pressure runs. Measurements were delayed by 6 minutes after each pressure increment to allow temperatures and pressures in the vessel to stabilize. LabVIEW™ software was used to send an electric pulse to the piezoelectric transducers on one endcap one at a time, resulting in compressional or shear vibrations being created. Electric response was then recorded from both the pulsing and receiving transducers.

#### 4.1.2 ULTRASONIC MEASUREMENT RESULTS P WAVE

Each individual waveform recorded from each pressure and transducer was separately saved as a text file recording time and amplitude. Individual text files for each pressure and wave type were then combined into files based on wave type using MATLAB™. A routine written by Schmitt (2016) was used to combine waveforms and save in a SEG-Y format. Pressures are represented as geophone locations to create a “shot gather” for each wave type of each rock sample. Schlumberger Vista was then used to pick first breaks representing the travel time through the endcaps and core sample.

Due to the velocity difference between the aluminum end caps and core sample, a calibration run was also performed on just the end caps pressed together with no core sample in between. The calibration run was also transferred with MATLAB to SEG-Y format and first arrivals picked using Schlumberger VISTA™. Travel times through the core sample were then calibrated using the following formula:

$$V_s = \frac{L_s}{T_T - T_C} \quad (4.1)$$

Where  $V_s$  is the calculated velocity through the rock sample,  $L_s$  is the length of the rock sample,  $T_T$  is the total measured time of the core sample from VISTA™ first arrivals, and  $T_C$  is the calibration time of the aluminum endcaps. Calibration runs for compressional (P) and shear (S) waves exhibited traveltimes through both endcaps of 13.4 ms (P wave) and 21.8 ms (S waves) for 5MPa, 13.3 ms (P wave) and 21.5 ms (S wave) for the “kink” point at 35MPa, and 13.15 ms (P wave) and 21.4 ms (S wave) quicker for 100 MPa and greater.

The waveforms for the core plug from 18.3 meters depth are provided for illustration in Figure 4.5; images of the remainder of the compressional waveforms can be found in the appendix. Final core plug velocity results can be seen in figures 4.6 through 4.8. We notice many different pulses in the waveforms. The first pulse corresponding to the reflection off the first aluminum core boundary and being picked up by the pulsing transducer. The second arrival is the true travel time through the entire system as there will be no second reflection off the core aluminum boundary due to the velocity inversion. Close investigation shows a steeper increase in velocity across all samples during the up run of the experiment, but a much slower decrease. This is a result of the hysteresis (Ong et al., 2016) effect being caused by grains under stress remaining under stress even when the pressure is removed.

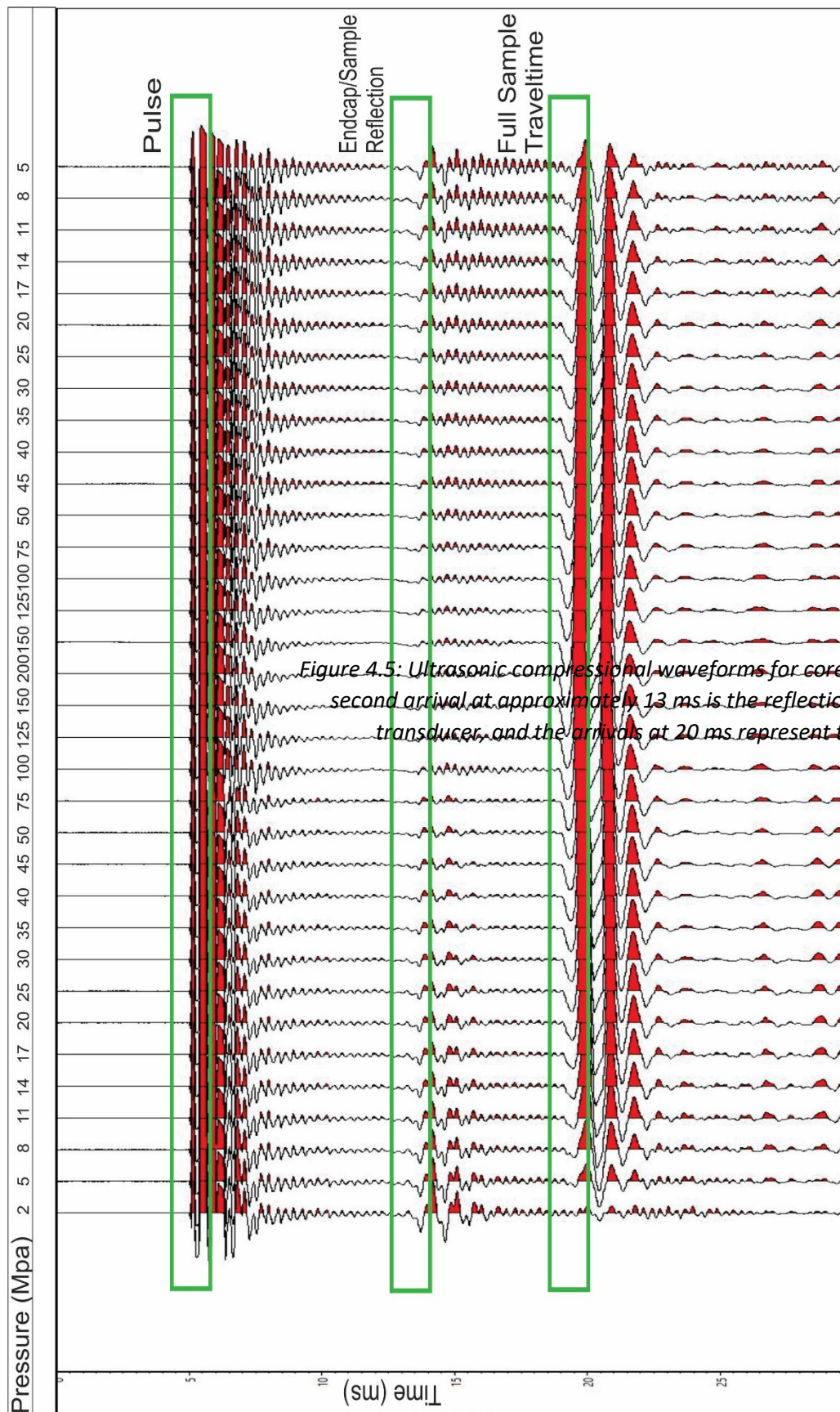


Figure 4.5: Ultrasonic compressional waveforms for core plug from 18.3 meters. The first arrival at approximately 5 ms is the pulse, the second arrival at approximately 13 ms is the reflection off the aluminum end cap/core plug transducer, and the arrivals at 20 ms represent the entire ultrasonic travel time through the sample.

Velocity measurements for all samples showed 2 main velocity slopes. A high increase in velocity with increasing pressure below 35 MPa and a much slower increase in velocity with increasing pressure Above 35 MPa. Lower pressure velocity data points exhibited higher R-squared values from the linear best fit for the velocity curves. At higher pressures, end caps are firmly pushed onto the core sample, creating a better seal for a more efficient transfer of energy. Attenuation in the core sample (Molyneux and Schmitt, 2000) outlines attenuation factors in hard rock media and its effect on phase and group velocity. It is likely that at lower pressures there is still a small gap between the buffers and the sample preventing good coupling between the surface of the end cap and core sample, resulting in a loss of energy. It is also likely that larger cracks and pores in the core sample are also resulting in the scattering of wave energy during propagation. Higher pressure causes these to close and create a denser medium that propagates the waves more effectively.

P wave velocities of core samples range from 4000 m/s to 6700 m/s. All velocity vectors exhibit a “kink” in their slope at roughly 35 MPa. It is suspected that this is the pressure at which all microcracks seal up, increasing the bulk and shear moduli of the sample. As expected, the velocities generally increase with increasing sample depth in the core; and this reflects changes in the mineral content. P wave velocities from BIF samples ranging in depths from 18m to 74m increase with depth while iron and silica content remains generally the same. Greenstone schist samples from 134m and 154m depth exhibit a drastic decrease in velocity compared to surrounding samples. The basement greenstone sample has a much higher velocity than the overlying lithologies and displays little to no variation with changing pressure.

All core samples save for 18.5m, and the deepest 134m, 154m, and 170m, exhibit a large increase in velocity with increasing pressure. The core sample from 74m depth increases from 5800m/s to 6400m/s over a 150 MPa increase. All other BIF samples save for the shallowest exhibit similar increases. In contrast, samples from 134m, 154m, and 170m exhibit nearly no velocity alteration with increasing pressure; this may result from the differences in their mineralogical content. The high-grade hematite/magnetite sample from 94m depth has a lower velocity than expected, with values increasing from 4750 m/s to 5450 m/s with pressure. It is interesting to compare this to published values on a sample of hot-pressed synthetic hematite ( $\text{Fe}_2\text{O}_3$ ) with P- and S-wave velocities of 7901 m/s and 4162 m/s, respectively, with a density of 5253 kg/m<sup>3</sup> (Liebermann and Schrieber, 1968), and with those for magnetite ( $\text{Fe}_3\text{O}_4$ ) of 7380 m/s and 4185 m/s, respectively, with a density of 6206 kg/m<sup>3</sup> (Hearmon, 1984). This is approximately 83% to 93% the velocities of the low-grade BIF core samples at similar hydrostatic pressures and may be indicative of greater porosity in the high-grade sample.

### 4.1.3 ULTRASONIC MEASUREMENT RESULTS S WAVE

Resulting velocities showed Sb waves (B direction propagation) to be only slightly faster than Sa waves (A direction propagation). Shear waves overall were approximately 60 % to 70 % the speed of compressional waves at same hydrostatic pressures, as is expected. Both Sa and Sb waves have velocities ranging between 3100 m/s and 4100 m/s. However, core samples from 45m depth and 154m depth have very slow Sa velocities spanning 2600 m/s to just over 3000 m/s. As with compressional wave velocities, core samples from shallower depths show a greater increase in wave speed with increasing pressure. All velocity vectors still follow a typical radical curve. Shallower samples exhibit higher R squared values when fitting a curve to data points, especially at lower pressures. As with compressional waves, once we increase pressure to above the “kink” point at 35 MPa to 50 MPa all microcracks close and we see a much smoother linear increase in velocity with pressure. Samples from deeper depths show less of a drastic increase in velocity, and in the case of Sa waves for samples from 45m, 23.8m, 18m, 170m and 134m we see a decrease in velocity during the first 35 MPa increase.

### 4.2 GRAIN DENSITY MEASUREMENTS

Measurements of bulk envelope density and grain (i.e., solid or mineral) density were performed on small discs cut from the cores immediately below the location of the velocity samples, as such there is a 30 mm to 50 mm difference in depth between the velocity samples and those for which density is obtained. Discs were cut to approximately 10 mm thick. Discs were then polished flat on both sides using the surface grinder to create a cylindrical disk with flat tops and bottoms. Volume was measured by taking 6 measurements of circumference and 6 measurements of thickness using calipers accurate to 0.005 mm. Volume of the cylinder was then calculated using the formula:

$$V = h \cdot \pi r^2 \quad (4.2)$$

Where V is the calculated volume, h is the height of the cylinder, and r is the radius. Water displacement volume calculations were attempted but due to size of core samples, a simple beaker had to be used and proved to be unreliable due to surface tension effects. Samples were instead weighed using a lab scale accurate to 0.005 grams and the bulk envelope density was then calculated by dividing the mass by the volume (Table 4.3).

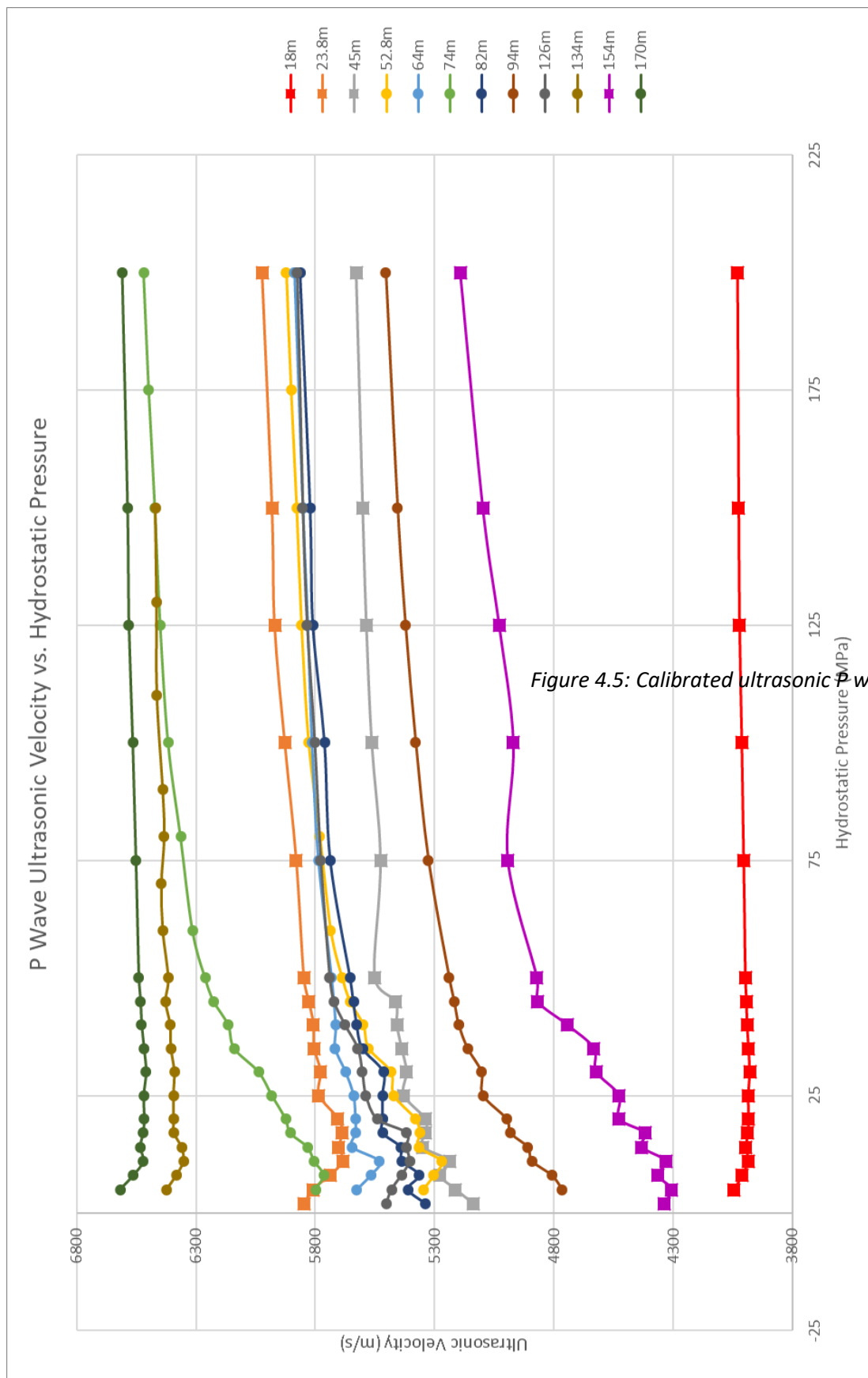


Figure 4.5: Calibrated ultrasonic P wave velocities vs. confining pressure

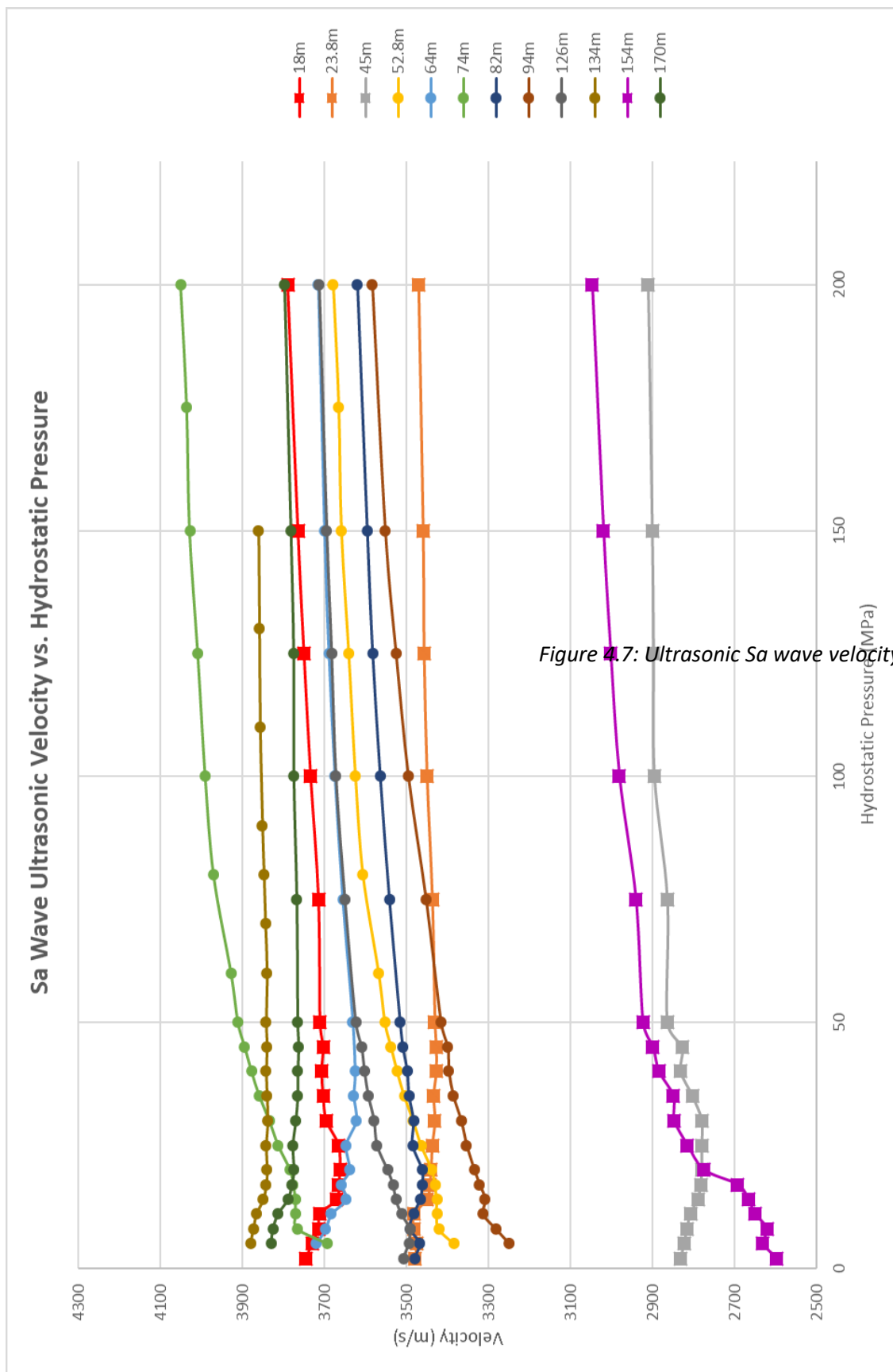


Figure 4.7: Ultrasonic Sa wave velocity vs. hydrostatic confining pressure

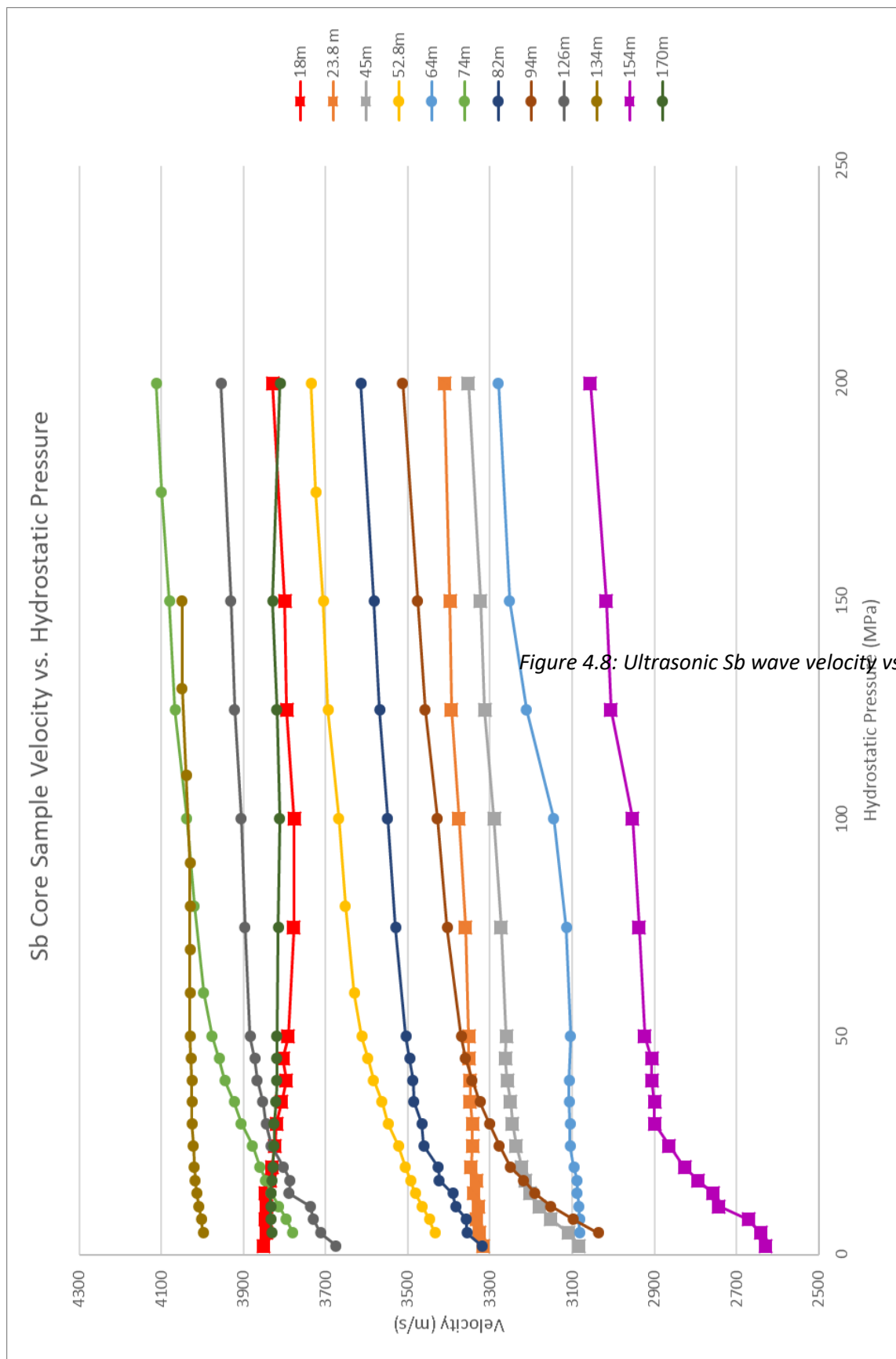


Figure 4.8: Ultrasonic Sb wave velocity vs. hydrostatic confining pressure

Grain density within the rock sample was measured on the same pieces using a Quantachrome Multipycnometer™ model MVP-6DC hooked up to a high-pressure helium tank. The pycnometer was calibrated each morning measurements were taken using a standardized steel ball of known volume and porosity. The core disc was placed inside the pycnometer chamber which had a known volume and sealed. Air was evacuated from the chamber using a vacuum pump. Once the chamber had a vacuum reading 150 millitorr, the system was sealed off and a helium gas inserted. The system contains two known volumes, a reference volume and the sample chamber volume separated by a valve. The reference volume is pressurized to a known amount and the pressure recorded so the volume of gas is known. The valve between the two chambers is then opened and the new pressure recorded. The new volume is now the reference chamber volume plus the sample chamber volume. The change in pressure is then measured, and using the known volumes and calibration data, the grain volume of the sample determined. This measurement is repeated between 5 and 10 times to ensure accuracy. The previously measured mass is then used to calculate grain density (Table 4.3).

Grain density is combined with envelope density to determine porosity of the rock. Envelope density is subtracted from the grain density then divided by the grain density. Grain density is higher than envelope density, and table 4.1 shows that the core plug from 23.8 m depth has a higher envelope density. This is likely caused by measurement errors for the envelope density and as such the porosity values should be ignored. Examining porosity, we see a general trend of increasing porosity with increasing iron content. Higher porosity values can have a slowing effect on the P and S wave velocities of the rock sample.

Grain densities measured all fall between 2.633 g/cm<sup>3</sup> and 2.769 g/cm<sup>3</sup> for low grade BIF samples. The 94-m magnetite sample has a not-unexpected jump in grain density to 3.384 g/cm<sup>3</sup> and basement samples vary between 2.745 g/cm<sup>3</sup> and 2.984 g/cm<sup>3</sup>. Resulting values and compression wave velocities do not follow Gardner's equation:

$$\rho = \alpha V_p^\beta \quad (4.3)$$

where  $\alpha$  and  $\beta$  are constants defined by geology and are set to 0.31 (if V is in m/s) and 0.25 respectively,  $V_p$  is compression wave velocity in m/s and  $\rho$  is the density in g/cm<sup>3</sup>. The inconsistencies we see with Gardner's equation likely result from the fact that it was developed for porous sedimentary rocks for which even at the best of times one must take care in its use. The poor results here argue further for limited application of empirical fits such as Eqn. 4.3 outside of the data set they were acquired for.

Sample Depth (m)	Iron Content (wt. %)	Silica Content (wt. %)	Aluminum Content (wt. %)	Grain Density (g/cm <sup>3</sup> )	Measured Volume (cm <sup>3</sup> )	Mass g	Calculated Density (g/cm <sup>3</sup> )	Porosity (%)
18.5	6.37	69.99	11.36	2.75	8.30	22.4	2.70	0.67
23.8	8.65	60.31	14.42	2.63	10.96	28.9	2.64	0.76
37.2	8.27	61.94	16.1	2.74	19.64	53.4	2.72	0.86
45.7	8.3	61.69	15.88	2.77	15.44	42	2.72	0.82
52.8				2.73	20.20	54.4	2.69	0.87
65.1				2.75	10.80	31.5	2.92	0.73
73.5	5.49	65.92	15.5	2.77	20.01	54.5	2.72	0.86
82.5	5.15	68.98	14.28	2.72	17.22	46.8	2.72	0.84
94.2	56.65	41.69	0.47	3.38	16.06	52.2	3.25	0.80
126.1				2.98	15.29	44.9	2.94	0.81
134								
154.7				2.71	19.93	52.7	2.64	0.87
170	5.68	56.37	18.06	2.75	13.97	35.7	2.55	0.82

Table 4.1: Rock Physics Measurements made on borehole core plugs

Sample Depth (m)	Iron Content (wt. %)	VP 5MPa (m/s)	VP 35MPa (m/s)	VP 150MPa (m/s)	Sa 5MPa (m/s)	Sa 35MPa (m/s)	Sa 150MPa (m/s)	Sb 5MPa (m/s)	Sb 35MPa (m/s)	Sb 150MPa (m/s)
18.5	6.37	4046	3985	4027	3730	3704	3765	3844	3808	3800
23.8	8.65	5810	5805	5981	3476	3435	3460	3325	3349	3397
37.2	8.27									
45.7	8.3	5212	5437	5600	2823	2803	2901	3108	3250	3323
52.8		5348	5577	5878	3385	3506	3660	3434	3563	3706
65.1		5625	5716	5852	3720	3629	3701	3082	3108	3252
73.5	5.49	5799	6139	6471	3694	3860	4029	3780	3923	4080
82.5	5.15	5410	5602	5821	3468	3494	3597	3356	3485	3583
94.2	56.65	4764	5162	5456	3250	3387	3553	3036	3325	3476
126.1		5479	5622	5853	3495	3593	3695	3713	3854	3931
134		6424	6405	6470	3881	3841	3861	3999	4026	4050
154.7		4306	4632	5098	2631	2850	3020	2641	2900	3017
170	5.68	6618	6518	6587	3831	3766	3783	3831	3821	3829

Table 4.2: Key ultrasonic velocity measurements made on borehole core plugs.

### 4.3 MAGNETIC SUSCEPTIBILITY

Magnetic susceptibility measurements were made using a Bartington MS2 sensor probe attached to a Bartington MS2 meter on the core samples used during the ultrasonic measurements. Typically, magnetic susceptibility measurements are taken on the flat surfaces of the vertically split cores. This gives a much more reasonable measurement of magnetic susceptibility with depth. However, core samples here were limited and could not be cut. Magnetic susceptibility measurements were instead taken on the top of each core sample multiple times to average out different readings. The Bartington MS2 sensor probe was calibrated against a cube of known magnetic susceptibility provided with the instrument. The magnetic susceptibility probe is extremely sensitive, and placing the tip on a silica crystal would result in a far different reading than if the tip were to be placed on an iron rich mineral. As such, multiple readings were taken around the surface each core plug, with atmospheric magnetic readings measured in between. The total magnetic susceptibility measurement was given by:

$$M_{atm} + M_{sample} = M_{total} \quad (4.4)$$

Where  $M_{atm}$  is the magnetic susceptibility of the atmosphere taken before the reading, and  $M_{sample}$  is the magnetic susceptibility of the core sample. Results were then averaged and can be seen in Table 4.3.

### 4.4 Whole Rock Analysis

#### 4.4.1 X-RAY FLUORESCENCE

X-ray fluorescence (XRF) techniques are standard in the determination of the elemental composition of materials in general. The technique relies on measuring the flux of fluorescent x-rays emitted when electrons higher in the electron shells of elements drop to a lower energy shell to replace an electron that was ejected by primary x-ray radiation into the sample. The wavelength of the fluorescent x-ray emitted when this happens is defined by quantum mechanical energy states in the element and as such is unique to a given element. Measuring the flux of the fluorescent x-rays at a given wavelength consequently relates directly to the concentration of that element in the sample. In this way a highly accurate measure of composition is obtained. In the geosciences this is often referred to as 'whole rock analysis' and the results are provided in terms of 'oxides' such as  $\text{SiO}_2$ ,  $\text{MgO}$ , and  $\text{CaO}$  under the presumption that most rocks are composed of silicate minerals most of which can be constructed stoichiometrically by combining basic oxides.

Depth (m)	$\chi$ ( $\times 10^{-5}$ SI)															Average
	1			2			3			4			5			
	Matm	Msample	Mtotal	Matm	Msample	Mtotal	Matm	Msample	Mtotal	Matm	Msample	Mtotal	Matm	Msample	Mtotal	
11.2	-6	20	26	-8	21	29	-7	20	27	-7	20	27	-7	21	28	27.4
13.9	-7	44	51	-7	45	52	-7	45	52	-7	45	52	-8	45	53	52
16.5	-7	25	32	-7	26	33	-7	25	32	-8	25	33	-7	24	31	32.2
23.8	-12	34	46	-13	33	46	-13	33	46	-14	34	48	-13	33	46	46.4
26.1	-7	55	62	-7	54	61	-7	53	60	-7	54	61	-7	52	59	60.6
28.3	-7	20	27	-7	20	27	-8	20	28	-7	19	26	-8	20	28	27.2
39.9	-8	34	42	-8	34	42	-8	33	41	-8	32	40	-8	33	41	41.2
42.2	-8	20	28	-8	20	28	-8	19	27	-8	20	28	-8	20	28	27.8
45.7	-12	23	35	-13	23	36	-13	24	37	-14	21	35	-14	22	36	35.8
47.8	-8	37	45	-7	36	43	-8	34	42	-9	35	44	-9	36	45	43.8
50.2	-7	30	37	-9	29	38	-9	30	39	-8	29	37	-8	29	37	37.6
52.8	-13	9	22	-13	9	22	-14	9	23	-13	9	22	-14	8	22	22.2
59.4	-7	14	21	-8	13	21	-9	12	21	-9	13	22	-9	13	22	21.4
67.3	-9	49	58	-9	49	58	-8	48	56	-9	48	57	-9	49	58	57.4
69.8	-8	22	30	-9	21	30	-8	21	29	-9	21	30	-8	21	29	29.6
73.7	-11	16	27	-13	16	29	-13	16	29	-13	15	28	-14	15	29	28.4
76.6	-7	18	25	-9	18	27	-9	18	27	-9	19	28	-9	22	31	27.6
79.4	-7	13	20	-9	13	22	-9	13	22	-9	13	22	-9	13	22	21.6
82.5	-9	15	24	-13	14	27	-13	14	27	-13	14	27	-12	14	26	26.2
88	-9	32	41	-10	31	41	-10	31	41	-10	32	42	-10	31	41	41.2
91.4	-9	39	48	-10	38	48	-9	34	43	-9	37	46	-10	36	46	46.2
94.2	-9	7263	7272	-11	9569	9580	-10	8459	8469	-11	6676	6687	-11	8912	8923	8186.2
96.7	-10	3092	3102	-9	9479	9488	-10	3278	3288	-8	6639	6647	-9	5693	5702	5645.4
99.5	-8	2838	2846	-8	1149	1157	-8	9529	9537	-8	2635	2643	-8	1249	1257	3488
102.1	-9	39	48	-9	38	47	-9	38	47	-10	39	49	-9	38	47	47.6
105.1	-9	804	813	-9	8243	8252	-10	5929	5939	-9	5414	5423	-9	5610	5619	5209.2
107.4	-8	549	557	-9	8268	8277	-8	9008	9016	-9	2344	2353	-9	9683	9692	5979
110.5	-10	4569	4579	-9	4486	4495	-9	3831	3840	-10	1620	1630	-10	4692	4702	3849.2
113.3	-9	2936	2945	-9	6568	6577	-9	4032	4041	-8	5672	5680	-8	3619	3627	4574
115.7	-8	143	151	-8	447	455	-7	9112	9119	-9	102	111	-8	9965	9973	3961.8
118.2	-8	9476	9484	-8	1673	1681	-8	7196	7204	-8	9913	9921	-8	9348	9356	7529.2
121	-6	3475	3481	-5	3507	3512	-6	2778	2784	-7	4515	4522	-6	4629	4635	3786.8
123.3	-9	5941	5950	-10	6112	6122	-10	7822	7832	-9	9232	9241	-10	3399	3409	6510.8
126.1	-10	2681	2691	-10	2766	2776	-10	3627	3637	-10	4514	4524	-10	4770	4780	3681.6
129	-7	720	727	-8	8854	8862	-7	9151	9158	-6	9711	9717	-5	8120	8125	7317.8
131.8	-7	4467	4474	-6	4219	4225	-6	4062	4068	-7	5022	5029	-7	4400	4407	4440.6
140.1	-6	74	80	-8	72	80	-8	73	81	-9	74	83	-9	74	83	81.4
143.1	-9	62	71	-9	64	73	-9	64	73	-10	63	73	-10	65	75	73
149.2	-7	33	40	-10	33	43	-10	32	42	-10	32	42	-10	33	43	42
151.9	-10	4772	4782	-10	4966	4976	-8	636	644	-9	7658	7667	-9	9318	9327	5479.2
154.7	-8	35	43	-8	35	43	-8	34	42	-9	34	43	-10	35	45	43.2
157.3	-7	5291	5298	-7	3350	3357	-7	141	148	-7	5969	5976	-7	4564	4571	3870
160.9	-5	5985	5990	-8	4475	4483	-9	5802	5811	-8	4247	4255	-8	4277	4285	4964.8
163.8	-8	39	47	-8	39	47	-9	38	47	-10	39	49	-9	39	48	47.6
167.2	-9	44	53	-10	45	55	-9	46	55	-10	38	48	-10	40	50	52.2

*Table 4.3: Magnetic susceptibility measurements made on all core samples recovered from Baffin Island. Measurements were taken 5 times with atmospheric measurements made between each measurement to calibrate the magnetic susceptibility probe. Values were then averaged. Magnetite is prevalent in the core samples between 94 and 130 meters. These samples had been split vertically.*

Eight samples were selected to be sent out ALS Laboratory Services (Vancouver) for standard XRF whole rock analysis. Sample depths were selected to encompass BIF and high-grade iron ore samples of varying velocities. The discs used in the previous pycnometer density determinations were prepared for XRF measurements by powdering. The samples were first broken down into small chunks with a hammer then ground into powder using a shatter box in the Department of Earth and Atmospheric Sciences. Powder was then sifted using a shaker table and 3 200 micron meshes. Approximately 20 grams of each sample was produced in a fine powder that was sent to ALS. XRF measurements were performed to investigate the iron and silica weight percent to compare to velocity measurements. We note that the standard XRF whole rock analysis may have been insufficient for finding the composition of the higher-grade ores, and this may be a consideration for future work, but we do not know at this time the errors in composition that may be obtained. It was expected that the higher density magnetite would also have the highest velocity and iron content. Low grade BIF samples from 18.5m to 84m depth all hosted lower than 8.65 wt. %  $\text{Fe}_2\text{O}_3$ , with iron content slowly decreasing as samples moved deeper. The high-grade sample at 94m measured 56.65 wt. %  $\text{Fe}_2\text{O}_3$  and had a higher density than all BIF samples, yet was roughly 400 m/s slower than all BIF samples. Basement greenstone had a similar iron content to the BIF at 5.68 wt. %. Silica contents for BIF samples ranged from 60 wt. % to 70 wt. %, samples with higher iron content had lower silica content. All BIF samples had higher alumina content ranging from 11.36 wt. % for the shallowest 18.5m deep sample to 16.1 wt. % for the 37.2m deep sample. The basement greenstone sample has an alumina content of 18.06 wt. %.

#### **4.4.2 X-RAY POWDER DIFFRACTION**

20 grams of each sample was also prepared as stated above and sent to the University of Alberta Geology XRD lab for analysis. The results can be seen in Table 4.5. Sample spectrums for 37.2 and 94.2 meters depth can be seen in Figures 4.9 and 4.10. Remaining XRD spectrums can be found in the appendix. All low-grade BIF's from 18.5 meters depth to 82.5 meters depth exhibit high concentrations of quartz with the limited amounts of Fe appearing likely in the mineral clinocllore. Save for the high-grade sample from 94.2 m, mica minerals increase with depth suggesting a higher grade of metamorphism as we move downward. All shallow BIFs are high in magnesium and aluminum hosting minerals including clinocllore, oligoclase, cummingtonite and oligoclase.

#### **4.5 SUMMARY**

Measurements made in this chapter were done to improve understanding and interpretation of results from geophysical datasets and their inversions presented in chapters 5 and 6. It is important to note that



Fe wt. % for all BIF samples is typically too low for samples to be properly considered BIF. However visual hand sample analysis shows typical BIF structures of thin dark bands of iron rich minerals banded with chert and silica. Laboratory measurements for magnetite and BIF suggest velocity ranges from 4600 to 5500 m/s and as such ultrasonic velocities should be considered slightly high.

<b>Sample Depth</b>	<b>XRD Mineral Content</b>
18.5	Quartz, Ferrotschermakite, Oligoclase, Clinochlore, Cummingtonite, Phlogopite
23.8	Quartz, Orthoclase, Clinochlore, Muscovite, Albite
37.2	Quartz, Fluor-phlogopite, Clinochlore, Orthoclase, Oligoclase
45.7	Quartz, Oligoclase, Clinchlore, Phlogopite
52.8	
65.1	
73.5	Quartz, Clinochlore, Albite, Pigeonite, Muscovite
82.5	Quartz, Oligoclase, Clinochlore, Biotite, Muscovite
94.2	Quartz, Magnetite
126.1	
134	
154.7	
170	Quartz, Oligoclase, Clinochlore, Cummingtonite, Muscovite, Tremolite

*Table 4.5: XRD mineral assemblages for core plugs.*

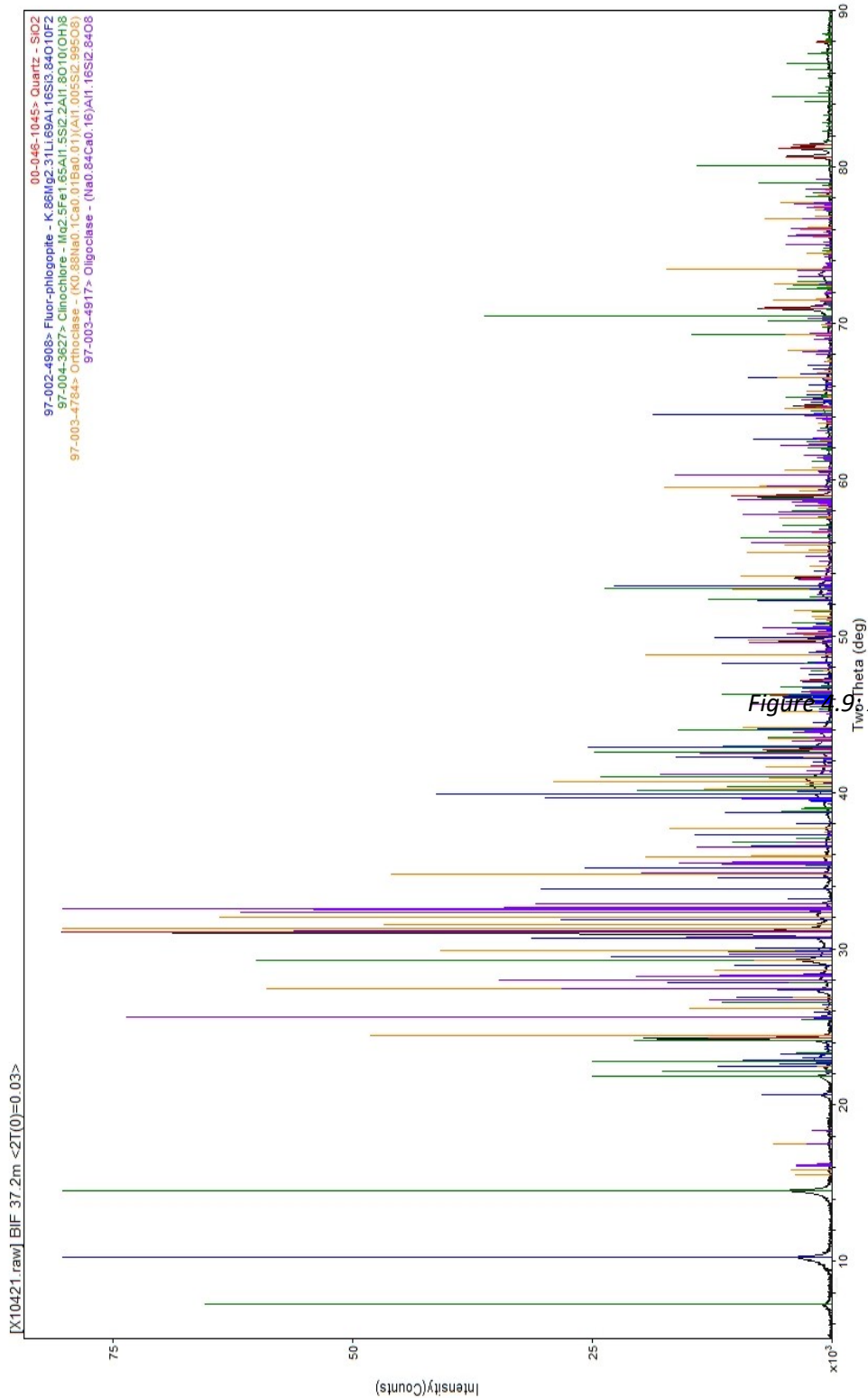


Figure 4.9 XRD Spectrum for core sample 37

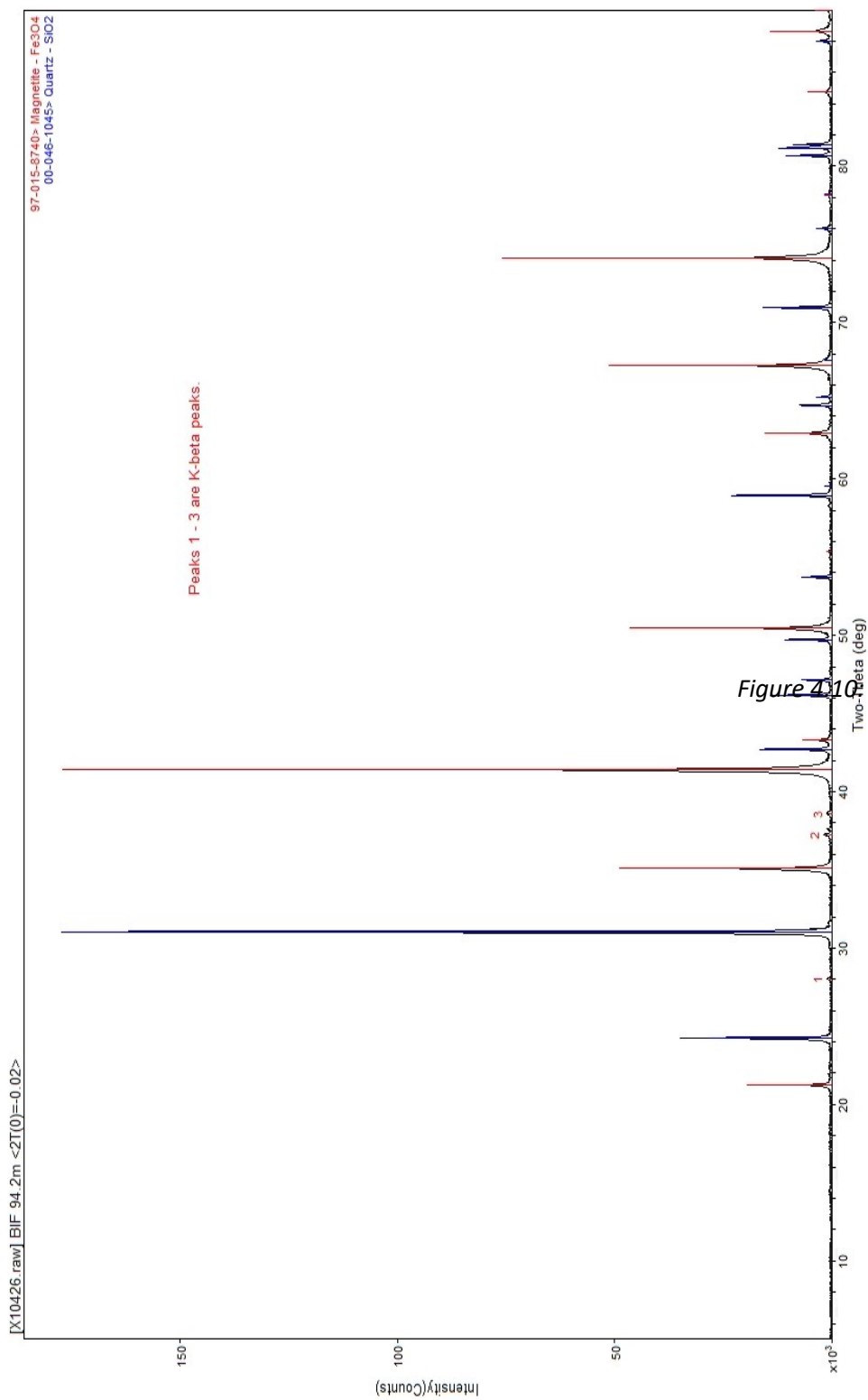


Figure 4.10 XRD Spectrum for core sample 94

## CHAPTER 5      MAGNETIC AND GRAVITY INVERSIONS

This chapter will focus on the design and implementation of both the airborne magnetic and ground based gravity survey. The airborne magnetic survey was originally performed to identify highly magnetic areas of interest for geological reconnaissance. It has been used in this thesis as an additional dataset to assist in site characterization and subsurface modelling. An inversion model was created using the 3D magnetic anomaly dataset and local geological knowledge with the goal of defining the limits of the subsurface ore body and determining high grade zones.

### 5.1 MAGNETIC GRIDDING

#### 5.1.1 SENSOR AND SURVEY

Magnetic surveys are performed in regions where magnetic minerals that are indicative of economic ores are suspected. Magnetic minerals with high values of magnetic susceptibilities  $k$  will result in a strong anomaly over the Earth's regular magnetic field. Generally, magnetic surveys are planned perpendicular to the strike of the suspected magnetic anomaly, as capturing the full 2D wavelength of the magnetic anomaly is useful for later interpretation with regards to depth (Milsom, 2003). For this study, a total magnetic field strength data were collected with a Scintrex CS-3 Optically Pumped Cesium Split Beam Sensor inside a stinger assembly deployed behind a helicopter. A KMAG-4 magnetometer counter was used to separate the incoming data stream and provided a resolution of 0.0075 nanoTesla. Accurate positioning was recorded using a U-BLOX RCB-LJ sixteen channel GPS receiver and TRA 3500 radar altimeter mounted in the stinger. This results in accurate positioning of the magnetometer to a known altitude above topography. As seen in Figure 5.1, flight lines were spaced apart 100m and trended NNW to SSE parallel to the Central Borden Fault in the region, the eastern bound of our survey zone. The aircraft maintained an altitude between 30m and 60m above the topography.

A Cesium Scintrex CS-3 was deployed as a magnetic base station during the survey. The base station was deployed away from any high intensity anomalies in an area of low magnetic gradient with no nearby mine related noise sources. Raw data collected along the survey lines were then corrected for diurnal variations in the magnetic field, which are essentially constant regionally, with data from this continuously recording base station. Heading and lag corrections created by the optically pumped cesium magnetic sensor were estimated and corrected for. Finally, the dataset was corrected for levelling issues using a control line, creating the Total Magnetic Induction (TMI) dataset.

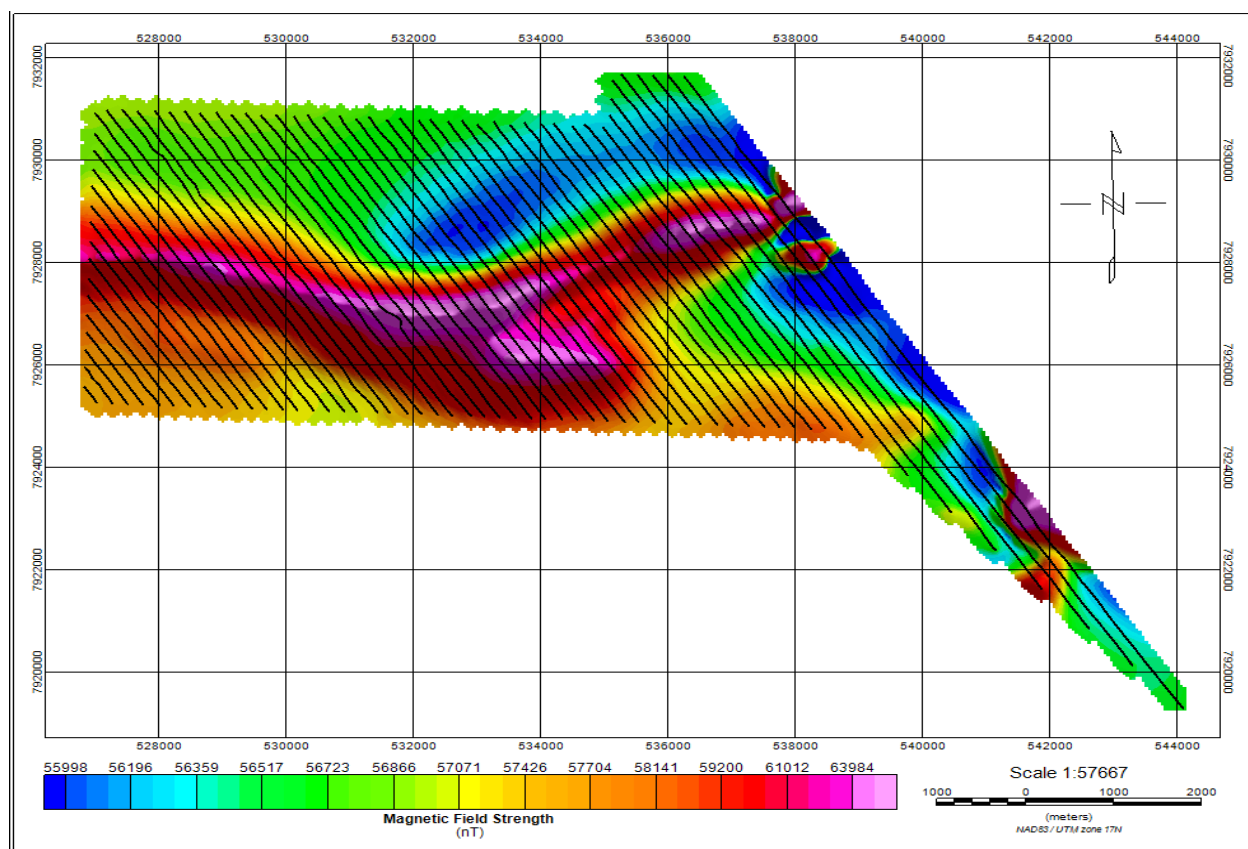


Figure 5.1: Total Magnetic Induction (TMI) Field for region west of Deposit 4 and the Central Borden Fault. Airborne flight lines are superimposed in black over data.

### 5.1.2 RESULTING MAGNETIC FIELD

Aeromag survey data made available spans 11 km east-west from 526753 meters west to 538740 meters west in UTM zone 17N. North-south the region spans 6km from 7924772 meters north to 7930991 meters north in UTM zone 17N. Data were gridded into a magnetic anomaly map using a minimum curvature method to fit data points along with a 50-meter cell size. Due to the spacing of the lines and frequency of the data points within the lines, smaller cell sizes resulted in gaps in coverage. Investigating Figure 5.1, a long-wavelength, linear anomaly strikes primarily east west along the entire survey region. A 'dipole effect' is observed where a region immediately beside the magnetic high exhibits an immediately adjacent minimum; this results from the magnetic response of the body when the Earth's magnetic field has a declination and inclination. This region exists to the north along the eastern side of the anomaly, such features are common in many magnetic ore bodies and reflect the orientation of the body within the earth's magnetic field. Magnetic intensities in the region range from 56000 nanoteslas in the magnetic

lows to 66000 nanoteslas directly over the iron ore body. Two specific high intensity zones exist, the eastern one right beside the Central Borden Fault and one directly in the middle of the grid that is suspected to be high grade.

## 5.2 MAGNETIC INVERSION MODEL

The resulting Geosoft VOXI™ inversion model maps out magnetic susceptibility based on both the magnetic field's strength and magnetic vector orientation. The magnetic anomaly was plotted at the GPS height of the survey helicopter, and a localized digital terrain model created by subtracting the radar altimeter reading of the helicopter from the GPS elevation. A grid of the TMI magnetic dataset was used to run the inversion.

A cell structure was created to define the limits of the inversion under the anomaly grid approximately 50x28x20 cells with each cell being a 100x100x50 meter cube. A rough large polygon surrounding the survey area was created to encompass the entire magnetic anomaly spanning from 534100 to 539100 meters easting and 7927300 to 7930100 meters northing. The vertical extent of the inversion spans from 1501 meters below sea level to 338 meters above sea level. The sensor elevation was set using the sensor elevation GPS data from the survey helicopter and the digital elevation model mentioned above was set. Bounds for magnetic susceptibility were set based on laboratory measurements of core samples from chapter 4. Initially the lower and upper bounds were set at 0 SI and 50 SI, respectively, with the latter later reduced to 10 SI.

The inversion model was created initially using a simply constructed voxel as a starting point based on inversion constraint guidelines from multiple sources (MacLeod and Ellis, 2013; Ellis et al., 2012; Williams et al., 2009; Williams and Oldenburg, 2009). A cubic voxel of the same cell size and dimensions as the inversion mesh was created and broken down into 4 sections spanning the upper and lower east and west sides of the Central Borden Fault. On the west surface side of the Central Borden Fault, a magnetic susceptibility of 1 SI was input for the top 100 meters. This results from known BIF outcropping on the surface. Below the surface region, a magnetic susceptibility of 0.2 SI was input. The surface region east of the Central Borden Fault was given a magnetic susceptibility of 0 SI due to known geology of limited magnetic limestone and glacial till. The region below this was given a magnetic susceptibility of 1 or greater to encompass the BIF and possible high-grade regions.

Confidence in the model decreases with depth. A parameter weighting voxel was created to assign higher confidence values to shallower depths. The surface 50 meters was assigned a value of 1 for a high

confidence. 50 to 100 meters below the surface was assigned a value of 0.5 as this is where the expected limestone BIF contact is and variability in the model is required. 100 meters from the surface and below was assigned a value of 0.01 as little is known regarding the dimensions of the iron ore body at depth. The initial VOXI inversion created a smooth magnetic susceptibility in X-Y-Z directions. The inversion result was iteratively reweighted to focus the anomaly at depth using a reweighting value of 1.

A second inversion was performed focusing on the specific region containing the seismic refraction survey grid. The smaller survey grid focuses on the region spanning 535500 meters to 538000 meters easting and 7972650 meters to 7929750 meters northing. Depths span from 310 meters above sea level to 575 meters below sea level. The tighter grid allowed for a smaller cell size of 50x50x25 meters in the X, Y, and Z directions, thus increasing resolution. The same parameter reference model and parameter weighting model were used though clipped for the smaller region.

### **5.2.1 MAGNETIC INVERSION RESULTS**

The resulting inversion model can be seen Figures 5.2, 5.3 and 5.4. Magnetic susceptibility values shown in the model are relative to the surrounding rock. A sharp edged vertical slab trends from east to west and deepening as it extends westward. The eastern edge of the model which sits on the Footwall of the Central Borden Fault exhibits an extremely high magnetic susceptibility of 4.41 SI immediately on the surface. This is expected as BIF outcrops in the area. Limited resolution of the model prevents us from observing any structure of the Central Borden Fault. Immediately west of the Central Borden Fault the ore body is approximately 70 meters below the surface and dips westward. Laboratory measurements of magnetic susceptibilities of BIF made in chapter 4 show magnetic susceptibility values of 0.1 SI correspond to low grade and randomly oriented BIF, the contact between the surface till/limestone and BIF occurs between 70 and 120 meters below surface. This value is variable due to the poor resolution of the model. This lower magnetic susceptibility zone extends to a depth of approximately 980 meters below the surface.

Deeper inspection shows the magnetic susceptibility increasing with depth directly under the high of the magnetic anomaly at 537255 meters easting and 7929120 meters northing in UTM grid 17N. The magnetic susceptibility zone has a core high susceptibility structure with magnetic susceptibility values ranging from 1.2 to 4.0 beginning at an approximate depth of 210 meters and extending down to a depth of 730 meters below the surface. The western edge of the survey grid exhibits a lower magnetic susceptibility at a deeper depth. Magnetic susceptibility values only range from 0.1 SI to 0.6 SI. There is no higher

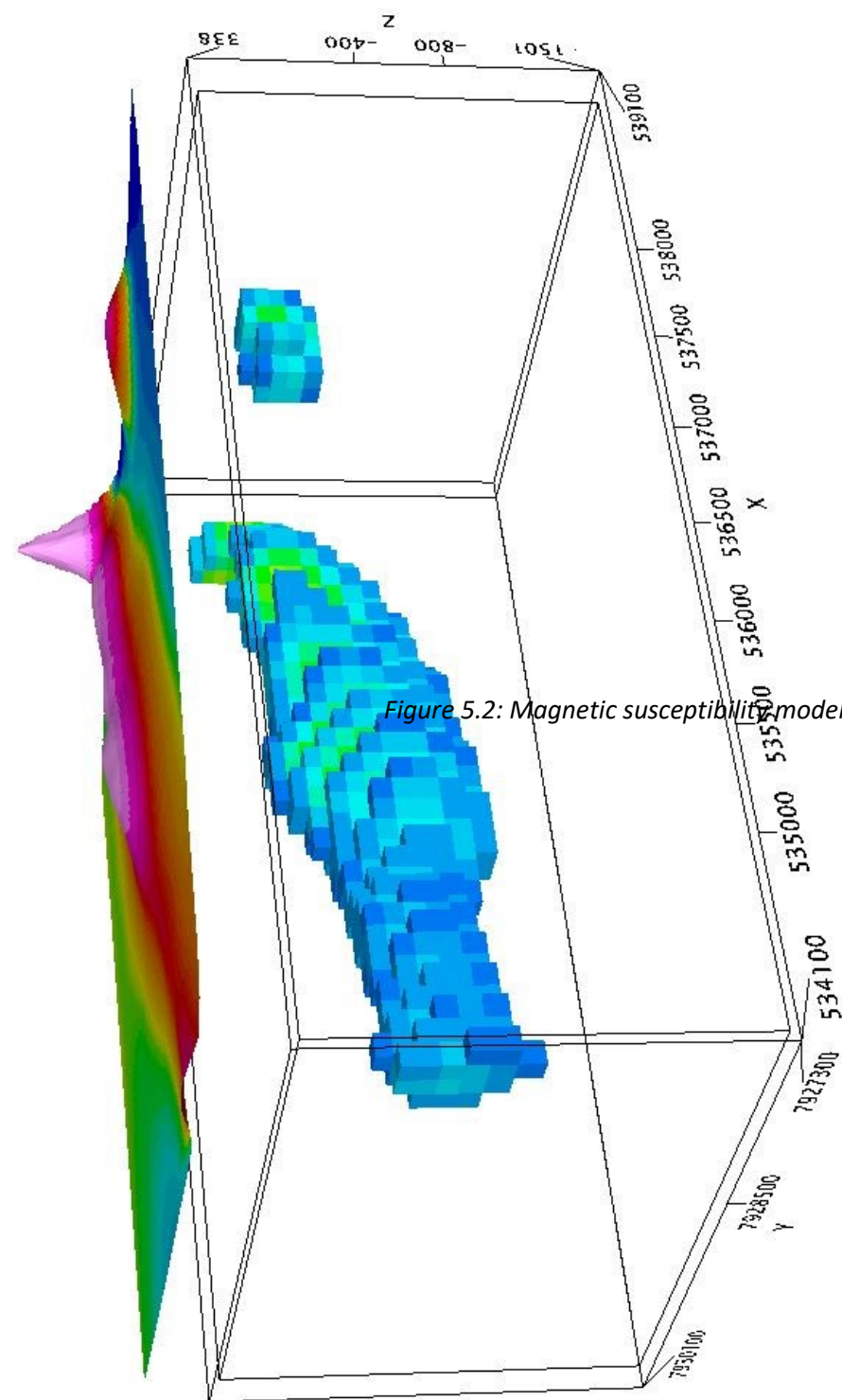
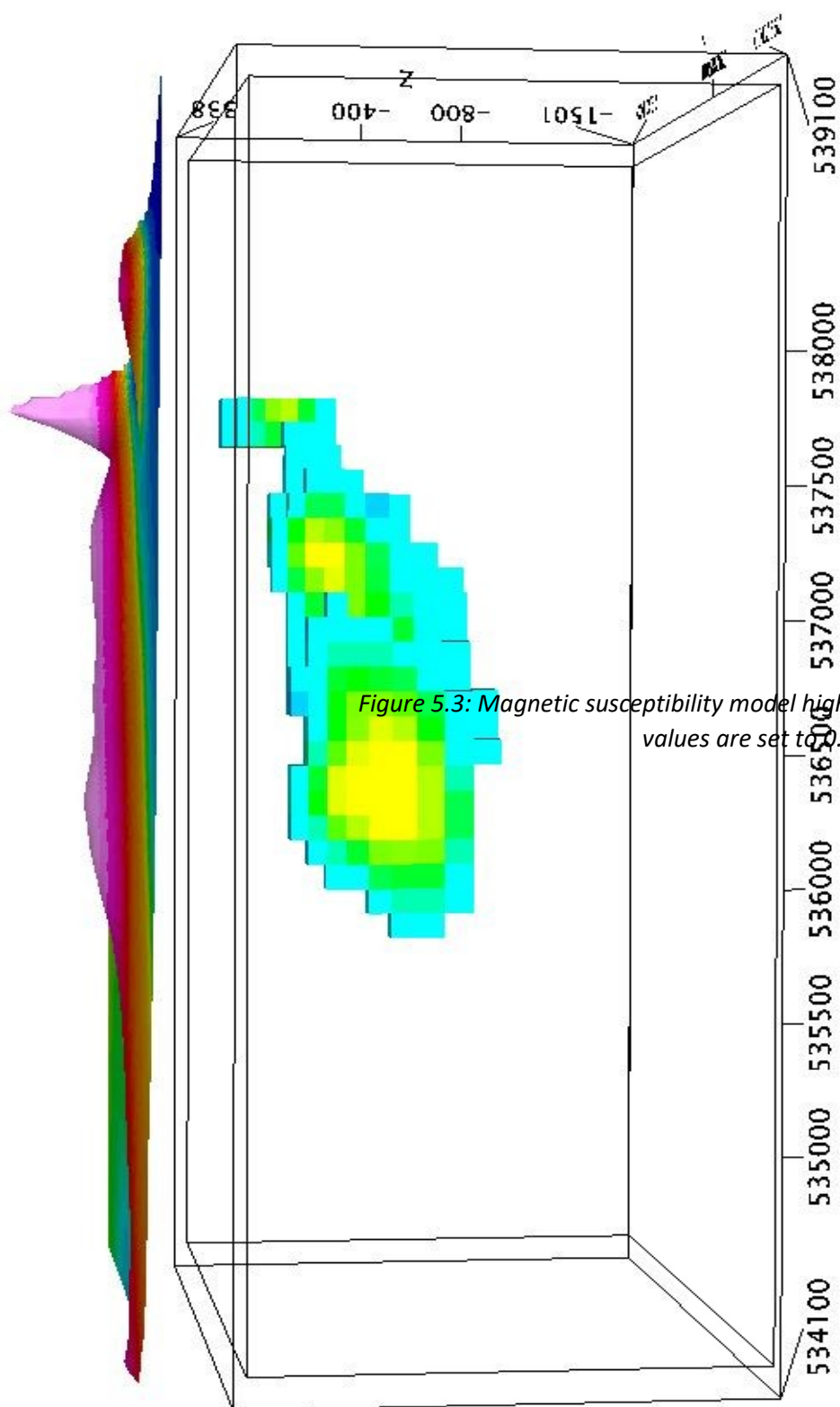


Figure 5.2: Magnetic susceptibility model showing magnetic susceptibility values and background cells.



susceptibility core to the anomalous body at this location. Topography slopes downward as we move westward, and the high magnetic susceptibility anomaly plunges shallowly westward as well with 0.1 SI values occur at approximately 130 meters to 180 meters below the surface value of 160 meters above sea level. However, it is important to note that there is no correlation between surface topography and the magnetic values/subsurface ore body. The bottom of the increased magnetic susceptibility zone occurs between 930 meters and 980 meters below topography. Peak values of 0.6 SI on the western edge occur at approximately 410 meters below the surface.

The inversion model resulting from the focused inversion can be seen in Figure 5.4. The smaller cell sizes begin to show some coarse structure. The high susceptibility zone shows a vertical south face and higher magnetic susceptibilities pushing north as depth increases, suggesting the iron ore body dips northward. Magnetic susceptibility values range from 0.1 SI to 2.92 SI relative to background. The higher susceptibility region begins at a depth between 50 meters and 75 meters and extends down to a depth below the bottom of the model at 8750 meters below the surface. A well-defined core of high magnetic susceptibilities is also observed with values ranging from 0.6 SI to 2.92 SI relative to background. These values occur at 100 meters below the surface on the eastern side of the anomaly and extend down to approximately 450 meters below the surface. The western edge of the survey grid shows a slight plunge in the anomaly and the depth to the top of the higher susceptibility are increases to 160 meters.

### **5.3 GRAVITY GRIDDING**

A small-scale reconnaissance gravitational survey was performed to further assist with subsurface modelling and site characterization. Gravitational surveys were planned around identifying non-magnetic hematite zones such as the one extending off the western edge of the survey area. Limited time prevented the survey from providing full coverage throughout the survey area. A 3D subsurface inversion model was created to assist in identifying the limits of the ore body and potential high-grade zones.

#### **5.3.1 SENSOR AND SURVEY**

A reconnaissance ground-based gravity survey was carried out over a three-day period at the end of the field season in 2014. The geometry of this survey was planned based on the results of the magnetic anomaly survey performed earlier in 2008 (Fig. 5.1) and consisted of 3 north-south lines perpendicular to strike with 2 parallel cross lines connecting them. North-south lines had 50 meters spacing between survey stations and the east-west lines were spaced at 100 meters apart. This coarse station spacing was a consequence of the limited time available before the end of the summer survey season. In total 99

stations were measured from two different base stations. Both base stations were tied into a master base station created at the Mary River camp site. However, only 74 survey stations from the same base station were used in the final Bouguer map due to proximity to each other.

A rented Scintrex™ CG-3+ Gravimeter was used to perform the relative ground gravity survey. To obtain good readings, a gravimeter must be stably mounted and leveled. Unfortunately, the loose, wet glacial till covering most of the survey area made maintaining the gravimeter level on the immediate ground surface nearly impossible; and to overcome this the measurements were made on top small platforms from surrounding rocks. The rocks selected were within 10 meters of the planned grid point and level with the local topography and slope of the land. The height of the gravimeter in relation to the ground was measured to be 17.4 cm when properly levelled on the gravimeter stand. This height was then added to the GPS elevation to improve accuracy of the free air anomaly correction. The gravity measurements taken are an average of the instruments response over a 2-minute interval sampled at approximately 2Hz. The values were rejected if their standard deviation exceeded 0.03 mGal. Accurate GPS locations were recorded using a Trimble™ R8 Kinematic GPS. A known set base station was used, and a rover GPS communicated by radio, allowing gravity stations to be measured with 1 cm horizontal and 2 cm vertical accuracy in near real time.

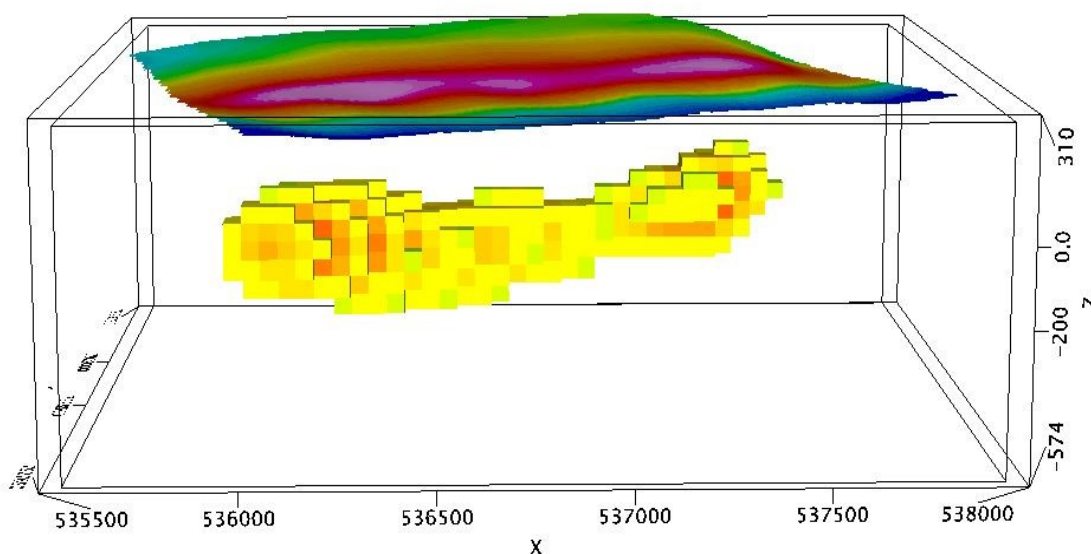


*Figure 5.4: High resolution susceptibility close up of potential high-grade zone. Relative magnetic susceptibility values are set to display 1.3 SI and greater.*

Raw gravity data were loaded directly into Oasis™ Montaj Geosoft where tidal and drift corrections were performed. The 1967 Geodetic Reference Gravity (Woolard, 1975) was used to create the reference gravity for the base station:

$$g_{\varphi}(1967) = 9.78031846(1 + 0.005278895 \sin^2 \varphi + 0.000023462 \sin^4 \varphi) \text{ m/s}$$

Where  $g$  is the theoretical gravity at latitude  $\varphi$ . This resulted in a theoretical gravity value of 980673.58 mGal. An automatic tidal correction was performed using the Scintrex™ CG-3+ Gravimeter and double checked using the tidal correction with Oasis Montaj™ Geosoft. A terrain correction was performed using a digital elevation model of the survey site and region (spanning approximately 4km in each direction from the gravity grid) created with GPS and altimeter data from the 2008 helicopter magnetic survey. The average terrain density was set to 2.67 g/cm<sup>3</sup> for the terrain correction calculation. Free air corrections and Bouguer corrections were automatically calculated and the final Bouguer anomaly map created without attempting to remove the longer wavelength regional trends. A grid of the Bouguer anomaly was created using a minimum curvature fit between the data points and a cell size of 100m to make up for the sparse data points.

### 5.3.2 RESULTING BOUGUER ANOMALY

Initial analysis of the gravity data shows that the high for the Bouguer anomaly lines up with the magnetic high, however Figure 5.6 shows that the full north to south wavelength of the gravity signal was not captured as the magnetic high continues to drop well beyond the limits of the gravity survey. Further comparison of the Bouguer anomaly to the total magnetic field also shows a direct overlap between the Bouguer high with the magnetic field high. Typically, this is not the case when comparing two dimensional gravity anomalies with magnetic anomalies. It is typical to see a small offset between the two data peaks. Figure 5.6 shows the peaks lining up due to the coarse sample spacing of the gravity survey. A higher resolution survey would likely have shown a 50 meter to 100 meter offset in the north-south direction between the two datasets. Quality checks in the field determined this but there was insufficient time left to survey the remaining area. The region surveyed covers only a third of the total seismic and magnetic survey area. Setting the reference gravity to the theoretical latitude gravity of 980673.58 mGal, an anomaly ranging from -1.4 mGal to +1.9 mGal of the reference gravity is observed. The anomaly exhibits a long wavelength spanning the entire 1800 meter north south extent of the survey. The anomaly appears to extend westward towards the Central Borden Fault and drastically drops off in strength as it moves

eastward, dropping from +1.9 mGal to -0.3 mGal in just 400 meters. This could be the result of a density decrease or, more likely, the high-density BIF and high-grade zones moving deeper.

#### 5.4 GRAVITY INVERSION MODEL

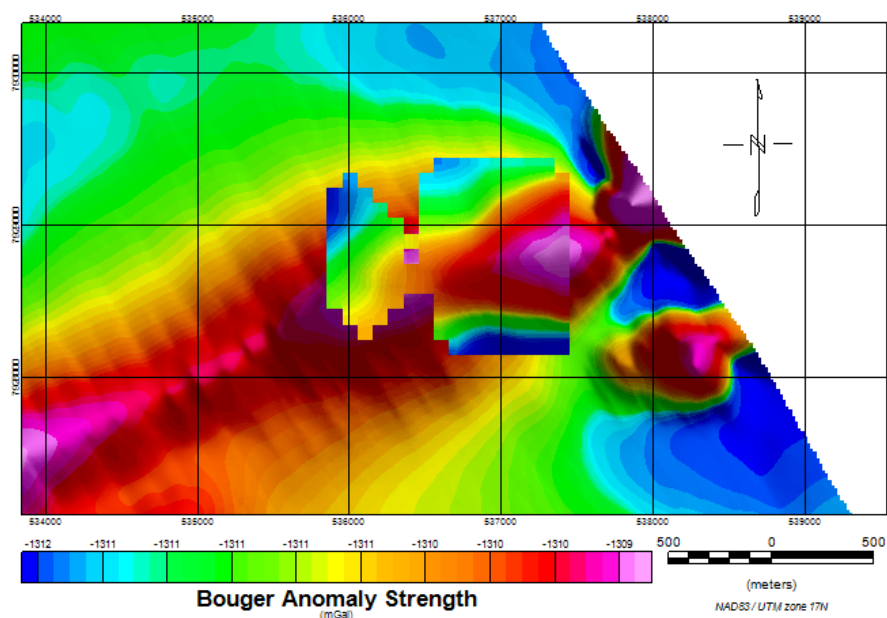


Figure 5.6: Bouguer anomaly overlaying the magnetic anomaly.

The gravity inversion model maps out a cell structure of relative densities based off the Bouguer anomaly strength. The Bouguer anomaly was plotted at the recorded gravimeter elevation plus half of the vertical cell width of 12.5 meters as per the best inversion practices for Geosoft ground gravity surveys (Ellis et al., 2012; MacLeod and Ellis, 2013; MyGeosoft, 2017). The digital terrain model created from the airborne magnetic survey was uploaded as it had better resolution.

A cell structure was made to model the average densities of the structure producing the observed anomaly. A 38x47x27 grid of cells with each cell measuring 25m x 25m x 12.5m in the X, Y and Z directions respectively was created. These dimensions were chosen to equal half the station spacing. The 6 westernmost stations were omitted from the polygon region selected for inversion. The large gap between these 6 stations and the remainder of the survey grid caused issues in the inversion and yielded undesirable results. The resulting polygon region spanned from 536450 meters to 537450 meters easting and 7928150 meters to 7929350 meters northing in UTM grid 17N. The depth of the model spans from

313 meters above sea level to 229 meters below sea level. The area directly over the suspected ore body is at an average elevation of 188 meters above sea level.

Due to the limited size of the Bouguer anomaly, coupled with the large station spacing, an initial VOXEL modelling the subsurface density was not created. The resulting unconstrained model was iteratively reweighted to help focus the density anomaly using a reweighting value of 2. This resulted in sharper contacts between the anomaly and surrounding rock and less of a gradual transition.

#### **5.4.1 GRAVITY INVERSION RESULTS**

The resulting 3D gravity inversion can be seen in Figures 5.7 and 5.8. Density values shown in the model are relative to that for the surrounding host limestone of approximately  $2.1 \text{ g/cm}^3$ . Relative values range between  $-0.17 \text{ g/cm}^3$  and  $1.77 \text{ g/cm}^3$ . Based on the limited laboratory measurements taken in chapter 4, we can expect BIF samples to begin at densities of approximately  $2.65 \text{ g/cm}^3$ . Thresholding the initial anomaly for Figure 5.7 to show only relative density values of  $0.5 \text{ g/cm}^3$  and greater we see the high-density zone take shape quickly due to the sharp contact between the low density and high-density region. The higher resolution inversion shows a similar structure to the magnetic inversion where a shallow plunge to the west and a dip to the north is observed.

Densities of  $2.6 \text{ g/cm}^3$  appear at a depth between 90m and 105 meters below the surface immediately beneath the Bouguer high. Densities increase quickly with depth to the average BIF density of  $2.75 \text{ g/cm}^3$  which occurs at approximately 115m to 130m below the surface. Densities of  $3.0 \text{ g/cm}^3$  begin at a depth of 130 m to 145 m below the surface and span downwards to 315m to 330m. Densities of  $3.3 \text{ g/cm}^3$  (consistent with lab measurements of magnetite) occur in a small pod directly under the peak of the Bouguer anomaly measuring 250 meters in the east-west direction, 60 meters thick in the north-south direction, and a vertical of 140 meters ranging from 150m below the surface to 290m below the surface. The pod hosts densities starting at  $3.3 \text{ g/cm}^3$  and increasing to  $3.8 \text{ g/cm}^3$ . Densities show a drastic decrease westward to the point where densities greater than  $2.6 \text{ g/cm}^3$  do not occur west of 536825 meters easting.

#### **5.5 SUMMARY**

Inversion models created by both gravity and magnetic inversions yielded subsurface structures consistent with geological interpretations of surface rocks and nearby ore bodies. Additionally, all relative magnetic susceptibility and density values obtained from inversions were consistent with laboratory measured values described in chapter 4 when compared to standard limestone values for magnetic

susceptibility ( $\sim 0$ ) and density ( $2.1 \text{ g/cm}^3$ ). Potential high-grade zones were uncovered and correlate well with strongest highs in the total magnetic induction map and Bouguer anomaly map.

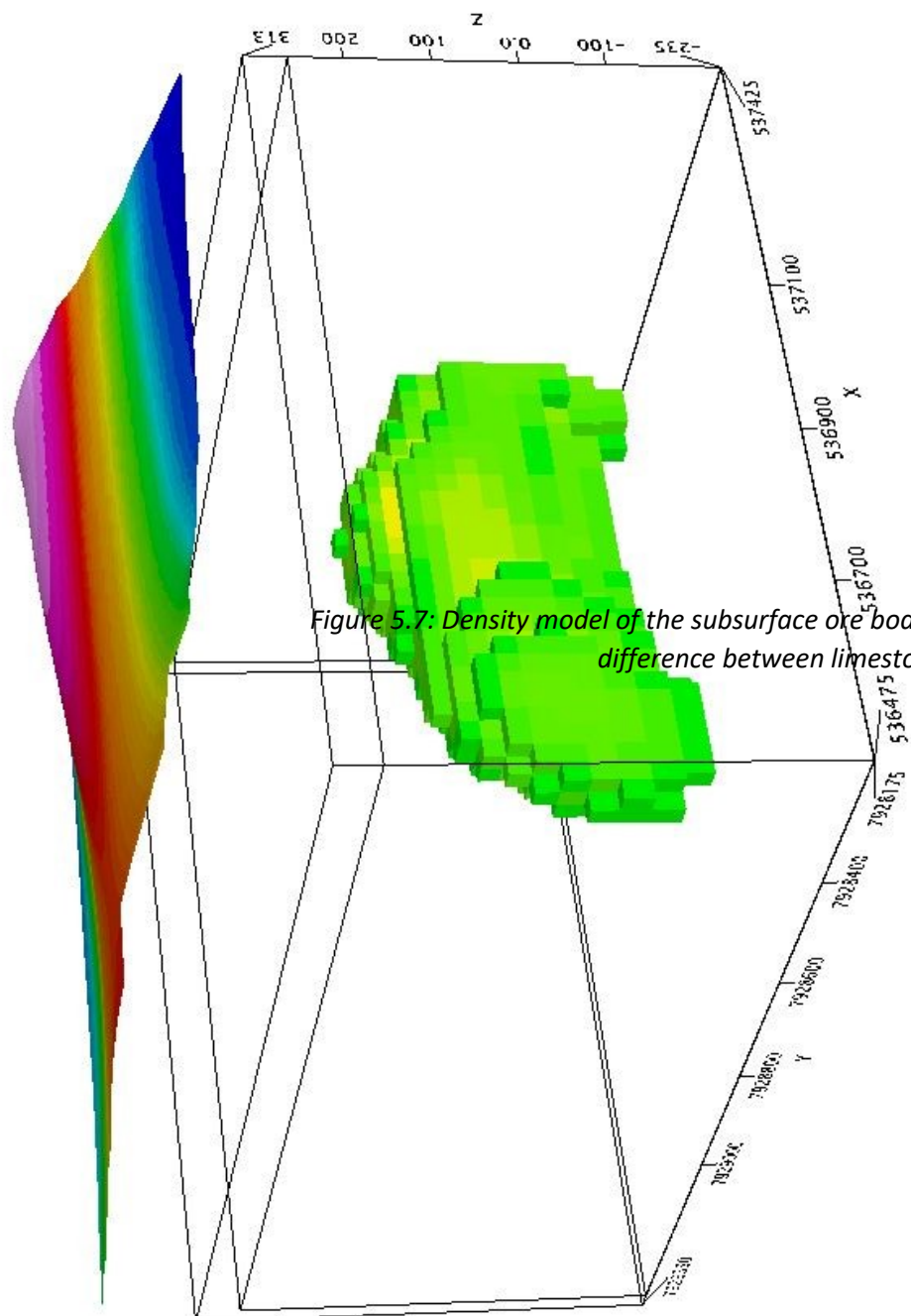


Figure 5.7: Density model of the subsurface ore body. Relative density values are set difference between limestone at  $2.1 \text{ g/cm}^3$  and low-grade B

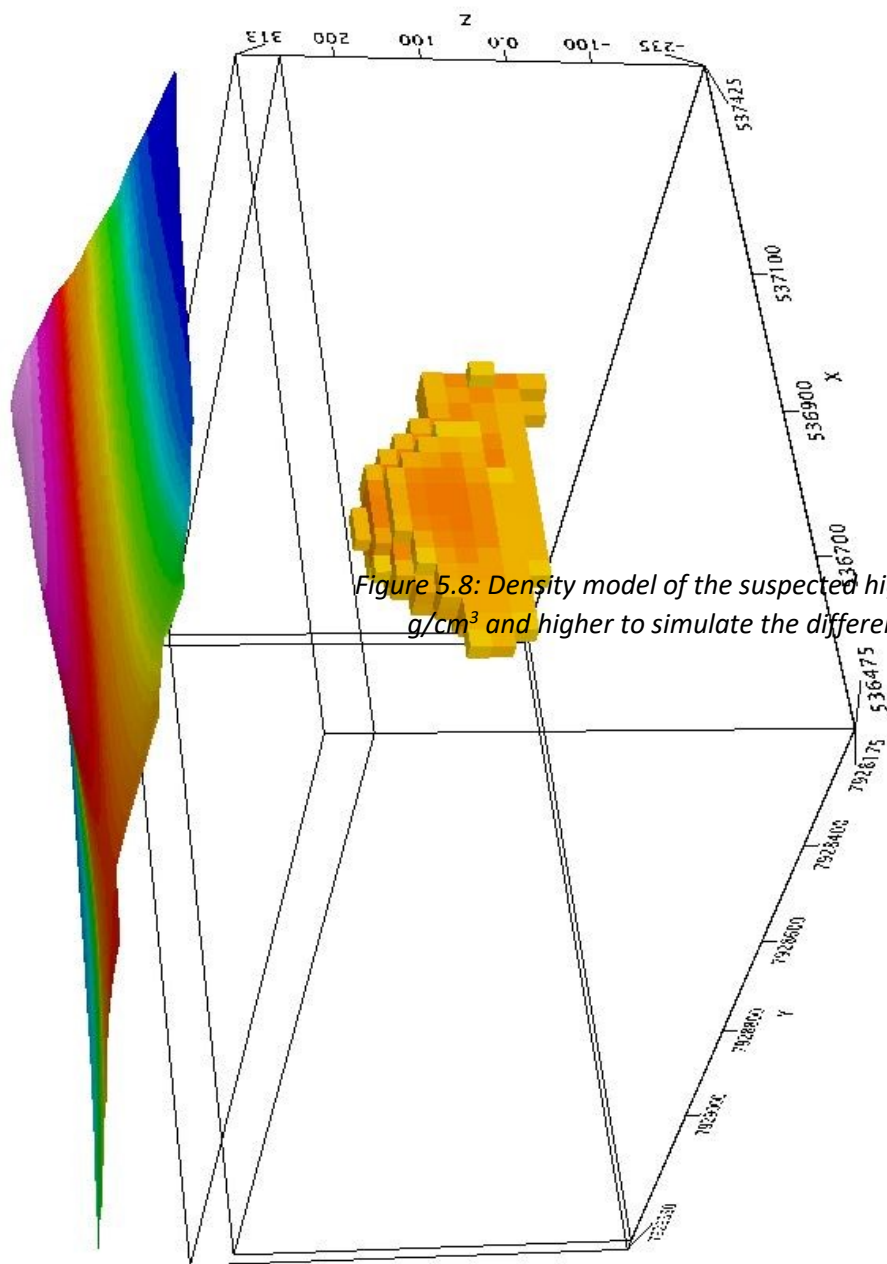


Figure 5.8: Density model of the suspected high-grade zone with higher densities. Ranges from 2.1 g/cm<sup>3</sup> and higher to simulate the difference between limestone at 2.1 g/cm<sup>3</sup> and higher.

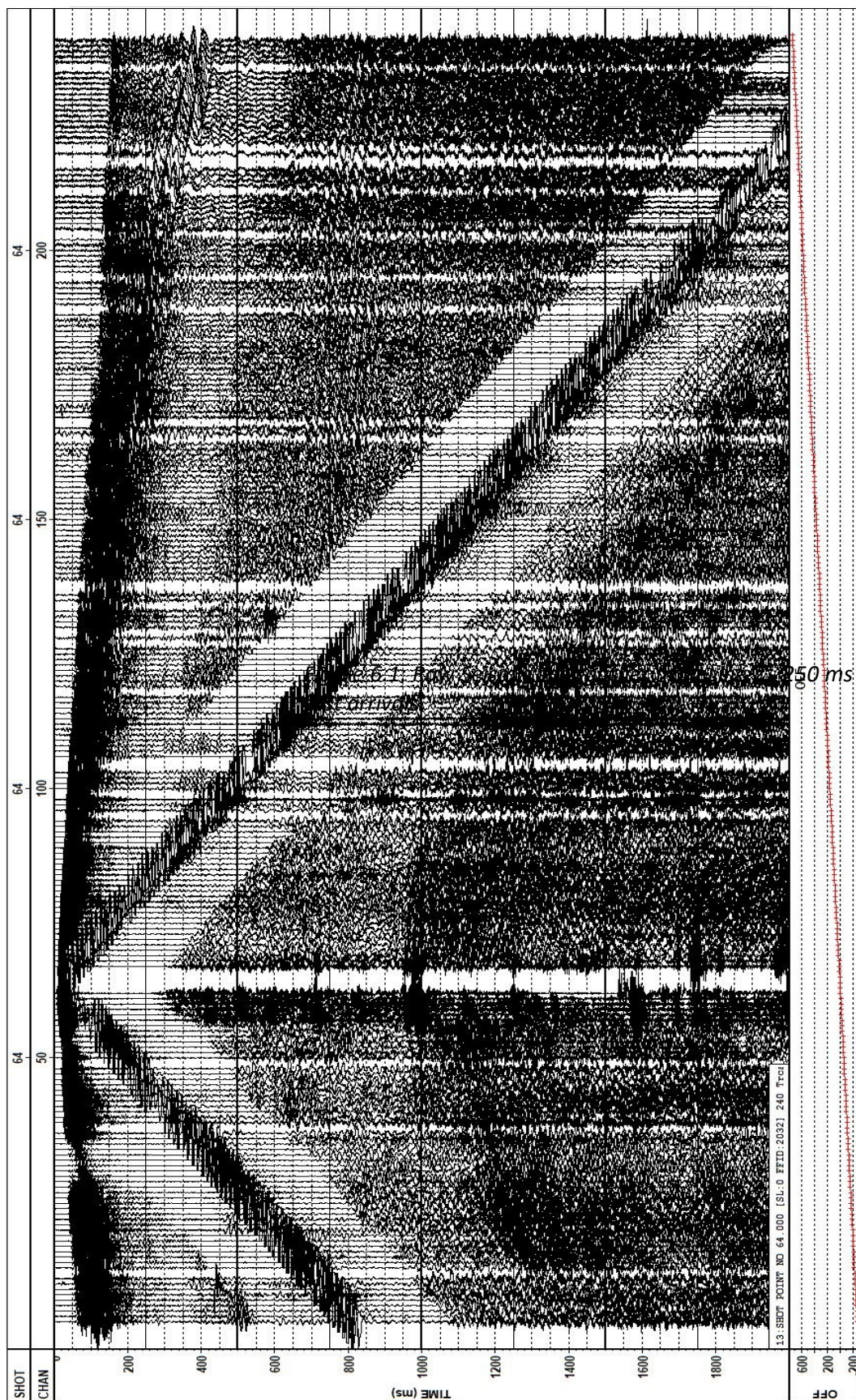
## **CHAPTER 6 SEISMIC REFRACTION ACQUISITION AND ANALYSIS**

Chapter 6 will provide a brief explanation of the field practices used to obtain the seismic reflection and refraction data. This will be followed by an explanation of methods used to select first arrivals of refraction energy. Filtering techniques used to remove ground roll and the air wave and improve signal to noise ratio will be discussed and appropriate background provided. Finally, refraction tomography and velocity models will be proposed and discussed.

### **6.1.1 RAW SEISMIC DATA**

To review, raw seismic data were collected using 240 low frequency (15 Hz) geophones connected to 10 geophone spread cables. These spread cables were connected to 10 24-channel Geometrics™ Geodes linked together with communication cables and powered by 12-volt car batteries. A Dell Precision M70 laptop hosting Geometrics Seismodule Controller software was used to record data. Seismic data were recorded in SEG-2 format from the field. Each shot was saved as an individual SEG-2 file. Data were recorded at a sampling frequency of 2000 Hz for a full record length of 8 seconds, resulting in 16000 samples per geophone per shot (see Figure 3.4). The final data set resulting from 133 shots is approximately 5.45 gigabytes.

Triggering issues caused difficulties while recording data in the field and necessitated these otherwise excessively long 8 second recording periods. A manual workaround was established in which the seismodule controller software was triggered by the operator in the 'doghouse' tent who then communicated by radio to the shooter who initiated the source. This resulted in a 2 to 4 second delay in the activation of the source after the recording had commenced. Examination of the longest source-receiver offsets (1080m on line 4) indicated that at most 4 seconds of seismic record was required to adequately capture the data. Hence, the full 8 seconds of data allowed for the delay plus the required recording time to be fully obtained given the timing issues with the human initiated source activation. The disadvantage of this procedure was that the seismic processor later had to analyze each shot individually to determine an appropriate bulk time shift necessary to accommodate the delay. This was accomplished by assuming that the geophone response closest to the source (only a few meters) would give a reasonably accurate measure of zero time, but this does introduce some small additional errors to the travel time determinations. GPS coordinates were measured at each geophone and shot station with uncertainties being less than 3 cm for both horizontal and vertical. These GPS data points were uploaded and paired to stations in the header file for each line. Absolute source



250 ms AGC. It is important to notice the

receiver offsets were calculated for each line using the X (easting), Y (northing), and Z (elevation) positions for each pair.

All shots on each line were individually inspected to find and then remove 'bad' traces. Killed traces were selected based on variable criteria: A repetitive pulse in the trace with time caused by a bad geophone or connection, an extremely noisy geophone caused by poor coupling and surface wind, or geophones close to the source being overdriven.

An example of a raw seismic shot gather after correcting for shooting delays can be seen in Figure 6.1. a number of different first arriving seismic phases are seen in these shots that arise from various direct, refracted, and surface waves and these have 'moveouts' across the images that indicate the speeds at which such arrivals propagate away from the source to the receivers at increasing offsets. Generally, the seismic data exhibits first arriving slopes of  $\sim 2800$  m/s within 100 meters of the shot, 4500 m/s within 500 meters of the shot, and 6500 m/s at offsets greater than 500 meters. These vary by up to 500 m/s depending on shot location and topography. A very strong air wave is also present throughout every shot gather propagating at 343 m/s, this is not surprising given that the shot explosions were easily audible for long distances.

It is challenging to acquire seismic data in permafrost environments. Multiple studies performed over the past decade have attempted to characterize velocity alterations caused by permafrost (Schmitt et al., 2005; Schijns et al., 2009; Maurer and Hauck, 2007; McClymont et al., 2013) with varying results due to locality. Studies performed by King (1977), King et al. (1988) and Carcione and Seriani (1998) have found that the slowness vector is heavily dependent on the concentration of and averaging model of 3 phases within the rock matrix: solid and ice matrices and unfrozen water. However, the proportion of unfrozen water within a rock matrix and temperature are closely related, changing the possible velocity alteration regionally, with rock type, and with depth (Timur, 1968; Carcione and Seriani, 1998).

A rapidly travelling and exceptionally strong surface wave runs directly below the first arrivals with an amplitude ranging from 3 to 5 times stronger than the first arrival. The strong amplitude surface wave arrival has a velocity of roughly half that of the first break for each section as offset increases. The remainder of the data shows linear trends mirroring surface waves. The unprocessed data set shows no sign of seismic reflections. It is suspected that strong surface waves and air waves are overwhelming the weaker reflections.

### 6.1.2 FIRST BREAK PICKS

The large amplitude of the surface waves immediately following the first arrivals made automatic first break selection difficult for the selected software. As such, all 35 thousand traces were picked by hand using VISTA's first break picking software. Initially, a 500 ms automatic gain control (AGC) was performed to increase and sharpen first break amplitudes at larger offsets. Top and bottom mutes were applied as close to the first arrivals as possible to remove any other large amplitude noise or surface waves. A 20 ms search window was selected with a 5 ms sliding/threshold window and a threshold scalar of 2. The search software was directed to look for the first trough before the primary arrival of energy. Manual first break pick mode was then selected, and a center line drawn onto the shot gather in the seismic window. The center line provided a guide for the first break picking parameters. The search window was centered on the manually drawn center line, allowing the parameters to pick the bottom of the trough within the search window. This allowed first breaks to be selected quickly on a shot by shot basis.

First arrivals in all shot gathers from lines 2, 4 and 5 displayed a shingling effect caused by a combination of both topography and horizontal surface velocity discontinuities. Accurately picking first arrivals became difficult at these offsets due to the first arrival jumping down to a larger surface wave. Original first arrival slope exhibits a weakening amplitude until noise becomes more prevalent. At this point, the first break center line would be shifted and drawn on the new first arrival horizon which was previously assumed to be a strong surface wave. This allowed for the introduction of errors into the resulting first break analysis and topographic corrections.

Larger offsets of 800 meters and greater exhibited a poor signal to noise ratio. First arrivals became difficult to interpret because of poor geophone placement, surface noise and terrain. First breaks in these regions were selected based on strongest trough amplitude that was closest to the slope of the first arrivals in the immediate 100-meter offset region before the decrease in signal to noise ratio. A 90 Hz low pass filter was applied to remove the high frequency air blast to assist with first break selection. The low pass filter caused first arrival wavelengths to increase slightly. Using 'rules of thumb' the short survey lines (960 meters) would result in refraction results of approximately 250 to 300 meters depth. Geological data suggested a simple 3-layer case consisting of surface till and limestone followed by a high-density ore body. As such an extrapolation of first arrivals to assist with first break picking at larger offsets was deemed acceptable. During this selection method, care was taken to compare far offsets to surface topography to minimize the risk of not detecting a shingling effect caused by a sudden elevation change.

### **6.2.1 ORMSBY TRAPEZOIDAL FILTER**

Frequency analysis of traces on all lines resulted in two primary frequencies with strong amplitude spectra. Figure 6.3 shows average frequencies across all lines are strongest at approximately 75 Hz and 140 Hz, with 75 Hz being nearly twice as strong as 140 Hz. Waterfall plots of the power spectrum of each line show energy peaks to be focused at small offsets, with energy levels being nearly 40 decibels stronger within 250 meters of the shot point than beyond. Higher frequencies are associated with the strong air wave. A 300 ms AGC was performed on the data to minimize the shadow zone surrounding the surface waves and air blast. An Ormsby trapezoidal filter with edges at frequencies 20 Hz, 30 Hz, 90 Hz, and 100 Hz were applied to attenuate the high-frequency air blast in hopes that underlying reflections might become visible. Figure 6.7 shows the Ormsby and FK filtered data sets and the noise removed. The air wave and surface wave zone are however still prevalent in the filtered data set. Amplitude spectrums across all traces are much more reasonable and balanced across all offsets with the average amplitude spectrum in decibels dropping from -12 dB to -16 dB between 30 Hz and 80 Hz. First breaks appear sharper and deeper reflections are stronger. The deeper reflections that appear at small offsets (<400 meters) exhibit slower velocities (roughly 2500 m/s), suggesting these reflections are multiples of a reflection off the first permafrost layer in limestone. Noise near the source caused by the strong surface wave and air blast are concealing the original permafrost limestone layer reflection.

## **6.2 FK DOMAIN, RADON TRANSFORMS AND FILTERING**

Shot gathers were processed using a variety of methods to attenuate the surface waves, air wave, and noise to better highlight subsurface reflections and enable more precise selection of first arrivals (Boustani et al., 2013). A workflow for data reduction was established. Surgical top and bottom mutes were applied to focus on the estimated window of interest. Top mutes were applied to just before first arrivals. A horizontal bottom mute was established at 2000 ms after shot time. This bottom mute time was chosen as the survey was implemented to focus on shallow geological structures where economically accessible ore resides.

### **6.2.1 REFRACTION STATICS**

The near surface layer for many seismic surveys is highly weathered, variable topography, and non-uniform in thickness across the surface. It is important to accurately account for these variable's because otherwise the shot gather and velocity model can become corrupt and locations of deeper structures and

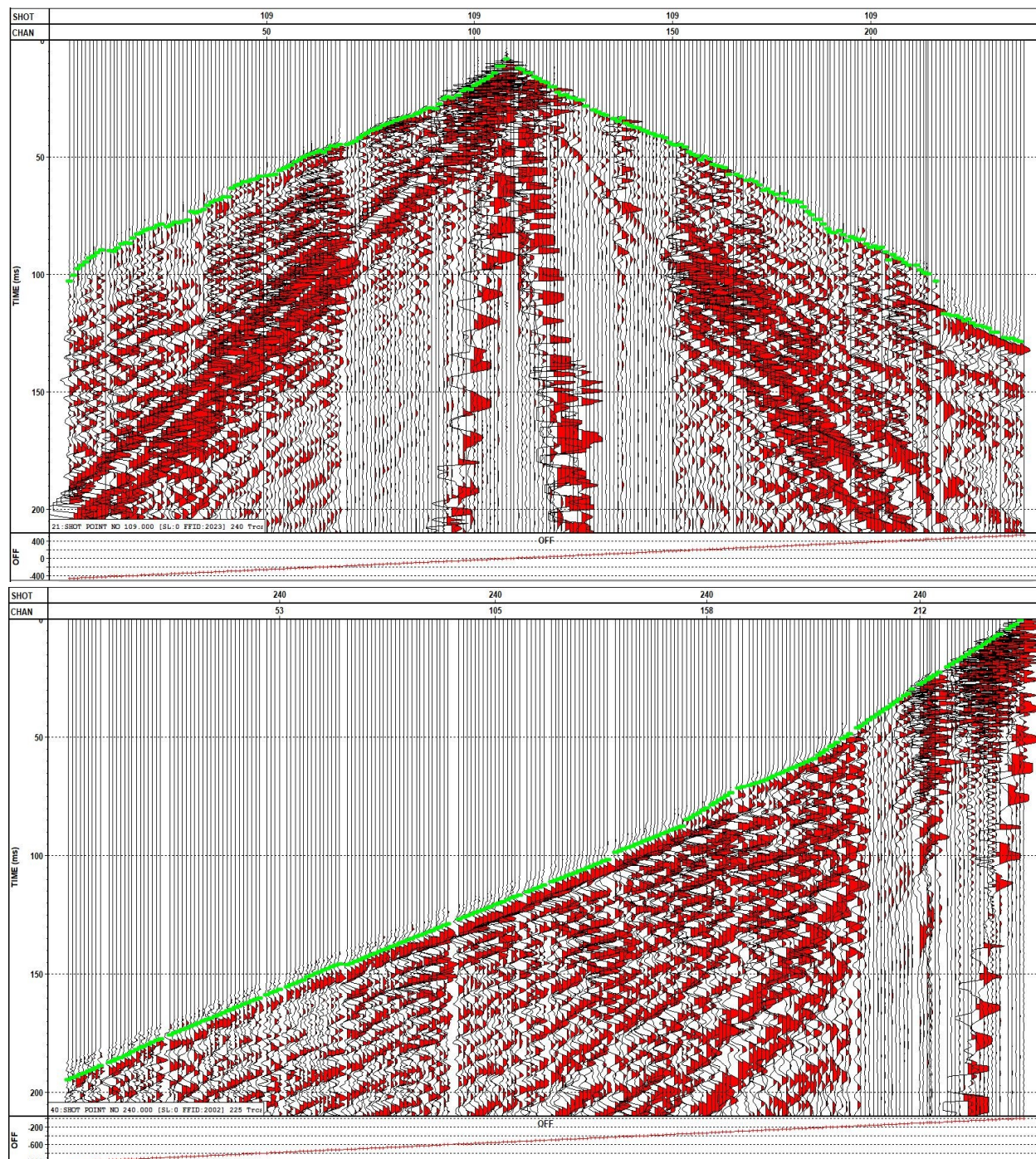


Figure 6.2: Top: Near offset first break selection for line 2 running east-west. Near offsets exhibit 2 distinct velocity slopes of approximately 2800 m/s and 4500 m/s. Shingling effect is noticed on the western side of the line caused by a large rocky cliff.

Bottom: Far offset first break selection. A third velocity slope is seen at further offsets of approximately 6500 m/s.

reflectors will be shifted to a large degree. By interpreting near surface refractions, information regarding the structure

and velocities of the near surface layer can be gained, and then corrected for. Typically, a floating datum is used to correct all near surface areas to an averaged horizon.

The first break times were transferred to the elevation refraction statics window. The parameters were set to create a 3-layer model to recreate a simple subsurface believed to consist of 1) surface frozen glacial till and permafrost limestone, 2) a middle limestone layer, and 3) the ore body. A spatial varying weathering velocity of 800 m/s was chosen to simulate the frozen glacial till. A fixed datum elevation was chosen close to the base of the weathering layer on each seismic line. Setting the fixed datum to below the weathering layer created allowed the use of a horizontally continuous replacement velocity for the variable surface layer. A refraction replacement velocity of 1500 m/s was selected. Due to higher errors in first break times caused by the bulk time shifts to correct for the shot triggering, a larger branch point delta offset for velocity lines between continuous layers was chosen to be 100 meters. The delta offset sets a range of offset distances to be used for each layer. The branch points of these layers refer to the range allowed for the intersection between continuous layers. By increasing the branch point delta offset, the software is allotted more room to shift layer boundaries into a more data-biased model, allowing for a simpler fit to a more scattered first break time vs. offset dataset.

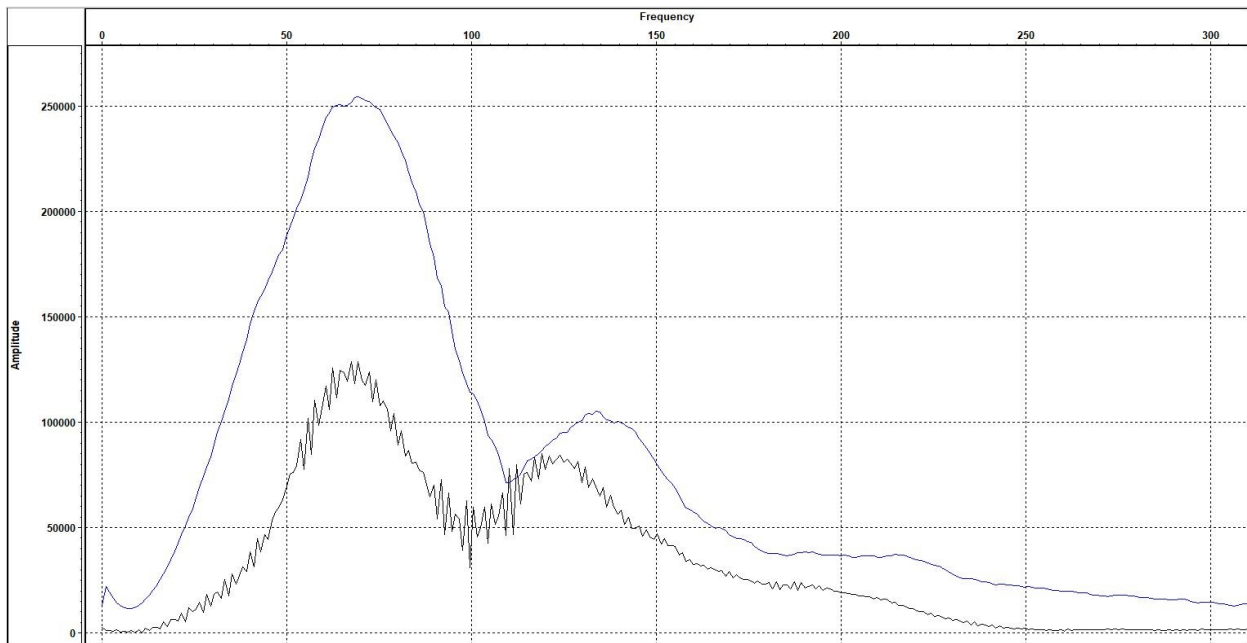


Figure 6.3: Average amplitude spectrum of all traces in dataset. *Trace 130 of shot 98 from line 2 for scale. Fourier spectrums all primarily show two main peaks at approximately 75 and 140 Hz.*

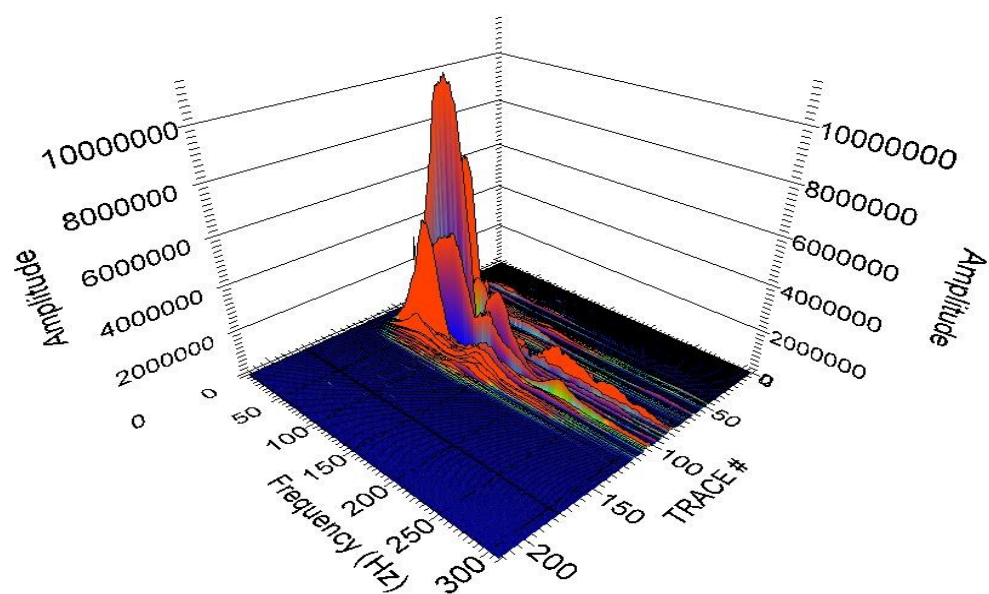


Figure 6.4: Waterfall diagram of all traces in line 2 shot 98. Strongest amplitudes are located directly beside the shot point with an exponential decrease in energy as offset increases.

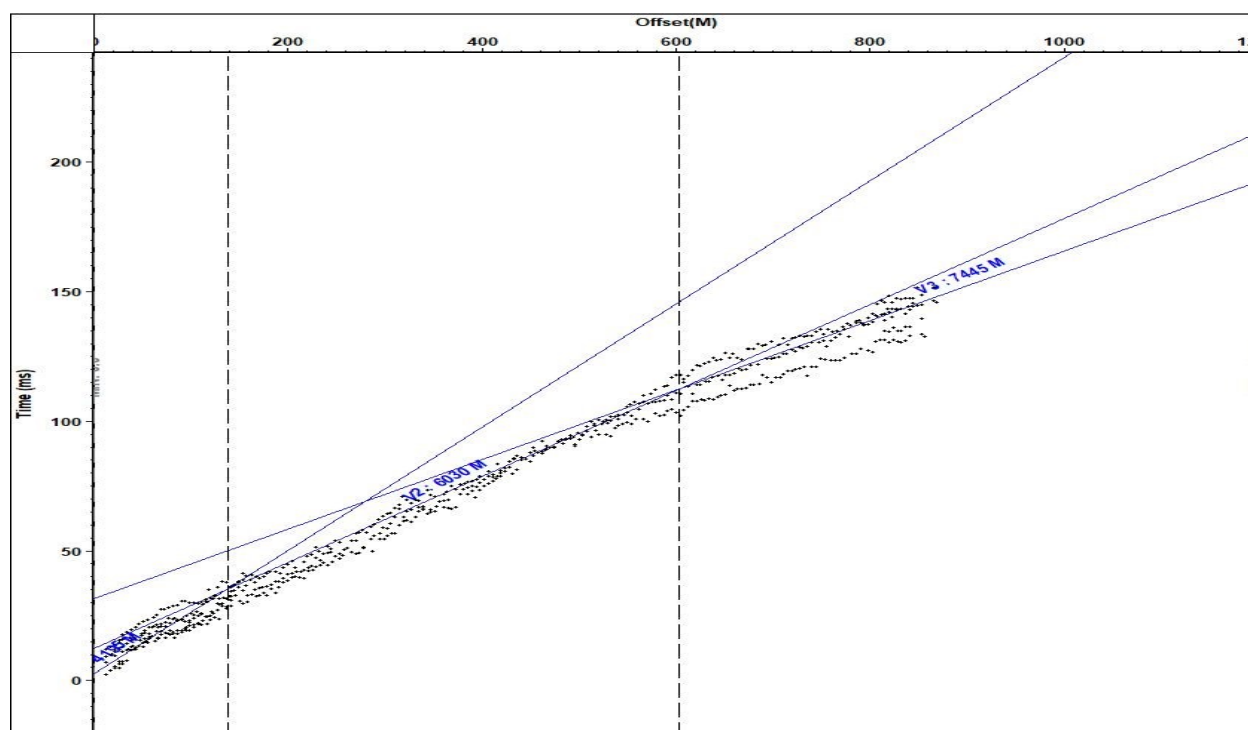
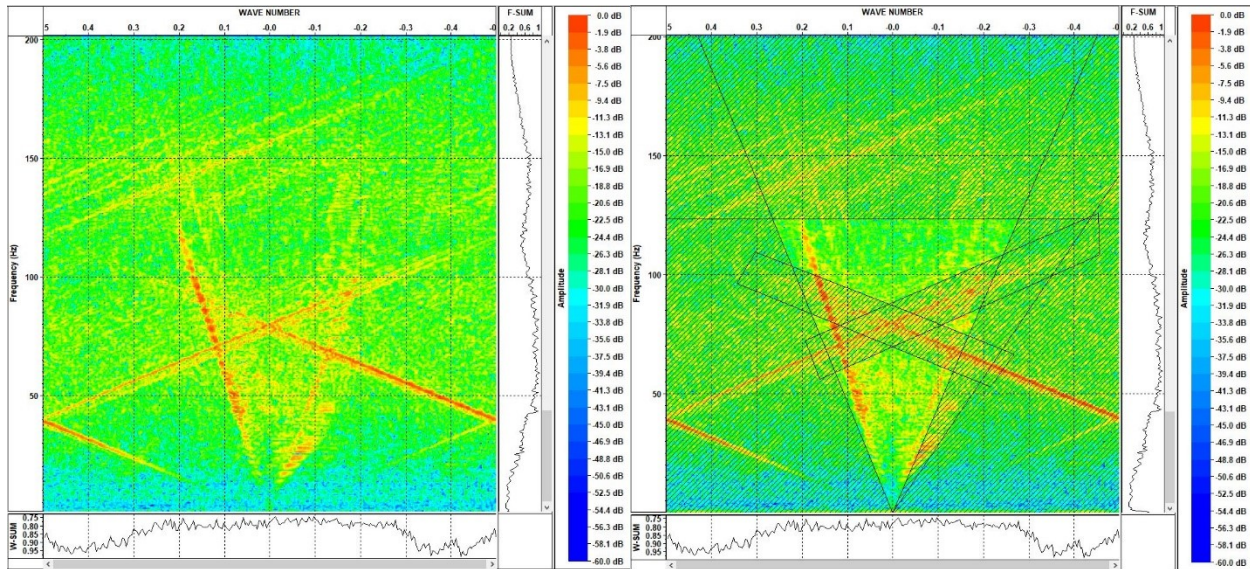


Figure 6.5: Refraction statics and tomography analysis. Offset vs travelttime first arrivals are plotted. The 10 ms range is caused by both surface topography and error in shot zero-time adjustment. Velocity slopes are manually plotted and adjusted for a best fit through the local scatter plot.

First break times were plotted versus offsets for sets of 3 shots spanning 50-meter intervals. Velocity slopes were traced out by manually tracing a best fit line through each distinct slope of first arrival points. A 10 ms wide swath was added to the traced velocity line to include all data points. The shingling effect caused by topography was dealt with by tracing out the velocity line down the middle between the two sets of first break points. A floating datum, short wave and refractions statics were then calculated using the VISTA software.



*Figure 6.6: Left: FK Domain for line 2 shot 98. All FK spectrums exhibit similar aliasing of the air wave and stronger 50 to 100 Hz regions between wavenumbers 0.1 and 0.2 and -0.1 and -0.2. The surface waves are suspected to be in this region.*

*Right: FK Filter Design. Greyed areas were removed from the final time series data sets to remove the air wave and ground roll.*

## 6.2.2 FREQUENCY WAVENUMBER FILTER

By performing a two-dimensional Fourier transform with respect to both time and offset, the Frequency wavenumber spectrum can be observed. Plotting the amplitudes spectrum against frequency and wavenumber allows ground-roll, air wave, and aliasing to more readily be observed than in the frequency domain. Creating two dimensional selective filters to remove certain zones of the F-K spectrum allows for a more accurate separation of unwanted noise and signal.

Transferring to the F-K domain highlights a heavily aliased air blast wrapping through all wavenumbers and frequencies. Both the air blast and remaining signal have approximately the same energy. A pie rejection zone was established to remove wavenumbers 0.2 and -0.2 outwards. Polygon rejection zones

were traced over the wrapped around aliased air blast within wavenumbers 0.2 to -0.2. All rejection filters had a smoothed edge spaced over 7 traces with a smoothing frequency of 5 Hz to avoid ringing in the time domain. This had the effect of removing a good amount of the air wave, but also created noise surrounding the first arrivals and removed higher frequencies from the near surface. The air wave is still slightly visible in the resulting data.

Various filter designs and shapes were applied in the FK domain to remove the stronger surface waves. Figure 6.6 shows a typical FK filter design applied. Surface wave energy is closely interspaced with desired signal and all attempts to remove surface waves and leftover air wave removed or diminished desired signal strength.

#### 6.2.4 TAU P FILTER

Radon transforms change data from the time domain to the Radon domain where input data with different moveouts and velocities are mapped to slowness vectors vs. zero-time offsets. Linear objects in the time domain become points in the radon domain. This makes filtering in the radon domain more accurate for filtering curved and dipping events than the FK domain. VISTA uses the generalized form of the radon transform:

$$m(\tau, q) = \int_{x_{min}}^{x_{max}} d(\tau + q \cdot \theta(x), x) dx \quad 6.1$$

Where  $m(\tau, q)$  is our radon transform in radon space,  $d(t,x)$  is the input seismic data,  $\tau$  is the zero time offset,  $x$  is the offset,  $q$  is the slowness vector, and  $\theta$  is the integration curve. The integration curve is selected based on the curvature of the input data:

$$\text{Linear: } \theta(x_i) = x_i \quad 6.2$$

$$\text{Parabolic: } \theta(x_i) = x_i^2 \quad 6.3$$

$$\text{Hyperbolic: } \theta(x_i) = \sqrt{x_i^2 + z_{ref}^2} - z_{ref} \quad 6.4$$

$$z_{ref} \approx t_{ref} * V_{nmo} \quad 6.5$$

Where  $z_{ref}$  is the reference depth at which the reflection event is focused.  $V_{nmo}$  is the moveout velocity, and  $t_{ref}$  is the time where the reflection event is focused.

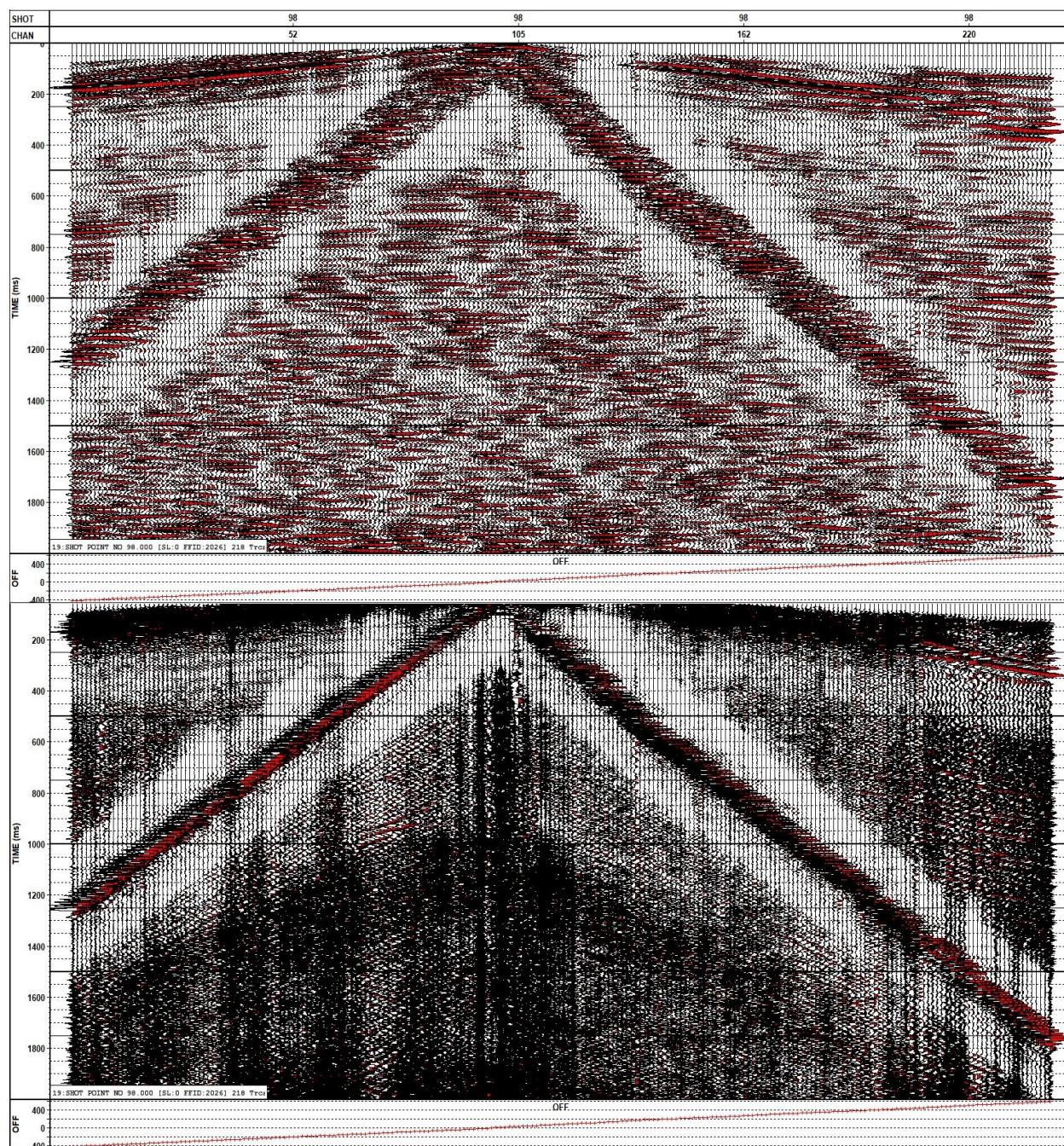


Figure 6.7: Top: Shot gather from line 2 shot 98 after FK filter, 15/25/70/85 Hz Ormsby filter, and 250 ms AGC applied.

Bottom: Removed noise from shot gather.

The Tau-P transform is a unique case of the radon transform where all time domain data is modelled as linear effects. Parabolic and hyperbolic events in the time domain result in elliptical curves in the Tau-P domain. The Tau-P provides an excellent platform to remove strong linear noise such as surface waves and air blast. Setting up a Tau-P forward and Tau-P inverse transform in cascade allows the selection of slowness vectors and desired frequencies to allow for the removal of noise or known undesired objects. Slowness vector windows were created around measured refraction velocities to remove the air blast and surface waves. Figure 6.8 shows the resulting pre- stack shot gathers and removed noise. The majority of the air blast has been removed. However due to the strength of the air wave and encompassed frequencies there was little to no seismic signal visible afterwards. The effect on surface waves were unnoticeable at offsets less than 550 meters. Beyond 550-meter offsets surface wave noise was removed but possible reflections are still hidden within remaining surface wave noise.

Varying slowness selection zones did little to further remove surface waves and return seismic data to the air wave zone. The cascaded forward and reverse transforms had the effect of adding horizontal artifacts to the pre- stack data. Applying Ormsby filters, FK filters, and Tau-P filters did little to remove the surface waves and resulting horizontal artifacts. This illustrates the difficulties encountered when working with near surface data in permafrost environments.

### **6.3 REFRACTION TOMOGRAPHY MODELS**

Section 6.3 will showcase the resulting models from the data processing listed above coupled with the inversion methods discussed in Chapter. 3. Resulting inversions from both the SEISOPT 2D software and VISTA Seismic Suite software will be introduced. Key features in both models will be explained in conjunction with areas where our confidence in the results is lacking.

#### **6.3.1 SEISOPT 2D MODELS**

The observed first arrival times were corrected to account for residual short wavelength topographic and refraction static time shifts. These times were then input to the SEISOPT 2D™ software to invert for subsurface velocity models as given in Figures 9 through 12. Processing was performed by Optim™ staff proficient in SEISOPT 2D operation.

All 4 seismic profiles show large lateral variations in the velocity structure. This situation was expected due to the geological expectation that a nearly vertically dipping ore body caused both the magnetic and gravity anomalies described earlier. All large vertically exaggerated high velocity zones pair up close to

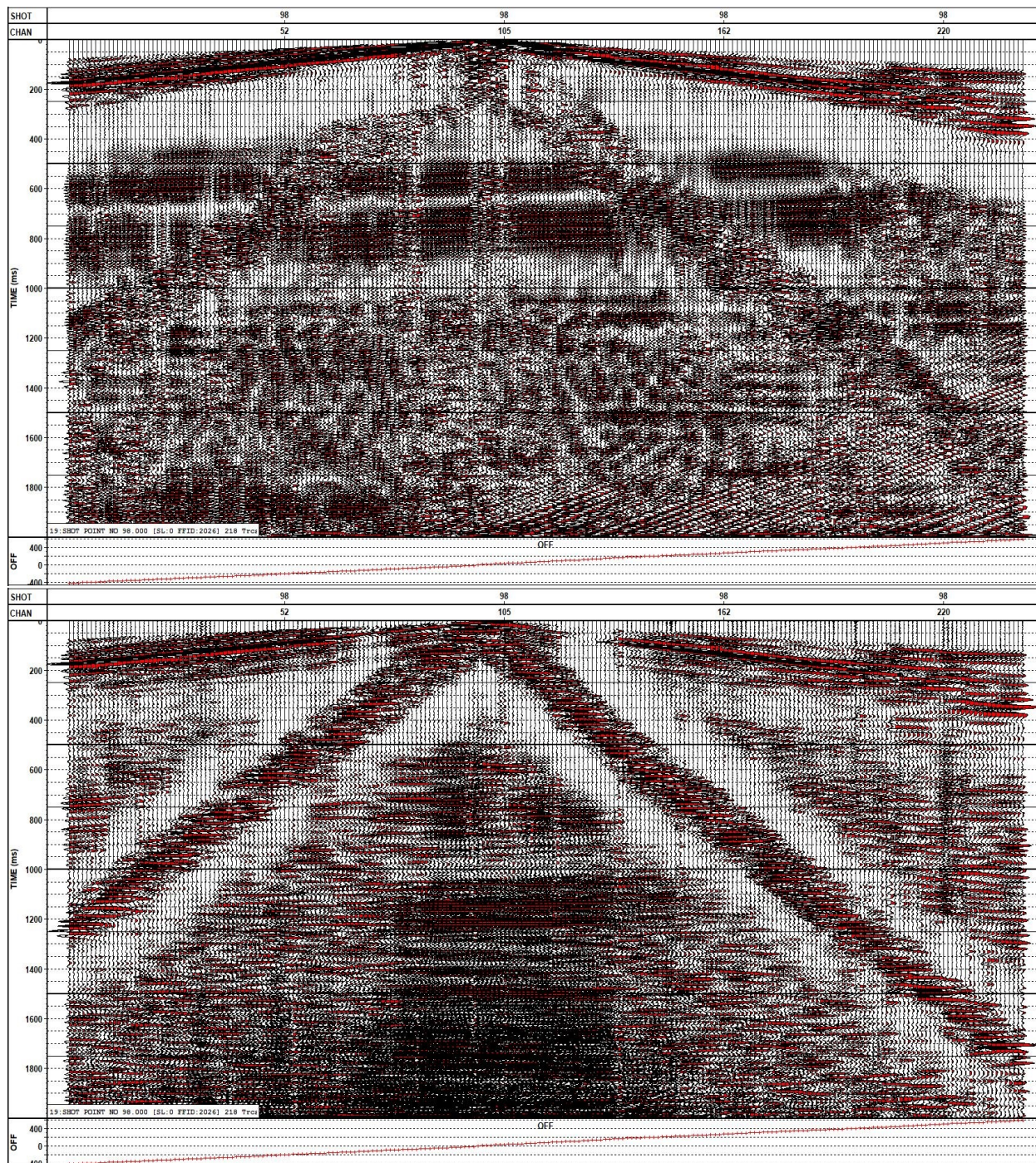


Figure 6.8: Top: Line 2 Shot 98 shot gather after Tau-P filter applied to remove linear (constant velocity) features. A horizontal artifact has been added to the resulting dataset.

Bottom: Noise removed by the Tau-P filter.

near surface ultra low velocity zones. However, the vertical extent of the high velocity zones and the ultra low surface velocities is not geologically reasonable, and this is likely an artifact resulting from inaccuracies in the input corrected times together with smearing within the inversion algorithm applied. In particular, the fact that all of the vertical high velocity extensions seen in the inversions also correspond to areas where deep snow drifts existed is worrisome. In many areas, the snow drifts were too deep to allow one to dig through in order to place geophones on the earth's solid surface; and so, the exact elevation for the geophone is unknown. Further, those geophones planted in the snow generally had poor data quality. This combination may have led to poor estimation of the static correction that needed to be applied.

Further, Lines 4 and 5 exhibit large edge effects on their western edges. On line 5 these effects may be a result of a 30-meter cliff that separated the end of the line from the majority of off-end shots. This was further complicated as the positions of these off-end shots on line 5 could not be placed perfectly in line with the geophone profile. These problems were deemed acceptable in the end as the high velocity edge zone is outside of the region of interest of the survey.

Lines 2 and 3 run nearly parallel to the strike of the ore body and the magnetic anomaly (refer back to Figure 3.4). Inspection of Figures 6.9 and 6.10 show a high velocity zone beginning in the east (right side of figures) and plunging westward at a shallow angle of approximately 3 degrees as the high velocity zone moves westward across the figures. The east (right) side of line 2 shows the 5000 m/s velocity contour at an elevation of 130 meters ASL. 2 km away on the west edge (left) edge of line 3 (Figure 6.10) the 5000 m/s contour has dropped to only 65 meters ASL. The center of line 2 is located at both the topographic high of the survey region and the strongest point of the magnetic anomaly. The 5000 m/s velocity contour pushes upwards here suggesting a local tomographic high of the iron ore body coupled with a potential high-grade iron ore region.

Lines 4 and 5 are oriented with 0 m along line being north with distance increasing southward. The high velocity zones reaching the surface are the intersection points with lines 2 and 3. Line 4 intersects line 3 at 720 meters and line 5 intersects line 2 at 1040 meters. High velocity zones reach the surface in these areas creating a discontinuity with lines 2 and 3. Velocity decreases steeply to the south, but extends to the north, suggesting the iron ore body is dipping to the north.

### **6.3.2 VISTA SEISMIC SUITE REFRACTION STATIC MODELS**

Inputting the first arrival times with offset distances into the VISTA™ Seismic Suite software, a layered model with 3 discrete layers was determined as discussed in Chapter 3. A grid size of 40 meters in the X

direction and 20 meters in the Y direction was set for use in the inversion. A spatial mesh size of 4 meters (equal to geophone spacing) was set for the ensuing ray tracing to assist in minimizing error between resulting forward modelling and original dataset. A 150-meter wide moving averaging window was used on the layer boundaries and velocities of layers 2 and layer 3 to create a more realistic surface.

The refraction static analysis for line 2 (Figure 6.13) shows a depth to the high velocity ore body of approximately 100 meters in the middle of the line and 77 meters on the eastern edge. The high velocity ore body begins to drop deeper as all other models suggest on the western edge, dropping to an elevation of 150 meters below the surface. A drop in the lower layer velocity is observed at 580 meters and a drastic increase in surface layer velocity is observed at 350 meters along the line similar to those seen in line 2 of the SEISOPT 2D model. Line 3 (Figure 6.14) shows a flat high velocity layer with a slight dip to the west as expected. Depth to the top of the layer is approximately 100 meters, and it continues deeper on both the east and west sides of line 3 to approximately 130 meters below the surface on the western edge and 150 meters below the surface on the eastern end of the line due to surface topography. Two high velocity zones extend upwards from the high velocity layer towards the surface similar to those seen in the SEISOPT 2D models. A sharp high velocity change from 3500 m/s to 5700 m/s occurs at approximately 420 meters along the line a wider more gradual velocity change of 4800 m/s to 5300 m/s is seen from 680 meters to 800 meters along the line.

Line 4 had a high standard deviation of first break points vs. offset for desired slopes. This is likely caused by noisy shot gathers and poor geophone coupling with the ground. A 150-meter wide smoothing filter was applied to layer boundaries for layers 2 and 3. The resulting model is seen in Figures 6.5. It does follow the estimated trend of the iron ore body and shows similarities to the SEISOPT 2D model. A high velocity zone extends upwards towards the surface at the base of the slope. Higher velocities continue laterally upslope rather than downslope suggesting the ore body dips in the upslope (north) direction. The peak of the high velocity zone is approximately 110 meters below the surface, dropping off steeply to the south to 180 meters below the surface on the southern end of the model and increasing to 200 meters below the surface on the north end due to the drastic increase in topography. The second layer exhibits lower velocities than expected for limestone but mimics a high velocity vertical extension to the surface as seen in the SEISOPT 2D model. The peak of the high velocity zone agrees with the surface of layer 3 in line 3.

The model for line 5 can be seen in Figure 6.16. The layers were smoothed with a 150-meter wide moving average window. The high velocity zone extends upwards to a depth of 70 meters below the surface. The depth to the top of the layer drops off quickly southward to 190 meters below the surface. Northward

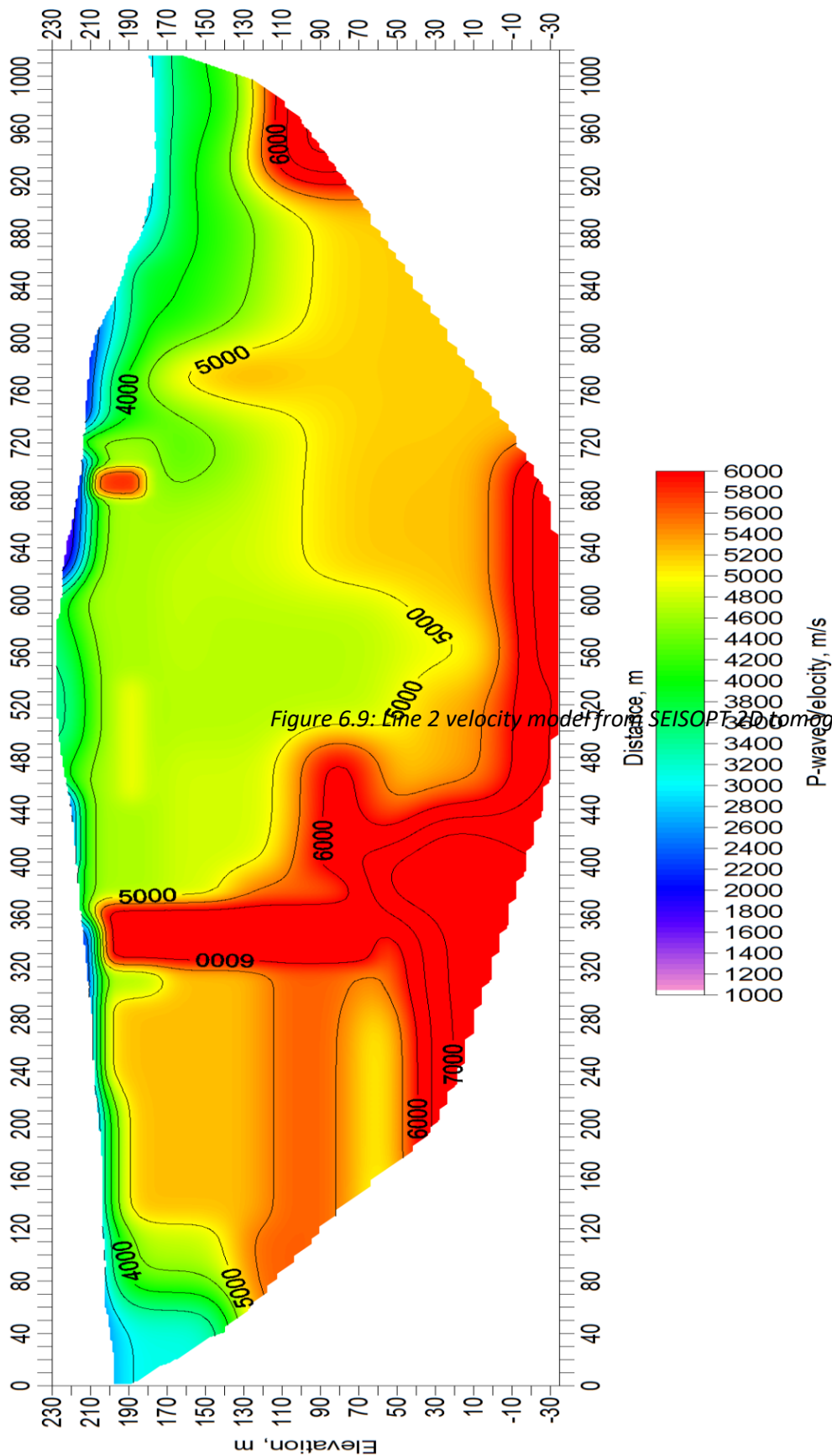


Figure 6.9: Line 2 velocity model from SEISOPT 3D tomography software. Model runs west (0 m

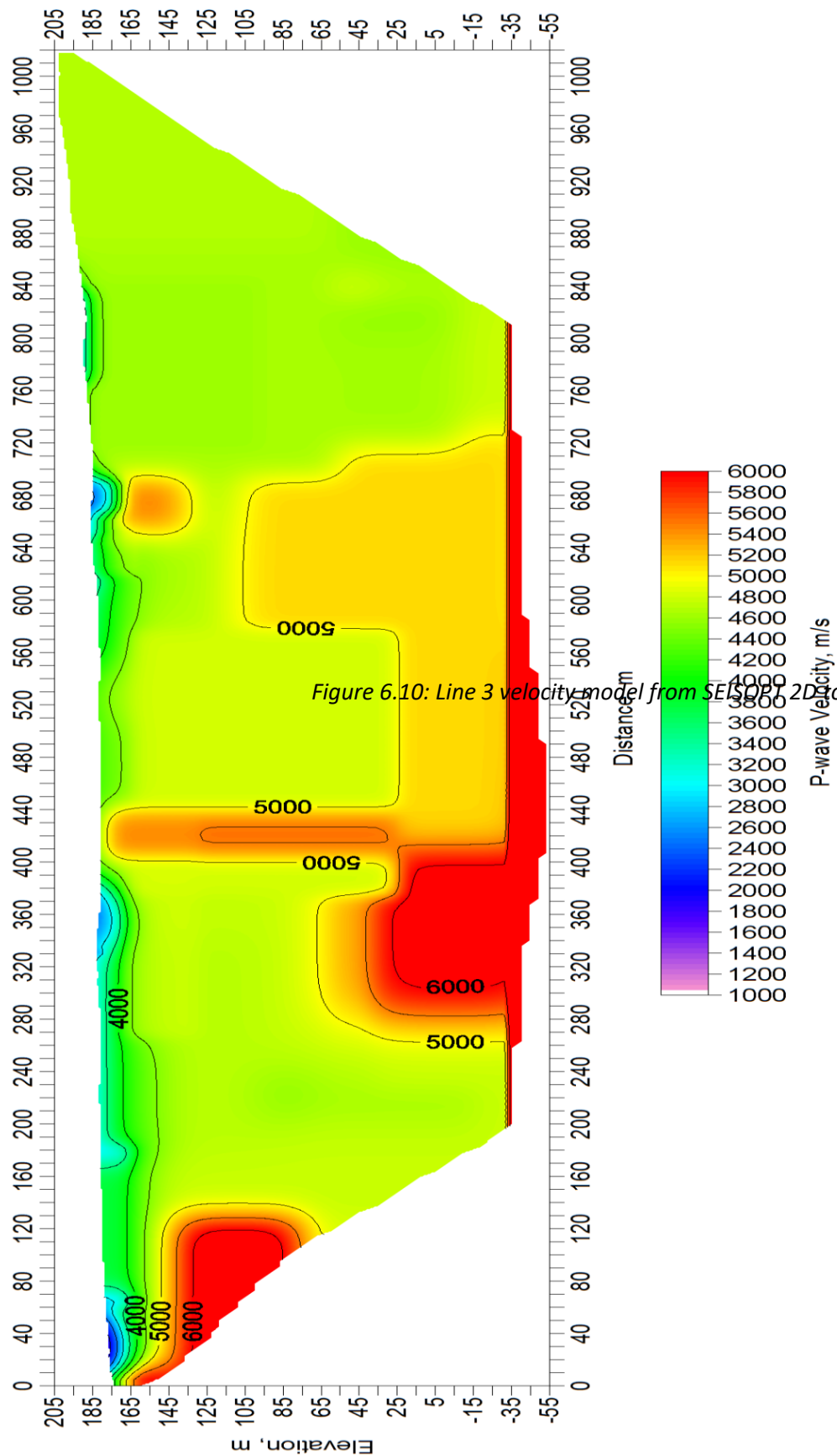


Figure 6.10: Line 3 velocity model from SEISOPT 2D tomography software. Model runs west

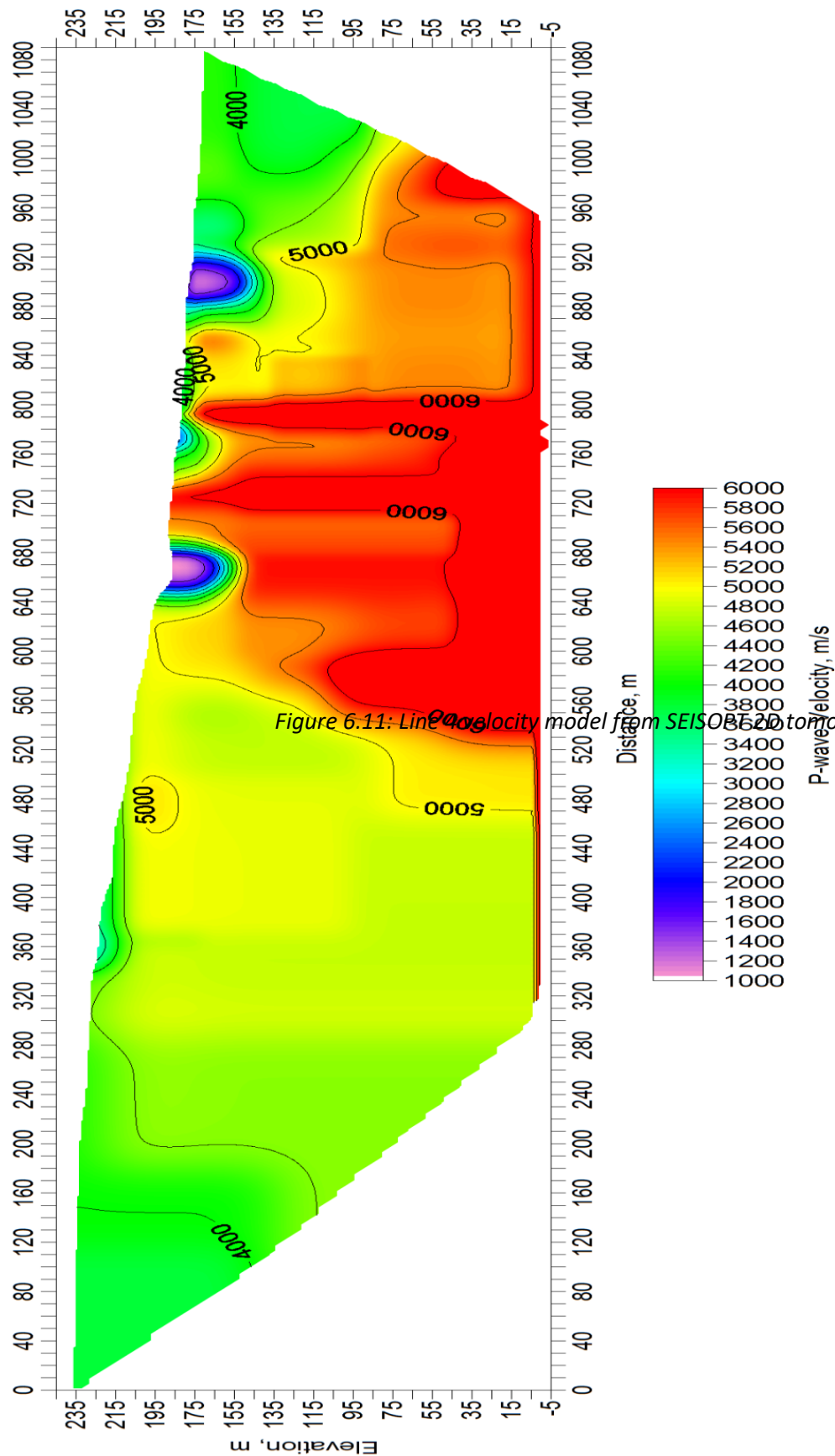


Figure 6.11: Line P-wave velocity model from SEISOB520 tomography software. Model runs North (0

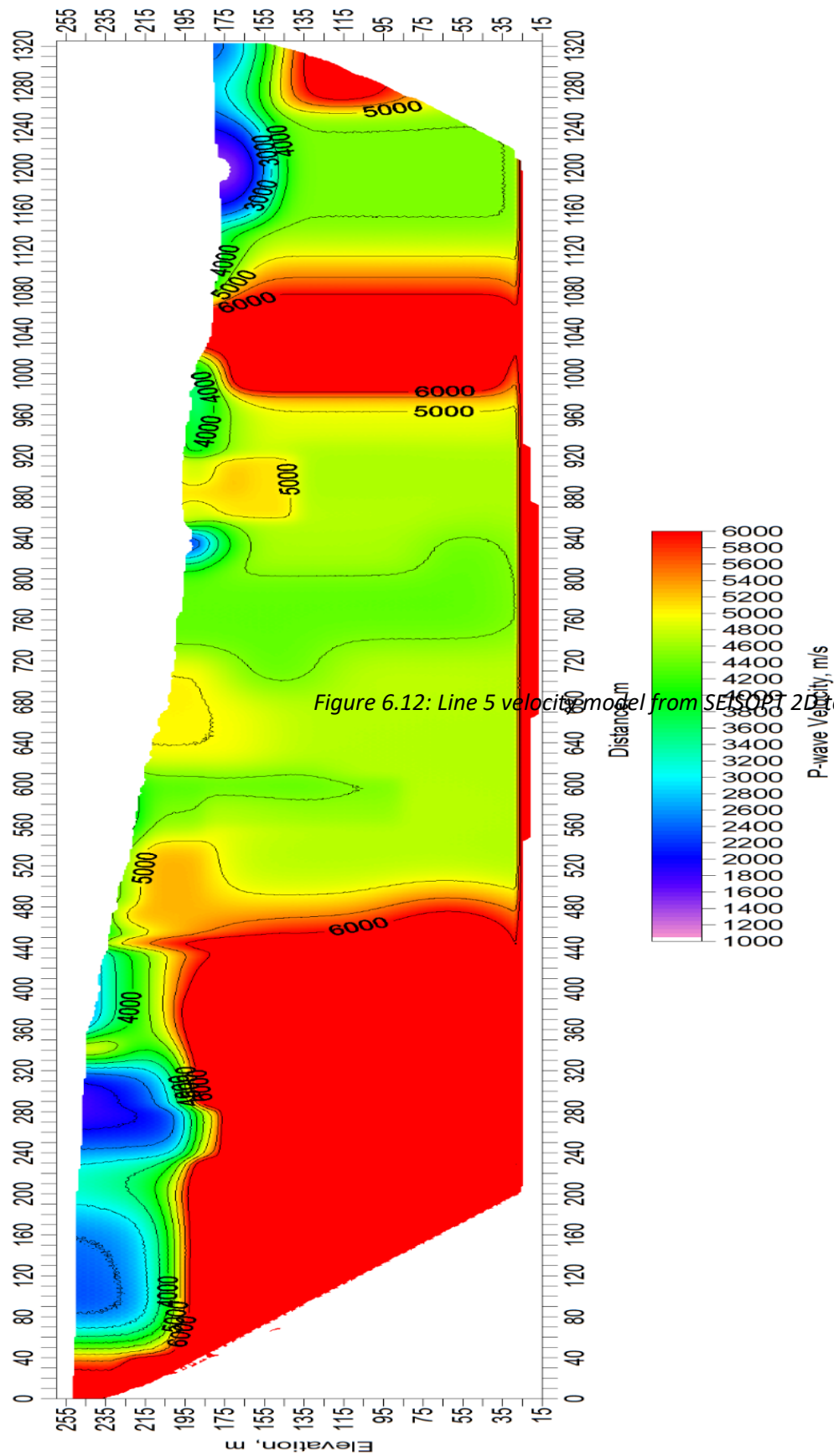
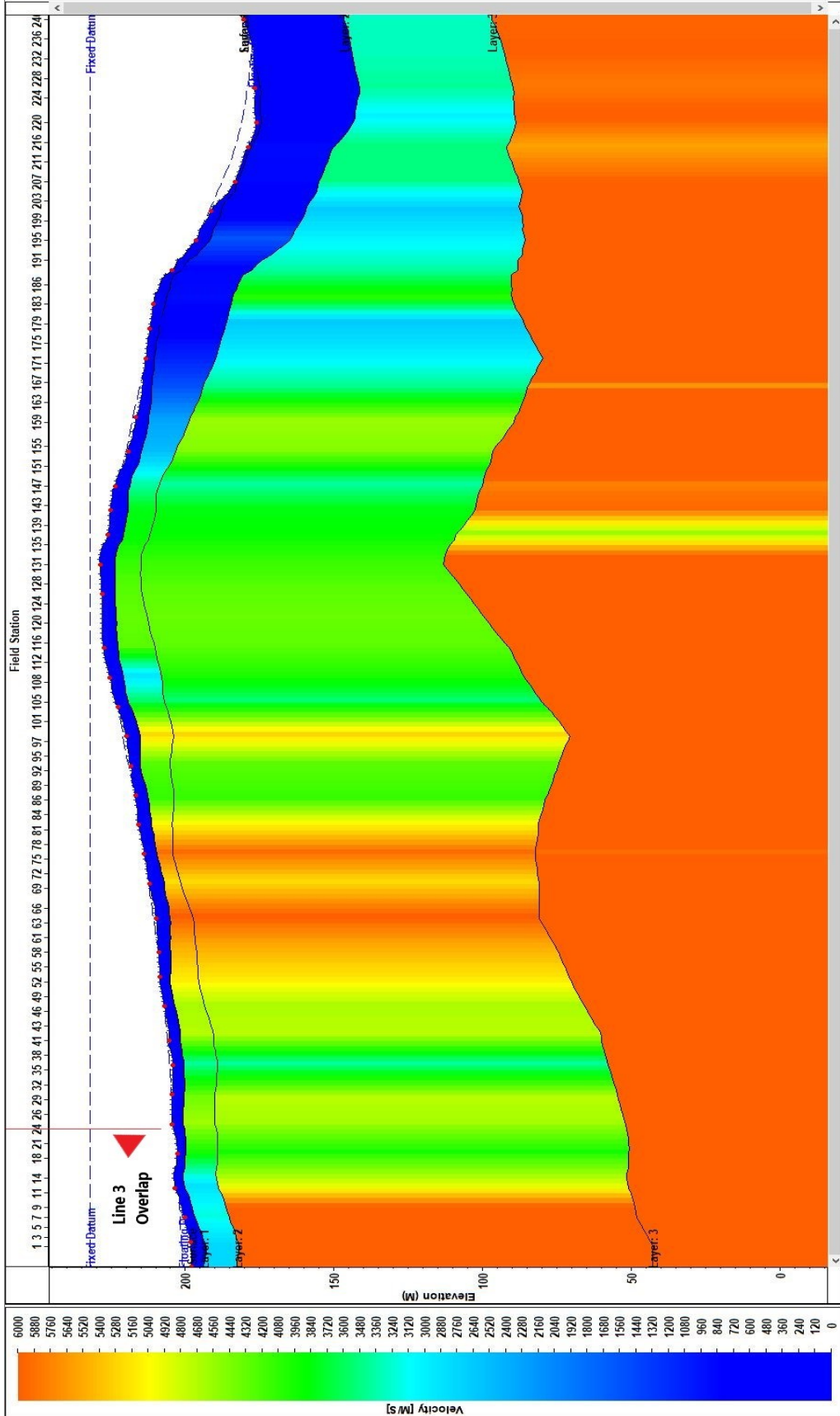
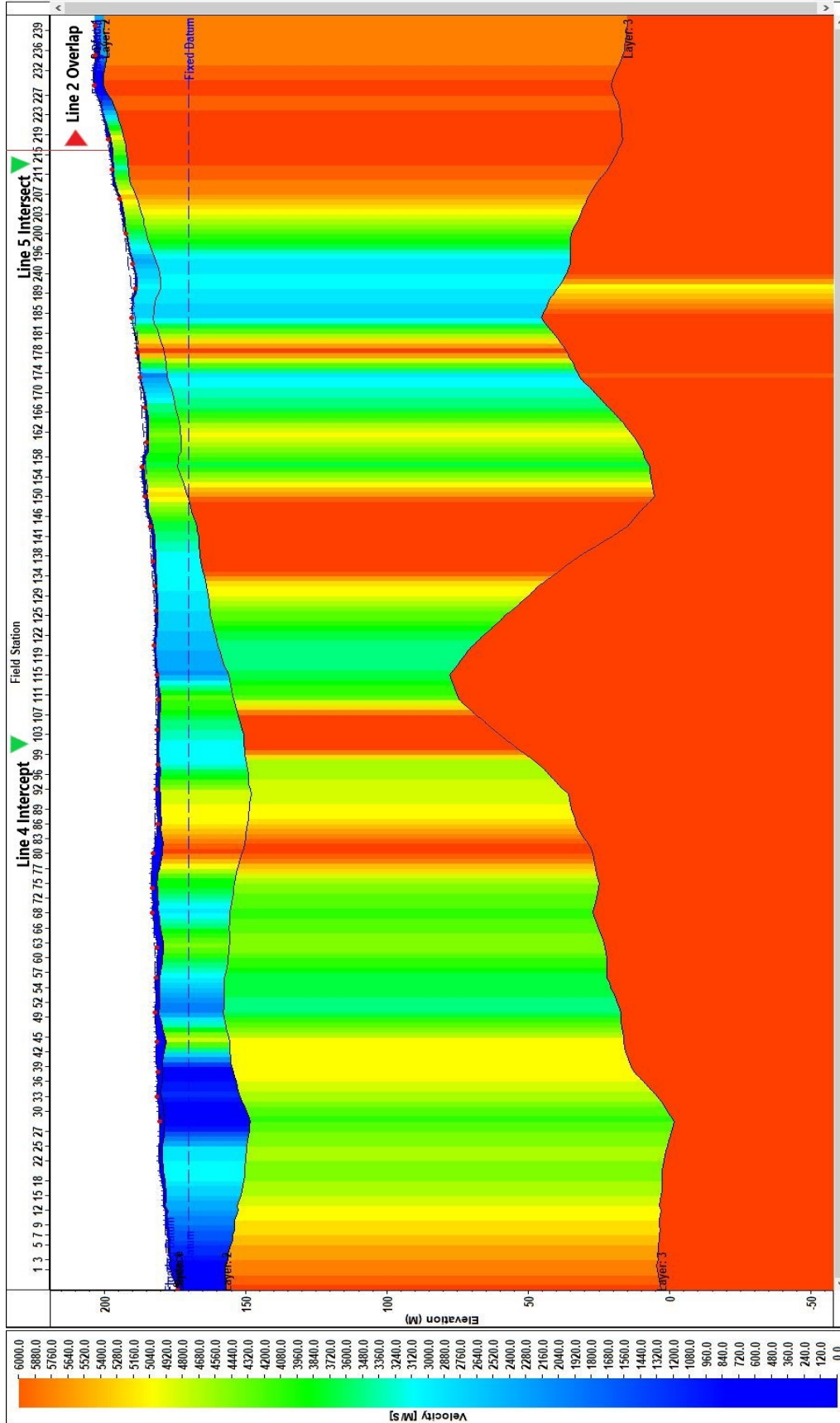


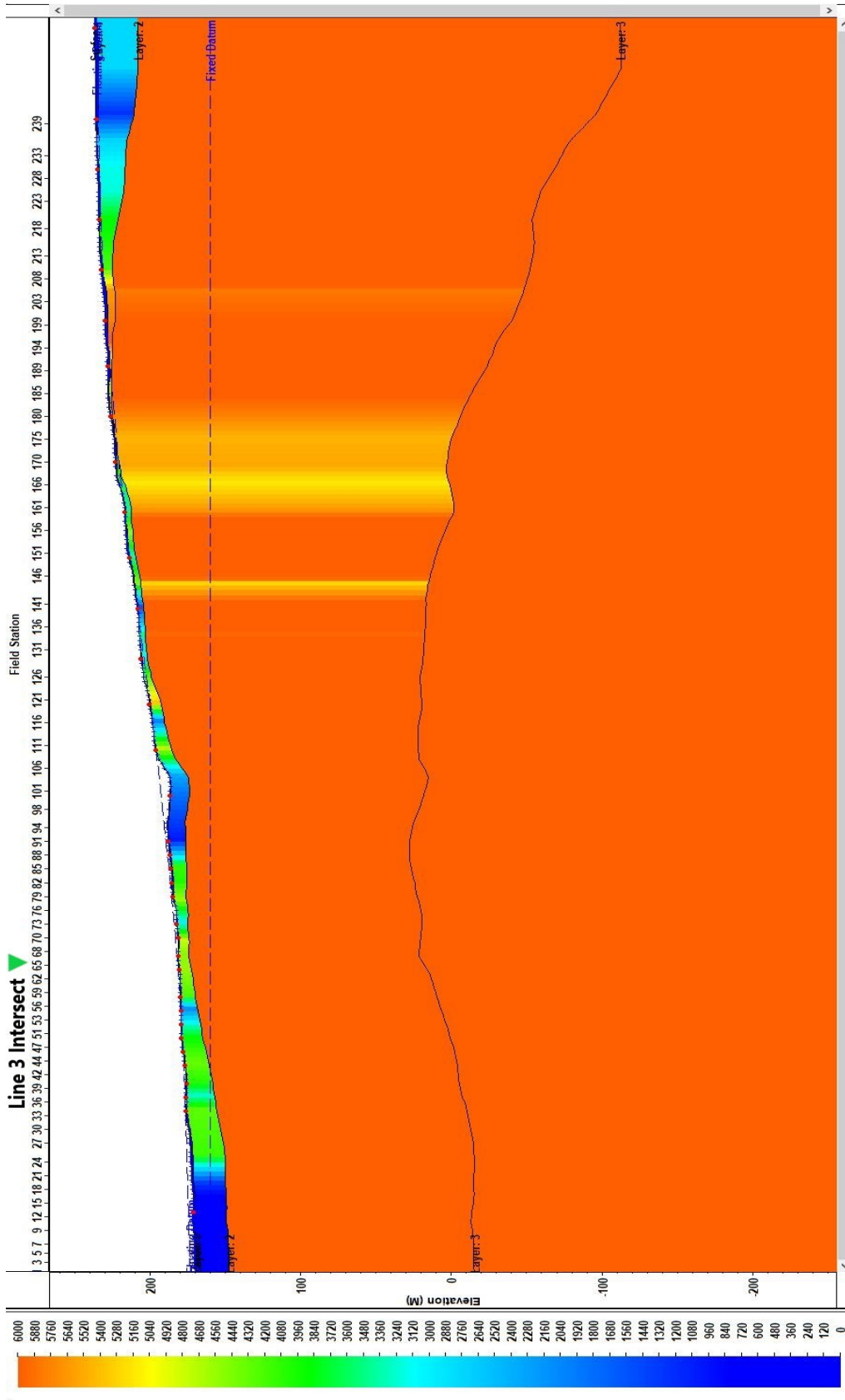
Figure 6.12: Line 5 velocity model from S150P9 2D tomography software. Model runs North



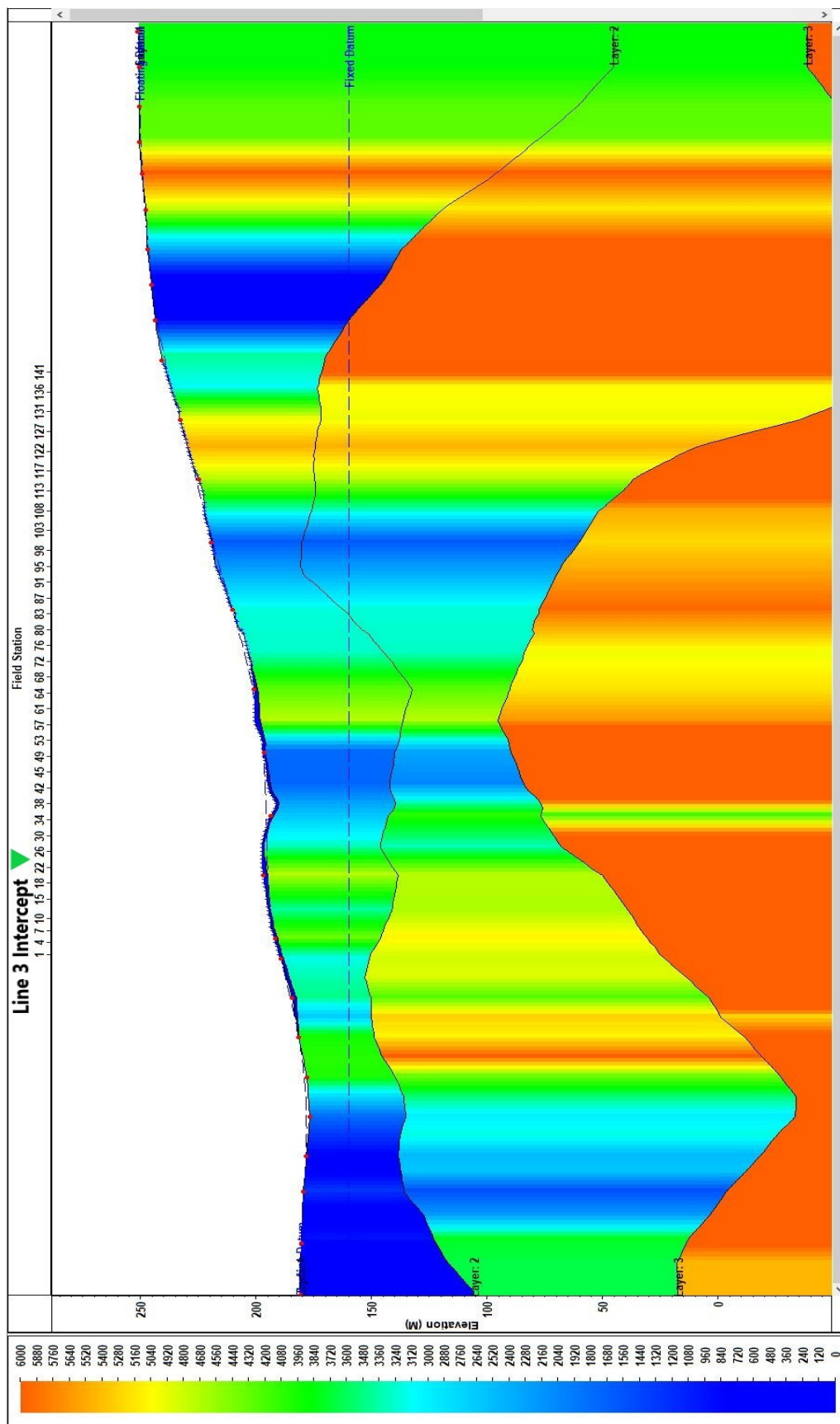
Seismic Suite. Model runs East (field)



Seismic Suite. Model runs East (field



Seismic Suite. Model runs South (fie



ismic Suite. Model runs South (fiel

the layer drops at approximately the same angle but begins to flatten out quickly and the depth to the surface of the layer is 165 meters. The layer depth on the north side is larger due to the increasing topography as we move northward. The high velocity zone is shifted approximately 50 meters north of where the ore body is expected and where the high velocity zone is in the SEISOPT 2D model. The depth to the high velocity zone does correlate with the depth to the high velocity zones in lines 2 and 3 where they intersect.

#### **6.4 SUMMARY**

While attempts at removing noise from the shot gathers using a variety of different methods proved unsuccessful in finding shallow reflection, the filtering did allow for more accurate selection of first arrivals, and assisted in developing a deeper understanding of filtering processes in hard rock permafrosted environments (King et al., 1988). First arrivals were used with offsets to develop seismic tomography and velocity models using two different pieces of software: SEISOPT 2D™ and VISTA™ Seismic Suite. Resulting tomography and velocity models showed many similarities with interpreted geology and ore body structure. Further similarities and differences between models will be discussed in Chapter 7.

## **CHAPTER 7    PROPOSED SITE CHARACTERIZATION MODEL**

### **7.1 INTRODUCTION**

The goal of this thesis is to provide a preliminary geophysical site characterization of the McQuat Lake iron ore synform. By collecting and processing refraction seismic data, airborne magnetic data, and ground based gravity data, this has largely been accomplished. Rock physics properties of all known rocks in the area have been collected to further the understanding of the modelled results. All resulting models and rock physics measurements are integrated in this chapter to provide a final interpretation of the subsurface ore body and possible high-grade zones. The two refraction inversion models created from both VISTA™ Seismic Suite and SEISOPT 2D™ are compared in Section 7.2. While both models were created using the same first arrival travel time data, and have similarities, there are differences resulting from the inversion techniques employed, noise in the data, and differences in starting models. Section 7.3 will investigate the magnetic inversion susceptibility model presented in chapter 5 and interprets it given the constraints of the seismic refraction models. Section 7.4 will focus on the resulting gravity and density model presented in the latter sections of chapter 5 and compare it to both the magnetic susceptibility results and the refraction tomography. Rock physics measurements from chapter 4 will be used to assist in constraining the overall results throughout the chapter. All results are then combined to form a finalized tomographic model of the survey site highlighting the depth to the ore body and suspected high-grade zones.

### **7.2 REFRACTION MODEL COMPARISON**

The two different refraction tomography models were compared on a line by line basis, and many different tests were carried out. Here we attempt to compare the two different inversion methods more quantitatively directly.

First, the sensitivity to the input travel times obtained using the VISTA™ Seismic Suite were tested by removing 10 percent of the control points (Schijns et. al, 2008). This procedure examined the reliability of the final solution, and the inversions calculated using the decimated number of control points still exhibited all main tomographic features and reproduced the layer depths were within 10 meters of the full regular models.

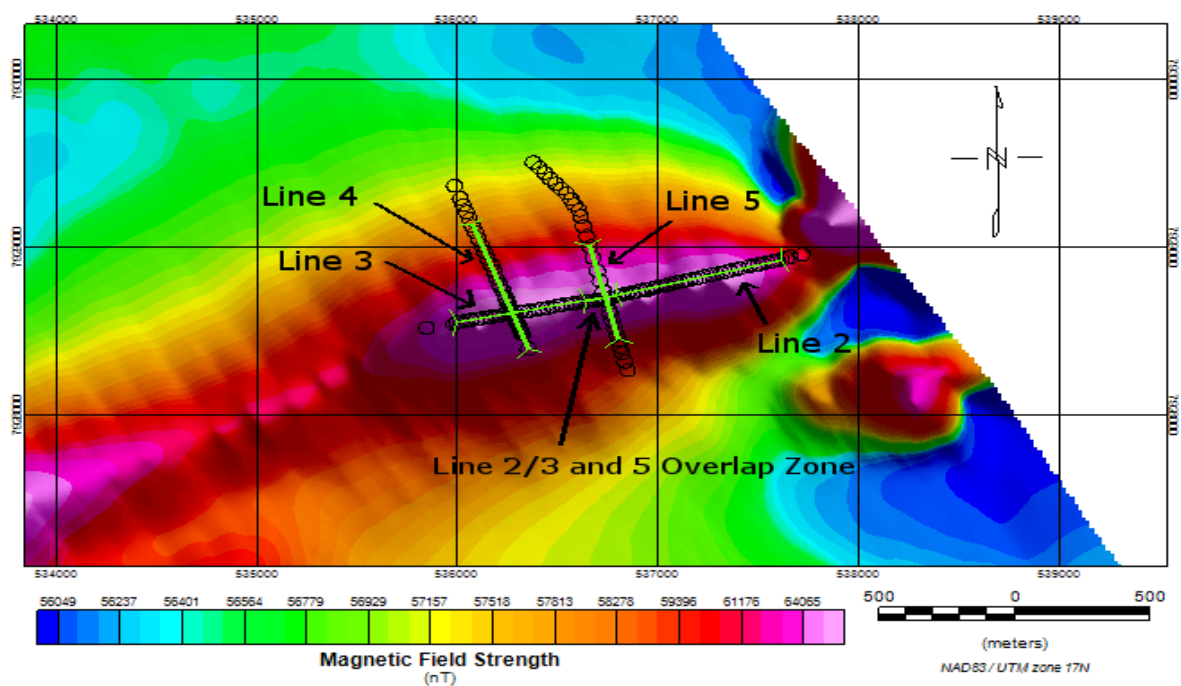


*Figure 3.4 Review: Quick reference of survey lines (green) overlaying all shot locations (circles). Each line was laid down and shot individually.*

A smoothing filter was applied with MATLAB's meshgrid function™ to smooth the layer-constrained VISTA™ models in order to better compare them to compare less controlled SEISOPT 2D's™ output. Resulting velocity and tomography models and differences can be seen in Figures 7.1 through 7.4.

Line 2 extended from the Central Borden Fault on the east side (1000 meters along line) to the top of the central topographic rise in the survey site. Both VISTA™ and SEISOPT's™ inversion models have upper velocities in the 7000 m/s range, with SEISOPT™ showing large horizontal discontinuities likely caused by poor first break selections and static corrections. These high values of wave speed are likely not encountered in reality but are not excessively greater than the values near 6700 m observed in the laboratory for the sample from 170 m depth (Chapter 4) within the greenstones. The two-dimensional smoothing filter applied to the VISTA™ inversion yields unrealistic high velocities extending upwards to shallower depths. The VISTA ore body surface layer has been plotted on both the VISTA and SEISOPT tomography model. On the SEISOPT model the ore body surface follows the 5000 m/s contour closely, and has tomographic highs at both the large vertical artifact at 320 meters along the line and the medium to high velocity zone from 550 to 700 meters along the line. High velocity zones along the edges are not necessarily real and are attributed to edge effects within the inversion. Interestingly, when plotting the

difference between the two models the high velocity zones show the least amount of difference between the two models.

Results from chapter 4 suggest that the ore body velocity begins at approximately 5000 m/s due to the wavespeeds recorded in low grade (15% iron content) BIF. The VISTA model suggests much higher velocities at the limestone/ore body interface pushing upwards towards 7000 m/s. These numbers suggest a higher confining pressure in the VISTA model. The SEISOPT model suggest a limestone/ore body velocity of approximately 5500 m/s to 6000 m/s. Again, these numbers suggest a higher confining pressure in the model. However, crude pressure estimates using an average limestone density of 2000 kg/m<sup>3</sup> and glacial till density of 1600 kg/m<sup>3</sup> result in pressures at the ore body surface of between 1 and 5 MPa, far below the 35 MPa lab tests which resulted in acceptable velocities.

Lines 3, 4, and 5 all showed similar comparisons between the VISTA model and the SEISOPT model. High velocity zones extending towards the surface are similar between the models. VISTA models exhibit higher velocities by up to 3000 m/s, likely caused by the smoothing filter. All the VISTA models exhibit a much slower surface layer by nearly 2000 m/s. Subtracting the models always results in the lowest difference being at the zones where the iron ore surface extends vertically upwards, and the biggest differences are located laterally across layer 2, suggesting both models do agree in the location of the iron ore body. Line 5 shows a high horizontal variability in the location of the high velocity zone between the VISTA model and the SEISOPT model. The SEISOPT model has the high velocity zone shifted 300 meters south (lower X values) than the VISTA model. Lines 4 and 5 show larger edge effects than lines 2 and 3, with larger edge effects being on the north side and in the SEISOPT models. This effect is likely caused by the large topographic cliff located on the north end of lines 4 and 5.

Plotting the tomographic ore body surface calculated from VISTA we see that it generally follows the trend of the high velocity zone in both the SEISOPT and VISTA models. In all models (both VISTA and SEISOPT) the VISTA ore body surface follows the areas where velocity drastically increases from 5000 m/s to 7000 m/s. All localized highs are associated with vertically extending high velocity zones in both the VISTA and SEISOPT models except for the line 5 SEISOPT model where the high velocity zone is 300 meters south of the VISTA high velocity zone. The ore body surface trends deeper towards the western end of the survey grid with lines 4 and 5 showing the steeply dipping surface dipping northward and deepening from line 5 to line 4.

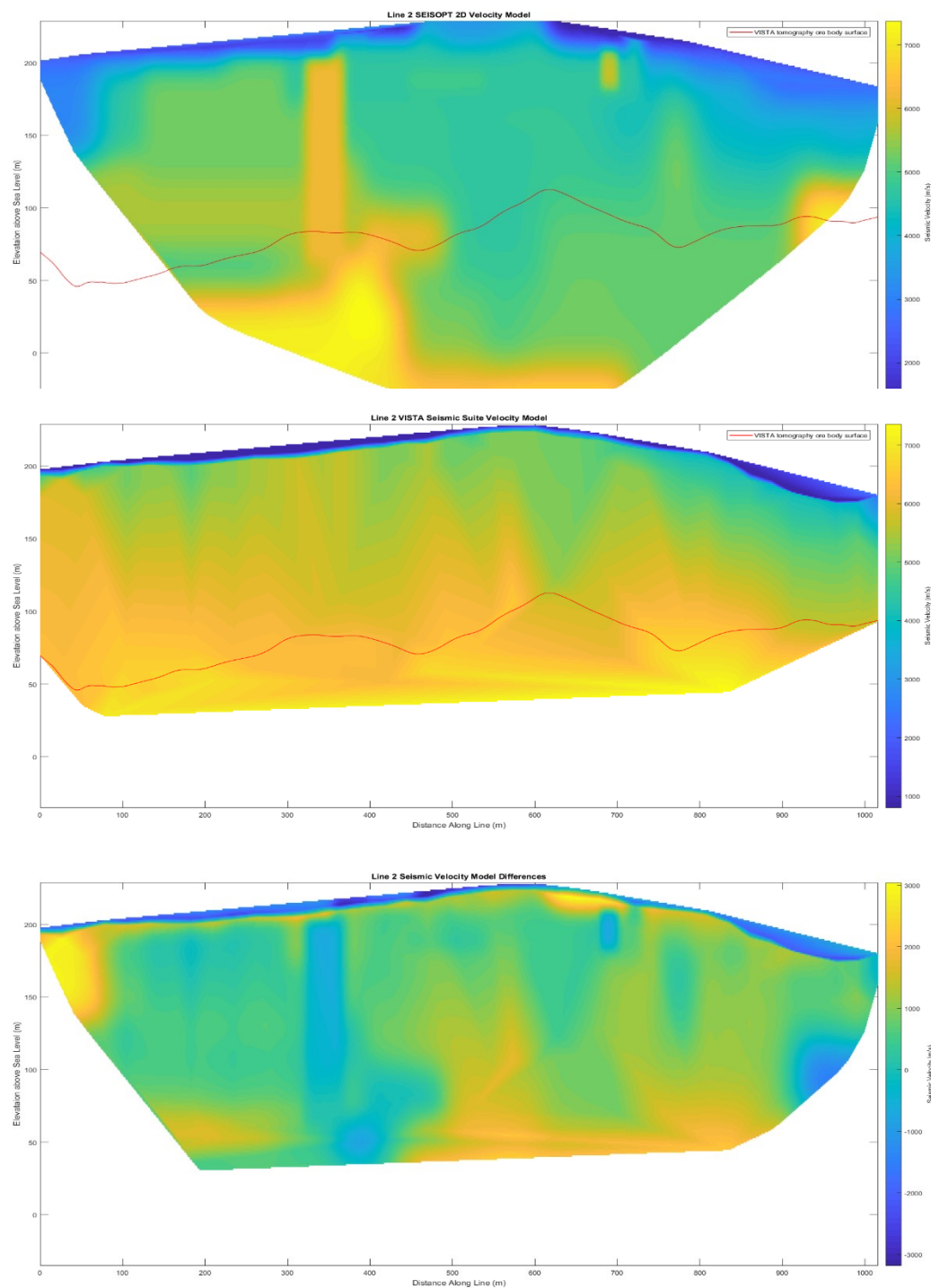


*Figure 7.1: Line 2 Velocity and Tomography Model*

*Top: SEISOPT 2D Velocity model. Red line is ore body topography from VISTA Seismic Suite  
 Middle: VISTA Seismic Suite velocity model with red line for ore body tomography.  
 Bottom: Velocity Difference between models.*

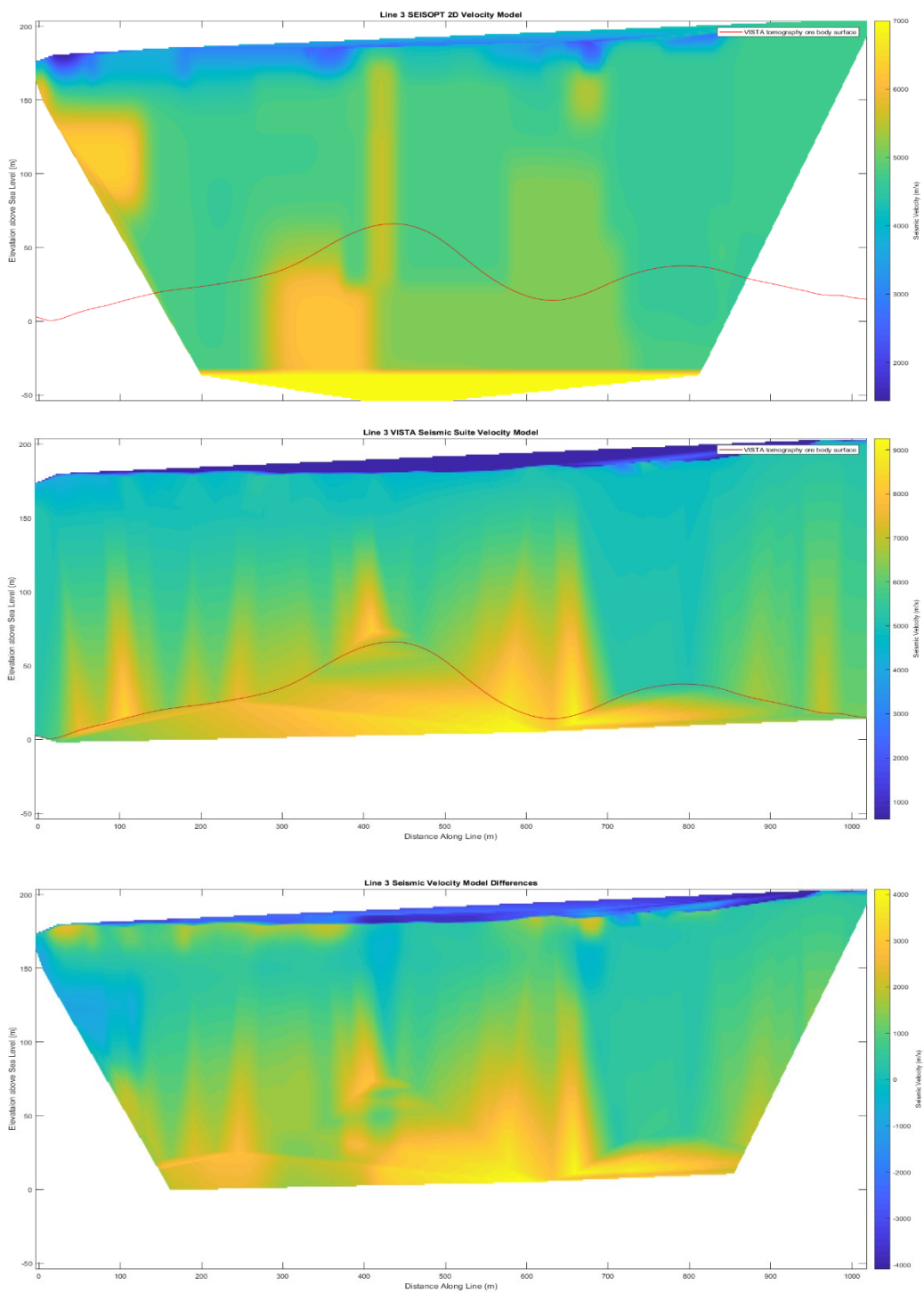


*Figure 7.2: Line 3 Velocity and Tomography Model*

*Top: SEISOPT 2D Velocity model. Red line is ore body tomography from VISTA Seismic Suite*

*Middle: VISTA Seismic Suite velocity model with red line for ore body tomography.*

*Bottom: Velocity Difference between models.*

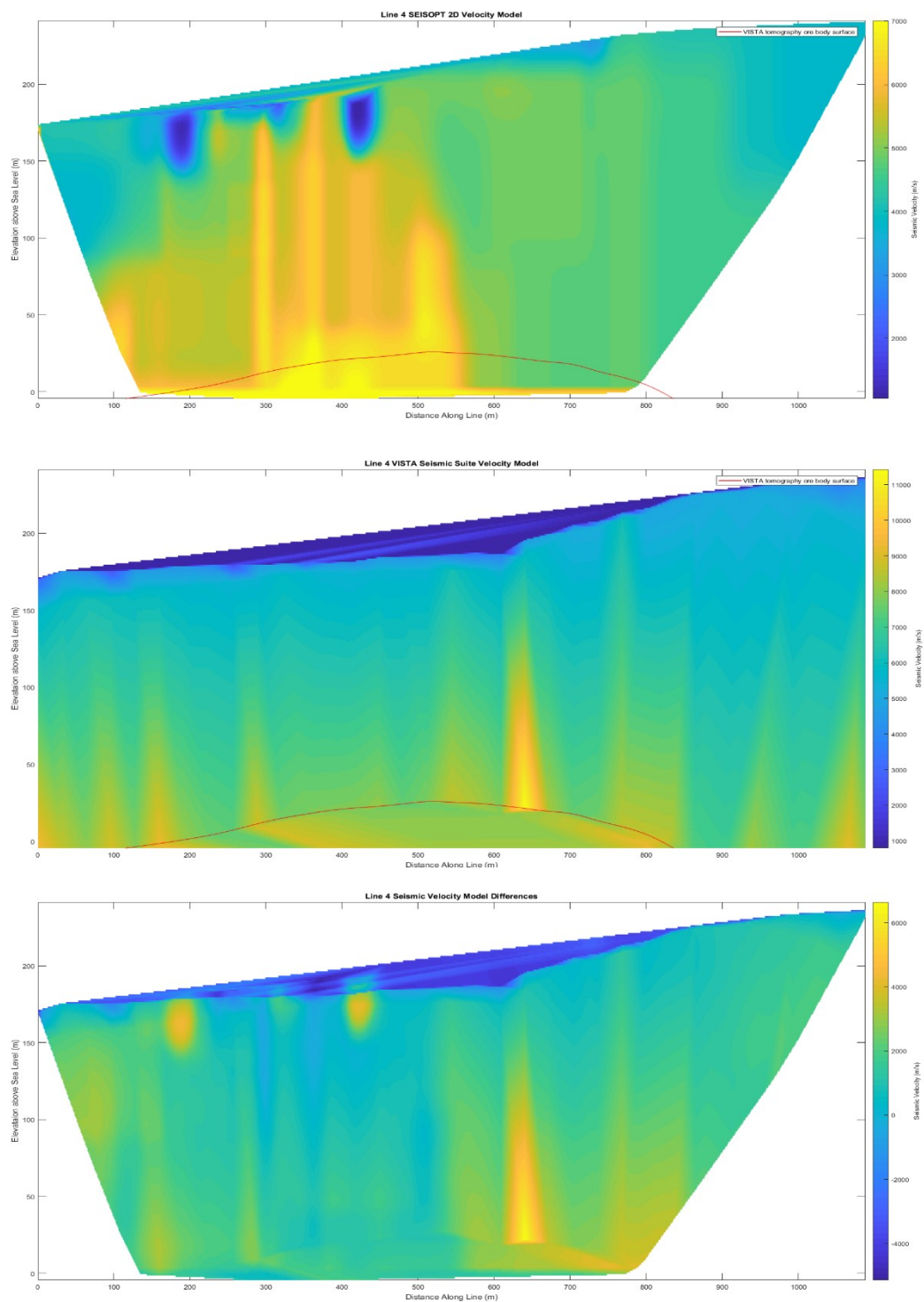


*Figure 7.3: Line 4 Velocity and Tomography Model*

*Top: SEISOPT 2D Velocity model. Red line is ore body tomography from VISTA Seismic Suite  
 Middle: VISTA Seismic Suite velocity model with red line for ore body tomography.  
 Bottom: Velocity Difference between models.*

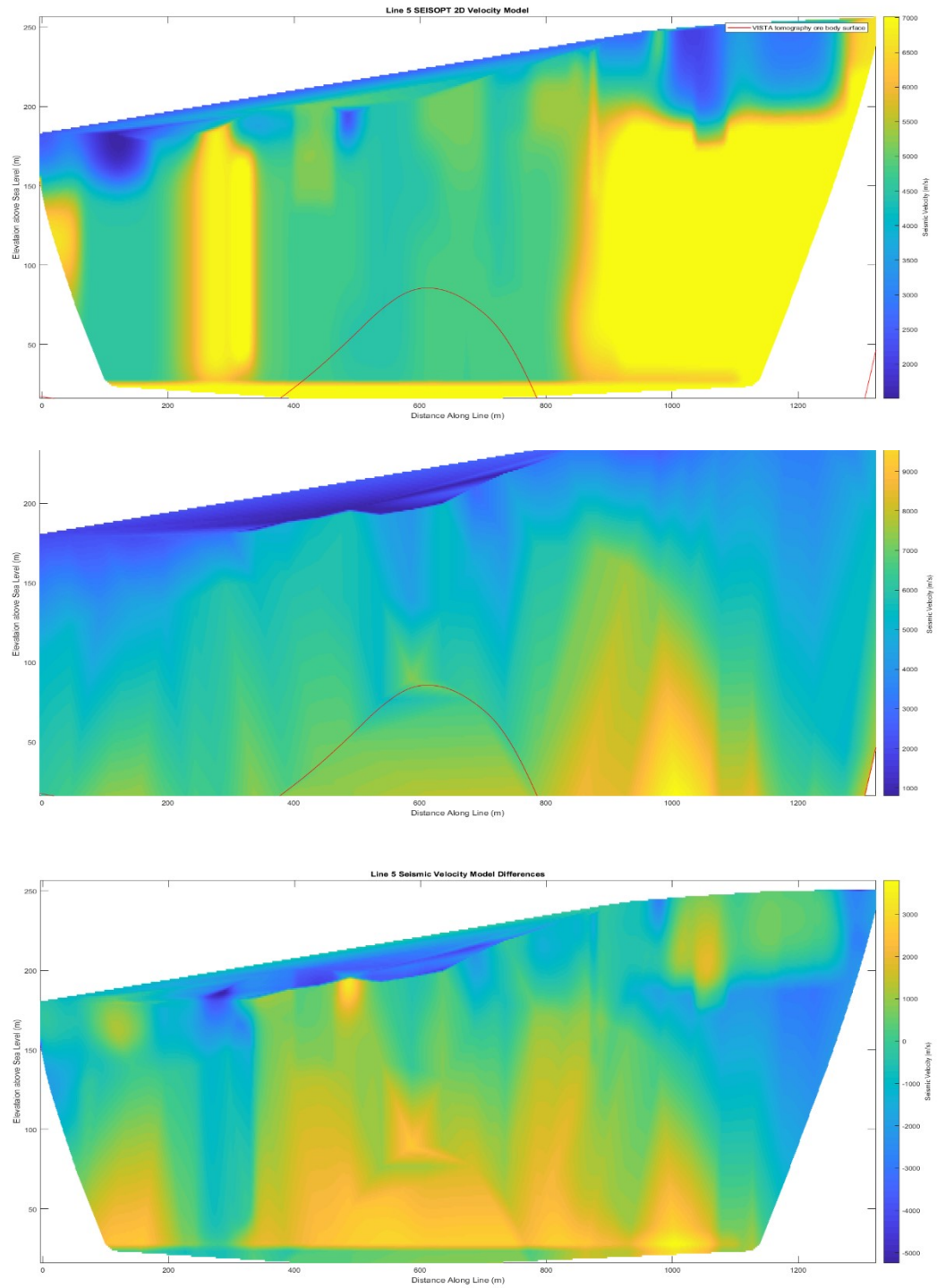


*Figure 7.4: Line 5 Velocity and Tomography Model*

*Top: SEISOPT 2D Velocity model. Red line is ore body tomography from VISTA Seismic Suite*

*Middle: VISTA Seismic Suite velocity model with red line for ore body tomography.*

*Bottom: Velocity Difference between models.*

Crossover points between line 3 with line 4 and lines 2 and 3 with line 5 exhibit small vertical discontinuities and velocity discontinuities. The 100-meter crossover containing the western edge of line 2 and eastern edge of line 3 have a 50-meter vertical discrepancy between the surface of the ore body. This is attributed to edge effects. Moving 100 meters into each model results in the ore surface lining up properly. The perpendicular crossover with line 5 in this region shows a 25-meter discrepancy with line 2 and a 75-meter discrepancy with line 3. This is again attributed to edge effects causing inaccuracies in the deep edges of the refraction tomography. Ray tracing throughout the 2D sections reveals little to no coverage at these depths and offsets. The line 3 and line 4 crossover occurs 100 meters in from the west end of line 3. The depth of the ore surface is consistent between the two lines, and the local velocities match up.

While the absolute velocities between the two models can differ significantly, there does appear to be similarities in the location of the high velocity zones as well as in the points of highest elevation of the calculated ore surface boundary. It is therefore decided that the ore surface boundary calculated from the VISTA refraction analysis is an accurate representation of the surface of the iron ore body. However, given that the ore body is constrained more laterally, a secondary interpretation is that this surface may correspond to the higher velocity greenstone rocks that were seen towards the bottom of the nearby borehole from which the sample was taken.

### **7.3 MAGNETIC MODEL COMPARISON**

A three-dimensional ore body surface was created using a minimum curvature fit between all elevation points of the tomographic layer created in section 7.2 with the resulting map shown in Figure 7.5. All discontinuous crossover points between lines were averaged and a minimum curvature interpolation with 5-meter grid cell size was used. The resulting surface exhibits a rough texture at shot points due to the roughness of the unsmoothed Vista seismic inversion. The surface exhibits a structural high in the east and shallow plunge as the ore body moves westward. Tomography contour lines space out larger northward and show a very steep gradient southward, suggesting the ore body is dipping steeply in this direction.

This surface appears to agree well with the ore body as determined from the inversion of the magnetic anomaly maps. Plotting the seismically derived ore body surface together with the 3D magnetic susceptibility VOXEL model (Figure 7.6) shows a good correspondence between the predicted depths. Setting the threshold for the minimum relative magnetic susceptibility values to 0.3 removes those voxels

associated with the lower susceptibility. This removes the surrounding limestone and overburden and better reveals the shape of the ore body. The high elevations of the ore body as estimated from the seismic refraction correlate well with those predicted from the magnetic inversion. Further, the overall westward plunge and the northward narrowing in shape can be interpreted from both data sets. Close investigation of the high velocity zones in lines 2 and 3 in both the VISTA and SEISOPT refraction models shows a good spatial agreement between the location of the high velocity zones at 300 meters in line 2 with the high magnetic susceptibility zone at 537255 meters easting and 7929120 meters northing and the line 3 high velocity zone located at 350 to 400 meters offset is located directly above the strongest magnetic high of the survey area located at 536660 meters easting and 7928857 meters northing in UTM grid 17N.

#### **7.4 BOUGUER ANOMALY MODEL COMPARISON**

The ore body surface created in section 7.3 was plotted with the 3D Bouguer anomaly density model and can be seen in Figure 7.7. Setting the surrounding limestone body to an average density of  $1.9 \text{ g/cm}^3$ , the minimum relative density for the density model was set to  $0.7 \text{ g/cm}^3$ . The resulting model hosts relative densities of  $0.7 \text{ g/cm}^3$  to  $1.5 \text{ g/cm}^3$  which correspond to approximately  $2.6 \text{ g/cm}^3$  to  $3.4 \text{ g/cm}^3$ . These densities correlate well with the grain density measurements taken for BIF to high grade magnetite in chapter 4. The ore body surface seen above exhibits a strong agreement (in depth and shape) with the density model of the ore body, though not as well as the magnetic susceptibility model. The limited survey region of the gravity survey has resulted in the density model being confined to line 2 and the surrounding area. We see the ore body surface matching the general trend of the density model with tomographic highs located at 537059 m easting and 7928782 m northing and 537292 meters easting and 7928793 meters northing. However, the density model extends above the surface of the ore surface model between these two points by approximately 25 meters. Comparison of the density model with the magnetic susceptibility model shows the density model to be thinner by nearly 50 percent in the north-south direction. A high-density zone of an absolute density of  $3.4 \text{ g/cm}^3$  is located at 537189 m easting and 7928774 m northing. This high-density zone aligns well with the high magnetic susceptibility zone from the magnetic susceptibility model and the high velocity zones at approximately 350 meters offset in both the VISTA and SEISOPT velocity models. It is suspected that the density model is poorly resolved due to a limited grid size and large station spacing. The entire Bouguer anomaly wavelength was likely not captured and could result in a poor inversion of resulting data, pulling higher density zones closer to the surface. In addition, a 25m cell size being used in the inversion coupled with 200-meter station spacing is

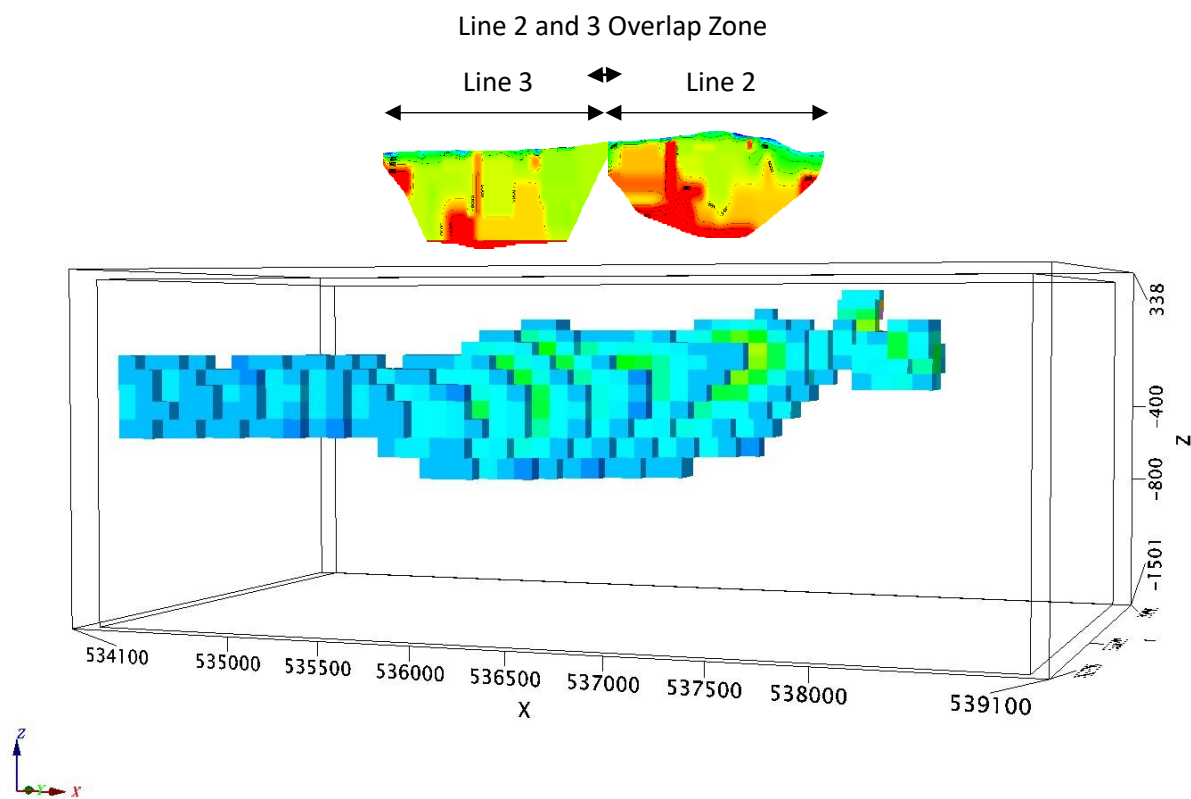


Figure 7.5: SeisOpt 2D seismic sections lined up over magnetic anomaly. *All high velocity zones correspond with stronger magnetic susceptibility zones at similar depths.*

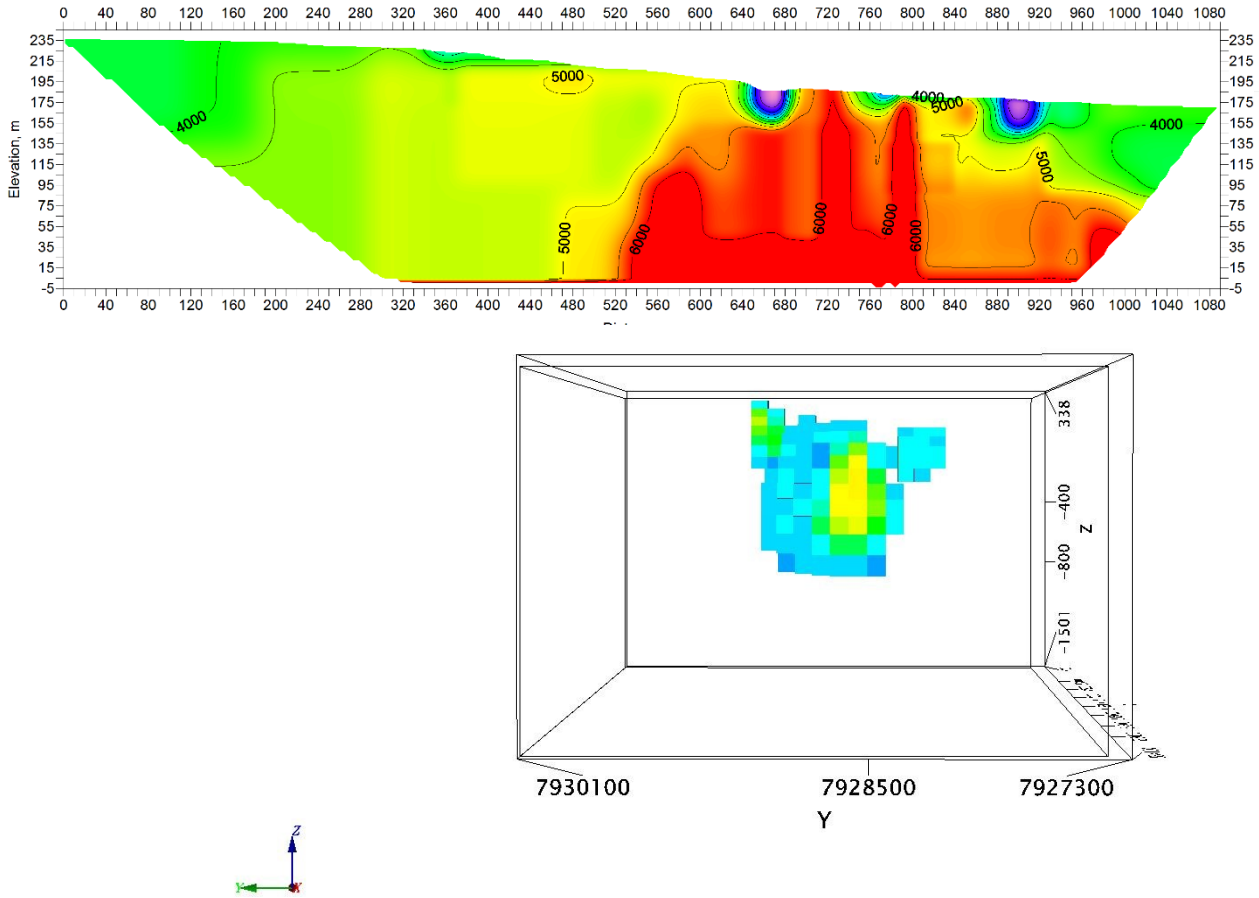


Figure 7.6: SeisOpt 2D seismic line 4 intersecting iron ore body. Magnetic anomaly looking east lined up with north-south seismic section.

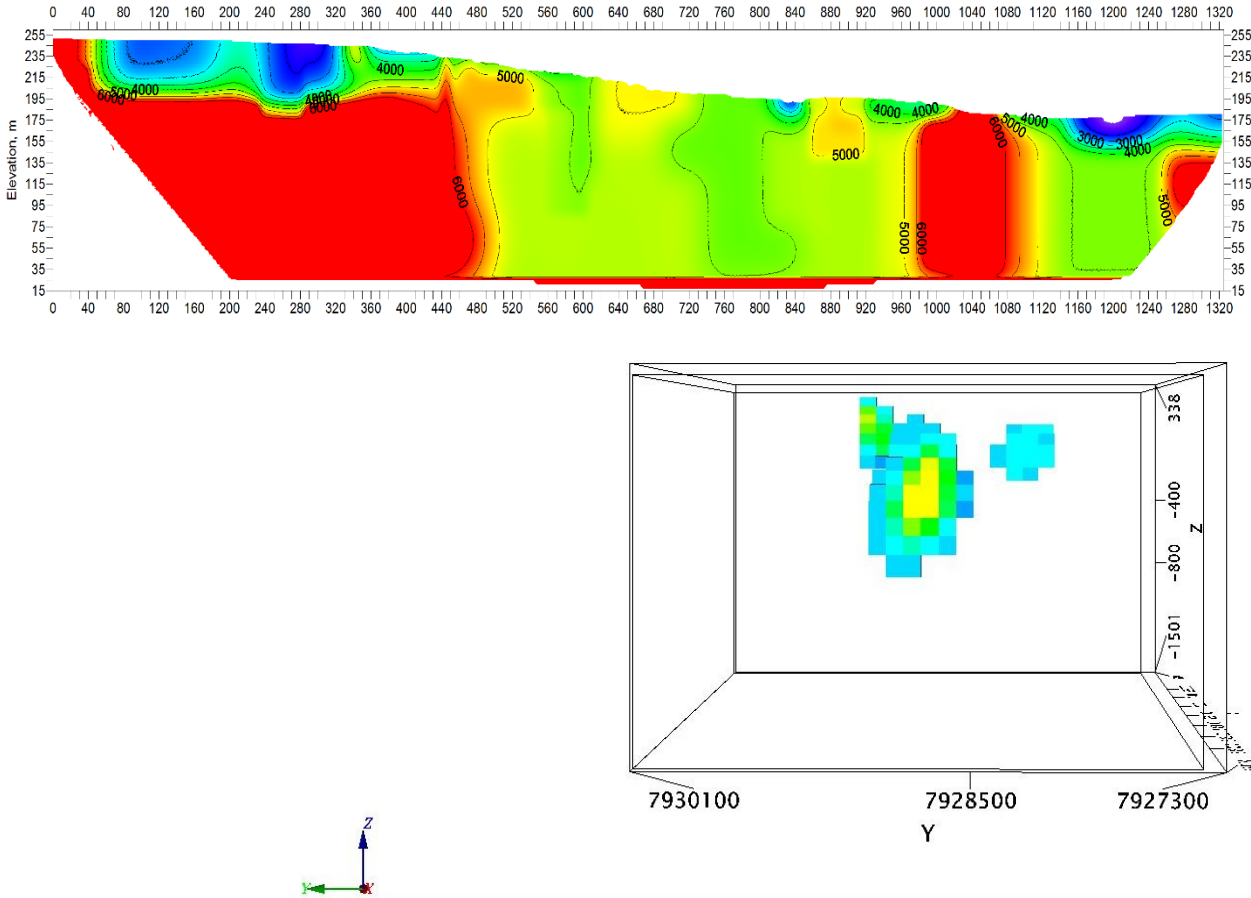


Figure 7.7: SeisOpt 2D seismic line 5 intersecting iron ore body. Magnetic anomaly looking east lined up with north-south seismic section.

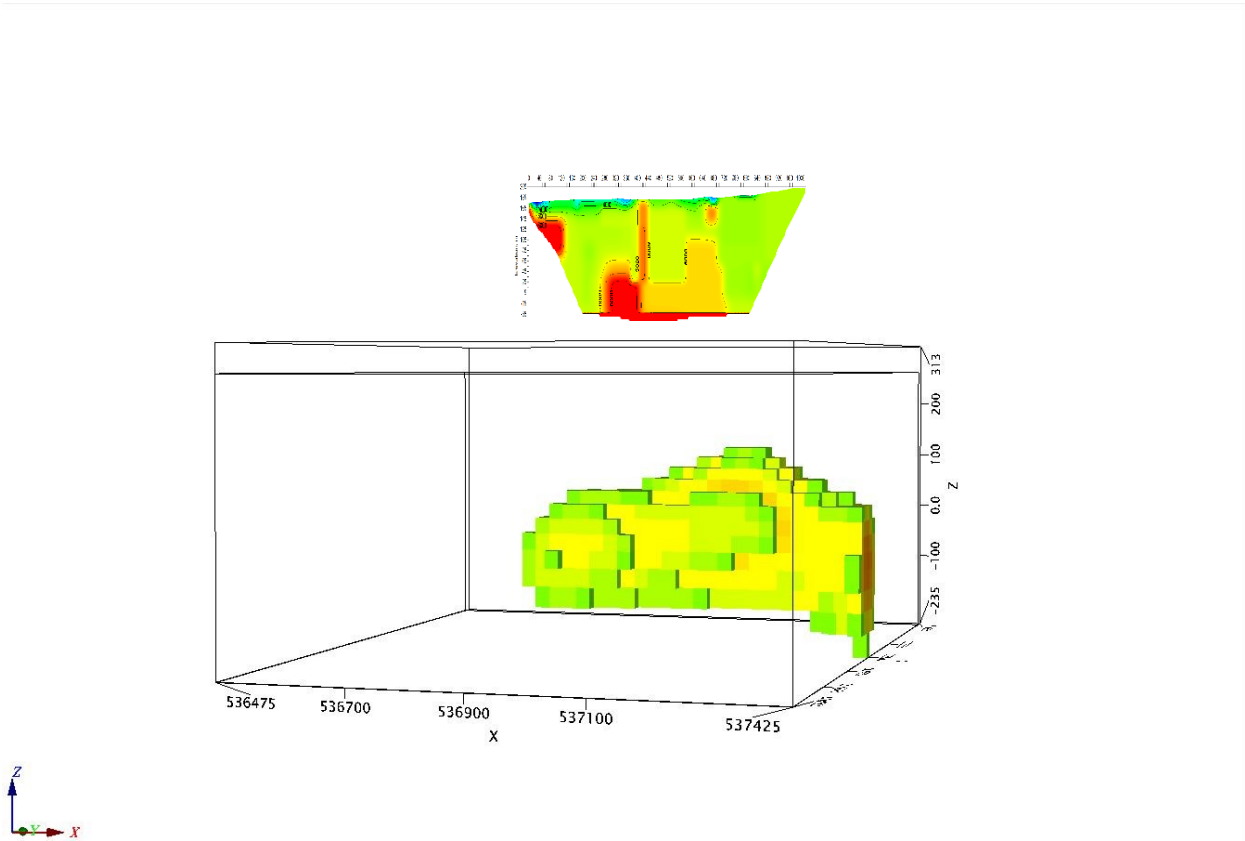


Figure 7.8: SeisOpt 2D seismic line 3 intersecting iron ore body.

likely to introduce artifacts in the inversion. Confidence in the density model is high as the tomographic high points and westward plunge all still agree across all models, it is suspected that a larger survey area with denser station spacing could further resolve the differences between the magnetic susceptibility model and density model.

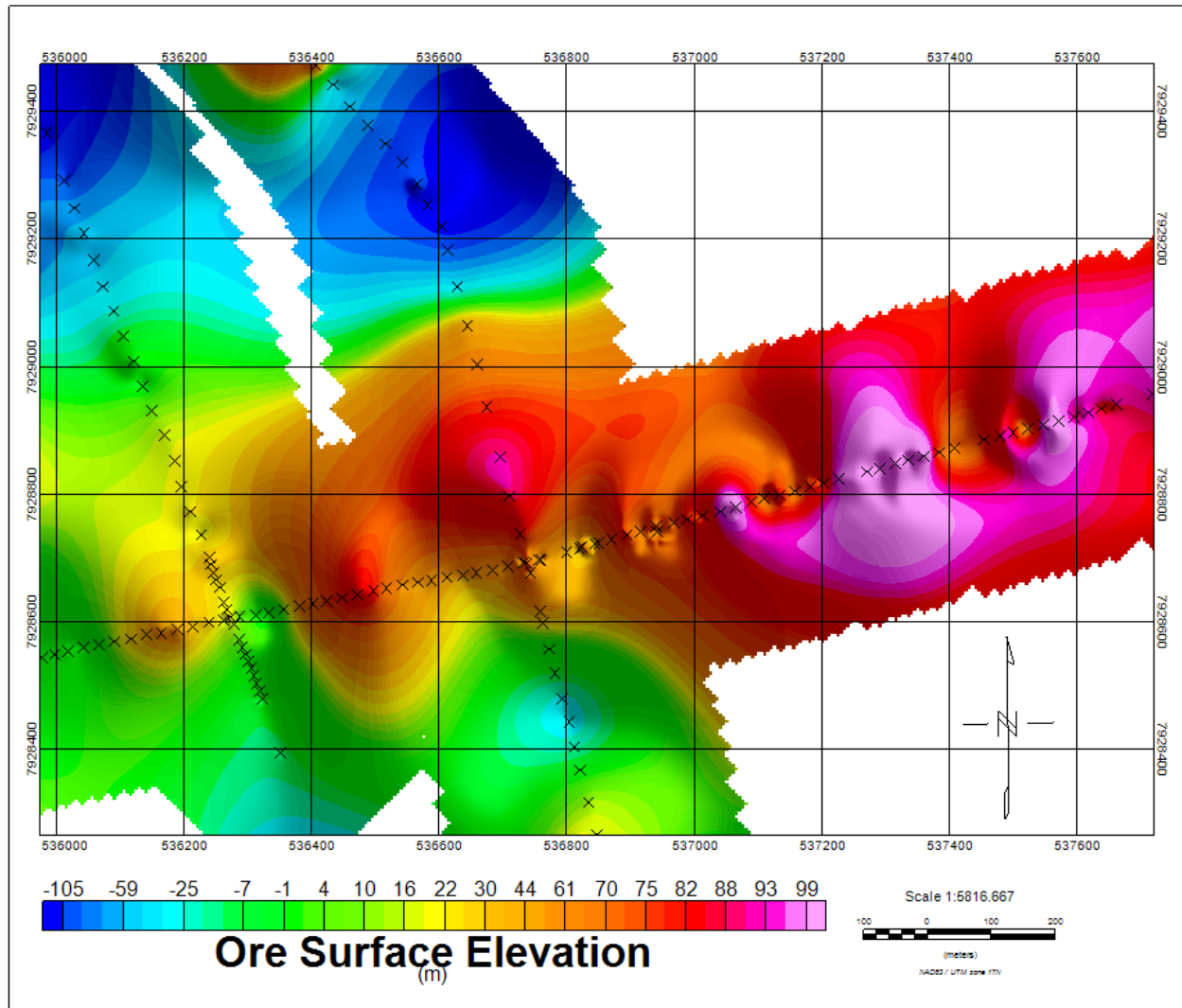


Figure 7.9: Ore surface as estimated using Vista seismic tomography. Surface was created using a minimum curvature fit with a 5-meter grid size. X's mark shot locations for refraction survey.

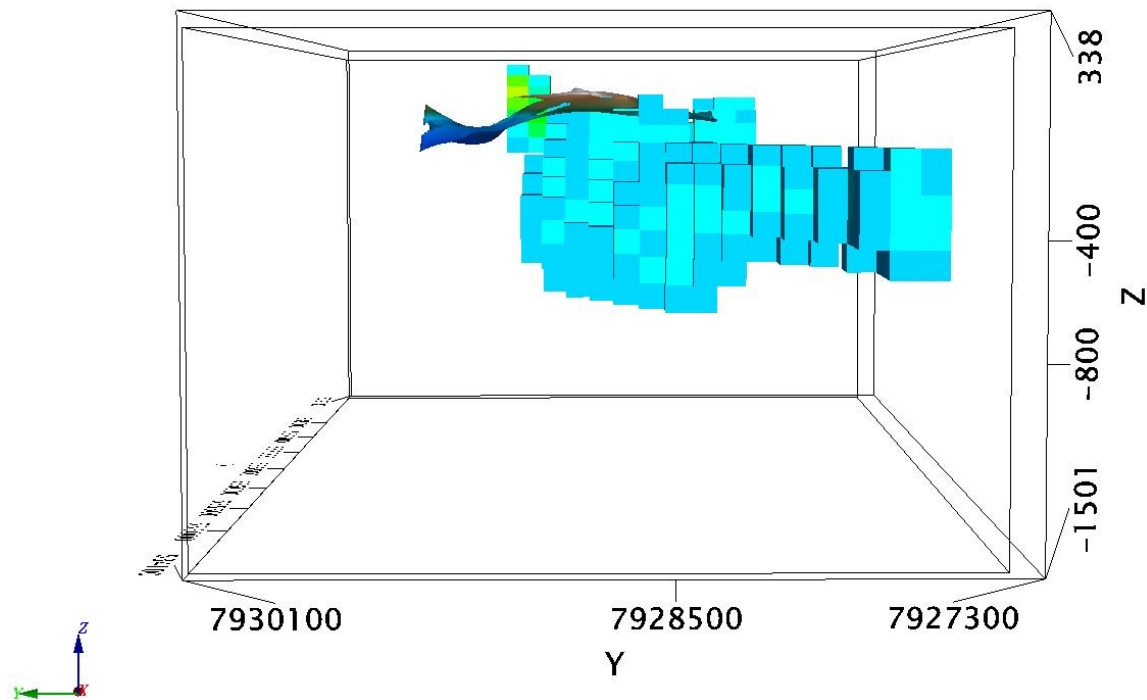
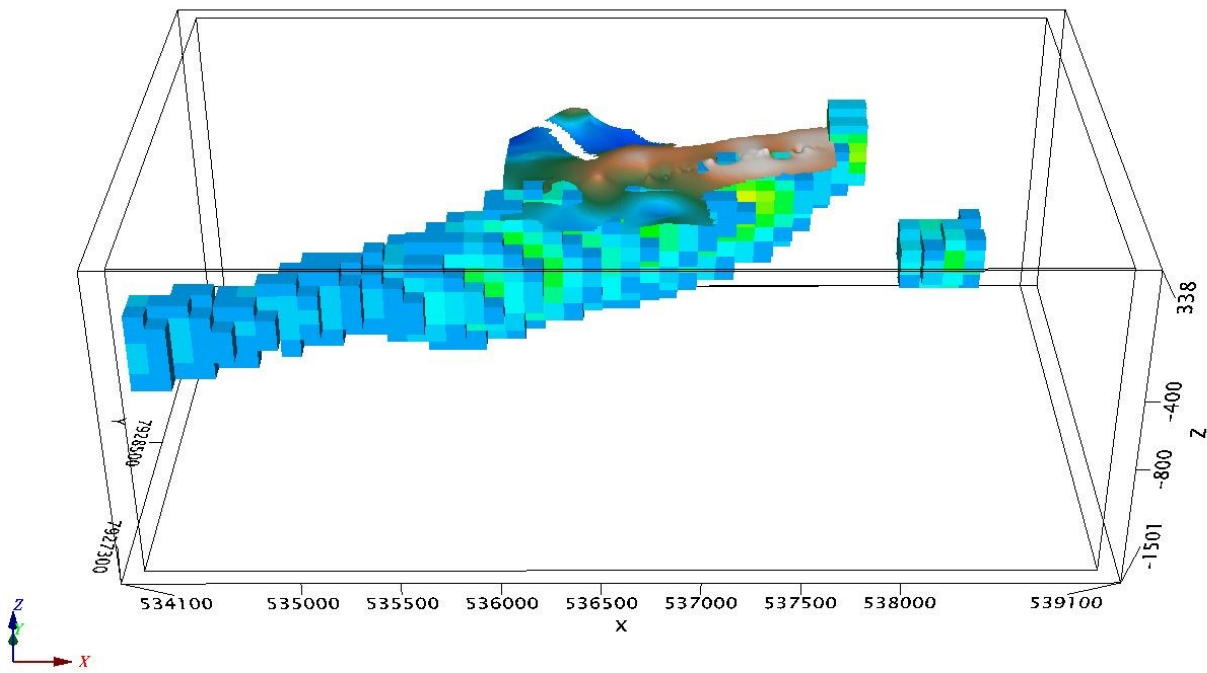


Figure 7.10: Top: Ore body surface overlaying magnetic susceptibility model. View looking directly north and 45 degrees down. The magnetic susceptibility shows a strong agreement with the surface of the ore body.

Bottom: Ore body surface overlaying magnetic susceptibility model. View looking directly east.

## 7.5 FINAL PROPOSED ORE BODY TOMOGRAPHY

The high degree of consistency between all models increases confidence in the results for the McQuat Lake synform site characterization. The final model is an estimation of overburden thickness seen in Figure 7.8. The model proposes a near vertical iron ore body dipping at approximately 70° to the North as determined from the magnetic susceptibility model. The ore body strikes at approximately 257° and plunges at roughly 3° westward. Magnetic susceptibility inversion models estimate the width of the ore body to be 250 meters wide +/- 50 m due to cell size. Vista velocity inversion shows the width of the ore body to be 400 meters to 600 meters wide. The ore body is modelled as being 500 meters thick, however the bottom depth is limited due to the resolution of the inversion and survey area.

Superimposed over the ore body is a limestone layer broken down into two zones a shallow highly fractured zone and a dense high velocity zone. Limestone velocities are within the expected range for limestone recorded by Kohnen (1974) of 1700 m/s to 7000 m/s. It is expected that the typical limestone velocities within this region should have magnitudes of approximately 3000 m/s to 4000 m/s. A deep penetrating permafrost layer has likely increased limestone velocities to 4500 m/s to 5500 m/s as determined by the refraction models. Surfaces for the highly fractured limestone layer and the solid limestone layer can be seen in Figure 7.8. Overtop this layer is a thin surface layer of glacial till.

### 7.5.1 ROCK PHYSICS INCORPORATION AND HIGH-GRADE ZONES

Measurements of velocity show seismic velocities of low grade BIFs to be approximately 5700 m/s. Face value application of Gardner's equation would suggest that increasing iron content would result in an increase in density that would correspond to a large increase in seismic velocity. However, Gardner's equation is not more than an empirical fit to a set of logging data obtained in a sedimentary environment and it ignores the basic physics in the equations describing velocity in terms of the material's elastic moduli and density  $\rho$  which for the compressional wave is:

$$V_P = \sqrt{\frac{K + 4\mu}{\rho}} \quad 7.1$$

where  $K$  and  $\mu$  are the bulk and shear moduli, respectively, and for the shear wave:

$$V_S = \sqrt{\frac{\mu}{\rho}} \quad 7.2$$

These equations clearly show that higher density lowers wave speeds. The reason that empirical curves, such as Gardner's relation show wave speed increasing with density is because often the corresponding moduli also increase. However, this is not necessarily the case with the very high-grade ores where the density term begins to dominate and lowers the wave speeds if the material is porous.

Magnetic susceptibility measurements for BIF samples yielded lower values than expected. Traditional magnetic susceptibility measurements taken on core samples are done after the core has been split presenting a flat face for the measurement device. Due to the limited amount of core available, core plugs could not be split, and as such magnetic susceptibility measurements were highly variable based on mineral contact between the magnetic susceptibility probe and the core sample. The values reported in Chapter 4 represent an average of 5 measurements taken on each core sample.

The laboratory measurements of magnetic susceptibility on the limestones gives very low values and is in good agreement with the inversion results of Fig. 7.6. The magnetic susceptibility of the magnetite sample, however, was a factor of 10 greater than the largest value seen in the inversions. This is perhaps not surprising given that the cell dimensions for the inversion are many 10's of metres and because the inversion process cannot avoid smearing across numerous cells. The combination of the knowledge of physical properties together with the results of the seismic and magnetic inversions suggest that there are two high-grade magnetite zones within the BIF complex. The shallower of the two is centered at 537255 meters easting and 7929120 meters northing and is 210 meters below the surface. It is approximately 100 meters wide +/- 50 meters and it dips north within the ore body but the higher magnetic susceptibility zone dissipates at 350 meters +/- 50 meters below the surface and the refraction lines don't penetrate deep enough to detect the bottom of this local high. The second potential high-grade zone is deeper and located at 536660 meters easting and 7928857 meters northing. It is 200 +/- 50 meters thick meters and 150 +/- 50 meters wide.

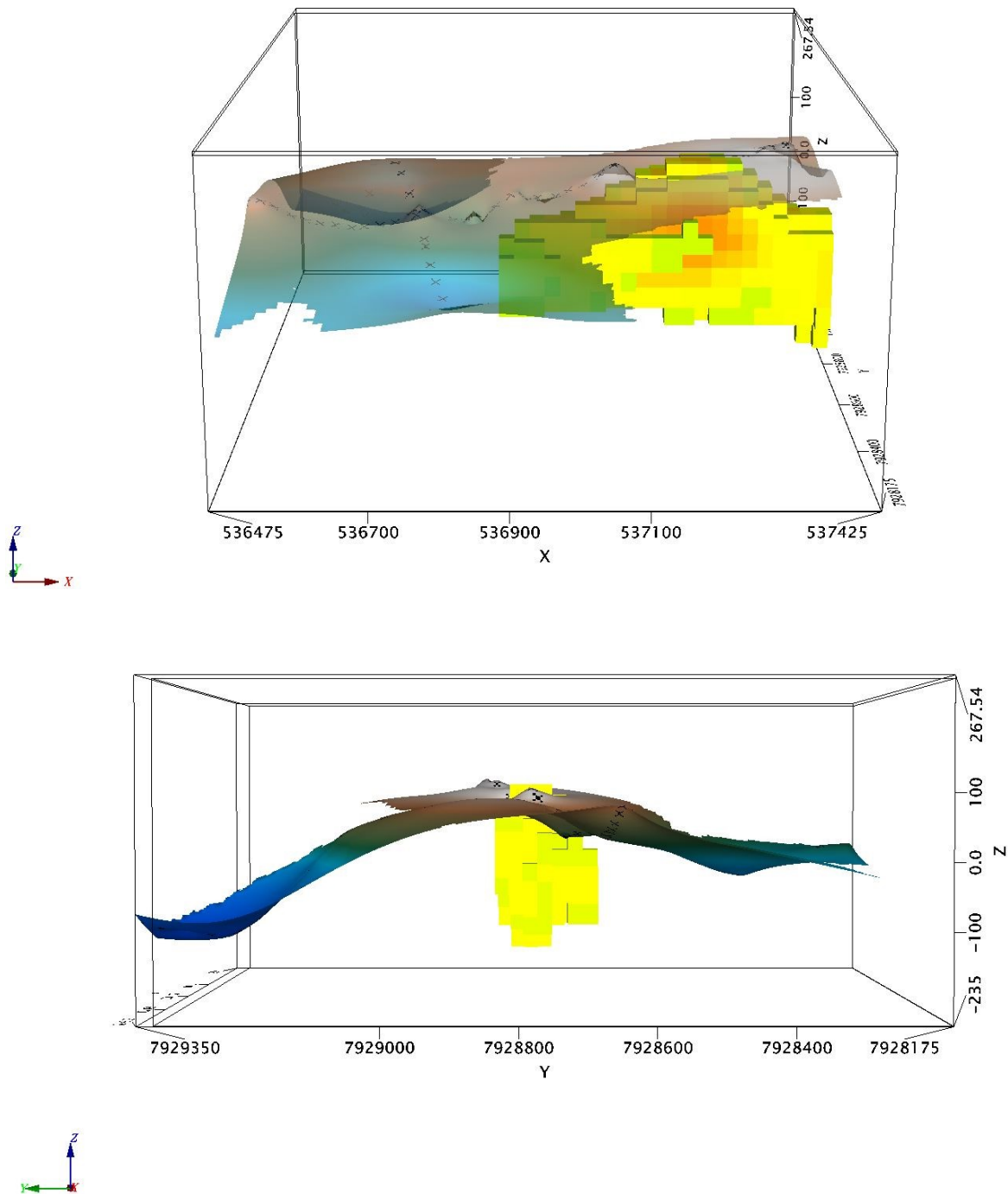


Figure 7.11: Top: Ore body surface overlaying gravity density model. Relative densities are set to 0.7 and greater. View looking directly north and 30 degrees down. Ore body tomographic surface is slightly transparent.

Bottom: Ore body surface overlaying gravity density model. View looking directly east.

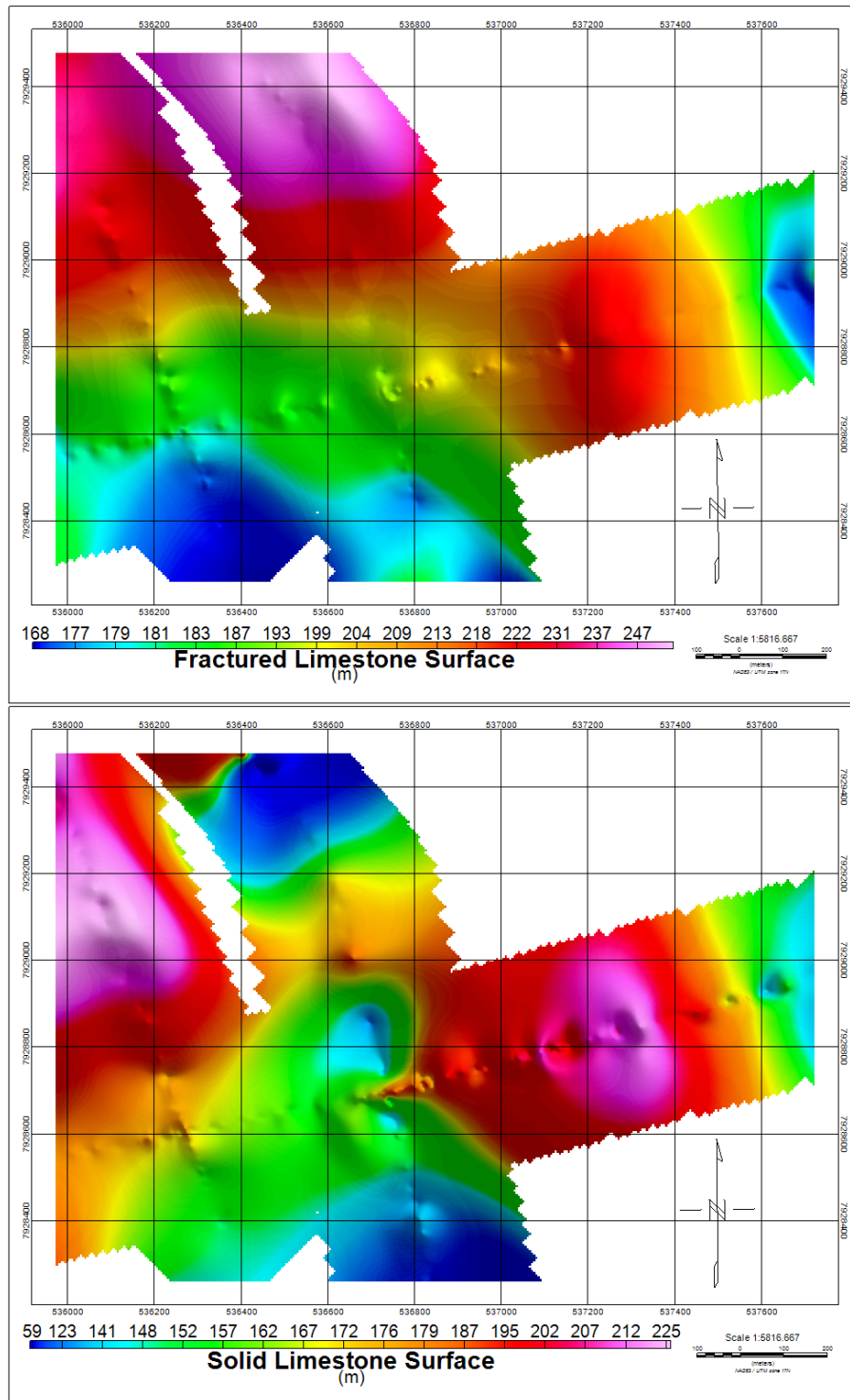


Figure 7.12: VISTA Seismic Suite modelled subterranean surfaces for the fractured frozen limestone layer (top) and the solid limestone layer (bottom).

## 7.6 SUMMARY

The resulting seismic refraction models correlate well with both each other and the magnetic and gravitational inversions. High velocity zones line up spatially in the same areas in both the VISTA™ and SEISOPT 2D™ models. However, the velocity varies between the two models. This effect is likely due to the difference in the methods of inversion, and the two-dimensional smoothing filters applied afterwards. Due to the similarities, we can confidently model the surface of the ore body from VISTA's™ seismic refraction statics analysis. The ore body surface from VISTA™ agrees with both the gravitational and magnetic inversions, mirroring the surface of the ore structure and mirroring both the westward plunge and northward dip. Potential high-grade zones correlate across all three models by highlighting high velocity, high density, and stronger magnetic susceptibility areas.

## **CHAPTER 8 CONCLUSIONS AND FINAL OVERBURDEN MODEL**

### **8.1 INTRODUCTION**

The final proposed site model aims to combine a variety of geophysical exploration methods to characterize potential high-grade zones and overburden thickness to determine feasibility for future mining operations at the McQuat Lake site. The final overburden and 3D site model is presented, and overburden thickness discussed with respect to refraction models. This is followed by a short discussion of applications to methods used in this thesis. Finally, future work required to further the understanding of the seismic properties of iron ore deposits proposed.

### **8.2 SITE CHARACTERIZATION MODEL**

The Mary River Group iron ores and BIFs have been subject to dome and keel tectonics which have resulted in multiple synclines and anticlines over a regional scale. This makes regional and local mapping difficult if no Mary River Group outcrop is visible, and can leave the structure and composition of the mineable shallow subsurface structure largely unknown. Often due to the lack of knowledge of the capabilities of geophysical investigations, traditional exploration programs have often only employed drilling to probe the subsurface. Drill programs, however, are time consuming and expensive and reveal structure at only one location. By combining geophysical surveys with exploration drill programs, the non-uniqueness problem introduced by data inversion can be minimized and exploration targets can be modelled at a fraction of the cost of large scale drill programs.

In this thesis, an airborne magnetic survey, a reconnaissance ground-based gravity survey, and a seismic refraction survey were conducted and analyzed. The inversion results from each of these data sets were compared. While we had hoped to obtain seismic reflections, for a variety of reasons the seismic dataset was very poor and no clear reflections were readily visible. This is in part due to the presence of strong and rapidly propagating surface waves within the permafrost layer; these are a perennial problem for workers collecting seismic data in such environments. First arrivals were chosen and refractions models created from travel times vs. offsets and topography. To increase confidence in the results, different inversion methods were used. Both refraction models tended to agree with each other, although velocities were different by up to 3000 m/s. The seismic velocities from the inversion were generally higher than those obtained in laboratory measurements on what is believed to be similar rock types from a borehole drilled in the vicinity. This may be due to the fact that the laboratory measurements were taken at room temperature and were not in their natural permafrost state where frozen water would

saturate the pore spaces. This would be a particularly strong effect in the porous limestones. Further, the laboratory measurements were carried out at frequencies of  $\sim 1$  MHz far above  $\sim 100$  Hz band of the field seismic data and frequency dispersion may result.

High velocity zones in the resulting velocity inversion models have been interpreted to be high-grade ore bodies. However, the complications due to permafrost together with the results of the laboratory measurements suggest that this may be more complicated, and that further analysis is necessary. That said, however, the high velocity zones in the refraction tomography (see Fig. 7.1 to Fig. 7.4) do appear to overlap with those of high magnetic susceptibility (Figure's 7.6 and 7.7) and as found in their respective

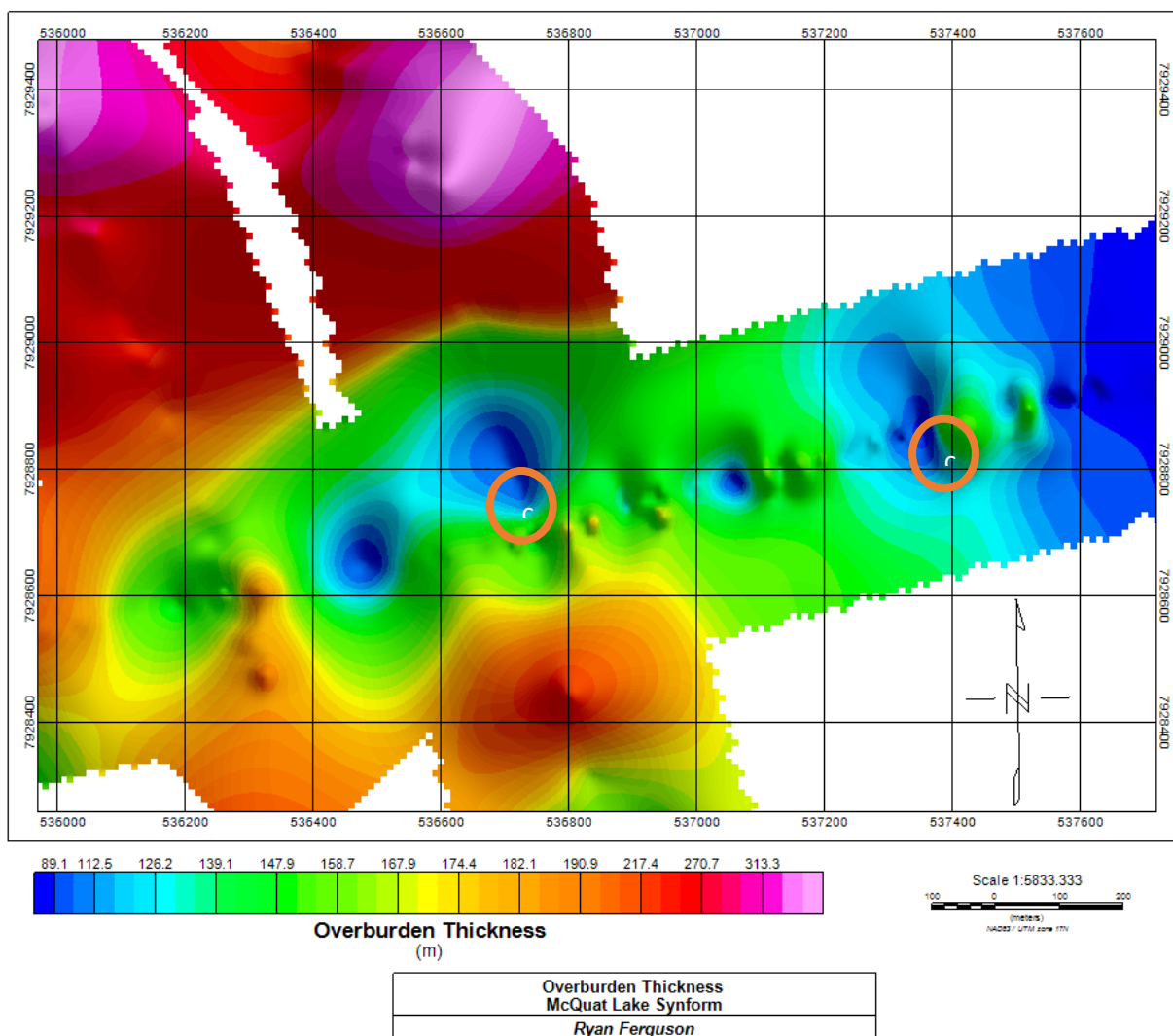


Figure 8.1: Final overburden thickness model. Ore body is shallowest to the west and plunges eastward. Potential high-grade zones are located under the orange markers.

inversions. This lends confidence to the interpretation that the high velocity zones correspond to potentially high-grade ore. All models show strong agreement in overlapping areas, and the ore body surface lines up well between all inversions. Combining these methods, we can confidently map the ore body to be approximately 80 meters below the surface on the east side of the survey zone with an East-West trending strike plunging westward at roughly 3°. It is steeply dipping northward at roughly 70° and has a thickness of 250 meters +/- 50 meters. Velocity, density, and magnetic susceptibility values suggest the majority of the ore body is BIF with an iron content ranging between 10 to 30 wt. percent iron. Two high-grade zones were detected and are suspected to be magnetite with 50 to 60 wt. percent iron.

Our final proposed model can be observed in Figure 7.5 and 8.1 where we model the surface of the ore body and the depth of the overburden. Ore body structure can be viewed in Figure's 7.6 and 7.7. This overburden depth joined with ore body structure can be used to determine future drilling plans, determine economic feasibility, and plan long term overburden logistics for removal and storage.

### **8.3 APPLICATIONS**

This thesis was undertaken to characterize a potential future iron ore deposit, and in this sense the work differs in that it was more focussed on potential development of a mine than on exploration. While there is still room for improvements in the methodology, in the quality and quantity of data acquired, and in the inversions and interpretation, this study does demonstrate that the combined use of a variety of geophysical methods can provide information cost-effectively in advance of more expensive solutions including drilling programs and result in a larger picture of local geology and trends. Employing geophysical surveys in connection with well ties in unconventional environments such as areas with deep permafrost and steeply dipping high velocity zones can still yield fruitful results. Refraction surveys can yield velocity info of the shallow subsurface which in turn can be interpreted to extract rock competency, stratigraphy, and density information for construction, mining, and gas exploration purposes.

### **8.4 FUTURE WORK AND RECOMMENDATIONS**

In many ways much of the work in this study was exploratory. For example, we are not aware of similar refraction seismic surveys carried out in similar permafrost environments. It is the recommendation of the author that further studies into the region be performed to both improve data quality, expand models, and truth existing data. More specific recommendations include:

- A small drilling program should be performed to drill two 400 meter holes at a steep angle from north to south designed to test the interpretations and to, hopefully, intersect the ore body

surface at the high grade zones and penetrate through the high grade zones. Recovered core will allow further understanding into the rock properties of the region.

- Any drilled holes should be logged using a variety of geophysical methods. The logging tools and instruments to do this in an open hole mining environment are highly cost effective and can easily include logs to obtain measures of the magnetic susceptibility, the electrical resistivity, the compressional and shear wave velocity, and the natural radioactivity. Use of radioactive source tools would provide direct measures of mass density (using  $\gamma$ -ray scattering) and hydrogen content (neutron scattering). The latter might provide some indication of ice content in the permafrost regions. Image logging using ultrasonic reflections from the borehole wall could also provide additional information with regards to geologic structures (e.g. fractures, faults) that could affect the development of mines later. The borehole logging, too, should be able to provide direct measures of the thickness of the permafrost. This is easily accomplished by measurements of the in situ electrical conductivity that, in porous, fresh water-saturated materials will be highly resistive.
- Core logging methods may also be of great utility for later analysis. Modern core logging systems used in scientific drilling programs provide continuous measurements of the rock magnetic susceptibility and density reliably, and measures of electrical conductivity and P-wave speeds at room pressure. These data would all assist in determining the depths to different geological levels within the formations and better inform the calculation of appropriate Bouguer gravity corrections.
- Other types of geophysical surveys may also be of interest. Carrying out an 'electrical resistivity tomography' test, for example, would provide additional data on in situ physical properties that may correlate with the seismic, magnetic, and gravity surveys. Such surveys are often used to determine the thickness of the permafrost zone.
- Borehole geophysical logging should then be performed to map permafrost depth and ultrasonic velocity with depth to allow for a well tie, further increasing the accuracy of the refraction models. Finally, an expansion and densification of the existing gravity survey to properly map the full wavelength in all directions of the Bouguer Anomaly.
- Future shallow seismic work done in the region should proceed with less energetic surface sources. 2 lb booster charges resulted in the trapping of all excess energy in the surface permafrost layer creating overpowering surface waves. A modern buffalo gun firing 12 gauge blanks and stacking 3 to 4 gathers per shot point may result in more reliable triggering (and hence

timing) allowing for more easily processed data for seismic exploration targets less than 1km depth. Other seismic sources, such as seismic vibrators, may work but this could be complicated by the highly variable near surface conditions. Such sources may not be feasible where the surface is quite soft due to the extrusion of sands during freeze-thaw cycles, this surface is even difficult to walk on and large seismic sources would undoubtedly result in some environmental damage unless the work was carried out during periods when the ground was fully frozen.

## REFERENCES

- Baffinland Iron Mines Corp. (BIM). 2009. Web. Accessed June 10, 2017. <http://www.baffinland.com>
- Barley, M.E., Pickard, A.L., Hagemann, S.G., and Folkert, S.L. 1999. Hydrothermal origin for the 2 billion old Mount Tom Price giant iron ore deposit, Hamersley Province, Western Australia. *Mineralium Deposita*, v. 34, p. 784-789
- Berman, R.G., Sanborn-Barrie, M., Stern, R.A., and Carson, C.J. 2005. Tectonometamorphism at ca. 2.35 and 1.85 Ga in the Rae Domain, Western Churchill Province, Nunavut, Canada: Insights from structural, metamorphic and in situ geochronological analysis of the Southwestern Committee Bay Belt. *The Canadian Mineralogist*, v. 43, p. 409-442
- Bethune, K.M. and Scammell, R.J. 2003a. Geology, geochronology, and geochemistry of Archean rocks in the Ege Bay area, north-central Baffin Island, Canada: constraints on the depositional and tectonic history of the Mary River Group of northeastern Rae Province. *Canadian Journal of Earth Sciences*, v. 40, p. 1137-1167
- Bethune, K.M. and Scammell, R.J. (2003b). Distinguishing between Archean and Paleoproterozoic tectonism, and evolution of the Isortoq fault zone, Ege Bay area, north-central Baffin Island, Canada. *Canadian Journal of Earth Sciences*, v. 40, p. 1111-1135
- Beukes, N.J., Gutzmer, J., and Mukhopadhyay, J. 2002. The geology and genesis of high grade hematite iron ore deposits. *Australian Institute of Mining and Metallurgy Publication Series 7/2002*, p. 23-29
- Beukes, N.J., Gutzmer, J., and Mukhopadhyay, J. 2003. The geology and genesis of high grade hematite iron ore deposits. *Transactions of the Institution of Mining and Metallurgy*, v. 112, p. B18-B25
- Blais, R.A. 1964. Geological Report on the Baffinland Iron Deposits, Mary River Area, N.W.T. Internal report prepared for Baffinland Iron Mines Ltd. University of Montreal
- Boustani B., Torabi S., Javaherian A., Mortazavi S.A., 2013. Ground roll attenuation using a curvelet-SVD filter: a case study from the west of Iran. *Journal of Geophysics and Engineering*. Vol. 10, 10 p.
- Carcione J.M., Seriani G., 1998. Seismic and ultrasonic velocities in permafrost. *Geophysical Prospecting*, Vol. 46, p. 441 - 454
- Cassinis R., Borgonovi L., 1966. Significance and Implications of Shingling in Refraction Records. *Geophysical Prospecting*, Vol. 14, Issue 4, p. 547-568
- Cholach P.Y., Molyneux J.B., Schmitt D.R., 2005. Flin Flon belw seismic anisotropy: Elastic symmetry, heterogeneity and shear wave splitting. *Canadian Journal of Earth Sciences*, Vol. 42, p.533-544
- Cloud, P. 1983. Banded iron-formation – a gradualist’s dilemma. In: *Iron Formation: Facts and Problems*, (eds.) Trendall, A.F., and Morris, R.C. *Developments in Precambrian Geology* 6. p. 401-416
- Clout, J.M.F. and Simonson, B.M. 2005. Precambrian iron formation and iron formation hosted iron ore deposits. *Economic Geology*, v. 100, p. 643-679

- Crawford, W.J. 1973. Metamorphic iron formations of Ege Bay and adjacent parts of Northern Baffin Island. Ph.D thesis, University of Washington, 101 p.
- Dufour J. and Foltinek D.S., 1996. The Plus-Minus time analysis method and its implementation. CREWES Research Report, Vol. 8, Sec, 13.
- Ellis R.G., De Wet B., MacLeod I.N., 2012. Inversion of Magnetic Data from Remanent and Induced Sources. 22<sup>nd</sup> International Geophysical Conference and Exhibition. 26<sup>th</sup> – 29<sup>th</sup> Feb. 2012, Brisbane Australia
- Findlay, D. 1994. Diagenetic boudinage, an analogue model for the control on hematite enrichment iron ores of the Hamersley iron province of Western Australia, and a comparison with Krivoi Rog of Ukraine, and Nimba Range, Liberia. *Ore Geology Reviews*, v. 9, p. 311-324
- Fournier D. (2015). A cooperative magnetic inversion method with Lp-norm regularization (T). University of British Columbia. Retrieved from <https://open.library.ubc.ca/cIRcle/collections/24/items/1.0166794>
- Fulcher, S. 2011. Geological context and character of the schist unit at Deposit No. 4, Mary River iron ore deposit, Baffin Island, Nunavut. Unpublished B.Sc thesis, University of Ottawa, 72 p.
- Gardner G.H.F., Gardner L.W., 1974. Formation velocity and density – the diagnostic basics for stratigraphic traps. *Geophysics*, Vol. 39, p. 770-780
- MyGeosoft Support Center. Web. Accessed July 2017.  
<https://my.geosoft.com/elearning/lessons/#/video/461>
- Gole, M.J., and Klein, C. 1981. Banded iron-formations though much of Precambrian time. *Journal of Geology*, v. 89, p. 169-183
- Gross, G.A. (1965). *Geology of Iron Deposits in Canada. I. General Geology and evaluation of iron deposits.* Geological Survey of Canada, Economic Geology Report 22, vol. 1, 181p.
- Gross, G.A. (1980). A Classification of iron formations based on depositional environments. *Canadian Mineralogist*, vol. 18, p. 215-222
- Hagemann, S.G., Barley, M.E., Folkert, S.L., Yardley, B.W., and Banks, D.A. 1999. A hydrothermal origin for the giant Tom Price iron ore deposit. In: *Mineral deposits: Processes to processing*, (eds.) Stanley, C.J., et al. Rotterdam, A.A. Balkema, p. 41-44
- Hearmon R.F.S., 1984. The elastic constants of crystals and other anisotropic materials in, in *Landolt Bornstein Tables, III/11 pp. 1-244*, edited by K.H. Hellwege and A.M. Hellwege, Springer-Verlag, Berlin, 854 pp.
- Henderson, J.R., Jackson, G.D., and Morgan, W.C. 1980. The Cumberland Sound metamorphic culmination: a major tectonic element of the Hudsonian orogen in northeast Canada and West Greenland. *Geological Association of Canada – Mineral Association of Canada, Program of Abstracts*, vol. 5, 59 p.

- Heywood, W.W. 1967. Geological notes, northeastern District of Keewatin and southern Melville Peninsula, District of Franklin, Northwest Territories (parts of 46, 47, 56, 57). Geological Survey of Canada Paper 66-40, 20 p.
- Hoffman, P.F. 1988. United plates of America, the birth of a craton: Early Proterozoic assembly and growth of Laurentia. *Annual Reviews of Earth and Planetary Science*, vol. 16, p. 543-603
- Hoffman, P.F. 1990a. Subdivision of the Churchill Province and extent of the Trans- Hudson orogen. In: *The Early Proterozoic Trans-Hudson orogen of North America*, (eds.) J.F. Lewry and M.R. Stauffer. Geological Association of Canada Special Paper, vol. 37, p. 15-39
- Hoffman, P.F. 1990b. Dynamics of the tectonic assembly of northeast Laurentia in geon 18 (1.9-1.8 Ga). *Geoscience Canada*, vol. 17, p. 222-226
- Ilya Inozemtsev, "Land-Based Vector Magnetic Survey of a BIF-Hosted Iron Ore Depository, Mary River, Baffin Island, Nunavut" (2015). McMaster University Dissertations and Theses Communities. Paper 11375/17212
- Ivansson S., 1983. Remark on an earlier proposed iterative tomographic algorithm. *Geophysical Journal International*, Vol. 75, Issue 3, p. 855-860
- Jackson, G.D. 1965. Geology of NTS map sheets 37G/5 and 37G/6, 1:50,000 scale. Geological Survey of Canada (unpublished geology maps)
- Jackson, G.D. 1966. Geology and mineral possibilities of the Mary River Region, Northern Baffin Island. *Canadian Mining Journal*, v. 87, 6, pg. 57-61
- Jackson, G.D. 1969. Reconnaissance of north-central Baffin Island. Geological Survey of Canada, Paper 69-1, Part A
- Jackson, G.D. and Taylor, F.C. 1972. Correlation of major Archean rock units in the northeastern Canadian Shield. *Canadian Journal of Earth Sciences*, vol. 9, p. 1650- 1669
- Jackson, G.D., Frisch, T., Hegner, E., and Hunt, P.A. 1990a. U-Pb geochronology, Nd model ages and tectonics of the eastern Arctic Canadian Shield. Geological Survey of Canada, Current Activities Forum, 12
- Jackson, G.D., Hunt, P.A., Loveridge, W.D., and Parrish, R.R. 1990b. Reconnaissance geochronology of Baffin Island, N.W.T. In: *Radiogenic Age and Isotopic Studies: Report 3*, Geological Survey of Canada, Paper 89-2, p. 123-148
- Jackson, G.D. and Berman, R.G. (2000). Precambrian metamorphic and tectonic evolution of northern Baffin Island, Nunavut, Canada. *The Canadian Mineralogist*, v. 38, p. 399-421
- James, H.L. 1954. Sedimentary facies of iron-formations. *Economic Geology*, v. 49, p. 235-293
- Johns, S.M. and Young, M.D. 2006. Bedrock geology and economic potential of the Archean Mary River group, northern Baffin Island, Nunavut. Geological Survey of Canada, Current Research 2006-C5, 13 p.

King, F.H., 1989. The rocks speak. Australian Institute of Mining and Metallurgy Monograph, v. 15, 316 p.

King M.S., Zimmerman R.W., Corwin R.F., 1988. Seismic and Electrical Properties of Unconsolidated Permafrost. Geophysical Prospecting, Vol. 36, p. 349 - 364

Klein, C. 2005. Some Precambrian banded iron-formations (BIFs) from around the world: Their age, geologic setting, mineralogy, metamorphism, geochemistry, and origin. American Mineralogist, vol. 90, p. 1473-1499

Lanz E., Maurer H., Green A.G., 1998. Refraction tomography over a buried waste disposal site. Geophysics, Vol. 63, No. 4, p. 1414-1433

Lascelles, D. 2002. A new look at old rocks – an alternative model for the origin of in situ iron ore deposits derived from banded iron-formation. Australasian Institute of Mining and Metallurgy Publication Series 7/2002, p. 107-126

Lascelles, D.F. 2007. Black smokers and density currents: A uniformitarian model for the genesis of banded iron-formations. Ore Geology Reviews, v. 32, p. 381-411

Lascelles, D.F. 2008. Banded Iron Formation to High-Grade Iron Ore – The Fallacy of Supergene Enrichment. Pacrim Conference, Queensland.

Liebermann R.C., Schreiber E., 1968. Elastic Constants of Polycrystalline Hematite as a Function of Pressure to 3 Kilobars. Journal of Geophysical Research, Vol. 73, Issue 20, p. 2156 – 2202

Lillie R.J., "Chapter 4: Seismic Refraction Interpretation." Whole Earth Geophysics: an Introductory Textbook for Geologists and Geophysicists, Prentice Hall, 1999

Li Y., Oldenburg D.W., 1996. 3-D Inversion of magnetic Data. Geophysics, Vol. 61, Issue 2, p. 394-408

Li Y., Oldenburg D.W., 1998. 3-D Inversion of gravity Data. Geophysics, Vol. 63, Issue 1, p. 109-119

Li X., Gotze H.J., 2001. Tutorial: Ellipsoid, geoid, gravity, geodesy and geophysics. Geophysics, Vol. 66, No. 6, p. 1660-1668

Li, Z.X., Powell, C.M., and Bowman, R. 1993. Timing and Genesis of Hamersley ironore deposits. Exploration Geophysics, v. 24, p. 631-636

Lobato, L.M., Figueiredo e Silva, R.C., Hagemann, S., Thorne, W., and Zuchetti, M. 2008. Hypogene alteration associated with high-grade banded iron formation. Reviews in Economic Geology, v. 15, p. 107-128

MacLeod I.N., Ellis R., 2013. Magnetic Vector Inversion, a simple approach to the challenge of varying direction of rock magnetization. 23<sup>rd</sup> International Geophysics Conference and Exhibition, 11<sup>th</sup> – 14<sup>th</sup> August, 2013, Melbourne Australia

MacLeod, M.E. 2009. Manganese and Phosphorous Enrichment in Baffinland Iron Mines Corp. Deposit No. 1, Mary River Iron Formation, Northern Baffin Island, Nunavut. Unpublished B.Sc thesis, University of Western Ontario, 52 p.

- MacLeod, M.E. and Duke, N.A. 2009a. Geology of IOL PI-17, 1:50,000 scale. Nunavut Tunngavik Inc.
- MacLeod, M.E. and Duke, N.A. 2009b. Field Report: Economic Potential of IOL PI-17. Nunavut Tunngavik Inc.
- MacLeod, M.E. 2010. Geology of Deposits 4-5, Mary River, Nunavut, 1:20,000 scale. Baffinland Iron Mines Corp.
- MacLeod, Meghan E., "Metallogenic Setting of High-Grade Iron Ores, Mary River District, North Baffin Island, Nunavut" (2012). *Electronic Thesis and Dissertation Repository*. Paper 542.
- MacLeod, W.N. 1966. The Geology and iron deposits of the Hamersley Range area. Geological Survey of Western Australia Bulletin, Perth, 170 p.
- Marshak, S., Tinkham, D., Alkmim, F., Brueckner, H., and Bornhorst, T. 1997. Domeand-keel provinces formed during Paleoproterozoic orogenic collapse – core complexes, diapirs, or neither?: Examples from the Quadrilatero Ferrifero and the Penokean orogen. *Geology*, v. 25, no. 5, p. 415-418
- Mathiassen, T. 1933. Contributions of the Geography of Baffin Land and Melville Peninsula, Vol. 1 No. 3 of Report of the fifth Thule Expedition 1921-24. Copenhagen. 101 p.
- Maurer H., Hauck C., 2007. Instruments and Methods: Geophysical Imaging of Alpine Rock Glaciers. *Journal of Glaciology*, Vol. 53, No. 180, p. 110 – 120
- McClymont A.F., Hayashi M., Bentley L.R., Christensen B.S., 2013. Geophysical imaging and thermal modelling of subsurface morphology and thaw evolution of discontinuous permafrost. *Journal of Geophysical Research: Earth Surface*, Vol. 118, p. 1826 - 1837
- Millsom J., 2003. "Field Geophysics," 3<sup>rd</sup> edition, John Wiley and Sons Ltd, Chichester, UK.
- Molyneux J., Schmitt D.R., 2000. Compressional wave velocities in attenuating media: A laboratory physical modelling study. *Geophysics*, Vol. 64 p. 1162-1167
- Morris B., Hernan U., 2007. Magnetic Remanence constraints on magnetic inversion models. *The Meter Reader: The Leading Edge*, August 2007, p. 960-964
- Morris, R.C. 1985. Genesis of iron ore in banded iron-formation by supergene and supergene-metamorphic processes – a conceptual model. In: *Handbook of stratabound and stratiform ore deposits*, (ed.) K.H. Wolf, Amsterdam, Elsevier, p. 73-235
- Nicpon, B. 2011. Chlorite Schist in the Footwall of High Grade Iron Ore Hosted within the Mary River Group, Northern Baffin Island. Unpublished B.Sc thesis, University of Western Ontario, 52 p.
- Nourse, J.E. 1879. Narrative of the second Arctic expedition made by Charles F. Hall: his voyage to Repulse Bay, sledge journeys to the Straits of Fury and Hela and the King William's Land, and residence among the Eskimos during the years 1864-'69.
- Ong, O.N., D.R. Schmitt, R.S. Kofman, and K. Haug, 2016. Static and Dynamic Pressure Sensitivity Anisotropy of a Calcareous Shale, *Geophysical Prospecting*, Vol. 64, p. 875-897,

Optim, 2005 (SeisOpt@2d Ver. 4.0), Seismic Refraction Tomography software, *copyright* Optim, Inc., University of Nevada, Reno, Nevada.

Palmer D., 1981. An introduction to the generalized reciprocal method of seismic refraction interpretation. *Geophysics*, Vol. 46, No. 11, p. 1508-1518

Parasnis D.S., 1986. *Principles of Applied Geophysics*, Chapman and Hall, London.

Powell C.M., Oliver, N.H.S., Li, Z.X., Martin, D.M., and Ronaszeki, J. 1999. Synorogenic hydrothermal origin for giant Hamersley iron oxide orebodies. *Geology*, v. 27, p. 175-178

Pullammanappallil, S., J.N. Louie, 1994, A generalized simulated-annealing optimization for inversion of first-arrival times. *Bulletin of the Seismological Society of America*, Vol. 84, No. 5, p. 1397-1409

Reynolds, John M., "Chapter 5: Seismic Refraction Surveying." *An Introduction to Applied and Environmental Geophysics*, Second Edition, Wiley-Blackwell, 2011

Rosiere, C.A., and Rios, F.J. 2004. The origin of hematite in high-grade iron ores based on infrared microscopy and fluid inclusion studies: The example of the Conceicao Mine, Quadrilatero Ferrifero, Brazil. *Economic Geology*, v. 99, p. 611-624

Schijns H., Heinonen S., Schmitt D.R., Heikkinen P., Kukkonen I.T., 2009. Seismic refraction traveltime inversion for static corrections in a glaciated shield rock environment: a case study. *Geophysical Prospecting*, Vol. 57, p. 997-1008

Schmitt D.R., Welz M., Rokosh C.D., 2005. High-resolution seismic imaging over thick, permafrost at the 2002 Mallik drill site, in *Scientific Results from the Mallik 2002 Gas Hydrate Production Research Well Program, MackenzieDelta, Northwest Territories, Canada*, edited by S. R. Dallimore, and T. S. Collett. *Bulletin, Geological Survey of Canada* Vol. 584, 14 p.

Scott, D.J., St-Onge, M.R., and Corrigan, D. 2003. Geology of the Archean Rae Craton and Mary River Group and the Paleoproterozoic Piling Group, central Baffin Island, Nunavut. *Geological Survey of Canada, Current Research 2003-C26*, 12 p.

Sirles P., Rock A., Haramy K., 2013. Advancements in 3D Subsurface Modelling Using Seismic Refraction Data – A new Perspective. SEG Online library: <http://library.seg.org/>

Skulski, T., Sandeman, H., Sanborn-Barrie, M., MacHattie, T., Young, M., Carson, C., Berman, R., Brown, J., Rayner, N., Panagapko, D., Byrne, D., and Deyell, C. 2003. Bedrock geology of the Ellice Hills map area and new constraints on the regional geology of the Committee Bay area, Nunavut. *Geological Survey of Canada, Current Research 2003-C22*, 11 p.

Sharma P.V., 1986. *Geophysical Methods in Geology*. Elsevier Science, New York, USA

Stockwell, C.H. 1982. Proposals for time classification and correlation of Precambrian rocks and events in Canada and adjacent areas of the Canadian Shield. 1. A time classification of Precambrian rocks and events. *Geological Survey of Canada, Paper 80-19*

- St-Onge, M.R., Lucas, S.B., Scott, D.J., and Wodicka, N. 1999. Upper and lower plate juxtaposition, deformation and metamorphism during crustal convergence, Trans-Hudson orogen (Quebec-Baffin segment), Canada. *Precambrian Research*, vol. 93, p. 27-49
- Taylor, D., Dalstra, H.J., Hardin, A.E., Broadbent, G.C., and Barley, M.E. 2001. Genesis of high-grade hematite orebodies of the Hamersley province, Western Australia. *Economic Geology*, v. 96, p. 837-873
- Telford W.M., Geldart L.P., Sheriff R.E., Keys D.A., 1990. *Applied Geophysics (2<sup>nd</sup> Edn)*, Cambridge University Press, Cambridge, UK
- Thorne, W.S., Hagemann, S.G., and Barley, M. 2004. Petrographic and geochemical evidence for the hydrothermal evolution of the North deposit, Mt. Tom Price, Western Australia. *Mineralium Deposita*, v. 39, p. 766-783
- Trampert J. and Leveque J., 1990. Simultaneous Iterative Reconstruction Technique: Physical interpretation based on the generalized least squares solution. *Journal of Geophysical Research*, Vol. 95, p. 12553 – 12559
- Van Der Sluis A. and Van Der Vorst H.A., 1987. Numerical solution of large, sparse, linear algebraic systems arising from tomographic problems. In *Seismic Tomography*, edited by G. Nolet (Reidel, Dordrecht), p. 49-83
- White D.J., Two-Dimensional Seismic Refraction Tomography. *Geophysics Journal International*, Vol. 97, Issue 2, p. 223-245
- Wikipedia Commons image files. 2010. Web, Accessed June 10<sup>th</sup>, 2017.  
[https://commons.wikimedia.org/wiki/File:Location\\_map\\_Canada\\_Baffin\\_Island.png](https://commons.wikimedia.org/wiki/File:Location_map_Canada_Baffin_Island.png)
- Williams N., Oldenburg D., 2009. An Automated Sparse Constraint Model Builder for UBC-GIF Gravity and Magnetic Inversions. 20<sup>th</sup> ASEG Conference in Adelaide, 22<sup>nd</sup> - 25<sup>th</sup> Feb. 2009.
- Williams N., Oldenburg D., Lelievre P., 2009. Constraining Gravity and Magnetic Inversions for Mineral Exploration using Limited Geological Data. 20<sup>th</sup> ASEG Conference in Adelaide, 22<sup>nd</sup> – 25<sup>th</sup> Feb. 2009.
- Yao Z., Galbraith M., Kolesar R., 2013. Regular grids travel time calculation – Fast marching with an adaptive stencils approach. CSEG Geoconvention: Integration submission
- Young, M.D., Sandeman, H., Berniolles, F., and Gertzbein, P.M. (2004). A preliminary stratigraphic and structural geology framework for the Archean Mary River Group, northern Baffin Island, Nunavut. Geological Survey of Canada, Current Research 2004-C1, 14 p.
- Zakeski, E., L'Heureux, R.L., Duke, N., Wilkinson, L., and Davis, W.J. 1999. Komatiitic and felsic volcanic rocks overlain by quartzite, Woodburn Lake Group, Meadowbank River area, western Churchill Province, Northwest Territories (Nunavut). In Current Research 1999-C; Geological Survey of Canada, p. 9-18
- Zaleski, E., Davis, W.J., and Sandeman, H.A. 2001. Continental extension, mantle magmas and basement cover relationships. In: Extended Abstracts, 4th International Archean Symposium 2001, (eds.) K.F.

Cassidy, J.M. Dunphy, and M.J. Van Kranendonk. Australian Geological Survey Organization-Geoscience Australia, Record 2001/37, p. 374-376

Zdhanov M.S., 2002. Geophysical Inverse Theory and Regularization Problems, Methods in Geochemistry and Geophysics 36. Elsevier Science B.V., Amsterdam, The Netherlands.

APPENDIX

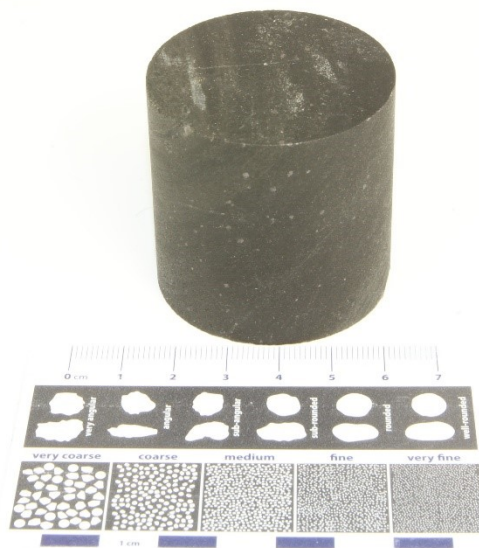
A.1 - CORE PLUG PHOTOS



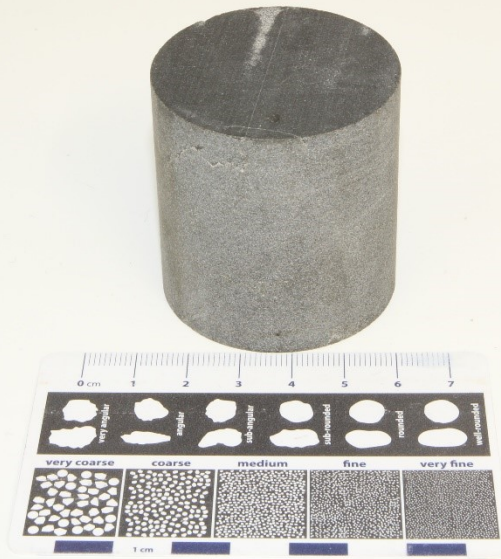
37.2 m



45.7 m



52.8 m



65.1 m



73.5 m



82.5 m



94 m



126 m



134 m



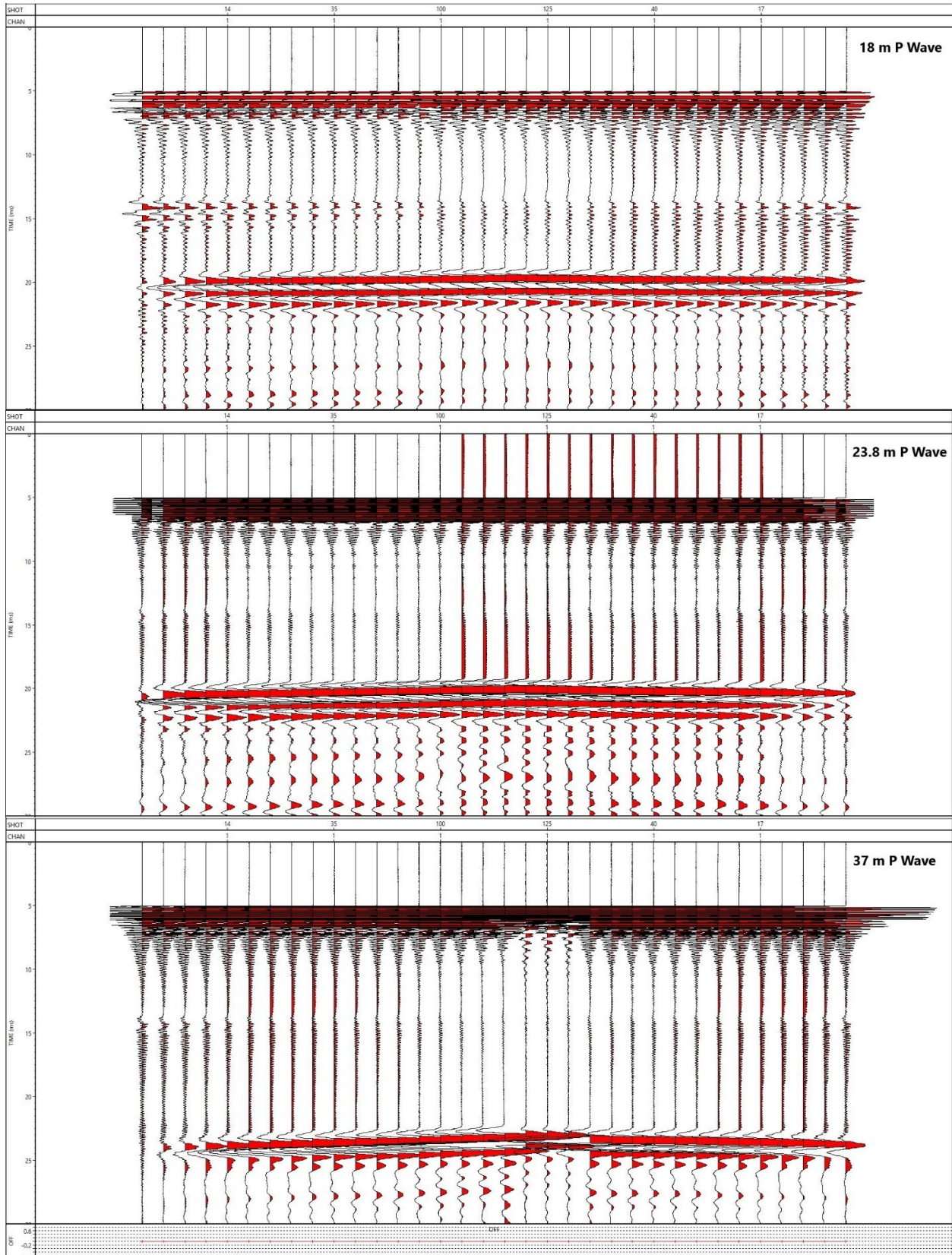
154 m

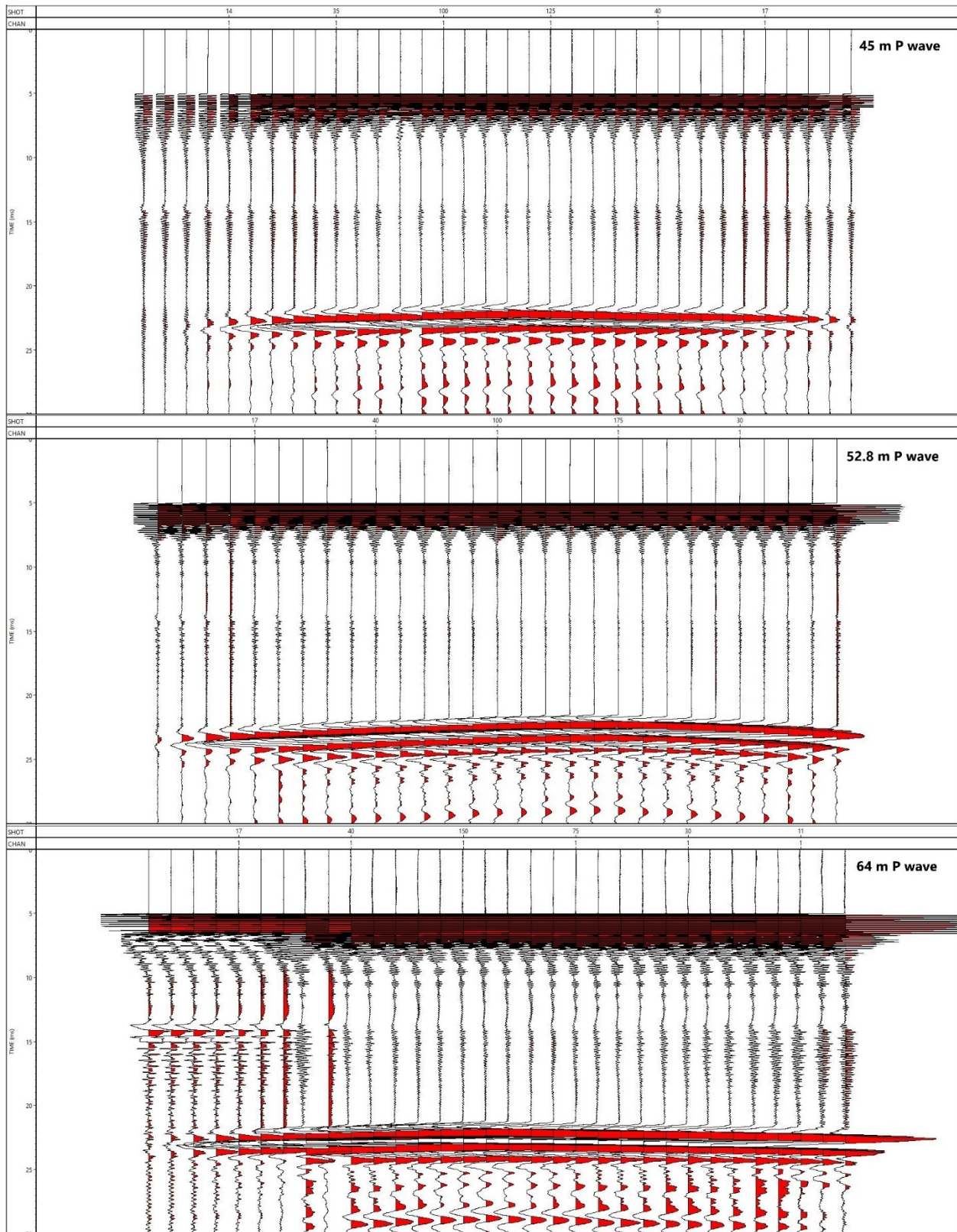


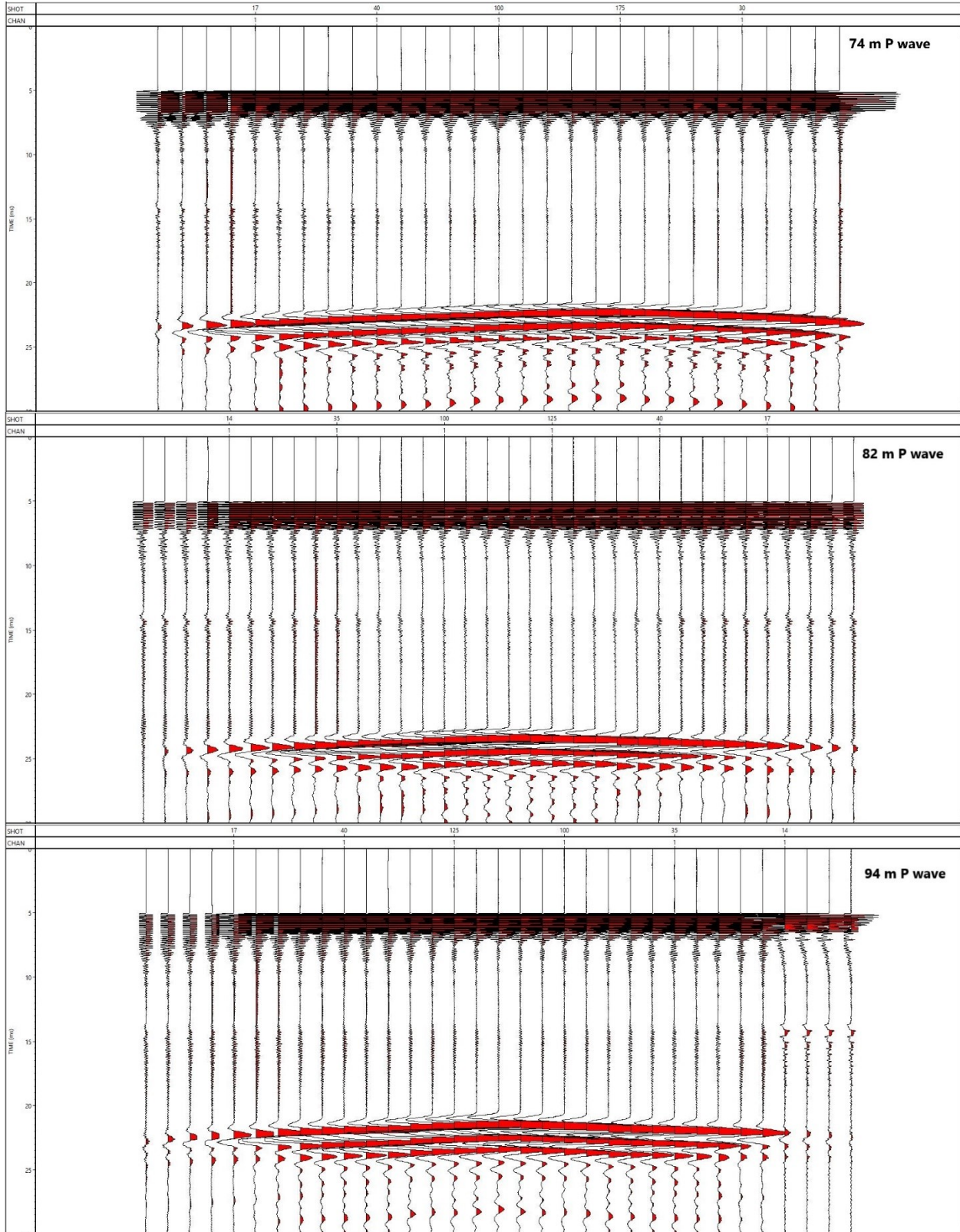
170 m

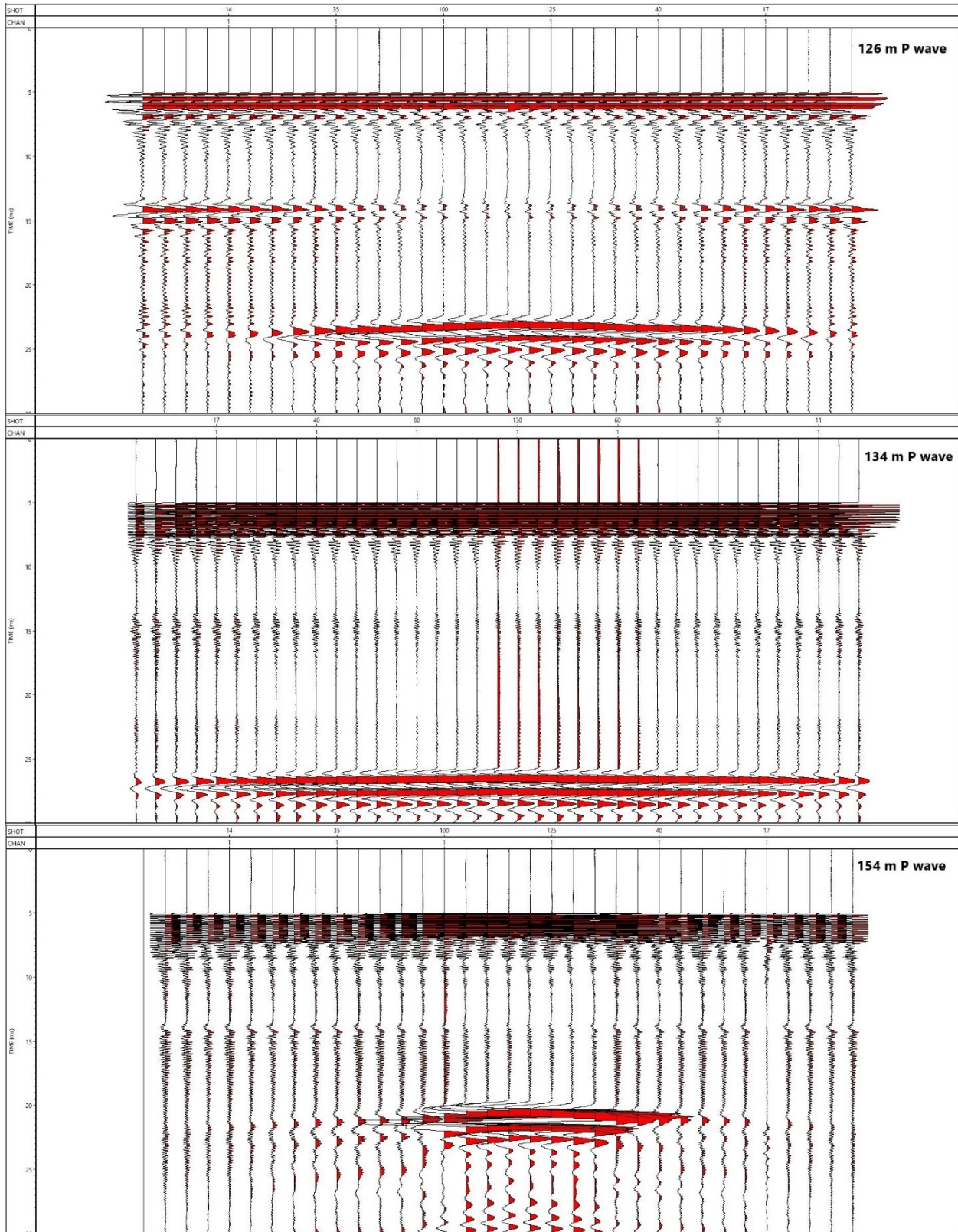


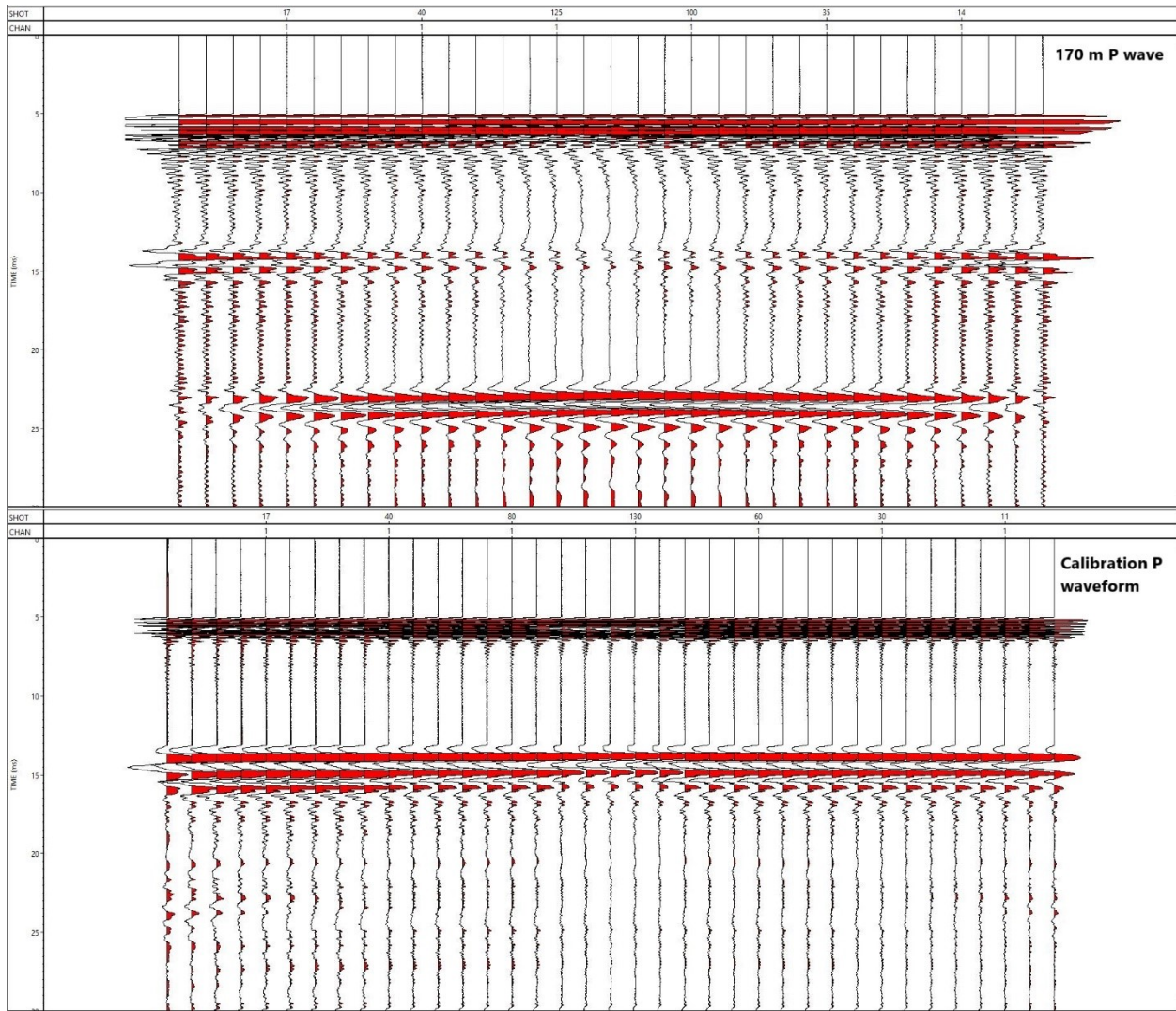
## A.2 COMPRESSIONAL ULTRASONIC WAVEFORMS



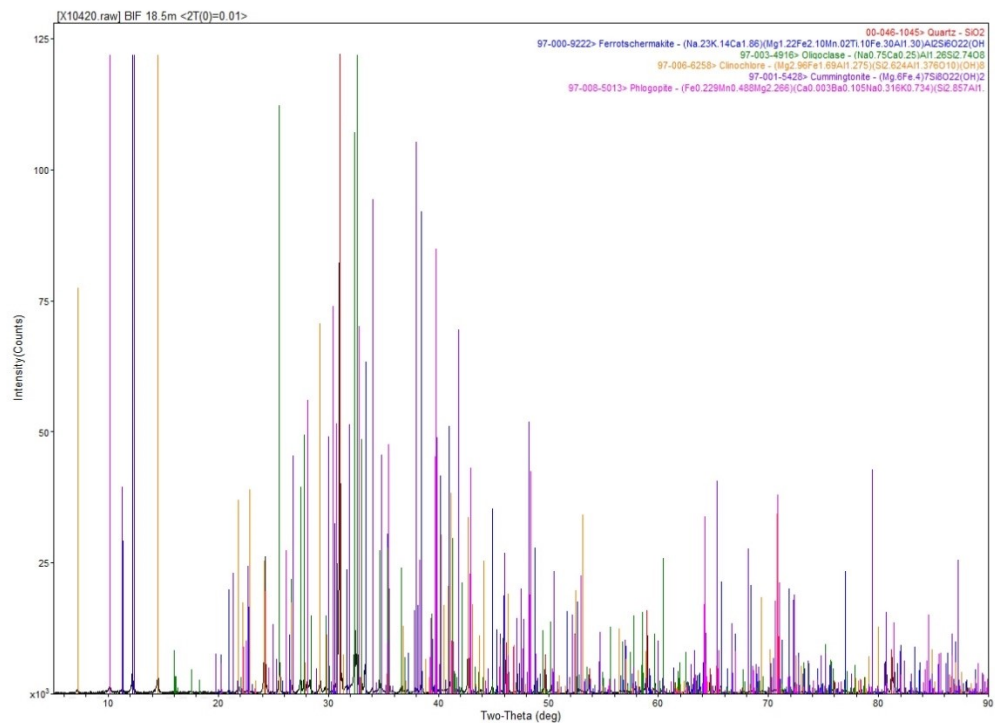






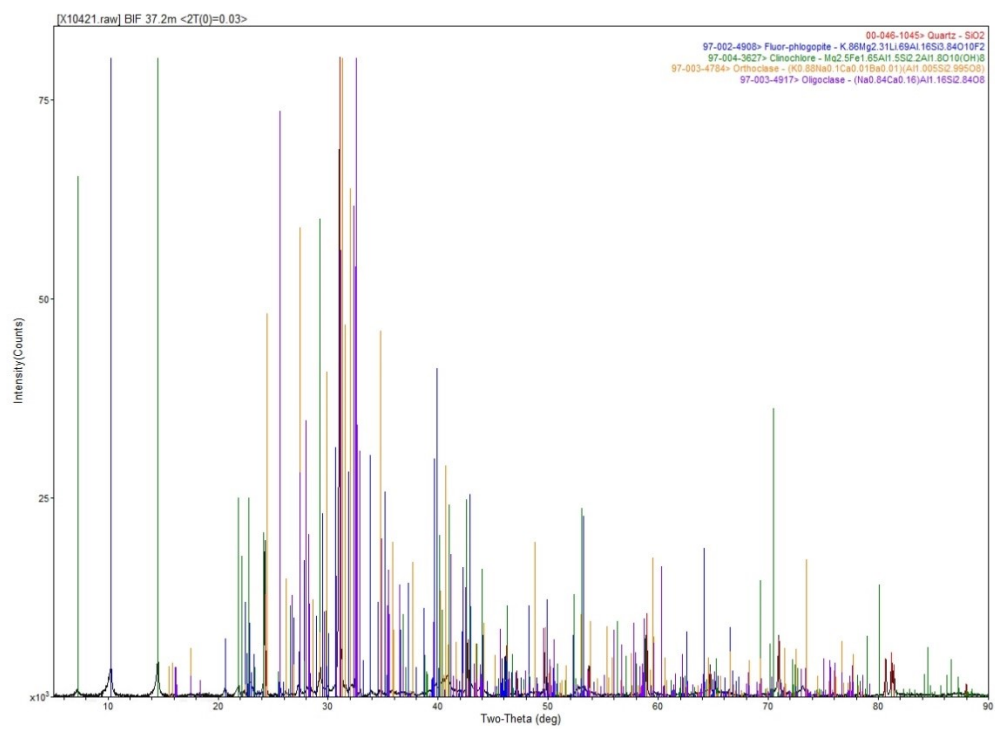


## A.3 XRD SPECTRUMS



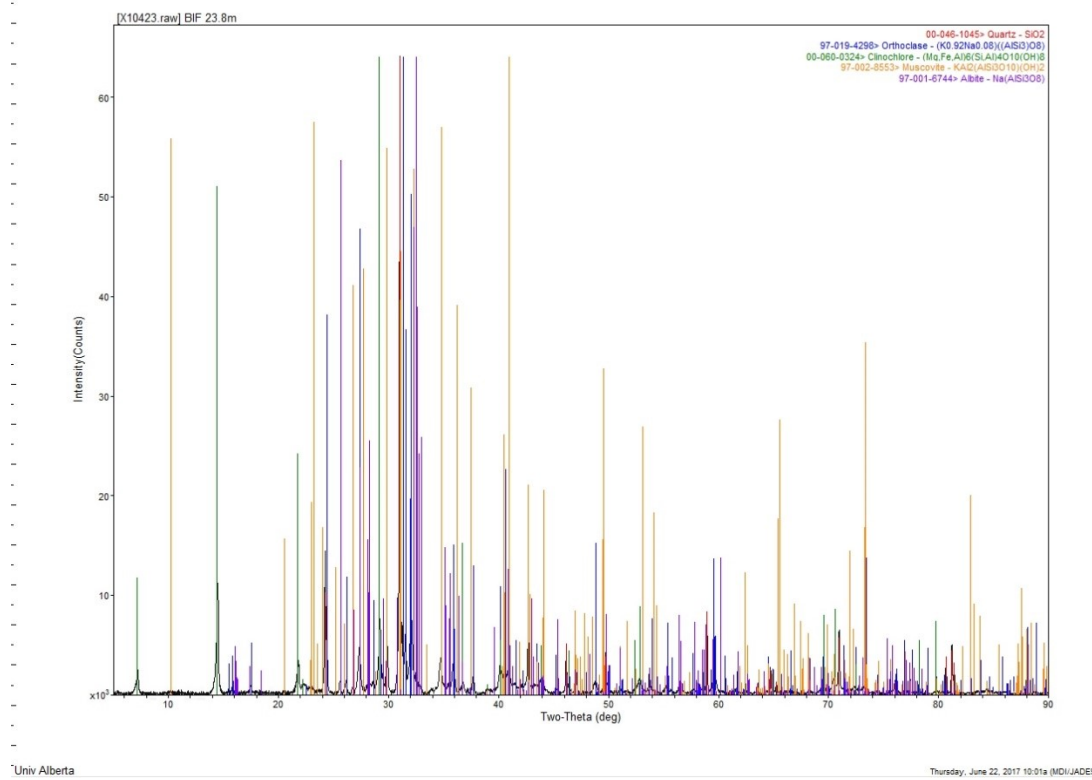
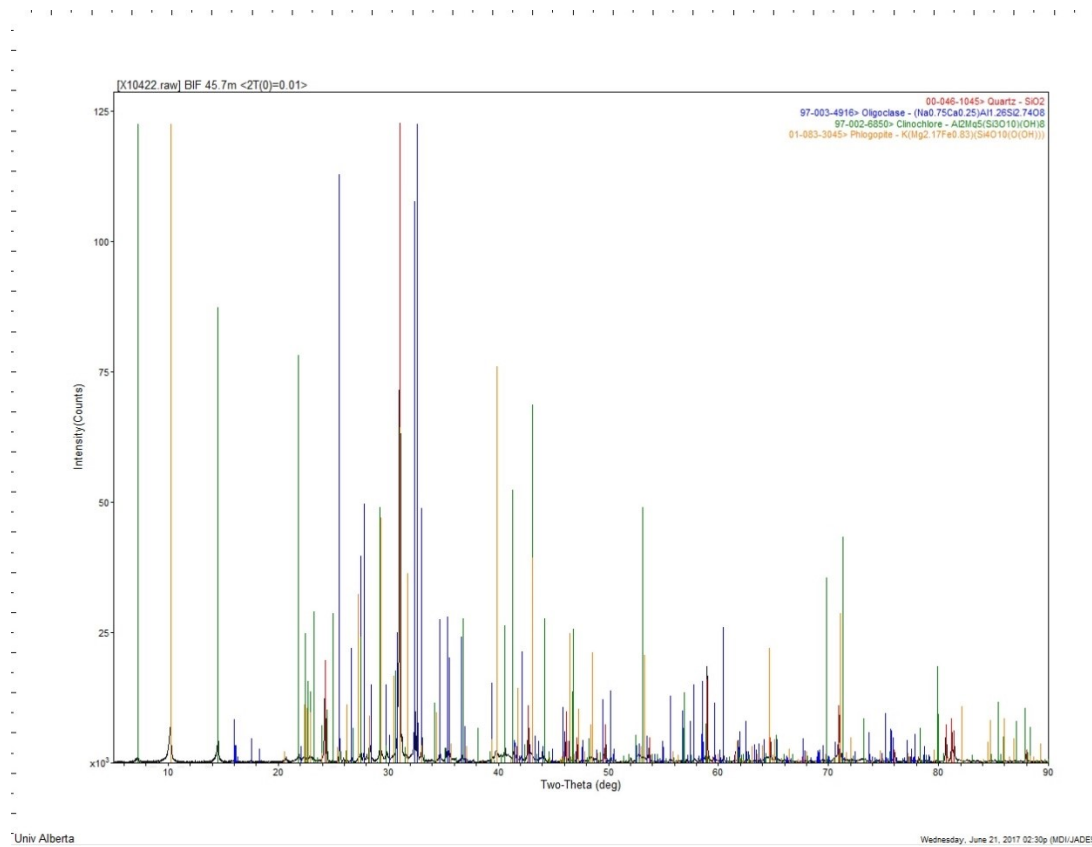
Univ Alberta

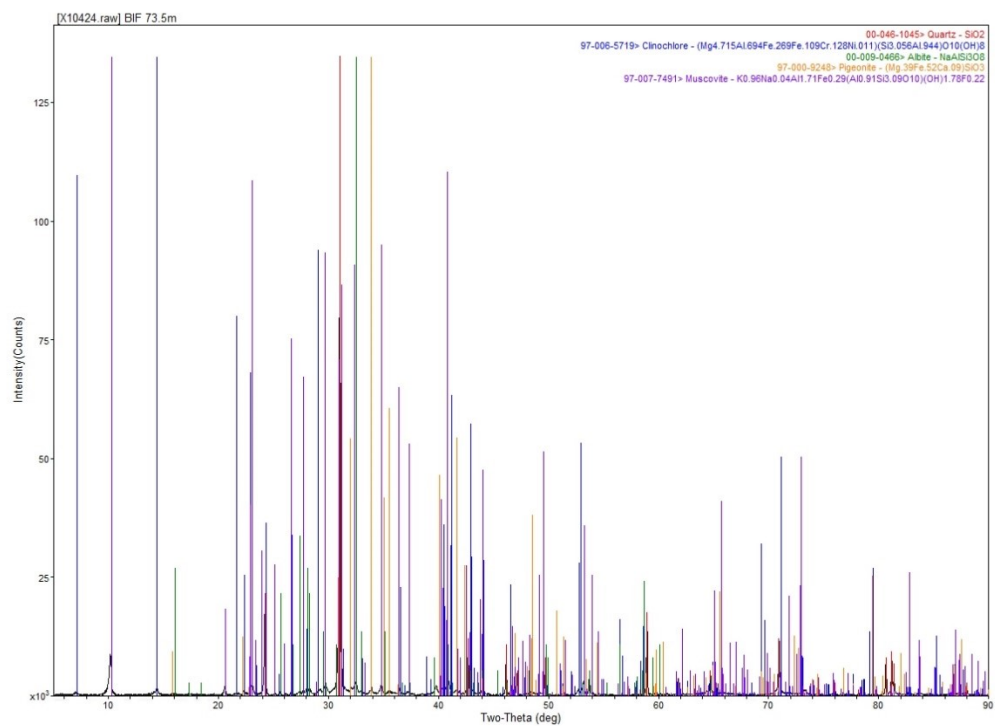
Wednesday, June 21, 2017 01:44p (MDI/JADE)



Univ Alberta

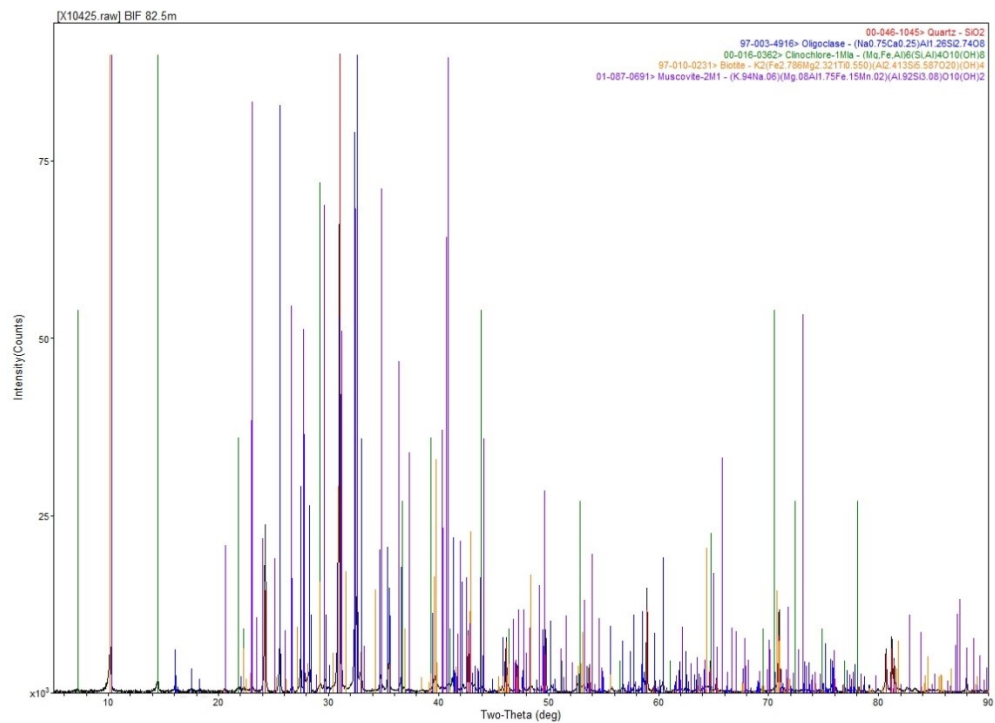
Wednesday, June 21, 2017 01:56p (MDI/JADE)





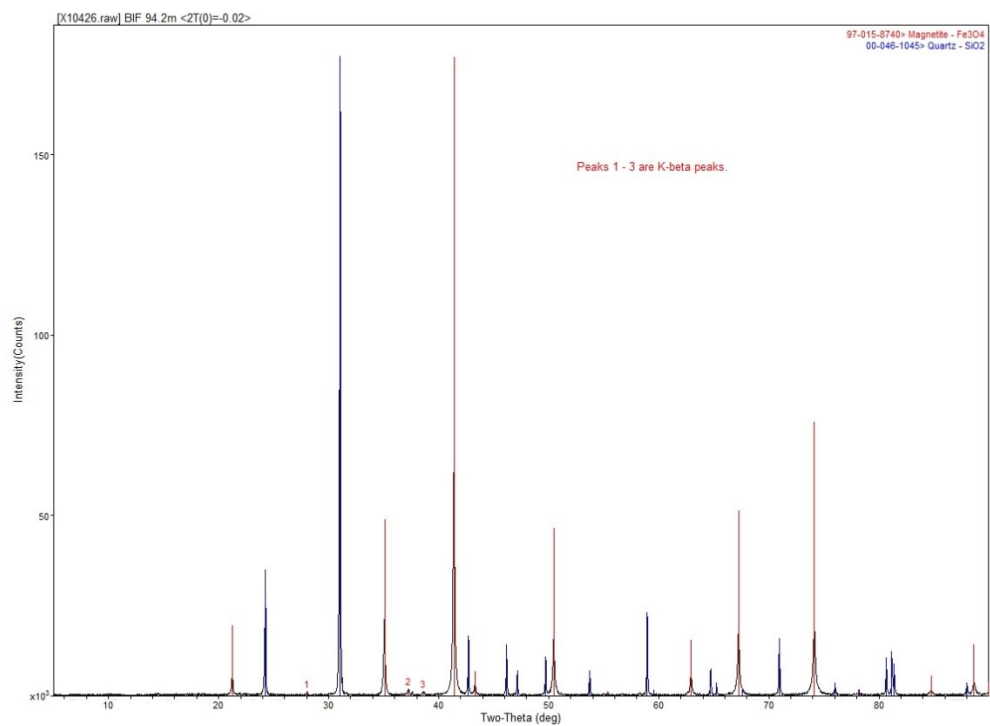
Univ Alberta

Thursday, June 22, 2017 10:32a (MDU/JADE9)



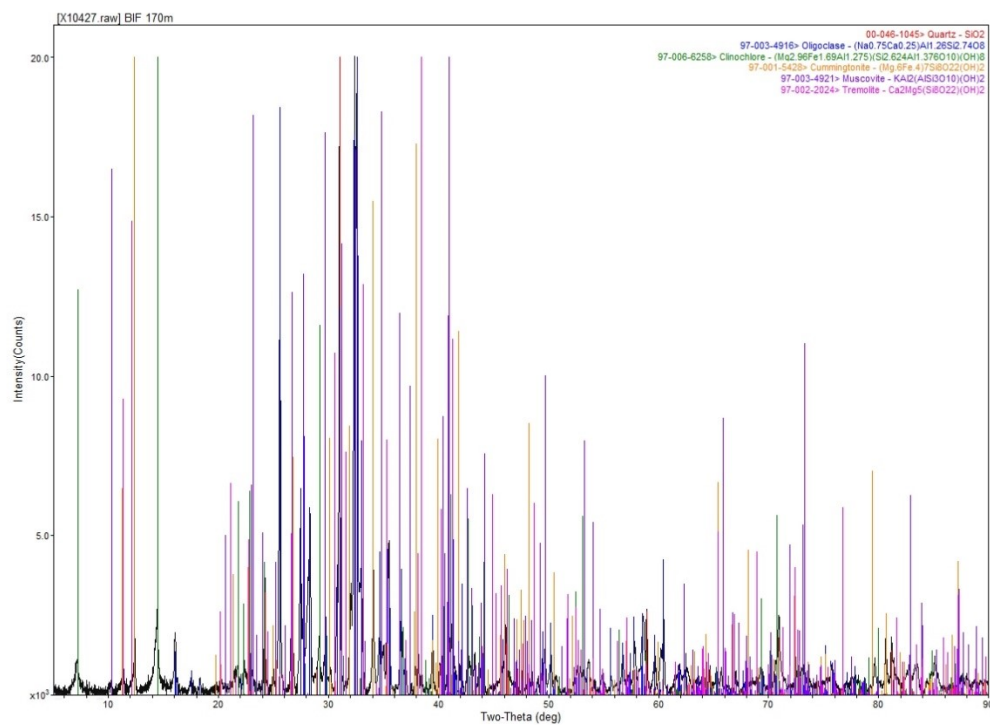
Univ Alberta

Thursday, June 22, 2017 11:15a (MDU/JADE9)



Univ Alberta

Wednesday, June 21, 2017 05:47p (MDU/JADE9)



Univ Alberta

Thursday, June 22, 2017 11:36a (MDU/JADE9)